PREPARATION AND CHARACTERIZATION OF NiO POWDERS AND THIN FILMS

A thesis submitted

by

Patta Ravikumar

to

Indian Institute of Technology Guwahati

in

Partial fulfillment of the requirement for the award of the degree of
Doctor of Philosophy in Physics

Department of Physics
Indian Institute of Technology Guwahati
Guwahati 781 039, Assam, India
December 2017

PREPARATION AND CHARACTERIZATION OF NiO POWDERS AND THIN FILMS

A thesis submitted

by

Patta Ravikumar

to

Indian Institute of Technology Guwahati

in

Partial fulfillment of the requirement for the award of the degree of
Doctor of Philosophy in Physics

Department of Physics
Indian Institute of Technology Guwahati
Guwahati 781 039, Assam, India
December 2017

STATEMENT

The work contained in the thesis entitled "***Preparation and characterization of NiO powders and thin films***" has been carried out by me under the supervision of Prof. Perumal Alagarsamy at the Department of Physics, Indian Institute of Technology Guwahati. This work has not been submitted elsewhere for the award of any degree.

December 2017

(Patta Ravikumar)
Roll No: 11612124
Department of Physics
Indian Institute of Technology Guwahati
Guwahati – 781039
India.

CERTIFICATE

It is certified that the work contained in the thesis entitled "***Preparation and characterization of NiO powders and thin films***" submitted by Patta Ravikumar, a Ph.D. student of the Department of Physics, Indian Institute of Technology Guwahati for the award of degree of Doctor of Philosophy has been carried out under the supervision of Prof. Perumal Alagarsamy. This work has not been submitted elsewhere for the award of any degree.

December 2017

(Dr. Perumal Alagarsamy)
Professor
Department of Physics
Indian Institute of Technology Guwahati
Guwahati – 781039
India.

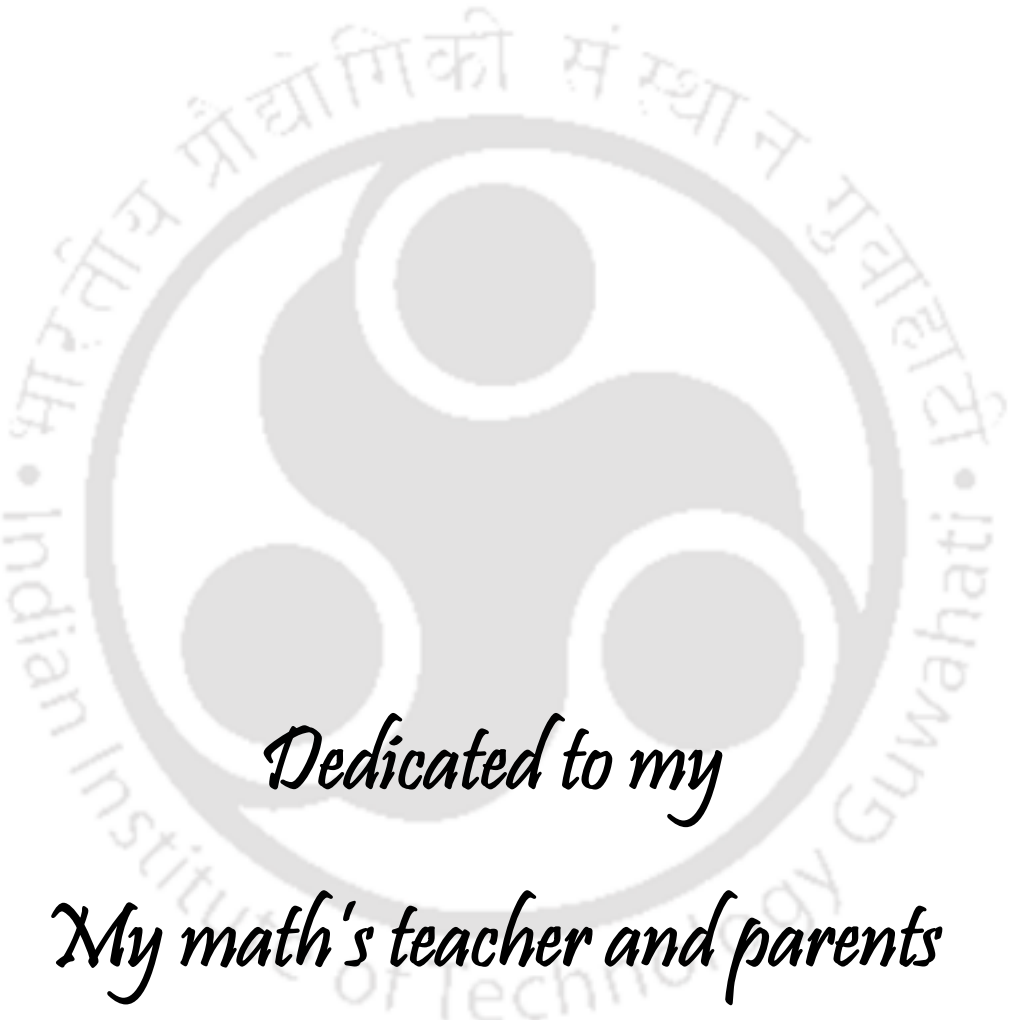

Dedicated to my

My math's teacher and parents

ACKNOWLEDGEMENTS

This thesis is the end of my journey in obtaining my Ph.D. This thesis has been kept on track and been seen through to completion with the support and encouragement of numerous people including my well-wishers, my friends and colleagues. At the end of my thesis, I take this opportunity to acknowledge them and extend my sincere gratitude to all those who contributed in many ways to the success of this study and made it an unforgettable experience for me.

At this moment of accomplishment, first of all I would like to express the deep sense of gratitude to my guide, Prof. Perumal Alagarsamy. This work would not have been possible without his guidance, support and encouragement. Under his guidance I successfully overcame many difficulties and learned a lot.

I am grateful to my doctoral committee members, Dr. D. Pamu, Dr. Dilip Pal, Prof. Sandip Paul for reviewing my research work regularly and providing valuable comments & suggestions for the improvement of my research work. I am thankful to current HOD, Department of Physics, Prof P. Poulose, and Prof. S. Basu, and Prof. S. Ravi, the former HODs, Department of Physics for their immense support. I extend my whole hearted thanks to all the faculty members of Physics department, who supported me in several ways during my research life in IIT Guwahati. I am thankful to IIT Guwahati for providing me financial assistantship during the research period.

I express my sincere thanks to Dr. Sidananda Sarma, scientific officer in the department of physics, for guiding me to handle various high precision instruments in the department of physics. Also, I thank Mr. Chandan Borgohain, Dr. Kula Kamal Senapati, Mr. Madhurjya Borah and Mr. Kesho Singh, the scientific officers of CIF, who have patiently and enthusiastically extended their expertise in handling various instruments that I have used for my research work.

I would like to acknowledge my lab seniors Bhagaban Kisan and Dr. P.C. Shyni for all their support and motivation during the initial days of my stay in the lab. Dr. Santhosh, Anabil, Camelia, Gobinda, Jumal (passed away), Dolly, Arnab, Rajkumar, Pratap, Bipul, Bibhuti, Dr. Junmoni, Dr. Mahesh and all other research scholars of Physics department always be remembered for the wonderful time we have shared together.

My acknowledgement will never be completed without the special mention of my special Telugu team. Big thanks to Rajender, Ranganadha, RamaKrishna, Venkanna, Jagan,

Srinivas for memorable life in IITG campus. The chit-chats we had near tea stalls and the funny moments we shared during those times will remain as unforgettable moments of my IITG life.

My heartfelt thanks to my school maths teacher, Mr. S. Naidu, who made me to believe in myself by his teaching skills. His way of teaching increased my confidence and motivated me to pursue physics.

I owe a lot to my parents, Mr. P. Suryanarayana and Mrs. P. Jaya who encouraged and helped me at every stage of my personal life, and longed to see this achievement come true. Their hard work and dedication in helping me to pursue higher studies is the strongest source of inspiration for me. I am very much indebted to my wife S. Madhuri, who supported me in every possible way to see the completion of this work. I would like to acknowledge the support received from my brothers, sister in law and my mother in law.

I am thankful to all my childhood friends especially Dr. Rajesh and Sarvaji for their well wishes and always being there in my ups and downs. I am thankful to my teachers for their kind blessings which motivated me to complete this voyage. Also, my sincere thanks to all those, who have been helped me in whatever manner and bring me to this position, some of whom I may have inadvertently forgotten to mention in this acknowledgement.

Patta Ravikumar

PREFACE

More, faster, better, cheaper are the modern mantras and demands of our device-happy and data-centered world. To achieve these, one requires technologies for processing and storing information. Two of the most successful technologies in existence today have created the semiconductor device industry and the data storage industry. Even though the semiconductor devices comprise high speed signal processing and excellent reliability, the memory elements are volatile due to data stored as charge in capacitors. On the other hand, the key advantage of magnetic memory technologies is that they are non-volatile since they employ ferromagnetic (FM) materials. This directs that bridging semiconductor and magnetism is necessary because it would provide new opportunities of utilizing spin degrees of freedom in semiconductor devices. As a result, a new field of research, called spintronics, is focused in multidisciplinary level and intensified by a strong cooperation between breakthroughs in basic science and industrial applications in the fields of magnetic recording, nonvolatile memories, semiconductor spintronics, etc.

Spintronics exploits both the intrinsic spin of the electron and its associated magnetic moment in addition to its fundamental electronic charge. As we add the spin degree of freedom, it provides significant versatility and functionality to future electronic products with several advantages like non-volatile, increased data processing speed, decreased electric power consumption and increased integration densities. In particular, the spintronics based on diluted magnetic semiconductors (DMS) provides a new technology that transforms reading and writing information for many uses by spin rather than by typical electronic charge. Hence, DMS materials are considered as one of the new kind of materials for spintronic applications, especially those materials whose Curie temperature (T_C) is above room temperature. In addition, DMS of nanocrystalline oxides are especially attractive due to their unique properties and finding applications in catalysis, sensor, optoelectronic devices, etc. There are two major criteria for selecting DMS materials for semiconductor spintronics: (i) FM in the materials should be retained to practical temperatures (> 300 K) and (ii) materials having semiconducting nature with tunable properties. Sundaresan et al proposed that FM behavior in nanoparticles of non-magnetic oxides is a universal feature and confined to the surface of the nanoparticles.

Among all other oxide based materials, Nickel-Oxide (NiO) based nanoparticles and thin films have been focused to obtain FM above room temperature such that these oxides with cubic structure could facilitate integration of spintronic devices. NiO is a *p*- or *n*-type

of semiconductor depending on the oxygen vacancies with tunable band gap (~4 – 4.3 eV). It is also an insulator with high resistivity of 10^{13} Ωm and behaves antiferromagnetically below the Néel temperature (T_N = 525 K). Néel suggested that fine particles of NiO should exhibit either a weak FM or superparamagnetism (SPM). Richardson et al reported the first investigation on the size dependent magnetic properties of NiO. Extensive studies have been reported over last decades on particle size dependent magnetic properties, finite size versus surface effects on magnetic properties, effect of substitution and room temperature magnetic crossover of NiO prepared by various techniques. The literature review from different groups reveals that most of the reported investigations are bottom-to-top approach summarizing that the resulting magnetic properties are significantly complex in nature. However, the approach of top-to-bottom method for studying the magnetic properties of un-milled NiO without any impurity phases are limited. Recently, Kisan et al reported finite size effects in magnetic and optical properties of AFM NiO nanoparticles without any detectable impurities. But, the systematic investigations of effect of milling conditions on the improvement of magnetic properties have not been reported.

Similarly, NiO based thin films have received much attention for emerging applications of the next generation devices. Interestingly, NiO thin films show unusual properties depending on the fabrication methods and growth conditions. For instance, Sugiyama et al reported that dislocations in NiO crystals show unique magnetic properties. Jang et al reported that electrical properties of sputtered NiO thin films are enhanced due to defects. Yang et al shown that non-stoichiometric in NiO thin films diffuses out during annealing and tunes the electrical, chemical and optical properties. Bruckner et al reported that the sputtered NiO films decompose into thermally stable oxygen poorer NiO and/or metallic Ni during high temperature annealing. Kawai et al reported that annealing of NiO films above 400 °C under high vacuum produces conducting filaments in single crystalline NiO. But, Jang et al reported that the decomposition reaction of NiO strongly depends on annealing temperature (T_A) and thickness of the films (t). However, the effect of thickness dependent decomposition on the vibrational and magnetic properties are not reported in detail.

The direct deposition of NiO thin film on to a substrate results in defects, vacancies and finite size particles and hence the exact control of amount of oxidation in the NiO becomes difficult. The alternative method of fabricating metal oxide thin films is thermal oxidation of the metallic thin films, which has been proven to be an easy *ex situ* technique

to obtain metal oxide films and to improve metal crystallization. It may be noted that there are only a few reports on oxidation evolution of Ni thin films at higher temperatures (> 900 °C). Recently Valladares et al studied thermal oxidation of 50 nm thick Ni thin films fabricated by conventional thermal evaporation process. As Jang et al [JANG2011] reported that the decomposition reaction of NiO strongly depends on T_A and t, the thermal oxidation behaviour of Ni thin films may also depend on t and T_A. But, there is no report on the oxidation process of Ni thin films as a function of t, the nature of oxidation mechanism and its effects on the vibrational, magnetic and electrical transport properties.

Therefore, this thesis work aims (i) to prepare NiO powders using ball mill process in a high-energy planetary ball mill with different milling speeds (t_s) and to understand the evolution of nanocrystalline microstructure as a function of t_s and T_A on the resulting vibrational, electronic, magnetic and resonance properties, (ii) to prepare NiO target from the milled NiO powders under different t_s and fabricate NiO thin films with different thicknesses (t = 50 - 300 nm) using magnetron sputtering technique. Subsequently, the thickness dependent thermal decomposition reaction of NiO will be studied by annealing the as-deposited NiO films at different T_A under various (vacuum and air) atmospheres to understand the structural, microstructural and magnetic properties of NiO films, (iii) to prepare Ni thin films with different thicknesses and investigate the effect of film thickness on the thermal oxidation process, nature of thermal oxidation mechanism and the resulting vibrational, magnetic and electrical transport properties, and (iv) to analyze the correlation between the structural, microstructural and physical properties of as-milled NiO powders, as-deposited and annealed NiO and Ni thin films.

Chapter 1 presents a detailed review of the literature relevant to the present thesis work and the motivations and objectives of the thesis work. In **Chapter 2**, the crystal structures, understanding of various types of defects, intrinsic and extrinsic origin of FM in NiO are discussed. The fundamental aspects of magnetism and various theoretical methods employed in the analysis of the data of the presently investigated samples are also summarized in this chapter. **Chapter 3** deals with the experimental techniques including the sample preparation methodologies used in the present study. The basic principle and theory behind the experiments, the experimental set up and measurement/methodology used for the determination of different properties are also briefly described.

In **Chapter 4**, the effects of t_s on the evolution of nanocrystalline microstructure and the resulting vibrational, electronic, magnetic and resonance properties of NiO powders

prepared by ball milling process in a high-energy planetary ball mill are reported. The ball mill process produces single phase face centered cubic (*fcc*) nanocrystalline NiO powders with the average crystallite size of nanometer range without any impurities within the detection limit of the techniques utilized. The average crystallite size decreases and lattice constant increases with increasing t_s. Microstructural studies reveal that the agglomeration of fine particles increases with increasing t_s and the nanocrystalline powders exhibit irregular shapes with broad size distribution. Raman spectra show that two-magnon band associated with Ni^{2+}-O^{2-}-Ni^{2+} super-exchange interaction and observed in pure un-milled NiO powder disappears dramatically, 1P LO band dominates along with notable broadening, 2P TO and 2P TO+LO bands disappear, 2P LO band broadens and shifts to lower value of Raman shift in milled NiO powders due to defects, size reduction and size-induced phonon confinement. This changes the color of the powder from the pale green for pure un-milled NiO into dark green for milled NiO powders due to non-stoichiometry, which is evidenced clearly from X-ray photoelectron spectroscopy (XPS) spectra. AFM nature of the un-milled NiO powders transforms into induced FM after milling due to defects and size reduction. The average room temperature magnetization increases with increasing t_s and attained a maximum magnetization of 1.26 emu/g at 12 kOe applied field for the NiO powders milled at 600 rpm. High temperature magnetization obtained in the temperature range between 300 K and 1000 K shows a well-defined magnetic phase transition at high temperature around 780 K due to induced FM phase. Electron paramagnetic resonance (EPR) results disclose a close correlation with magnetic properties. Annealing of as-milled NiO powders results in a large reduction in magnetization, but the rate of reduction in magnetization strongly depends on the milling conditions. Furthermore, the annealing studies confirm the origin of FM as intrinsic one due to defects, size reduction and non-stoichiometry.

In **Chapter 5,** we report the effects of initial crystallite size of the target powders, NiO film thickness and T_A under different environments on the decomposition reaction of NiO into Ni and the resulting magnetic properties of the NiO films deposited directly on thermally oxidized Si substrate using magnetron sputtering technique at ambient temperature. All the as-deposited NiO films exhibit *fcc* structure and highly orient along (200) plane. The as-deposited NiO films show large lattice constant due to the existence of interstitial argon atoms in the sputtered films and/or increase of nickel vacancies created from the non-stoichiometry. With increasing T_A, the lattice constant and strain decreases due to the release of interstitial argon atoms. The observation of thickness dependent decomposition reaction of NiO into Ni under vacuum annealing could be explained based

on the ideal model. However, the decomposition reaction is completely suppressed for the NiO films annealed under oxygen condition. The effect of initial crystallite size of the target powders on the thermal decomposition of the sputtered NiO films reveals a considerable decrease in the decomposition temperature (by about 100 °C) for the NiO films. All the as-deposited and annealed NiO films up to 400 °C (300 °C) under vacuum condition prepared from the NiO target made using 350 (600) rpm milled NiO powders show only AFM nature. On further increasing T_A, NiO decomposes into Ni and exhibits room temperature FM. The amount of induced FM strongly depends on the NiO film thickness. On the other hand, NiO thin films annealed at 500 ℃ under oxygen atmosphere exhibit only AFM nature. A close correlation between the structural and magnetic properties is observed for all the NiO films. The observed results are explained on the basis of thickness dependent thermal decomposition with increasing T_A under different environments.

Chapter 6 discusses the development of NiO thin films through alternative method of thermal oxidation of Ni thin films under air atmosphere. The effect of film thickness in the as-deposited Ni films and thickness dependent oxidation process in annealed Ni films and the resulting vibrational, magnetic and electrical properties of the Ni films deposited directly on thermally oxidized Si substrate using magnetron sputtering technique at ambient temperature are reported. All the as-deposited Ni films exhibit *fcc* structure and highly orient along (111) plane. The as-deposited Ni films show smaller crystals with large lattice constant at lower films thickness (< 50 nm) and the lattice constant decreases with increasing *t* approaching to its bulk value. With increasing T_A, the lattice constant decreases towards bulk Ni value due to the improvement in crystallization and further reduces below bulk Ni value for thickness more than 50 nm due to the formation of NiO phase caused by the oxidation process. The relative fraction of Ni and NiO phases in annealed films up to 400 °C strongly depends on the thickness due to thickness dependent oxidation process. Annealing Ni films at 500 °C results into complete oxidation of Ni into granular type NiO films. XRR studies reveal that the thermal oxidation process occurs from the surface of the films converting Ni into NiO through layer by layer process, which is again subtle to the thickness of the films. Raman spectra show that the intensity ratio between the 1P LO band and 2P LO band decreases and intensity of 2M band increases with increasing *t* for the films annealed at particular T_A. This suggests the growth of the NiO grains not only increases with increasing T_A, but also with increasing *t*. As-deposited films exhibit FM at room temperature. The presence of Ni and NiO crystallites in the annealed films implies

coexistence of FM and AFM interactions, leading to tunable exchange bias under zero-field-cooled and field-cooled conditions. The amount of exchange bias strongly depends on the ratio of Ni to NiO phases in the annealed Ni films. The electrical resistance of the as-deposited Ni films decreases largely with increasing *t* and follows the model proposed by Namba. Upon annealing, the resistance increases largely due to the formation of NiO phase. Furthermore, the increase in resistance strongly on *t* due to thickness dependent oxidation process. A close correlation between the structural, magnetic and electrical resistance properties is observed for all the as-deposited and annealed films. The observed results are explained on the basis of thickness dependent thermal oxidation process with increasing T_A.

The systematic investigations have brought out several interesting results which contribute to (i) the understanding of physical properties in nanocrystalline NiO powders under different milling speed conditions and (ii) the study of thickness dependent thermal decomposition of NiO into Ni and thickness dependent thermal oxidation of Ni into NiO and the resulting FM properties with tunable competing exchange interaction between Ni and NiO phases. These studies have also revealed the strong correlation between structure, vibrational, electronic, magnetic, resonance and electrical properties of NiO prepared under optimum conditions. **Chapter 8** provides the summary of the results obtained in the thesis and suggests possible directions of future work.

CONTENTS

Chapter 1

Prologue

1.1. Introduction

More, faster, better, cheaper are the modern mantras and demands of our device-happy and data-centered world. To achieve these, one requires technologies for processing and storing information. Two of the most successful technologies in existence today have created the semiconductor device industry and the data storage industry. While high-volume information-processing and communication devices are at present based on semiconductor devices, the information storage devices rely on multilayers of magnetic materials and insulators [HEDI2014, SHIN2014, SATO2015, SCHA2016]. Both continue to advance at a rapid pace. Although the semiconductor devices comprise high speed signal processing and excellent reliability, the memory elements are volatile, i.e., the stored information is lost when the power is switched-off, as data are stored as charge in capacitors. On the other hand, the key advantage of magnetic memory technologies is that they are non-volatile since they employ ferromagnetic (FM) materials, which by nature have tunable remanence. This insinuates that bridging semiconductor and magnetism is necessary because it would provide new opportunities of utilizing spin degrees of freedom in semiconductor devices.

Therefore, the new field of research, termed as spintronics, is focused in multidisciplinary level and intensified by a strong synergy between breakthroughs in basic science and industrial applications in the fields of magnetic recording, nonvolatile memories, magnetic field sensors, semiconductor spintronics, etc [SATO2015, XUY2015, BAND2016, SCHA2016]. In spintronics, the intrinsic magnetic property of the electron, its spin, is used for switching purpose in an electronic circuit instead of its charge. Once we add the spin degree of freedom to conventional charge based electronics, it will provide significant versatility and functionality to future electronic products with several advantages like non-volatile, increased data processing speed, decreased electric power consumption and increased integration densities. Thus, the operation principle of spintronic devices is based on completely different physical phenomena compared to their charge-based counterparts. In addition, the design of materials that combine semiconducting behavior with robust magnetism is very crucial and has long been a dream of materials physics. Figure 1.01 displays the typical phenomena and devices based on spintronics [ANDO2015]. Recently, the scope of spintronics has been expanding progressively and includes a phenomenon that relates the flow of spins with heat flow (called as spin-caloritronics) and high-frequency spintronics (called as magnonics) based on the extension of spin dynamics using lights. The road maps of various research fields of spintronics have been proposed by

Japan Society of Applied Physics. The typical academic roadmap for spinelectronics is shown in Figure 1.02 [HTTP0001].

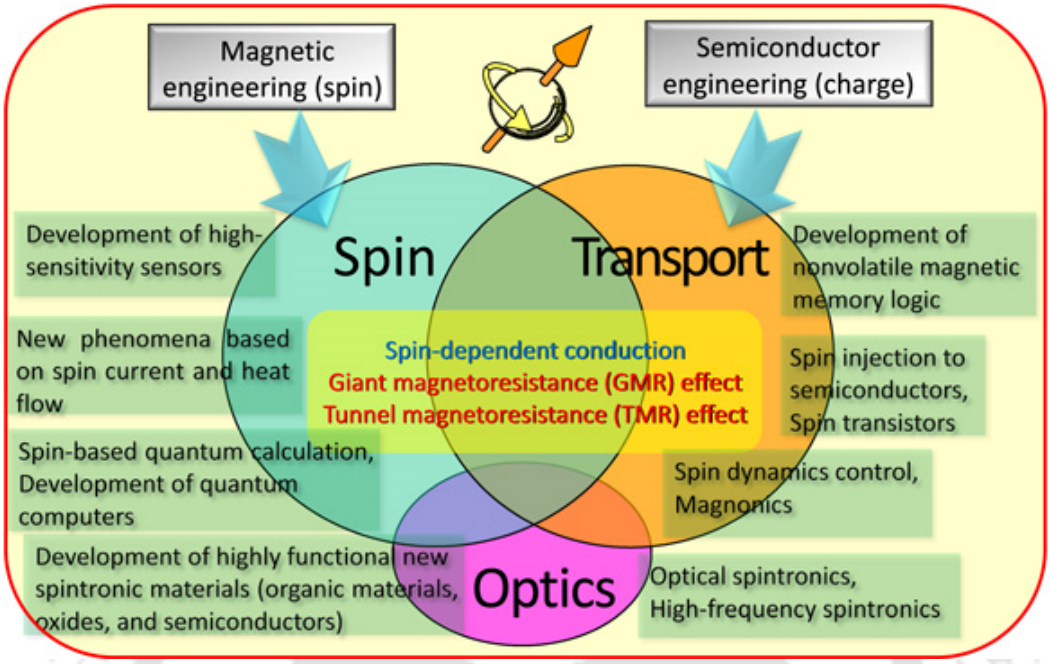

Figure 1.01: Conceptual diagram of spintronics [ANDO2015].

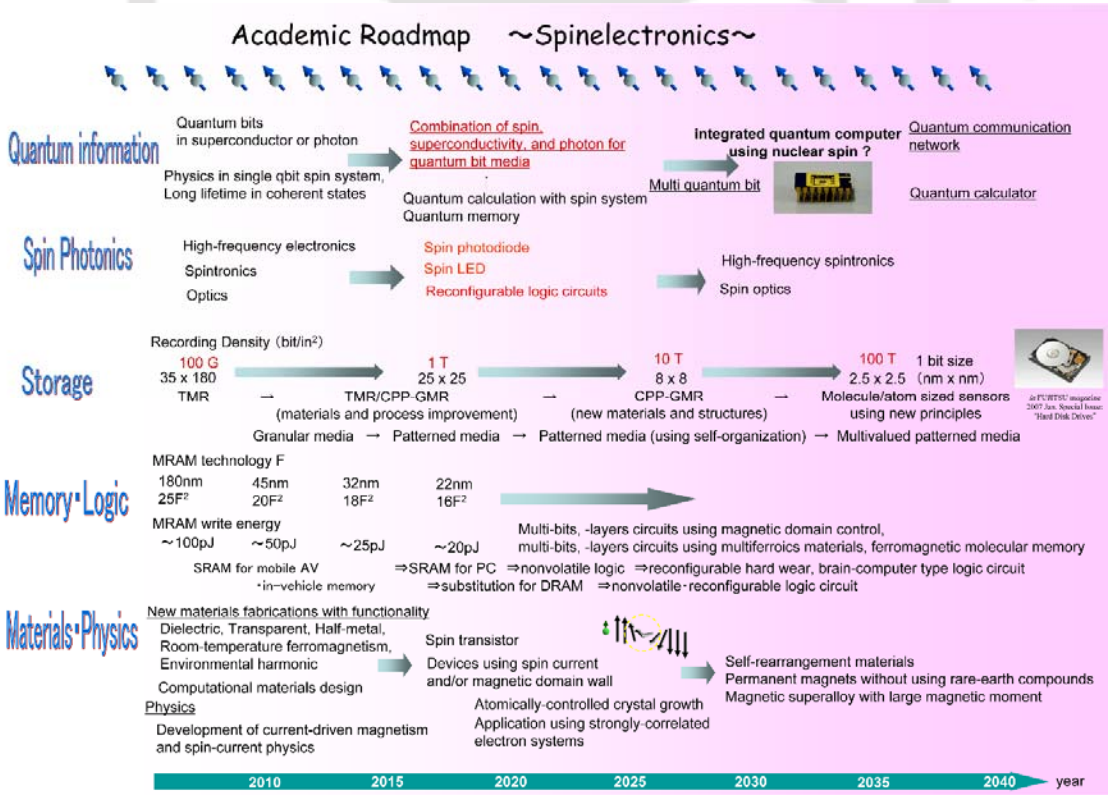

Figure 1.02: Academic roadmap for spinelectronics [HTTP0001].

The key elements of semiconductor spintronics are injection, manipulation, transfer and detection of spin-polarized carriers across a semiconductor device. Although there have been recent reports of successful and efficient spin injection from a metal to a semiconductor by ballistic transport at room temperature [TSYM2016], the realization of functional spintronic devices requires materials with ferromagnetic ordering at operational temperatures compatible with existing semiconductor materials. Thus, the topic of diluted magnetic semiconductor (DMS) has received extensive interest for spintronics [DIET2000, PEAR2003, LIUC2005]. In addition, DMS of nanocrystalline oxides are especially attractive due to their unique properties and finding applications in catalysis, sensor, optoelectronic devices, etc [OHNO1998, DIET2000, MATS2001, UEDA2001, RODE2003, SHAR2003, SHIN2003, WUJB2003, COEY2004, RAMC2004, SHIN2004, LINY20061].

1.2. Motivation behind the work

With the recent advances in the development of several spintronics devices based on the DMS materials, it is very much essential to study the properties of metal-oxide based DMS materials. There are two major criteria for selecting the most promising materials for semiconductor spintronics: (i) ferromagnetism in the materials should be retained to practical temperatures (> 300 K) and (ii) materials having semiconducting nature with tunable properties. Sundaresan et al proposed that FM behavior in nanoparticles of non-magnetic oxides is a universal feature and confined to the surface of the nanoparticles [SUND2006, SUND2009]. Among all other oxide based materials, Nickel-Oxide (NiO) based nanoparticles and thin films have been focused to obtain FM above room temperature such that these oxides with cubic structure could facilitate integration of spintronic devices where both charge and spin are used to transport, store and process information in novel ways [HUNG2017]. NiO is a *p*- or *n*-type of semiconductor depending on the oxygen vacancies [STAM2008] with tunable band gap (~4 – 4.3 eV). It is also an insulator with high resistivity of 10^{13} Ωm and behaves antiferromagnetically below the Néel temperature (T_N = 525 K). Néel suggested that fine particles of AFM nature should exhibit either a weak FM or superparamagnetism (SPM) [NEEL1962]. However, the exact contributions of various factors to the FM properties in NiO systems are still debatable. Nevertheless, the study of magnetism and magnetic interaction in NiO materials, as listed in Table 1.01, has generated much attention. But, the practical applications of these oxide materials are

strongly challenged by its low reproducibility of room temperature FM and controversial observations concerning over the origin of FM in DMS materials.

Table 1.01: Room temperature FM NiO with different preparation methods.

Materials	**Processing Method**	H_C **(Oe)**	M_S	**References**
NiO nanoparticles	Ball milling	259	0.06 emu/g	[MISH2004]
NiO nanorods	Sol-gel	620 at 5 K	---	[SEEH2005]
Fe doped NiO nanoparticles	Chemical	30	0.38 μ_B/Fe	[WANG20051]
NiO nanoparticles	Chemical	933	---	[LILL2006]
Li and Fe doped NiO Thin film	Sputtering	---	16 emu/cc	[LINY20062]
Ni and Ni-NiO nanoclusters	Cluster beam deposition	562	0.9 emu/g	[ZHOU2007]
Fe doped NiO nanoparticles	Co-precipitation	110-350	0.2 emu/g	[HEJH2008]
Fe doped NiO nanorods	Hydrothermal	614	0.6 emu/g	[MANN2008]
Fe and Li doped NiO Thin film	Pulse laser deposition	---	0.67 μ_B/Fe	[YANW2008]
NiO nanoparticles	Co-precipitation	250	1.5 emu/g	[MENE2010]
NiO nanoparticles	Precipitation	130-770	0.04 emu/g	[KART2011]
Fe doped NiO nanoparticles	Sol-gel	372	5.32 emu/g	[KHEM2011]
NiO thin films with Li, V, Cr, etc.	Sol-gel spin coating	-	5 – 45 emu/cc	[LINY2011]
NiO & (Ni, Zn)O nanoparticles	Chemical	---	1-3 emu/g T < 300 K	[PECK2011]
NiO nanoparticles	Thermal decomposition	433 at 5 K	12 emu/g	[DUAN2012]
NiO nanoparticle	Hydrothermal	---	12.5 emu/g	[KHAI2012]
Li and Fe doped NiO nanofibers	Electrospinning	---	0.7 emu/g	[LUOY2012]
NiO thin film	Thermal oxidation	190 – 400 Oe	105 – 355 emu/cc	[VALL2014]
NiO thin film	Pulsed laser deposition	100 – 265	0.2 – 30 emu/cc	[VERM2015]

Richardson et al [RICH1956] reported the first investigation on size dependent properties of NiO system. Later, the effect of particle size dependent magnetic properties and the competition between finite sizes versus surface effects on the room temperature magnetic crossover of NiO [KODA1997, TIWA2005, THOT2007, MAKH2008, MAND2011] prepared by chemical process [WINK2005, LILL2006, THOT2007, COPP2013, ALSE2014, ROYA2004], pulse laser deposition [HONG2006], sputtering [LUOX2015] and hydrothermal [WANG20052, WANG2011] techniques were reported. Out of these studies, a common theory put forward to discuss the unusual FM properties is a form of core-shell model, where the core spins are antiferromagnetically aligned and the shell spins give rise to FM moment [TIWA2005, MAKH2008, JAGO2009]. In addition, several other models such as two-sublattice model and multi-sublattice model were also proposed to account for the observation of large moment in NiO nanoparticles [KODA1997]. A combined experimental and computation study carried out by Yi et al [YIJB2007] showed a remarkable size-dependent magnetism with large magnetization of 105 emu/g and FM ordering temperature of 35 K, when the size of the NiO cluster is about 1 nm. With increasing the size of the NiO nanocrystals to 2 nm, they found AFM with uncompensated surface magnetization and shifted hysteresis due to the core-shell interactions. The careful literature survey from different groups reveals that most of the reported investigations are bottom-to-top approach summarizing that the resulting magnetic properties are very complex due to the interplay between finite size, surface effects and interface effects, etc. However, the approach of top-to-bottom method for studying the magnetic properties of pure un-doped NiO without any impurity phases are limited [DELB2008].

Similarly, NiO based thin films have received much attention for emerging applications of the next generation optoelectronics, thermoelectrics, electrochromic display devices and spintronics due to its excellent chemical stability, magnetic, electric and optical properties, and the low cost [HOTO2000, SRIR2013, JUAN2014, SHAR2014, CHEN2015]. In addition, NiO thin films show unusual properties due to the occurrence of structural disorder, vacancies of nickel and/or oxygen, aligned dislocations into NiO crystal, finite size effect, etc. For instance, Sugiyama et al [SUGI2013] demonstrated that dislocations in NiO crystals show unique magnetic properties with high coercivity due to the strong interaction between the ferromagnetic dislocations and surrounding AFM bulk phase. On the other hand, the annealing of as-deposited NiO thin films remarkably show unusual properties due to the occurrence of structural disorder, vacancies of nickel and/or

oxygen, aligned dislocations into NiO crystal, finite size effects, etc. For example, Bruckner et al [BRUC2003] reported that the sputtered NiO films having non-stoichiometric NiO decompose during heating at high temperatures (T_A) into thermally stable oxygen poorer NiO and/or metallic Ni. Kawai et al [KAWA2010] reported that annealing of NiO films at high temperature under vacuum condition produces conducting filaments in single crystalline NiO. Recently, Jang et al [JANG2011] reported that the decomposition reaction of NiO films strongly depends on T_A and thickness of the films. However, the systematic investigation of thermal decomposition as a function of thickness and annealing temperature and the resulting magnetic properties of NiO thin films are not reported in details.

The direct deposition of NiO thin film on to a substrate results in defects, vacancies and finite size particles and hence the exact control of amount of oxidation in the NiO becomes difficult. The alternative method of fabricating metal oxide thin films is thermal oxidation of the metallic thin films, which has been proven to be an easy *ex situ* technique to obtain metal oxide films and to improve metal crystallization [HAUG2003, BIRK2006, VALL2012]. Thermal oxidation process consists in annealing fresh metal surfaces at high temperature in air flow or in oxygen atmosphere to obtain either partial or complete or desired oxidation of the metal films. The oxidation processes determine the oxide growth rate, surface reaction and oxygen diffusion for potential applications such as data storage devices [COUR2008, GOUX2010, UNUT2017]. Valladares et al [VALL2014] studied thermal oxidation of 50 nm thick Ni thin films fabricated by conventional thermal evaporation process and post annealed in air at different temperature between 300 °C and 700 °C. They have shown that the oxidation of Ni into NiO strongly depends on the annealing temperature and the complete oxidation of Ni into NiO occurs at 700 °C. Following the reports of Jang et al [JANG2011] that the decomposition reaction of NiO films strongly depends on T_A and thickness of the films, one would expect that the oxidation behaviour of Ni thin films may also depend on the thickness of the Ni film and annealing temperature. There is, however, no report on the nature and type of oxidation process of Ni thin films as a function of thickness and its effects on the structural, vibrational, magnetic and electrical properties.

The above literature noticeably reveals that the observed magnetic properties in NiO are critically dependent on fabrication methods, growth conditions, doping agents and the form of the materials. Several preparation methods such as chemical process, hydrothermal technique, vapor transport method, sputtering, pulsed laser deposition, spin coating etc.

were used to synthesize these NiO materials. Most of the reported investigations are bottom-to-top approach on selected size of the particles and revealed that the resulting magnetic properties in these oxide materials are complex. On the other hand, the approach of top-to-bottom method for studying the magnetic properties of pure NiO powders and fabrication and characterization of NiO thin films through different approaches without any impurity phases is still limited. This motivated us to plan this thesis work with the following objectives as given below:

1.3. Objective of the thesis work

- To prepare nanosized NiO powders using ball mill process in a high-energy planetary ball mill under dry milling conditions and argon gas atmosphere with different milling speeds.
- To understand the evolution of nanocrystalline microstructure in pure NiO powders as a function of milling speeds and the resulting vibrational, electronic, magnetic and resonance properties.
- To investigate the effect of annealing on the modification of microstructure and to study the origin of induced ferromagnetism in NiO powders.
- To prepare NiO target from the milled NiO powders under different milling speeds and fabricate NiO thin films with different thicknesses (t = 50 - 300 nm) using magnetron sputtering technique.
- To study thickness dependent thermal decomposition reaction of NiO by annealing the as-deposited NiO films at different temperatures and under vacuum and air atmospheres.
- To study thickness dependent structural, microstructural and magnetic properties of as-deposited NiO films and effect of decomposition in annealed NiO films.
- To prepare Ni thin films with different thicknesses and investigate the effect of film thickness on the structural and magnetic properties of as-deposited films.
- To study the effect of thickness dependent oxidation process of Ni thin films, nature of thermal oxidation mechanism and the resulting vibrational, magnetic and electrical transport properties.
- To analyze the correlation between the structural, microstructural and physical properties of as-milled NiO powders, as-deposited and annealed NiO and Ni thin films.

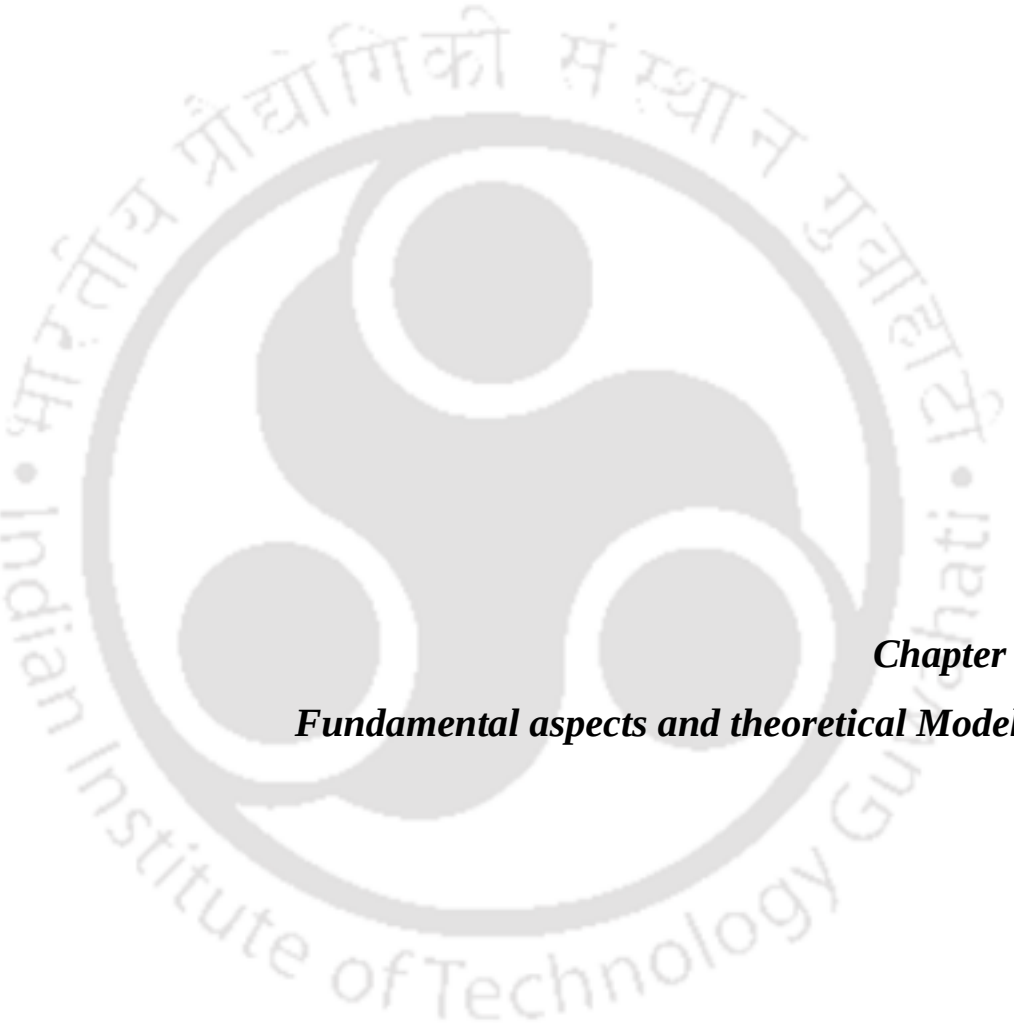

Chapter 2

Fundamental aspects and theoretical Models

2.1. Introduction

Magnetism is a physical phenomenon known for thousands of years by which materials exhibit an attractive or repulsive force. The history of magnetism is coeval with the history of science. However, the underlying principles and mechanisms which explain the magnetic properties of a material are still complex and mysterious. It is well-known that most of the modern devices such as electrical power generator, transformer, sensor, computer, components of sound and video reproduction systems, etc. rely on magnetism and magnetic materials. Hence, during last few decades, extensive studies on various types of magnetic materials have been executed both from fundamental and application points of views.

Recently, the tendency of miniaturization of electronic devices has created a demand for the search of new materials such as thin films and dilute magnetic semiconductor (DMS) and their production by various simple and inexpensive synthesis methods. In particular, the development of DMS exhibiting room temperature ferromagnetism (FM) has received enormous interest in the scientific community due to their dual characteristics of semiconductor and FM. These materials facilitate one more degree of freedom, i.e., spin polarization of charge carriers, to tune and control electrical transport in the devices. Such devices called spintronic devices and they have potential applications in electronic circuit for high speed signal processing, low power consumption, magneto-optic device, etc. As a result, over last few decades, large number of studies on various nanoparticles, thin films and new DMS material have been carried out. In this regard, the understanding of development of magnetic properties in these new types of materials and optimization of magnetic properties for different applications are very much essential. Thus, this chapter provides a brief description of structure of metal-oxides, the origin of magnetism, different types of magnetism, the phenomenon of FM in oxide materials and the various phenomena affecting FM properties of the materials prepared by different techniques for applications.

2.2. Structural properties

The crystal structure of the metal-oxide system [Nickel (II) oxide (NiO)] taken in the present investigation is discussed at first. Subsequently, other structural effects such as crystal field effect and Jahn-Teller distortion are also briefly introduced.

2.2.1. Crystal Structure

NiO is an important transition-metal (TM) oxide and received increasing attention owing to potential use in a variety of applications such as catalysis [DOOL1994], gas sensors

[MILL1997], battery cathodes [HOTO2000], magnetic materials [ICHI2003], electrochromic films [WANG20121] and supercapacitors [QIXW2016]. It adopts the NaCl structure as shown in Figure 2.01(a) with octahedral Ni(II) and O^{2-} sites and crystallizes in face structure cubic (*fcc*) structure (space group *Fm3hm* [225]) with the bulk lattice constant of NiO at 0 K is (*a* =) 4.1705 Å [BERT1971]. The simple NiO structure is known as the rock salt structure exhibiting pale green color when the Ni and O ratio is stoichiometrically correct.

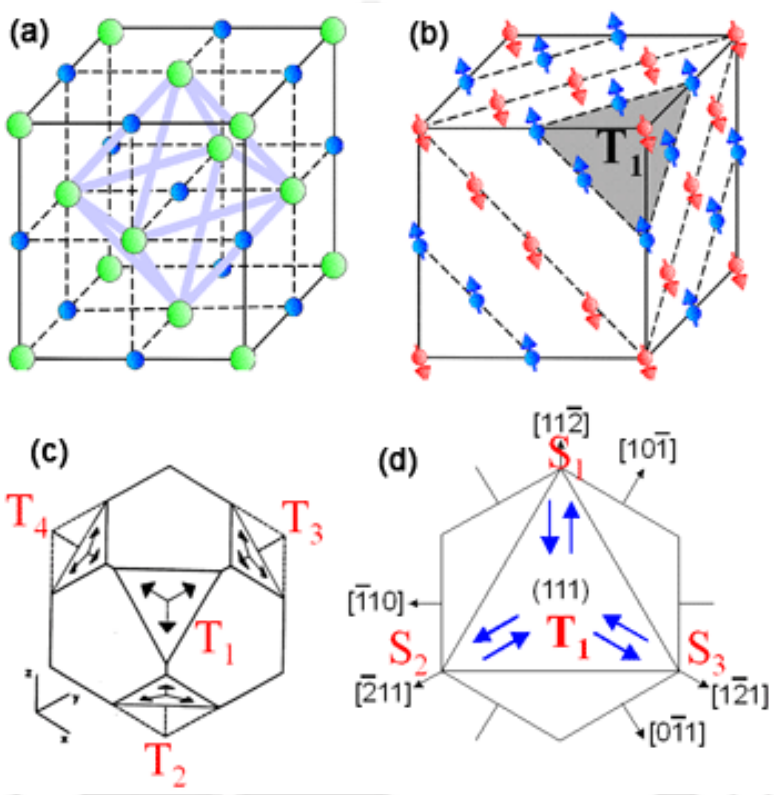

Figure 2.01: Schematic representation of collinear arrangement of magnetic (a) cation of NiO, (b,c) T_1 domains and (d) S_1 domain.

NiO is a type II antiferromagnetic (AFM) material and the magnetic unit cell is found to be close to cubic with a doubled lattice parameter in order to accommodate the AFM spin arrangement as shown in Figure 2.01(b). In fact, the spins were found to be parallel on cubic (111) planes, but antiparallel on neighboring (111) planes. The relative orientation of the spins with respect to each other is determined by exchange interactions. The main factor responsible for this particular AFM arrangement is the 180° super-exchange interaction. Assuming a collinear spin structure, a trigonal distortion restricts the number of possible spin structures to four experimentally observed T_x-domains (x = 1, 2, 3, 4). These are

characterized by AFM domains (*T* domains), in which the moments form FM foils parallel to one of the four equivalent (111) planes of the *fcc* lattice [KEFF1957, DUOL2010] with the spin aligned in the plane of the foil. This type of AFM ordering is further stabilized by a rhombohedral distortion in the direction perpendicular to the foils caused by magnetostriction. Inside each (111) foil, the spin is driven to align along one of the three equivalent $[11\bar{2}]$ directions by sources of smaller anisotropy as shown in Figure 2.01(b,c,d). This gives three equivalent so-called S_x-domains (x = 1, 2, 3). With increasing temperature, they transform into paramagnetic (PM) state having space group *Fm3m* above the Néel temperature (T_N) of 523 K [ROTH1958].

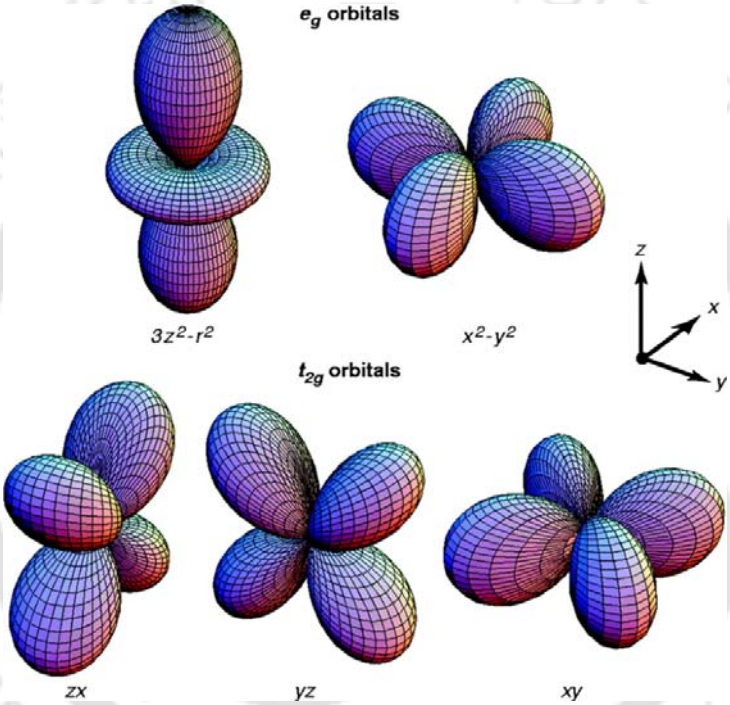

Figure 2.02: The electronic distribution of *3d* orbitals. In the cubic crystal field, the fivefold degeneracy is lifted to two e_g orbitals ($d_{3z^2-r^2}$ and $d_{x^2-y^2}$) and three t_{2g} orbitals (*zx*, *yz* and *xy*) [TOKU2000].

2.2.2. Crystal field effect

Atoms in a solid with an ordered crystal structure are influenced by the electric field of the neighboring atoms. This is called as crystal field [BLUN2003], which depends upon the local environments such as the nature of atomic co-ordination. The crystal field effect on *d* orbitals can be illustrated by moving a set of negative point charges close to a metal ion, owing to the Coulomb repulsion between *d* orbital electrons and the surrounding charges. The *d* shell has five orbitals, the first three are called t_{2g} orbitals, namely, d_{xy}, d_{yz} and d_{zx} and

last two are called e_g orbitals namely $d_{3z^2-r^2}$ and $d_{x^2-y^2}$. The electronic distributions of *d* orbitals are shown in Figure 2.02. In the absence of crystal field, all the five levels are degenerate. The t_{2g} orbitals point along in between *x*, *y* and *z* axes, but the e_g orbitals point along the direction of *x*, *y* and *z* axes. In case of surrounding negative charge is spherically symmetric, all five *d* orbitals are equally affected. In realistic, the surrounding negative charge is never spherically distributed, because the charge is associated with specific ions that occupy specific positions. The consequence is that each *d* orbital is affected differently, but the affection depends upon the geometry of the surrounding point charges. This effect is clearly seen in the splitting of energy levels for the five *d* orbitals. The crystal field effects are summarized in the chart shown in Figure 2.03. Each geometry of point charges (linear, square, planar, tetrahedral or octahedral) produces a characteristic splitting pattern for the five *d* orbitals (*xy*, *yz*, *zx*, x^2-y^2 and z^2).

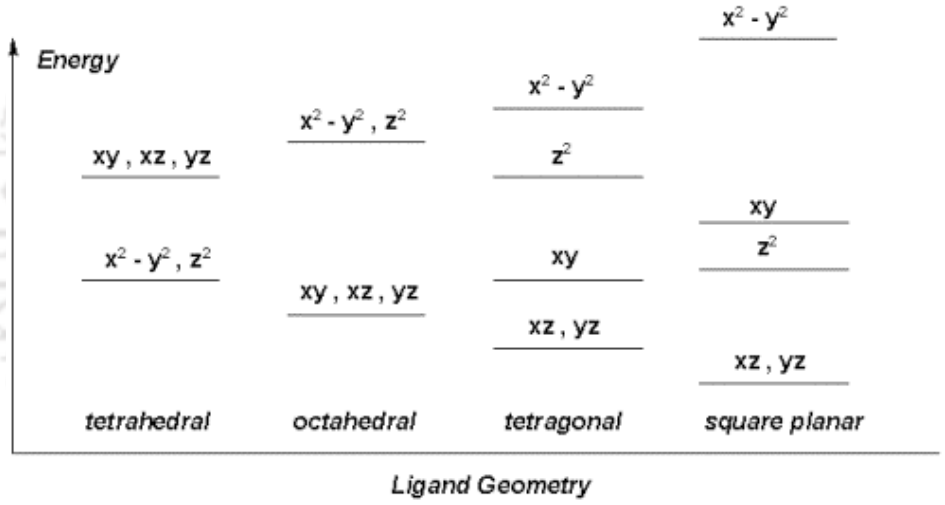

Figure 2.03: Schematic representation splitting of *d*-orbitals in presence of different anion configurations [BASO1964].

2.2.3. High spin and low spin arrangement

In the case of octahedral environment as shown in Figure 2.04, the 3*d* electrons will first fill up t_{2g} level before filling e_g. However, the competition between the crystal field energy and pairing energy will decide the manner in which each orbital is filled up. In the presence of weak crystal field, the electrons filling in the orbitals will take place as per Hund's rule. On the other hand, in the presence of strong crystal field, electrons doubly occupy in some of the orbitals (t_{2g} or e_g) before they are filled in higher energy orbitals. For example, Figure 2.05 shows the electronic arrangement in 3*d* shell of Co^{2+} ion under weak and strong crystal

field cases. The net spin quantum number for the weak field case is found to be $S = 3/2$, whereas $S = 1/2$ for the strong field case.

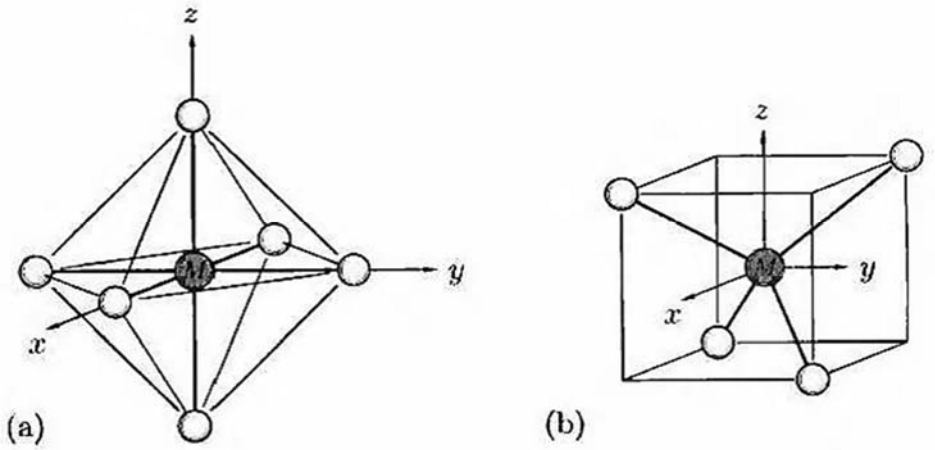

Figure 2.04: Schematic representation TM ion in (a) octahedral (b) tetrahedral configurations [BASO1964].

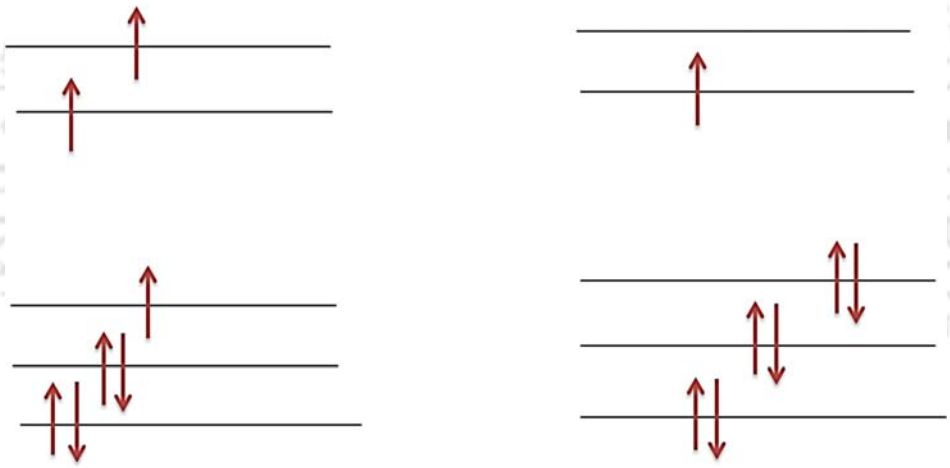

Figure 2.05: Electronic configuration of (left) high-spin (weak field) (right) low-spin (strong field) cation $3d^7$ shell of TM ion.

2.2.4. Orbital quenching

In general, the effective magnetic moment of an ion is calculated by following the Hund's rule and taking the values of *S*, *L* and *J*. The formula is given by

$$\mu_{eff} = g\mu_B\sqrt{J(J+1)} \qquad (2.01)$$

where μ_{eff} is the effective magnetic moment per magnetic ion, g is the Landé g-factor whose value is equal to $g = 1 + [J(J+1) + S(S+1) - L(L+1)]/(2J(J+1))$ and $J = L + S$ is the total angular momentum quantum number. L and S are the orbital and spin angular

momentum number, respectively. In 3*d* shell of TM ions, the crystal field interaction is much stronger than the spin-orbit coupling interaction. As a result, the system chooses a ground state, such that $L = 0$. This is called quenching of orbital momentum, which leads to $J = S$ and $g = 2$. Thus, eqn.(2.01) modifies to

$$\mu_{eff} = 2\mu_B\sqrt{S(S+1)} \qquad (2.02)$$

The theoretically calculated μ_{eff} values for selected ions by considering total angular momentum number, *J* (P1) and independently by taking only spin quantum number *S* (P2) are tabulated in Table 2.01.

Table 2.01. Theoretical effective magnetic moment by considering Hund's coupling (P1) and orbital quenching (P2) along with experimental values for selected TM ions [BLUN2003].

Ion	Shell	*S*	*L*	*J*=*L*+*S*	g	P1=$g\sqrt{J(J+1)}$ (μ_B)	P2=$2\sqrt{S(S+1)}$ (μ_B)	$P_{Expt.}$ (μ_B)
Fe^{2+}, Co^{3+}	$3d^6$	2	2	4	3/2	6.70	4.9	4.82
Co^{2+},Ni^{3+}	$3d^7$	3/2	3	9/2	1.33	6.63	3.87	4.90
Ni^{2+}	$3d^8$	1	3	4	5/4	5.59	2.83	3.12

2.2.5. Jahn-Teller Distortion

The observed degeneracy in the crystal field splitting can be broken by lattice distortion. For example, in MnO_6 octahedral environment, the electrons in the 3*d* shell of Mn ions are under the Coulomb interaction of electrons from 2*p* shell of O ions. Since the p_x, p_y, p_z orbitals of O point along *x*, *y* and *z* directions, respectively, there will be overlapping with e_g orbitals of Mn ions. So, the energy of e_g orbitals is raised compared to t_{2g} orbitals. Figure 2.06(a) shows a two dimensional diagram of typical overlapping of one of the e_g orbitals ($d_{x^2-y^2}$) with *p* orbitals of neighboring O ions. On the other hand, we can see no such overlapping with a typical t_{2g} orbitals (d_{xy}) as shown in Figure 2.06(b). In view of the above crystal field effect, the degeneracy in e_g orbitals and t_{2g} orbitals of *d*-shell are lifted as displayed in Figure 2.06(c) for octahedral coordination [BLUN2003]. Thus, in addition to the splitting of *d*-orbitals into t_{2g} and e_g orbitals due to crystal field, there is further splitting of orbital within t_{2g} and e_g due to Jahn-Teller (JT) effect.

The oxygen ions are surrounded by Mn^{3+} ions. The readjustment of position of oxygen ions in MnO_6 octahedra can lead to asymmetry in MnO_6 octahedra. The above lattice

symmetry lifts the degeneracy of t_{2g} and e_g orbitals. The lifting of degeneracy due to orbital-lattice interaction is known as JT distortion, which is significant for partially filled orbitals, where there is a net energy gain. This distortion leads to an increase in elastic energy and decrease in electronic energy such that there is a net reduction in energy. Mn^{3+} ions have one e_g electron and decrease in electronic energy such that there is a net reduction in energy. Mn^{3+} ions are JT active, while Mn^{4+} ions are inactive for JT distortion in octahedral environment. Mn^{3+} ions have one e_g electron out of two e_g orbitals namely, ($d_{3z^2-r^2}$) and ($d_{x^2-y^2}$).

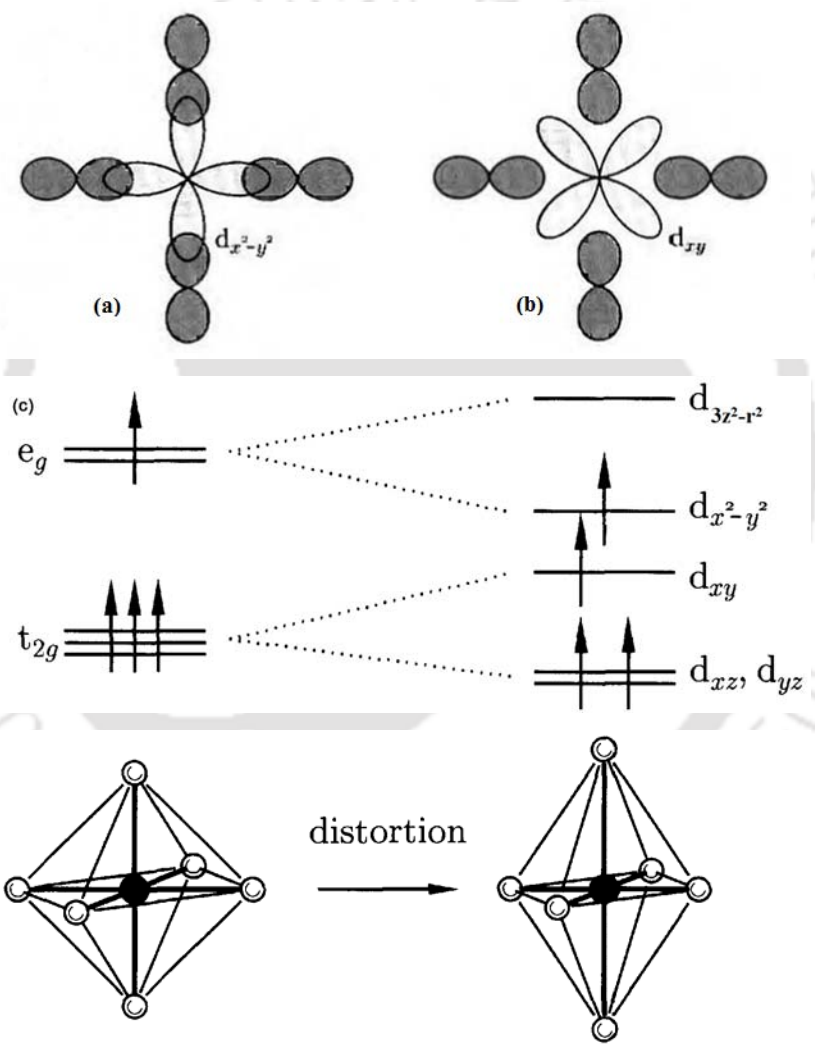

Figure 2.06: (a) Overlapping of one of the e_g orbitals ($d_{x^2-y^2}$) with *p* orbital of neighboring O in a two dimensional diagram (b) One O of the t_{2g} orbitals with *p* orbital. (c) The crystal field splitting of *d* shell in octahedral environment and Jahn-Teller distortion leads to a further splitting of both t_{2g} and e_g states.

The elongation of MnO_6 octahedra along z-axis gives rise to reduction in $(d_{3z^2-r^2})$ level compared to $(d_{x^2-y^2})$ level. Since there is only one e_g electron, which occupies the $(d_{3z^2-r^2})$ level, there is reduction in electronic energy. The splitting of e_g and t_{2g} orbitals due to JT distortion is shown in Figure 2.06(c). On the other hand, Mn^{4+} ion does not have any e_g electron, so reduction in electronic energy is not feasible and hence no JT distortion. The TM ion un-doped and doped semiconductors are also affected by the JT distortion as estimated theoretically in Cr-doped Group II-VI based DMS by Blinowski et al [BLIN1996]. The susceptibility data obtained by Brumage et al [BRUM2001] on Cu-doped ZnO samples could be explained based on the crystal field effect and by incorporation the JT distortion, where the doped Cu was in Cu^{2+} state with electronic configuration $3d^9$.

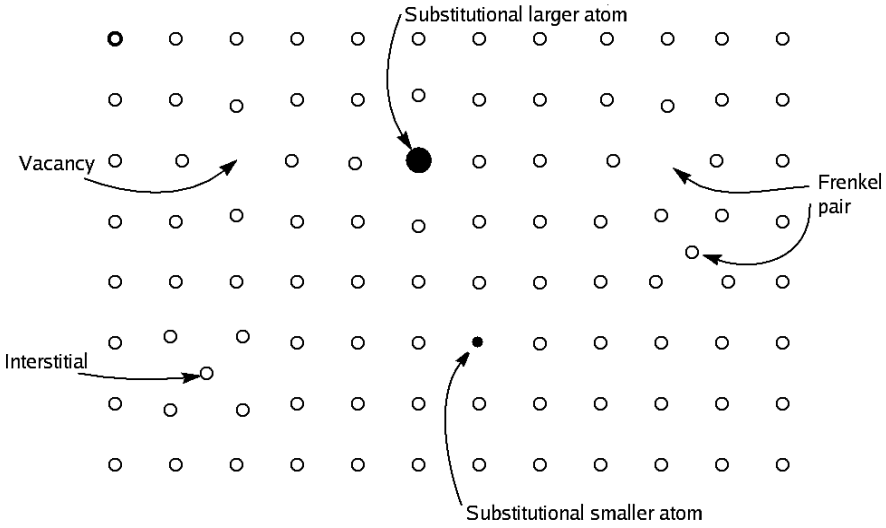

Figure 2.07: Schematic illustration of some simple point defect types in a solid.

2.3. Defects

Defect engineering in metal-oxide based nanocrystalline materials has received unprecedented attention because intrinsic as well as extrinsic defects in the materials play a very crucial and fundamental role in enhancing the materials/device performance. The types, concentration and spatial distribution of intrinsic point defects such as vacancies and interstitial atoms influence the performance of metal-oxides in gas sensing, electronics, photonics, solar-induced photochemistry for fuel production and environmental cleanup, and the realization of room temperature FM [LIM2000, TIWA2005, HONG2006, JING2006, BANE2007, SANY2008, PODI2010, WANG2011, DUAN2012, KISA2012, ACHA2013, CHEN2013, LIUX2013, PANX2013, SUJ2013]. Before going into the details of the defects, let us first introduce the types of defects and related modification in the

properties of metal-oxide based nanocrystalline materials. Any forms of deviation from perfect crystal can be treated as defects. Interestingly, the perfect metal-oxide material will not have a clear crystal structures, i.e., even in a single crystal of NiO, one finds point defects (misplaced lattice atoms/ions, vacancies, foreign atoms/ ions) and/or extended defects such as dislocations. This modifies the band structure of the materials, which in-turn changes the properties of the materials. For example, the single crystal of cubic NiO, shows different colors due to defects. Point defects as shown schematically in Figure 2.07 are further classified into native defects and external impurity defects (dopants) which can be found either on the lattice (substitutional site) or at the interstitial positions. Dislocations are the kind of defects that an extra line of atoms inserted or removed in/from the crystal which does not extend throughout the crystal.

2.3.1. Extrinsic defects

Doping is a process of adding small amount of foreign atoms/ions (dopant) into a parent material (host matrix) without forming any secondary phases. When a large amount of the dopant material is added, there is a formation of either different oxides or a secondary phase, which may or may not be the mixed oxide, depending on the mutual solubility limit of the two components. This can be referred as mixed oxide or cluster formation rather than the doping. The distribution of the dopant in the crystals/ grains of the matrix material may be homogeneous or heterogeneous. Doping in NiO is performed with the aim of enhancing the properties of the parent NiO for potential applications. For instance, Li doping NiO thin films enhances p-type conductivity due to the occupancy of substitutional sites in the films by Li ions [DUTT2010]. Similarly, Zn doping in NiO, i.e., $Ni_{0.98}Zn_{0.02}O$ induces FM at about 70 K [MAST2014]. On the other hand, Mg doping in NiO enhances the bandgap of NiO significantly [BENA2014].

2.3.2. Intrinsic defects

The understanding of intrinsic defect mechanism is very essential in metal-oxide system to improve the gas-sensing performance of the metal-oxide semiconductors. Roberts et al [ROBE1984] reported that high binding energy components of O 1s spectra at 531.4 eV and Ni $2p_{3/2}$ spectra at 856.1 eV obtained from XPS spectra can be correlated with the oxide defect structure. Jang et al [JANG2009] reported that nickel vacancy is the dominant point defect, which results in the electrical conductivity of NiO thin films. Similarly, Zhang et al [ZHAN2016] also reported that the nickel vacancies are the dominant defect type

determining the electrical properties of NiO samples. Thus, intrinsic defects altering the lattice parameters in NiO have some effects on the band gap [EKUM2011]. Vacancies and interstitial atoms are responsible for the occurrence of nonstoichiometric compounds. NiO is a good example of a compound with somewhat variable stoichiometry. When NiO is prepared at relatively low temperature (1100 K) by partial oxidation of excess nickel, its composition is $Ni_{1.0}O_{1.0}$. This exhibits pale green color and insulating properties. If the same substance is treated with excess oxygen at 1500 K, the cation vacancies occur and the composition approaches to $Ni_{0.97}O_{1.0}$ and changes the color of the powder into black with semiconducting properties. The deficiency of positive charge that would otherwise accompany cation vacancies is compensated by the presence of the appropriate amount of Ni^{3+}. This is majorly responsible for the electrical conductivity of non-stoichiometric NiO. If a Ni^{3+} ion exists at some point, an electron from elsewhere in the lattice may jump to it, converting it to Ni^{2+} and simultaneously creating a Ni^{3+} ion at a new lattice point. By a series of such electron jumps, charge can migrate through the crystal and producing properties different than the stoichiometric one.

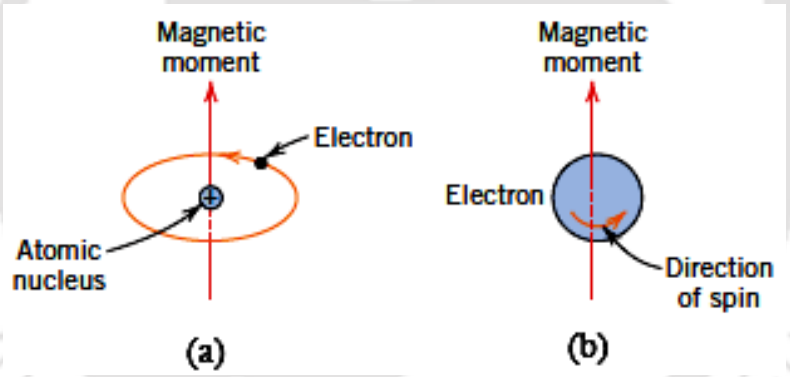

Figure 2.08: Schematic representation of the magnetic moment associated with (a) an orbiting electron and (b) a spinning electron.

2.4. Magnetic ordering

2.4.1. Origin of magnetism

The macroscopic magnetic properties of materials are the consequence of magnetic moments associated with individual electrons in an atom [OHAN2000, KITT2004]. Each electron in an atom has magnetic moment originating from two different sources: (a) One is orbital motion of electron around the nucleus, generating a small magnetic field and having magnetic moment along the axis of rotation, as shown in Figure 2.08(a) and (b) Other magnetic moment originates from the electron spin, which is directed along the spin axis

either up or down depending on the mode of rotation [see Figure 2.08(b)]. This suggests that each electron in an atom may be thought of as being a small magnet having permanent orbital and spin magnetic moments. Furthermore, in an atom, electrons are occupied according to the Pauli's Exclusion Principle and Hund's rule. The net magnetic moment for an atom is the sum of the magnetic moments of the each of constituting electrons, including both orbital and spin contributions and taking into the account of moment cancellation. For an atom having completely filled electron shells or subshells, when all electrons are considered, there is a total cancellation of both the moments. Thus, materials composed of atoms having completely filled electron shells are not capable of being permanently magnetized. Based on number of unpaired electrons in an atom, their orientation in the orbitals and the spin-orbit interaction between the electron orbital angular momentum and spin angular momentum and their response in the external applied field, materials are classified into diamagnetic, paramagnetic, ferromagnetic, antiferromagnetic and ferrimagnetic [KRON2003].

2.4.2. Diamagnetism

Diamagnetism is a fundamental property of materials and it is a manifestation of Lenz law, i.e., if one applies a field to a system of moving charges, then their motions change in such a way that they create a magnetization that opposes the original applied field [OHAN2000]. Such effect is present in all the materials, but is often hidden by the presence of other types of magnetism. It generally occurs in materials having completely filled electronic configuration. The atoms and molecules of diamagnetic substances do not possess any net magnetic moments (i.e., all the orbital shells are filled and there is no unpaired electron). However, when exposed to a magnetic field, the electrons orient themselves such that they try to oppose the applied magnetic field and hence they register negative magnetization and negative susceptibility. Most of semiconductor material likes ZnO, SnO_2 etc. are diamagnetic in nature.

2.4.3. Paramagnetism

For some solid materials, each atom possesses a permanent dipole moment by virtue of incomplete cancellation of electron spin and/or orbital magnetic moments. The orientations of these atomic magnetic moments are random in the absence of an external magnetic field and result no net macroscopic magnetization. However, these atomic dipoles are free to rotate and paramagnetism (PM) occurs when they preferentially align, by rotation, with an

external field [KITT2004]. Some of the atoms or ions in this class of materials have a net magnetic moment due to unpaired electrons in partially filled orbital. However, the individual magnetic moments do not interact electrons in magnetically. In the presence of an applied magnetic field, there is a partial alignment of atomic magnetic moments in the direction of the applied field, resulting in a net positive magnetization and hence positive susceptibility. Both diamagnetic and PM materials are generally considered to be non-magnetic because they exhibit magnetization only under the application of an external field. The tendency of alignment of magnetic moments along the field direction is opposed by the thermal energy, which tries to randomize the spin orientation. So they exhibit a temperature (T) dependent susceptibility, $\chi(T)$ known as the Curie Law,

$$\chi(T) = \frac{c}{T} \tag{2.03}$$

with a Curie constant C [BLUN2003]. In classical theory, each atomic moment is considered as magnetic dipole alignment in a particular direction with an angle θ with respect to applied field and average magnetic moment along the field direction, z is written as

$$< \mu^z > = \mu L(y) \tag{2.04}$$

Here, μ is the magnetic moment of each dipole and $L(y)$ is the Langevin function, $L(y) = \mathrm{Coth}y - 1/y$ and $y = \mu_B/(k_B T)$. This function explains the magnetization of small particles made up of atomic clusters. For low applied field or at high temperature, such that y is small, $L(y)$ tends to $y/3$. Therefore,

$$< \mu^z > = \frac{\mu y}{3} = \frac{\mu^2 B}{3k_B T} \tag{2.05}$$

or the magnetization

$$M = N < \mu^z > = \frac{N\mu^2 B}{3k_B T} \tag{2.06}$$

Hence, the susceptibility

$$\chi = \frac{M}{H} = \frac{\mu^2 N \mu_0}{3k_B T} = \frac{C}{T} \tag{2.07}$$

and the Curie law is obtained by the classical theory. According to quantum mechanical treatment and by considering the quantization of total angular momentum of each atom, the average magnetic moment per atom aligned along the magnetic field direction (i.e., z direction) of any PM sample can be written as [JILE1997, BLUN2003].

$$< \mu_J{}^z > = g\mu_B J B_J(x) \tag{2.08}$$

Here g is Landgé g-factor and it depends on spin-orbit coupling of electrons in each atom. J is the total angular momentum quantum number. $\mu_B = 9.27\times10^{-24}$ J/T is Bohr magnetron. $B_J(x)$ is Brillouin function, which can be written as,

$$B_J(x) = \frac{1}{J}\left[\left(J+\frac{1}{2}\right)Coth\left(J+\frac{1}{2}\right)x - \frac{1}{2}Coth\frac{x}{2}\right] \tag{2.09}$$

Here, the variable $x = (g\mu_B B)/(k_B T)$, where k_B is the Boltzmann constant and T is the temperature. If N is the number of atoms per unit volume, the volume magnetization M can be written as,

$$M = N < \mu_J{}^z > = Ng\mu_B J B_J(x) \tag{2.10}$$

For the selection of magnetic field B and temperature T such that x is small, $B_J(x) \sim [J(J+1)/3]x$. Such assumption holds true for PM sample in a wide temperature region and for low applied field. So

$$< \mu^z > = Ng\mu_B J\frac{(J+1)}{3}x = \frac{Ng^2\mu_B^2 B}{3kT}J(J+1) \tag{2.11}$$

or the susceptibility

$$\chi = \frac{\mu_0 N g^2 \mu_B^2}{3kT}J(J+1) \tag{2.12}$$

It is in the form of Curie law, C/T. Thus the magnetic susceptibility based on Brillouin function expression reduces to Curie-law. The examples of PM materials are W, Ce, Al, Li, Mg, etc. with typical χ value of 6.8×10^{-5}, 5.1×10^{-5}, 2.2×10^{-5},1.4×10^{-5},1.2×10^{-5} respectively in SI units [BLUN2003].

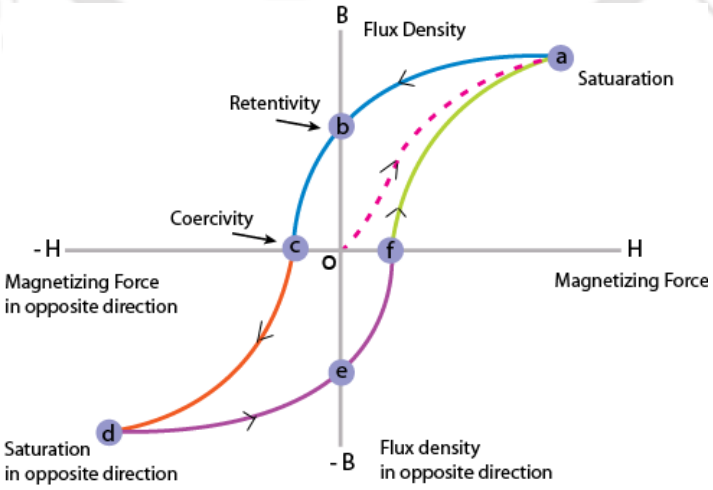

Figure 2.09: Magnetic hysteresis loop of a FM material.

2.4.4. Ferromagnetism

Certain materials possess a permanent magnetic moment resulting from strong interaction between the magnetic moments even in the absence of an external field. This dominates over the thermal energy and reveals an alignment of magnetization in a particular direction. Such behaviors are displayed by TMs and some of the rare earth metals. In FM materials, there are two distinct characteristics: spontaneous magnetization and magnetic ordering temperature. Spontaneous magnetization is the net magnetization that exists inside a uniformly magnetized microscopic volume even in the absence of external magnetic field. The magnitude of this magnetization at absolute temperature depends on the spin magnetic moments of electrons. The atomic moments in FM materials align either a parallel or an antiparallel arrangements showing very strong interactions, which are produced by electronic exchange forces. As a result, a large net magnetization even after removing the external applied magnetic field exists in FM materials. All FM materials exhibit magnetic hysteresis (*M*-*H*) loop under the application of magnetic field as displayed in Figure 2.09. The loop is generated by measuring the magnetic flux of a FM material while the magnetizing field is changed continuously. By studying the loop we get information about various magnetic parameters such as saturation magnetization (M_S, point *a*), remanence or retentivity (point *b* and *e*) and coercivity (H_C, point *c* and *f*) to understand the magnetic properties of a FM material. Furthermore, permeability, a property of a material that describes the ease with which a magnetic flux is established in the component, can also be obtained from initial loop. These parameters are not solely intrinsic properties but dependent on various parameters such as grain size, domain state, internal stresses and temperature. Since the hysteresis parameters are dependent on grain size, they are useful for magnetic grain sizing of natural samples. The elements Fe, Ni, and Co and their alloys are typical examples of FM materials. FM materials are mainly divided into two groups: (a) hard FM materials which exhibit very high H_C (> 1000 Oe). These materials are mainly used as media for magnetic recording and data storage and permanent magnets, and (b) soft FM materials with low H_C (< 100 Oe) are used for transformer core, read head and magnetic sensor applications.

Another important parameter is the magnetic induction [$B = \mu_0 (H + M)$], where μ_0 is the permeability of free space], which is the total flux of magnetic field lines through a unit cross sectional area of the material. From the initial magnetization curve, the initial magnetic permeability μ_I (= B/H), for very small applied magnetic field and maximum permeability μ_{max} [=$(B/H)_{max}$] can be obtained. These parameters indicate the amount of

induction generated by the material in a given magnetic field and are useful in characterizing magnetic materials. μ_I and H_C have a reciprocal relationship. So, materials exhibiting low H_C necessarily have a high μ_I. When increasing temperature, a transition from FM state to PM state occurs at a temperature called Curie temperature (T_C). The phenomenon of FM can often be described by mean field or molecular field model. The molecular field model simply assumes that all the interactions from the neighboring magnetic species can be described in terms of an effective internal or molecular field B_m, which is proportional to the magnetization, i.e., $B_m = \lambda M$, where λ is the Weiss molecular field constant. So the total magnetic field experienced by each dipole is the sum of applied field B and the molecular field B_m. The expression for magnetization can be written by following eqn.(2.13) with the modification that

$$M = \frac{Ng^2\mu_B^2 J(J+1)}{3kT}(B_a + \lambda M) \qquad (2.13)$$

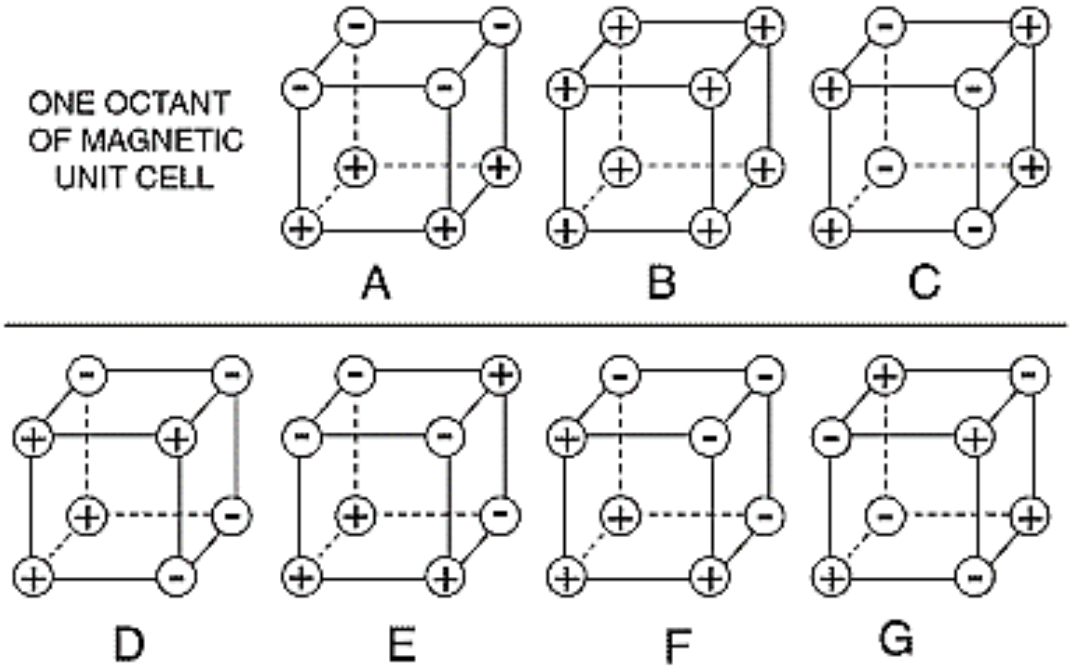

Figure 2.10: Different type of antiferromagnetic arrangement in a unit cell.

2.4.5. Antiferromagnetism

In AFM materials, the spins of electrons align in a regular pattern with neighboring spins pointing in opposite directions, below a certain temperature called Néel temperature (T_N). Above T_N, the material is typically PM. The magnetic susceptibility of AFM material will

appear to go through a maximum as the temperature is lowered. The AFM ordering is possible based on different type of magnetic unit cell structure as shown in Figure 2.10 except for *B* type, which is a FM one. In *A* type structure, the magnetic ions are coupled ferromagnetically in each (001) plane but with alternate planes aligned in opposite spin orientation such that they exhibit net AFM interaction. *B* type structure is a FM one with all six nearest neighbor magnetic ions coupled ferromagnetically. In *C* type structure, the atoms in (101) and (110) planes are ferromagnetically aligned. Each atom has two ferro and four AFM nearest neighbors such that there is net AFM unit cell. In *G* type structure, each ion is coupled antiferromagnetically to all its six nearest neighbors. Hence the atoms of positive and negative number of FM and AFM bonds are shown in Figure 2.10. The examples of AFM materials are NiO, MnF_2, MnO, CoO, FeO, Cr_2O_3, α-Fe_2O_3 with Néel temperature of 525 K, 67 K, 116 K, 292 K, 116 K, 307 K, and 950 K, respectively [BLUN2003].

2.5. Intrinsic properties of magnetic materials

Intrinsic properties of FM materials are M_S, T_C and magnetocrystalline anisotropy (MCA). These properties describe the equilibrium properties of the material on the atomic scale. Weiss (1907) reported that in addition to any externally applied field *H*, there is an internal molecular field or exchange field in a FM proportional to its magnetization.

$$\overrightarrow{B_E} = \lambda \vec{M} \qquad (2.14)$$

where, λ is a constant independent of temperature. According to eqn.(2.14), each spin sees the average magnetization of all the other spins. This molecular field is not really a magnetic field and therefore does not enter into the Maxwell equations. For example, there is no current density $\vec{j}$ related to $\overrightarrow{B_E}$ by $\vec{\nabla} \times \vec{H} = 4\pi\vec{j}/c$. The magnitude of the molecular field may be as high as 1000 Tesla, which is not due to the magnetic dipole interaction. This lingered as a mystery until Heisenberg introduced the concept of exchange interaction in 1928 [HEIS1928]. The origin of the Heisenberg exchange interaction is electrostatic, but the explanation involves quantum mechanics. The charge distribution of a system of two spins depends on whether the spins are parallel or antiparallel. Pauli's exclusion principle dismisses that no two identical electrons occupy the same quantum state simultaneously. However, it does not exclude two electrons of opposite spin. Therefore, the electrostatic energy of a system depends on the relative orientation of the spins: the difference in energy defines the exchange energy. The energy of interaction between the atoms *i* and *j* bearing electron spins S_i and S_j is defined from the Heisenberg model as [OHAN2000],

$$E_{exch} = -2\sum_{i<j} J_{ij} S_i . S_j \tag{2.15}$$

where, J_{ij} is the exchange integral and is related to the overlap of the charge distribution of the atoms i and j. Assuming that the exchange interaction is the same for each nearest-neighbor pair, eqn.(2.15) turns out to be

$$E_{exch} = -2J\sum_{i<j}^{nn} S_i . S_j \tag{2.16}$$

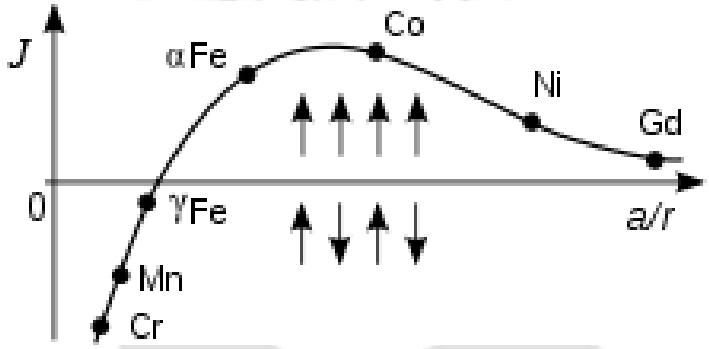

Figure 2.11: Bethe-slater curve: Elements above (below) the horizontal axis are FM (AFM).

For parallel orientation of the magnetization, J should be positive and for antiparallel alignment of spins, J should be negative. The variation of J with respect to inter-atomic distance is shown in Figure 2.11. This curve is also known as the Bethe-Slater curve. It is clear from the Figure 2.11 that the value of J and hence the short-range exchange interaction depends strongly on the inter-atomic distance. The eqn.(2.16) can be simplified further by considering the energy of a particular atom i interacting with its j nearest neighbor:

$$E^i_{exch} = -2JS_i\sum_j S_j \tag{2.17}$$

while for the entire material,

$$E_{exch} = -\frac{1}{2}\sum_j E^i_{exch} \tag{2.18}$$

Thus, the discrete, pairwise interaction can be replaced by assuming that the magnetic moment $\mu^i_m = g\mu_B S_i$ at site i interact with a molecular field. H_{eff} given by the net effect of the z nearest neighbor spins:

$$E^i_{exch} = -\mu_0\mu^i_m H_{eff} = -g\mu_0\mu_B S_i H_{eff} \tag{2.19}$$

where, g is the Landé g-factor, μ_B is Bohr magneton and μ_0 is the permeability of the free space (= $4\pi\times10^{-7}$ H/m or 1.256×10^{-6} H/m). Comparing eqn.(2.17) with eqn.(2.19) provides the effective field as,

$$H_{eff} = \frac{2J}{g\mu_0\mu_B}\sum_j S_j \cong \frac{2zJ}{g\mu_0\mu_B}\langle S_j\rangle \tag{2.20}$$

Here, the sum over z neighboring spins has been replaced by z times the average spin value $\langle Sj\rangle$. Using $M = N_v g\mu_B\langle S_j\rangle$, eqn.(2.20) gives,

$$H_{eff} \cong \frac{2zJ}{N_v g^2 {\mu_B}^2 \mu_0} M \tag{2.21}$$

From eqn.(2.21), it can be seen that H_{eff} is the Weiss molecular field defined as $H_{mol} = \lambda M$, provided

$$\lambda = \frac{2zJ}{N_v g^2 {\mu_B}^2 \mu_0} \tag{2.22}$$

Using the value of molecular field coefficient λ as 10^3, J is calculated to be 2×10^{-21} J or 0.01 eV/atom. Exchange interactions are weaker than the Coulomb interactions that distinguish levels of different principal and orbital quantum numbers, but stronger than spin-orbit interaction. Following the treatment of Weiss molecular field that $T_C = \lambda C$ with $C = N_v {\mu_m}^2 \mu_0/3k_B$, the expression for T_C can be obtained from eqn.(2.22) as

$$T_C = \frac{2zJ{\mu_m}^2}{g^2{\mu_B}^2 3k_B} = \frac{2zJs(s+1)}{3k_B} \tag{2.23}$$

where, $\mu_m = \sqrt{g\mu_B s(s+1)}$. Another important relation between exchange energy and the magnetization is defined as,

$$\frac{E_{exch}^{ij}}{V} = \frac{s^2a^2JN_v'}{2}\left(\frac{\nabla M}{M}\right)^2 = A\left(\frac{\nabla M}{M}\right)^2 \tag{2.24}$$

where, a is the distance between the spins, A is called the exchange stiffness constant having $1\text{-}2\times10^{-11}$ J/m for most ferromagnets and N_v' is number of nearest neighbor atoms per unit volume. Therefore, it is clear from the above equations that the exchange energy or the Heisenberg exchange interaction depends strongly on temperature due to the dependence of interatomic distance on temperature. In particular, the disorder FM system is the subject of low T_C due to the low value of J.

2.6. Anisotropy

When a physical property of any materials depends on the direction that property is said to exhibit anisotropy. In magnetism, the preference of magnetization to lie in a particular direction of sample is called magnetic anisotropy. As anisotropy plays an important role in tuning the nature of *M-H* loop, it is much essential to understand the various possible sources of the magnetic anisotropy and its influence on the control of the magnetic properties.

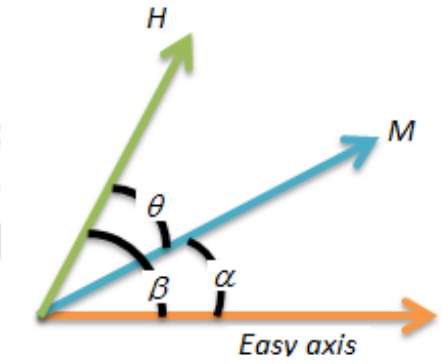

Figure 2.12: Schematic diagram of magnetization, applied field and easy axis for a given material.

Figure 2.12 displays a typical situation where for zero applied field, the magnetization would point along the easy axis shown ($\alpha = 0$). When a field is applied, the magnetization is pulled towards the field direction and approaches closer to the field direction with increasing the applied field. For any intermediate values of α, the magnetization is being attracted in opposite directions, i.e., up by the field and down by the anisotropy. Let us assume that all the magnetization is pointing in the same direction in a magnetic material and the material exhibits an easy axis of magnetization. In such scenario, we can describe the energy per unit volume of the magnetization of this material by

$$E = K\,sin^2\alpha \qquad (2.25)$$

where, K is called anisotropy constant with an unit of energy per unit volume (J/m^3). Hence, the energy term, E, is also energy per unit volume. In general, the magnitude of uniaxial anisotropy is described in terms of the anisotropy field, which is defined as the field needed to saturate the magnetization of a uniaxial crystal in the hard axis direction, as given in eqn.(2.26)

$$H_k = \frac{2K}{\mu_0 M} \qquad (2.26)$$

In general, the energy of the magnetization is given by,

$$E = K\,sin^2\alpha - \mu_0 MH\,cos(\beta - \alpha) \tag{2.27}$$

where, the first term is anisotropy energy. The second term is due to the magnetic field and the difference in the angle (β - α) is the angle between H and M. To get equilibrium, we required first derivative to be zero. Therefore, taking derivative of eqn.(2.27) with respect to the angle results in,

$$\frac{dE}{d\alpha} = 2K \sin\alpha \cos\alpha - \mu_0 MH\,sin(\beta - \alpha) = 0 \tag{2.28}$$

Taking the value of β as 90° for the equilibrium angle for the magnetization relative to the easy axis and considering the eqn.(2.28) gives

$$\sin\alpha = \frac{H}{H_k} \tag{2.29}$$

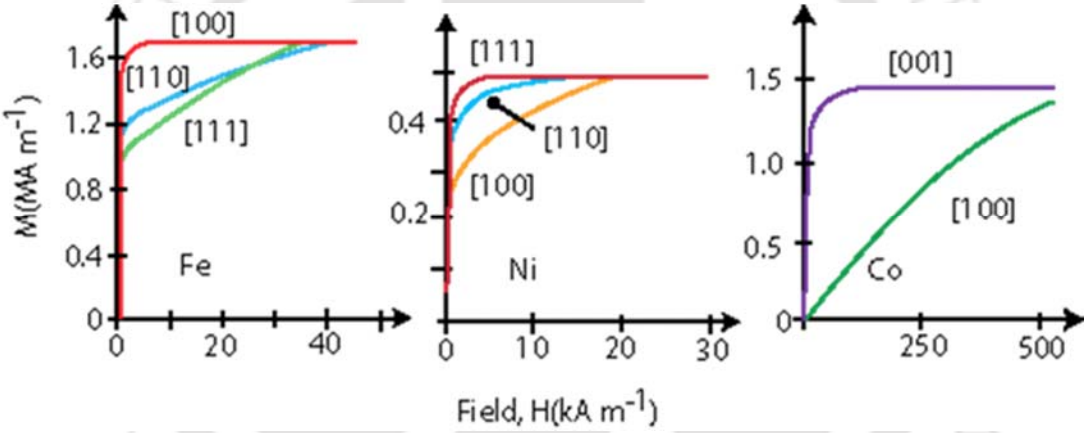

Figure 2.13: Initial magnetization curves of single crystals of Iron, Nickel and Cobalt.

2.6.1. Magnetocrystalline anisotropy

Figure 2.13 shows initial magnetization curves of single crystals of different 3*d* FM elements. It could be clearly seen that the magnetization approaches to saturation in different ways when magnetized in different directions. Iron displays [100] as easy direction and [111] as hard direction, while nickel exhibits [111] as easy axis and [100] as hard directions. This behavior can be understood by analyzing the development of anisotropy energy in different symmetries.

For cubic:

$$E_a = K_{1c}(\alpha_1^2\alpha_2^2 + \alpha_2^2\alpha_3^2 + \alpha_3^2\alpha_1^2) + K_{2c}(\alpha_1^2\alpha_2^2\alpha_3^2) \tag{2.30}$$

For hexagonal:

$$E_a = K_1 \sin^2\theta + K_2 \sin^4\theta + K_3 \sin^6\theta + K_3' \sin^6\theta \sin 6\phi \quad (2.31)$$

For tetragonal:

$$E_a = K_1 \sin^2\theta + K_2 \sin^4\theta + K_2' \sin^4\theta \cos 4\phi + K_3 \sin^6\theta + K_3' \sin^6\theta \sin 6\phi \quad (2.32)$$

where, α_i are the direction cosines of the magnetization. K_{1c} term is equivalent to $K_{1c}(\sin^2\theta\, cos^2\phi \sin^2\phi + \cos^2\theta \sin^2\theta)$. When, $\theta = 0$, $\phi = 0$, this term reduces to eqn.(2.25) [COEY2010].

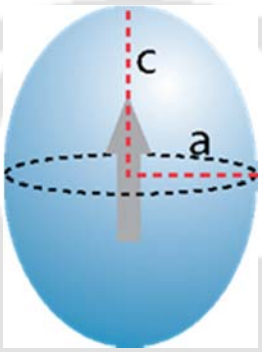

Figure 2.14: Magnetization of a prolate ellipsoid of revolution with $c > a$ and no magnetocrystalline anisotropy. c-axis is the easy direction of magnetization.

2.6.2. Shape anisotropy

Shape anisotropy arising due to the asymmetric shape of the material is important for thin films where one dimension is very short as compared to other dimensions. The demagnetization field inside the material or the stray field outside the magnetic material depends on the magnetization and shape of the material [JILE1997, OHAN2000, BLUN2003]. The magnetostatic energy of a FM ellipsoid as shown in Figure 2.14 with magnetization M_S is given as

$$E_m = \frac{1}{2}\mu_0 V N M_S^2 \quad (2.33)$$

The anisotropy energy is related to the difference in energy ΔE when the ellipsoid is magnetized along its hard and easy directions. N is the demagnetization factor tensor for the easy direction. N'=(1/2)(1-N) is the demagnetization factor tensor for the hard directions. Hence,

$$\Delta E_m = \frac{1}{2}\mu_0 V M_S^2 \left[\frac{1}{2}(1-N) - N\right]$$

$$\Delta E_m = \frac{1}{4}\mu_0 V M_S^2 [1-3N]$$

$$K_{sh} = \frac{1}{4}\mu_0 M_S^2 [1-3N] \tag{2.34}$$

In addition, the demagnetization factor tensor that relates the demagnetization field with a specimen magnetization as a function of position is given by [NEAL1994],

$$N(r) = -\frac{1}{4\pi}\iiint d^3r'\nabla'\left(\nabla'\left(\frac{1}{r-r'}\right)\right) \tag{2.35}$$

This tensor is given by an integral over the object volume and can be evaluated either inside or exterior to the body. The value of tensor *N* significantly depends on the specimen shape, which is difficult to obtain in closed-form. It may be calculated exactly for an ellipsoidal shape only. In many symmetrical materials such as any ellipsoids of revolution, the demagnetization factor tensor only has three principal components, i.e.,

$$\begin{pmatrix} H_1 \\ H_2 \\ H_3 \end{pmatrix} = -\begin{pmatrix} N_1 & 0 & 0 \\ 0 & N_2 & 0 \\ 0 & 0 & N_3 \end{pmatrix}\begin{pmatrix} M_1 \\ M_2 \\ M_3 \end{pmatrix} \tag{2.36}$$

where, $N_1 + N_2 + N_3 = 1$ (in SI) and $N_1 + N_2 + N_3 = 4\pi$ (Gaussian). The demagnetization factors for the selected shapes are summarized in Table 2.02. A detailed calculation of demagnetization factor for various objects can be found in [NEAL1994]. The shape anisotropy is zero for a sphere, as $N = 1/3$. Shape anisotropy is fully effective in samples which are so small that they do not break up into domains [COEY2010].

2.6.3. Induced anisotropy

In some materials, the magnetic anisotropy can be induced by many ways: (i) fabricate nanoparticles in the presence of a magnetic field, (ii) heat treat the materials in the presence of external applied magnetic field and (iii) apply uniaxial stress. In the first two cases, after such treatment, the material may exhibit an easy axis of magnetization that points in the direction of the magnetic field. This induced anisotropy is certainly independent of any crystalline anisotropy or any other form of anisotropy that might be present. Figure 2.15 shows the typical example of inducing the anisotropy in FM materials by field annealing.

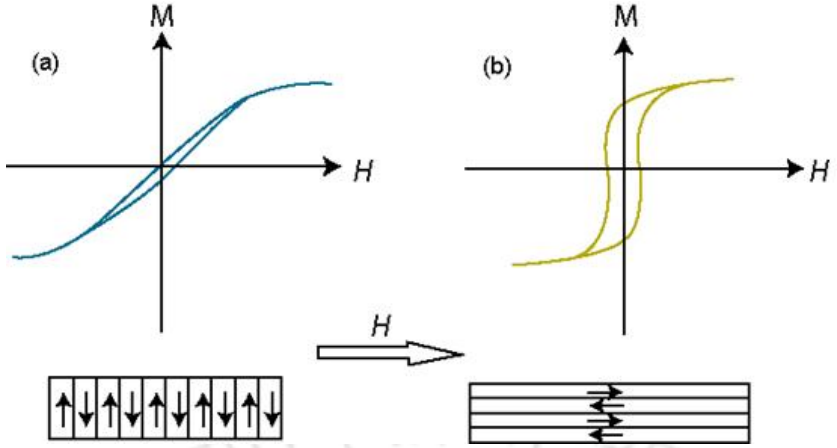

Figure 2.15: Magnetization of a thin film with induced anisotropy created by annealing in a magnetic field. The sheared (a) and open (b) loops are observed when the measuring field H is applied perpendicular and parallel to the annealing field direction, respectively.

Table 2.02: Demagnetization factors (in Gaussian units) of selected shapes.

Shape	N_1	N_2	N_3
Sphere	$4\pi/3$	$4\pi/3$	$4\pi/3$
Long Cylinder along z-axis	2π	2π	0
Infinite plate normal to z-axis	0	0	4π
Strip film normal to z-axis (t – thickness, W – Width, L – Length; $t \leq W \leq L$)	0	$8t/W$	4π

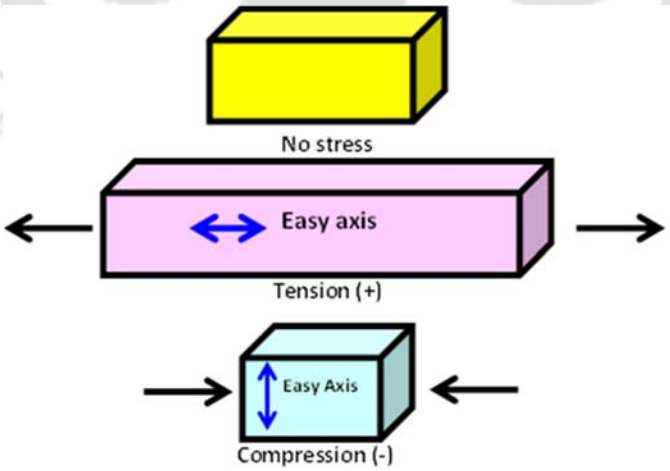

Figure 2.16: Schematic drawing of bars to demonstrate inducing an easy-axis in a material with the positive magnetostriction.

In the last case, the uniaxial anisotropy is induced by applying uniaxial stress (σ) in a FM solid [KRON2003]. The magnitude of the stress-induced anisotropy is

$$K_{u\sigma} = \frac{3}{2}\sigma\lambda_S \tag{2.37}$$

where, λ_S is the saturation magnetostriction. Both the single-ion and two-ion anisotropy contribute to the stress induced anisotropy. The highest values of uniaxial anisotropy are found in hexagonal and other uniaxial crystals. Smallest values are found in cubic alloys and amorphous ferromagnets.

2.6.4. Magnetostrictive anisotropy

Another important form of anisotropy in magnetic materials is due to magnetostriction, a change of volume of an isotropic crystal due to magnetic order. Magnetostriction relates the stress in a magnetic material to an anisotropy created by that stress. Figure 2.16 shows schematic views of bars with different applied stress conditions. If λ is positive, then application of a tensile stress to the bar creates an easy axis in the direction of the applied stress. If a compressive stress is applied, then the direction of the easy axis created will be perpendicular to the stress direction. On the other hand, if the magnetostriction constant for the material is negative, then the above phenomena would be reversed: a tensile stress will create an easy axis perpendicular to the stress direction and a compressive stress will create an easy axis in the direction of the applied stress.

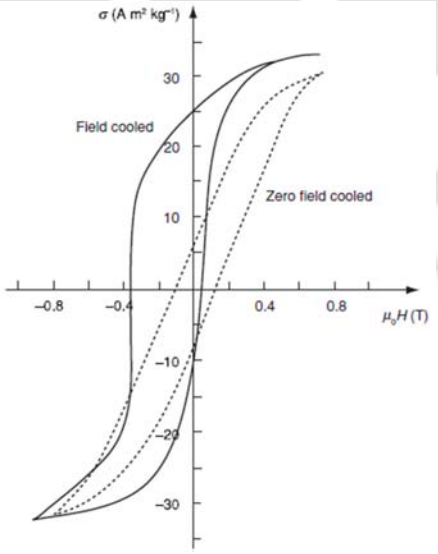

Figure 2.17: *M-H* loops at 77 K of oxide-coated Co particles. Solid line results from cooling in a field of 1 Tesla. The dashed line shows the loop when cooled in zero-field [MEIK1956].

2.6.5. Exchange anisotropy

Exchange anisotropy refers to the magnetic manifestations of an exchange coupling at the interface between two different magnetically ordered systems, i.e., when a FM and an AFM material are in contact, the coupling between them leads to an unusual unidirectional anisotropy, discovered first by Meiklejohn and Bean in 1956 in Co nanoparticles having T_C of 1390 K coated with CoO with a T_N of 291 K. Figure 2.17 depicts shifted *M-H* loops of partially oxidized Co particles measured after to 77 K in a field of 1 Tesla [MEIK1956]. The CoO was cooled through T_N in the exchange field of the Co, which has been aligned in an external field. This effect was a shifted FM *M-H* loop which is due to a new type of magnetic anisotropy, called as exchange anisotropy [MEIK1956, BERK1999]. This is the result of an interaction between an AFM and a FM materials. In the case of thin films with proper layer structures of AFM/FM [FANY2013], the nature of *M-H* loop and shift in the loop can be controlled effectively as shown in the Figure 2.18.

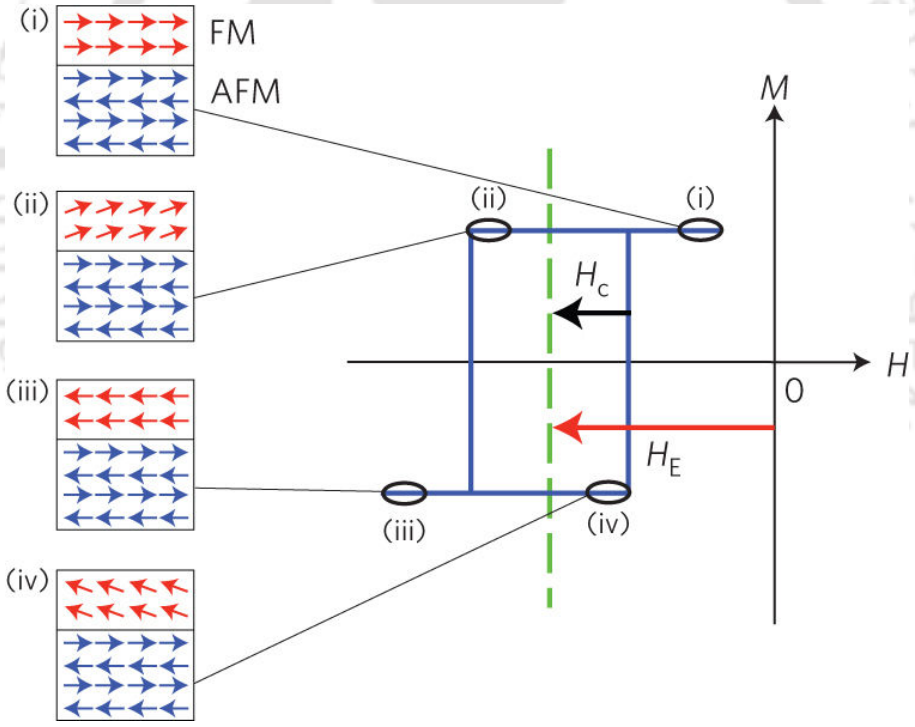

Figure 2.18: Relative orientations of the atomic moments in the AFM and FM are shown schematically, illustrating the lateral offset in the magnetization curve. The magnitude of the exchange bias field H_E and coercive field H_C are defined [FANY2013].

The exchange bias increases the magnitude of the applied magnetic field needed to reverse the magnetization of the FM from the normal coercive field H_C to $H_C + H_E$. Exchange

bias is of great technological importance in tailoring the operating characteristics of most magnetic devices, including hard disk read heads, magnetic memory and magnetic sensors.

2.7. Surface effects

The nanoparticles are smaller in size and hence large fraction of atoms in a nanoparticle are surface atoms [BATL2002]. Since the ratio of surface atoms to the bulk atoms is large, surface contribution to magnetization becomes significant. In general, the magnetic nanoparticles are considered to consist of single domain particles with uniaxial anisotropy. The orientation of its magnetic moment points either up or down in a zero-field along the easy axis. However, the surface atoms experience different environments than those in the core of the particles. As discussed earlier, there are several types of defects that exist on the surface. These defects result in uncompensated disordered spins at the surface of the nanoparticle leading to surface magnetization (FM or AFM). The surface magnetization is contributed by the surface uncompensated spins, which depend on the size of the particle and on the degree of surface disorder [DOBR2005, HOCH2006]. Because of surface effects, FM could be a universal feature of nanoparticles and their oxides, as reported by Sundaresan et al [SUND2006, SUND2009].

For example, nanoparticles of non-magnetic materials such as cerium oxide and aluminum oxide were found to display *M-H* loops at room temperature. Nanoparticles of metal nitrides, such as niobium nitride were also found to exhibit FM. Nanoparticles of some superconductors in the normal state were found to show FM. The smaller the nanoparticle, the larger is the FM. High field hysteresis and relaxation of the magnetization could result due to irreversible reorientations of the surface spins [KODA19991]. Nunes et al [NUNE1998] considered the structural relaxation of spinel ferrite nanoparticles using molecular dynamic modelling. They predicted non-uniform strains in the surface layers, with an average expansion of a few percent compared to bulk. They suggested that such an expansion might result in a stress-induced anisotropy field of up to 70 kOe, which could account for some of the anomalous magnetic behavior of ferrite nanoparticles. Kodama et al proposed that the canted spins in ferrite nanoparticles freeze into a spin glass-like phase at temperatures below 50 K [KODA1997, KODA19991, MORU2013]. Thus, the surface spins have multiple configurations for any orientation of the core magnetization. The nature of temperature dependence of coercivity of such particles is strongly dependent on the particle size and the nature varies from linear behavior to non-linear behavior with decreasing particle size. It is well understood that the changes in the physical properties can

be directly related to their microscopic origin and theoretical studies are required to confirm the surface effects. Several magnetic effects could also result in from the finite size effect of nanoparticles. These could include:

(i) Random oriented uncompensated surface spins.

(ii) Canted spins.

(iii) Spin glass like behavior of the surface spins.

(iv) Magnetically dead layer at the surface.

(v) Enhancement of the magnetic anisotropy which result for surface anisotropy.

However, surface effects lead to a decrease or an increase in the magnetization of the nanoparticle. It was reported that magnetization of oxide nanoparticles decreases up to creation size for some oxide nanoparticle [KODA19992]. On the other hand, the magnetization of some metallic nanoparticles (cobalt) was reported to increase [RESP1998]. The reduction of magnetization of oxide nanoparticles was attributed to the existence of a magnetically dead layer on the particle's surface and the existence of canted spins or the existence of a spin glass-like behavior of the surface spins [KODA19992]. Several experimental studies reported an increase in the effective magnetic anisotropy due to surface effects [JAME2001, LUIS2002, JAME2004]. Computational studies also reported different anisotropy and magnetic moment at the surface of magnetic clusters embedded in matrices [XIEY2004]. Binns et al reported that both spin and orbital moments at the surface are different from those of the bulk counterparts using Synchrotron radiation [BINN2002]. These studies suggest that the total magnetization of the nanoparticle is composed of two components: a component due to the surface spins and a component due to the core of the particle. This led to the development of model of core-shell to describe interaction between the core and the shell. In nanoparticles of AFM or ferrimagnetic materials, this interaction occurs at the interface between the FM surface and AFM (or ferrimagnetic) core. In some FM nanoparticles, the surface of the metal usually oxidizes in air and forms an AFM metal-oxide shell around the FM metal core. Thus, there will be an interaction between the core and the shell, called exchange bias or exchange coupling, which provides an additional magnetic anisotropy to help aligning the FM spins in certain directions. Core-shell exchange interaction and surface anisotropy were found to play significant roles in determining some magnetic properties of nanoparticles. The structural modifications at the boundaries of FM or ferrimagnetic nanoparticles, such as vacancies, broken bonds, may induce enough frustration, which leads to different canted magnetic structures [MAKO2009]. The canted surface spins may freeze giving rise to a glassy state at low temperatures. One of the

important features characterizing the surface spin glass state in nanoparticles is the flattening of the field-cooled magnetization at low temperatures [LABA2005]. The main origin of spin glass-like behavior in nanoparticles could be due to strong inter-particle interactions or due to surface spin effects within individual particles.

2.8. Magnetic interaction

2.8.1. Magnetic dipole-dipole interaction

Magnetic dipole-dipole interaction [BLUN2003] or dipolar coupling refers to the direct interaction between two magnetic dipoles. The energy of the interaction is given as

$$H = -\frac{\mu_0}{4\pi r_{ij}^3}[3(\mu_i.\hat{r}_{ij})(\mu_j.\hat{r}_{ij}) - (\mu_i.\mu_j)] \qquad (2.38)$$

where $\hat{r}_{ij}$ is a unit vector parallel to the line joining the centers of the two dipoles, μ_i, μ_j are the moments of two dipoles separated by a distance $|r_{ij}|$. This interaction is important in the properties of those materials, which order at milli-Kelvin temperature. The magnetic dipolar interaction is too weak to account for the ordering of most of the magnetic materials. There is a built in anisotropy to the dipolar interaction which can orient the spins either parallel (FM) or antiparallel (AFM). If the spins are oriented along r_{ij}, they couple ferromagnetically. Otherwise, they couple antiferromagnetically.

2.8.2. Direct exchange interaction

Two neighboring magnetic moments can interact with each other directly without the aid of any intermediate molecules or ions. This interaction is known as direct exchange. In reality, there is hardly seen any interesting magnetic phenomenon that could be explained based on the direct exchange. As there is insufficient overlapping of the participating magnetic dipoles, direct exchange is not an important mechanism in controlling the magnetic properties.

2.8.3. Super-exchange interaction

Kramer [KRAM1934], Anderson and his group [ANDE1955, ANDE1958], Goodenough [GOOD1995] and Kanamori [KANA1959] pointed out that FM and AFM interactions are possible by a mechanism called super-exchange interactions. Here, two magnetic ions interact through an intermediate non-magnetic ion. This is a common interaction in insulating magnetic oxides where the intermediate ion is O^{2-}.

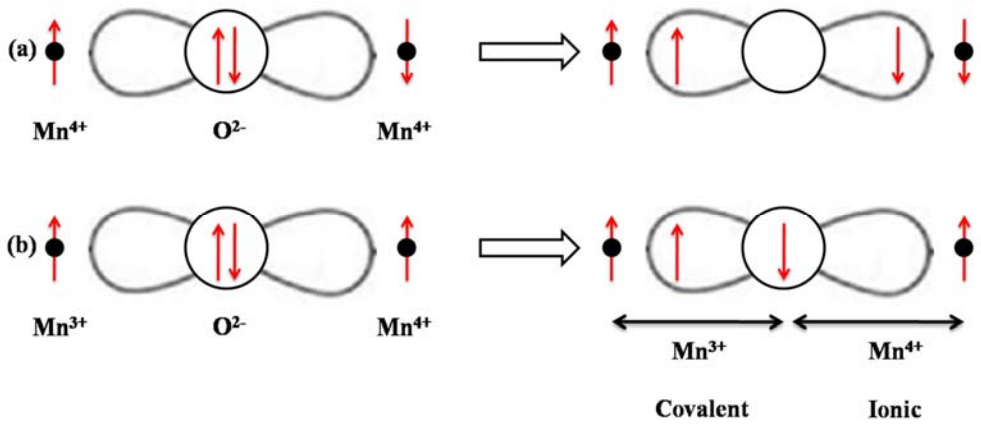

Figure 2.19: Arrangement of spins and orbitals in (a) an AFM super-exchange interaction, and (b) a FM super-exchange interaction.

A schematic representation of super-exchange interaction producing AFM and FM is shown in Figure 2.19(a) and (b), respectively. Figure 2.19(a) shows the situation where the 3*d* orbital is pointing towards the O-2*p* orbital. The overlapping between the 3*d* and *p* orbitals facilitates the simultaneous covalent bond formation between the cations (Mn^{4+}) and anions (O^{2-}) on both sides since the electrons of O^{2-} anion are shared with the 3*d* electrons. Here, out of two valence electrons of oxygen, the up spin electron spends some time with the cation in one side having up spin configuration and the down spin electron spends some time with other cation having down spin configuration to satisfy the Hund's rule. In this process, each cation-anion pair has FM (parallel) alignment of electrons and the net cation-cation interaction is AFM. According to Goodenough [GOOD1995], the above covalent bonding is not permissible if the core spins of magnetic cations are aligned parallel as shown in Figure 2.19(b). Under this situation, out of two valence electrons of O^{2-}, the spin up electron form covalent bonding with left side cation (Mn^{3+}) having spin up electron, while the spin down electron of oxygen forms ionic bond with right side cation (Mn^{4+}). The direct exchange between oxygen and the right side cation is AFM. So, overall FM interaction prevails between Mn^{3+} and Mn^{4+} ions. In many DMS materials, the super-exchange interaction comes into picture at large concentrations of TM-ion. The first principles study of the super-exchange interaction in (Ga,Mn)V, (V = N, P, As and Sb) by Chang et al [CHAN2007] reports that short-range super-exchange interaction is found to be AFM in nature and is found to be quite strong in (Ga,Mn)N and weak in (Ga,Mn)As and (Ga,Mn)Sb. The significant super-exchange interaction at large TM concentrations plays an important role in reducing Curie temperature.

2.8.4. Anisotropic exchange interaction

Dzyaloshinskii [DZYA1958] postulated a contribution to the exchange interaction between two neighboring spins, which was later identified by Moriya [MORI1960] as spin-orbit coupling between the spins. The excited state of one of the participating ions is not connected with oxygen ion but is produced by the spin-orbit coupling in one of the magnetic ions. Hence, there is an interaction between the excited states of one ion with the ground state of other ion. This interaction is known anisotropic exchange interaction and is mathematically expressed as

$$H_{DM} = D(S_1 \times S_2) \tag{2.39}$$

where S_1 and S_2 are two neighboring spins and D is Dzyaloshinskii-Moriya constant. The Dzyaloshinskii-Moriya interaction tries to align the vectors S_1 and S_2 at right angles in a plane perpendicular to the vector D. Its very effect is to cant the spins by a small angle. The Dzyaloshinskii-Moriya interaction is responsible for the observation of small FM moment for AFM samples.

2.8.5. Ruderman-Kittel-Kausya-Yosida Interaction

It is a special kind of indirect exchange interaction commonly seen in metals having localized magnetic moments and the interaction is mediated via the itinerant electrons. The localized magnetic moment of an ion spin-polarizes the conduction electrons and this spin-polarized electrons couple to the neighboring localized magnetic moment at a distance r away. The Ruderman-Kittel-Kausya-Yosida (RKKY) model [RUDE1954, KASU1956, YOSI1957] explains the magnetic interaction between the localized single magnetic ions and the delocalized conduction electrons band. The exchange interaction is thus indirect because it does not involve direct coupling between magnetic moments. The coupling takes the form of an r dependent exchange interaction $J_{ex}(r)$ given by

$$J_{ex}(r) = \frac{4\pi^2 m^* k_F^4}{r^2} F(2k_F r) \tag{2.40}$$

m^* is effective mass, k_F is the Fermi wave vector of the electron gas. The oscillating function is given as $F(x) = (xcosx - sinx)/x^4$ and plotted in Figure 2.20 as a function of x.

It is a long range interaction with oscillatory dependence on the distance between the magnetic ions. Hence depending on the separation it may be either FM or AFM [VEGA2001]. RKKY interaction is also found to play a major role in many DMS materials when the solubility of carrier level is quite high [STOR1986, DIET1997, NADO2002]. The

carrier concentration in such case is found to be quite high, i.e., on the order of 10^{19} cm^{-3} to 10^{21} cm^{-3} and it correspond to about 60 at.% of carrier doping in Group IV-VI based DMS [STOR1986, NADO2002].

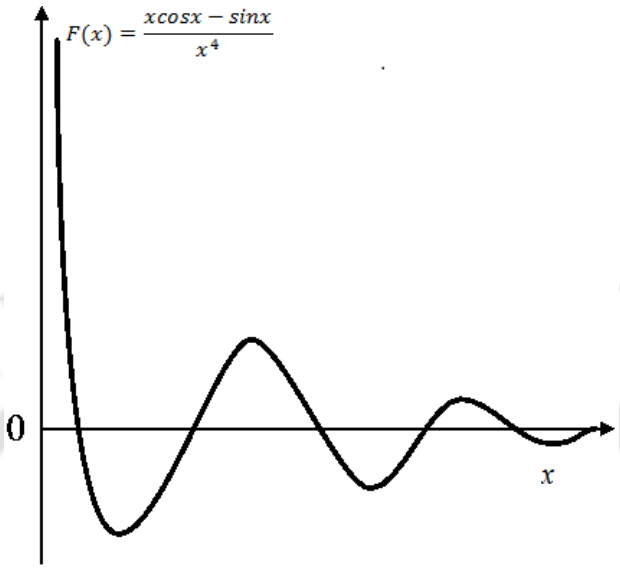

Figure 2.20: The oscillatory part of RKKY interaction energy.

In DMS materials, doping of extra charge carrier along with magnetic ions gives rise to enhanced FM [RISB2003, LIN2004, SLUI2005, THEO2006, LIX2007, GOPI2008]. (GaMn)As and (Ge,Mn) based alloys exhibit FM due to exchange interaction between Mn atoms with distance larger than the average nearest Mn and Mn distance. In addition, the exchange interactions exhibit oscillatory character and are exponentially damped by disorder. However, isolated Mn impurities in the semiconductor host with same number of valence holes exhibit undamped RKKY type behavior [BOUZ2003, KUDR2004].

Chapter 3

Experimental Methods

3.1. Introduction

In the course of present investigations, several experimental techniques are used for the preparation and characterization of the NiO samples. This chapter provides a brief description of these experimental techniques.

3.2. Techniques used for sample preparation

Material processing in the present thesis is carried out in two steps: (1) High-energy planetary ball milling of the pure Nickel-Oxide (NiO) powders followed by heat treatment of as-milled powders under different atmospheres. (ii) Preparation of NiO and Nickel (Ni) thin films with different thicknesses using RF/DC magnetron sputtering technique and post-annealing at different temperatures under different environments. A brief discussion on both the techniques is given below.

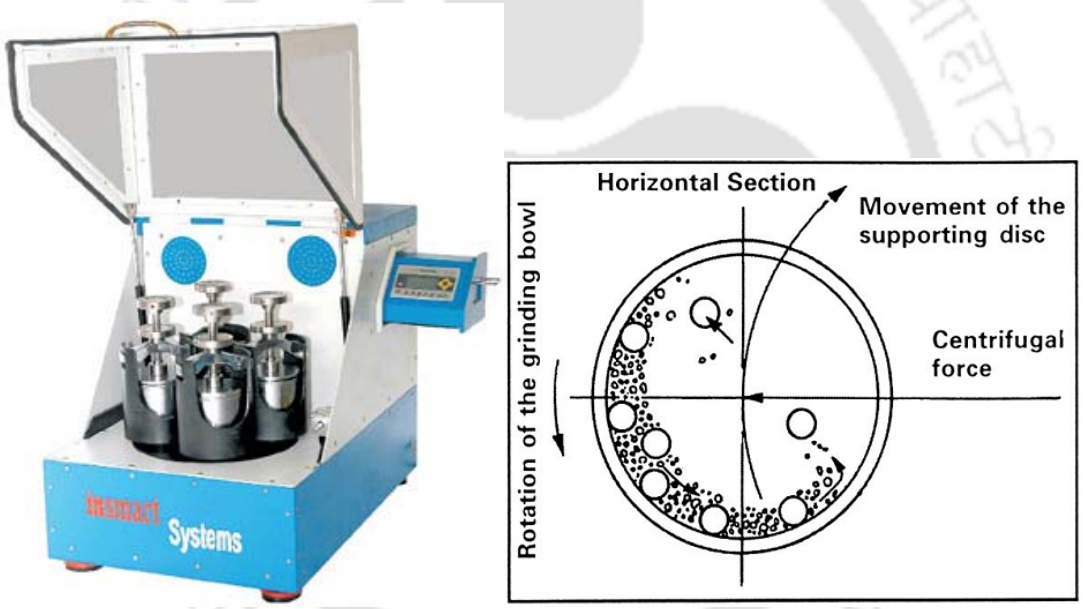

Figure 3.01: (left) Photographic view of the planetary ball mill used and (right) schematic diagram of the horizontal section of a vial depicting the movement of the balls inside the vial due to its planet like movement.

3.2.1. Ball milling technique

Milling of pure NiO powders is carried out by high-energy ball milling in a planetary ball mill (Insmart, India) under dry milling conditions in an argon (Ar) gas atmosphere. The photographic view of the planetary ball comprising of a horizontal support disc on which vials are mounted and the schematic view of milling process are depicted in Figure 3.01. The vials mounted on the horizontal disc rotates in a direction opposite to that of the disc

and thereby simulating a planetary like motion. This results in a large centrifugal force acting on the balls kept inside the vial and causes the balls to collide with themselves and to the wall of the vial with high impact. When the NiO powders are placed in the vial along with the balls, the powders are subjected to repeated cold welding and fracturing at the surfaces of the balls and the vial. This process leads to disintegration of the powders, which results in first in refinement of crystallite size to produce nanocrystalline alloys along with large number of defects in the parent powders [SONI2001, SURY2001, KOCH2002, SURY2004]. Hence, crystallite size refinement is a natural consequence of a ball milling process. As the milling time progresses the alloy becomes amorphous. The refinement and alloying processes are determined by the milling parameters such as ball-to-powder weight ratio, ball size, rotation speed, milling time, etc. Nature of the milling vials and balls also plays an important role in the process along with the milling media.

In the present thesis work, dry milling of high purity NiO powders is carried out under high purity Ar gas atmosphere. Hardened steel vial and hardened steel balls are used for milling of all the NiO powders. After a careful and systematic investigations, the ball-to-powder-weight ratio is fixed at 10:1 with different milling speeds of 350, 500, and 600 rotations per minute (rpm) for milling process. Prolonged milling under dry conditions results in a temperature rise inside the vial which usually deteriorates the final product. Thus, the milling process is programmed to pause for 15 minutes after every 15 minutes of continuous milling to avoid excessive heating. In addition, Ar gas is periodically purged inside the vial to avoid oxidation.

3.2.2. Sputtering technique

In 1852, surface coatings generated in the valve under a glow discharge was discovered by Sir W. R. Grove. This process was called as spluttering by Sir W. Thomson and soon it was adopted as sputtering. The ejection of atoms from the cathode surface by impinging of energetic positive ions of noble gases such as Helium, Argon, Neon and Krypton at a reduced gas pressure under high direct current (DC) voltage gives rise to the sputtering [OHRI1992, WAGE1994, SESH2002]. This process involves a momentum transfer between the impinging positive ions and the cathode surface atoms as shown in Figure 3.02 and as a result of which a physical removal of atoms from the target surface takes place. The sputtering yield is defined as ratio between the mean numbers of emitted atoms to number of incident ions on the target surface.

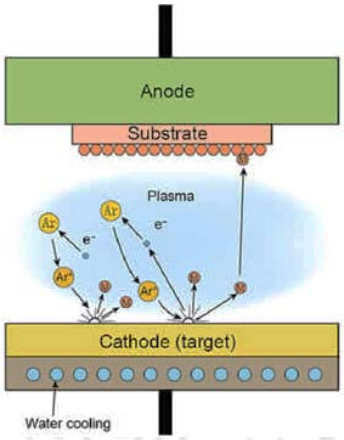

Figure 3.02: Schematic diagram of the sputtering process.

- The sputtering yield increases with a) energy, b) mass of the bombarding atoms and c) decrease of angle of incidence to the target.
- A minimum energy is required to start the sputtering process.
- Sputter atoms have higher energy than those of the thermally evaporated atoms.
- The sputter atoms are ejected along the crystallographic directions of the cathode metal lattices.
- Sputtering yield decreases with larger increase of the ion-energy because of the deeper penetration of ions inside the lattice.
- Sputtering is also accompanied by the emission of secondary electrons from the cathode surface.
- The sputtering yield is insensitive to the cathode temperature.
- If the sputtering process does not involve any of the chemical reaction between bombarding gas ions and the cathode, it is known as physical sputtering.
- If some reactions are involved then it is named as reactive sputtering.

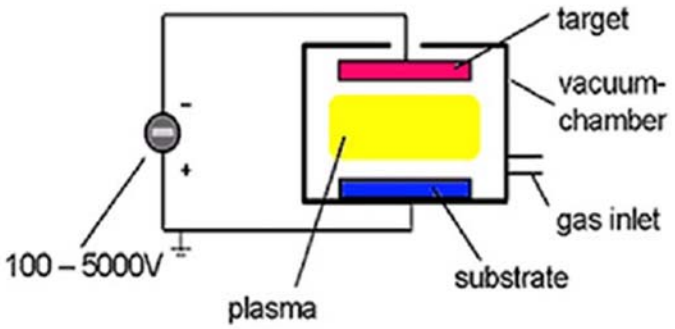

Figure 3.03: Schematic arrangement of DC sputtering technique.

The physical deposition process consists of three steps

1. Emission of the particles from a source,
2. Their transport to the substrate, and
3. Condensation on the substrate.

There are four different types of sputtering process [DC, Radio-frequency (RF), Magnetron and Reactive sputtering] used for thin film deposition. We have used magnetron sputtering for depositing the films of present investigation.

3.2.2.1. DC sputtering technique

Figure 3.03 depicts a typical arrangement used for DC sputtering. In this case, target and substrate oppose each other in the vacuum chamber having a distance of few centimeters to few tens of centimeters. The target is connected to a negative output of a DC power supply, acting as the cathode whereas substrate and chamber walls act as anode. After the creation of Ar atmosphere with a pressure of about 1 - 100 mTorr, the gas discharge is ignited by applying a DC voltage. The created Ar^+ ions are now accelerated toward the target and eject atoms from the target. These atoms subsequently are deposited on the substrate. At low pressures, the mean free path between collisions is large, the ionization efficiency is low and self-sustained discharges cannot be maintained below few mTorr. As the pressure increases at a fixed voltage, the electron mean free path is decreased, more ions are generated and large current flow. If the pressure is too high, the sputtered atoms undergo increased collisional scattering resulting in a low deposition process. The deposition rate is proportional to (a) power consumed, (b) square of current density and (c) 1/(electrode spacing). DC sputtering works with all types of target materials which are conductive in nature.

However, DC sputtering suffers from two major drawbacks as compared to conventional evaporation: (i) low deposition rates and (ii) high thermal load of the substrate due to bombardment of secondary electrons. In order to increase the deposition rate and to control the thermal load, magnetron sputtering as described below in Figure 3.04 is utilized for the fabrication of the films.

3.2.2.2. Magnetron sputtering technique

The main difference between magnetron sputtering and DC sputtering system described above is the addition of a strong magnetic field near the target area. In magnetron sputtering,

electrons ideally don't even reach the anode but are trapped near the target and thereby enhancing the ionization efficiency. This is accomplished by employing a magnetic field oriented parallel to the target and perpendicular to the electric field. Practically, this is achieved by placing bar magnets behind the target as shown in Figure 3.04.

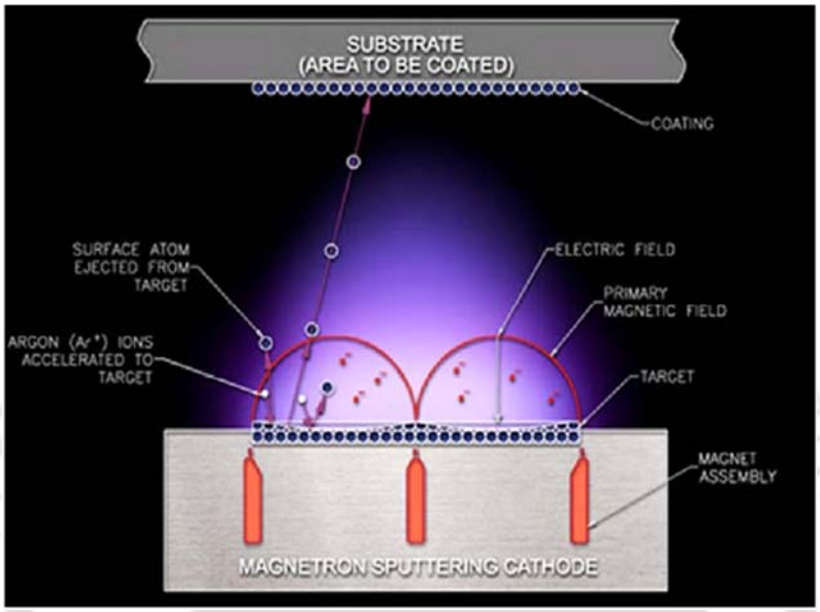

Figure 3.04: Schematic presentation of magnetron sputtering gun assembly.

The magnetic field lines emanate first normal to the target and then bend with a component parallel to the target surface and finally return to magnet completing the magnetic circuit. Electrons emitted from cathode are initially accelerated toward the anode, but executing a helical motion when they encounter the region of the parallel magnetic field. Therefore, they are bent in an orbit back to the target. The chief reasons of its success are (1) increased sputtering rates (~ 5 - 10 times) due to high plasma density around target, (2) low discharge voltages of 300 to 1000 V due to the reduced plasma impendence resulting from high plasma density and (3) low thermal load of the substrate due to deflection of secondary electrons by the magnetic field. Figure 3.05 depicts the typical set up of magnetron sputtering used in the present thesis work for fabricating Ni and NiO thin films with different thicknesses. The substrate is loaded on the rotating substrate holder. Subsequently, the chamber is pumped to high vacuum (< 10^{-3} Pa) using diffusion pump and rotary pump combination. Ar gas of fixed pressure is permitted into chamber continuously using mass flow controller (MFC) and the Ar gas pressure in the chamber is maintained by adjusting the MFC and process control valve. The optimized sputtering Ar gas pressures for thin films are fixed for different thickness. After stabilizing the constant Ar gas pressure in

the chamber, a constant sputter power is applied to commence the sputtering process. The deposition of the films is carried out after stabilizing the plasma and completing the pre-sputtering process.

Figure 3.05: Photographic view of the magnetron sputtering system used in the present work.

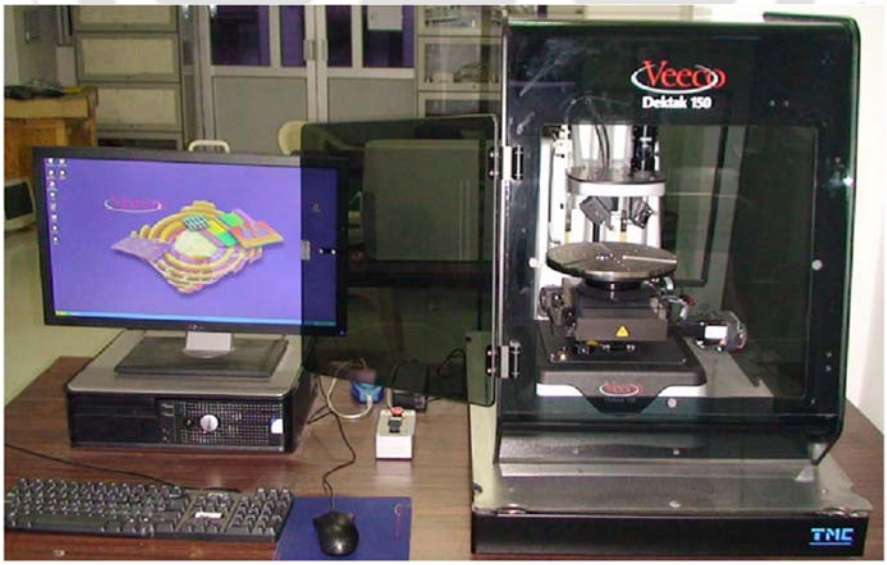

Figure 3.06: Photographic view of Vecco-Dektak 150 surface profilometer.

3.2.2.3. Deposition rate calibration

The deposition rate is calibrated with surface profilometer (Vecco, Dektak-150), as illustrated in Figure 3.06. Stylus profilers are versatile measurement tools for studying surface topography. Their primary function is to measure film thickness by scanning step heights and trench depths. The stylus profilers rely on a small-diameter stylus moving along a surface either by movement of the stylus or movement of the surface of interest. A true stylus profiler moves linearly to obtain the measurement. As the stylus encounters surface features, the stylus moves vertically to measure various surface features, such as deposited film and irregularities. To monitor the thickness of the deposited films, a proper marking using permanent marker is made on top of the cleaned substrate. Subsequently, the deposition is done under optimize condition. After the completion of the deposition, the film is cleaned through sonication in acetone. As a result, the film deposited on the substrate reveals a clear step. The step size is evaluated using surface profiler as displayed in Figure 3.07 and the average deposition rate is eventually calculated by dividing the average thickness measured at various locations on the substrate with deposition time. In order to confirm the reproducibility, more films are made under the same sputtering conditions and analyzed using surface profilometer. The stylus profiler used in the present work was sponsored by Defence Research & Development Organization (DRDO), New Delhi under the project scheme of ERIP/ER/0900363/M/01/1185 Dated 16 November 2009.

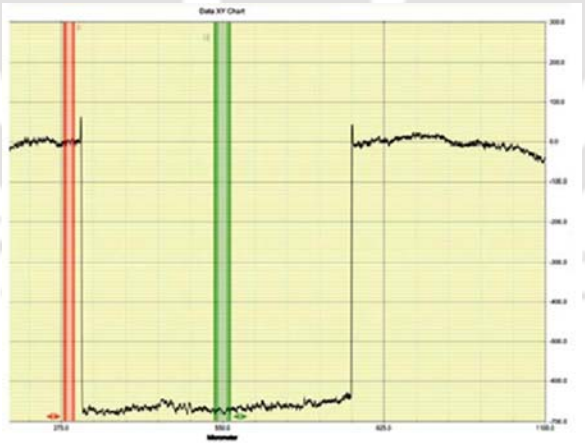

Figure 3.07: A typical scan profile of the surface profilometer.

3.2.3. Heat treatment at elevated temperatures

In order to optimize nanocrystalline microstructure and to release defects (strain) created during the milling process, the selected as-milled powders are undergone heat treatment at elevated temperatures (annealing) in an air atmosphere using a resistive tubular furnace

(Okay, India). This tubular furnace could be used up to a temperature of 1600 °C. The temperature of the constant temperature heat zone at the center of the furnace extends to 150 mm. The annealing temperature is controlled to ± 2 °C using a commercial temperature controller. The annealing temperature and annealing time are optimized based on the development of nanocrystalline microstructure, release of defects (strain) and magnetic properties of the nanocrystalline powders.

Similarly, all the as-deposited NiO and Ni films are annealed in a separate custom-made high vacuum chamber at different annealing temperatures (250 ºC, 300 ºC, 400 ºC and 500 ºC) for different annealing times. The annealing temperature and annealing time are optimized based on the development of nanocrystalline microstructure, thermal decomposition in NiO and oxidation behaviour of Ni and magnetic properties of the films. In the annealing process, the substrate with film is kept on a filament heater and attached close to a thermocouple (Chromel-Alumel) to avoid any temperature lag between heater, sample and thermocouple. The chamber is pumped to high vacuum (< 10^{-3} Pa) using diffusion pump and rotary pump combinations. After reaching the desired vacuum, temperature is raised constantly at a rate of 10 ºC/min to the annealing temperature. The sample is annealed at a given annealing temperature within the temperature stability of ±2 ºC accuracy. After the completion of heat treatment at a particular temperature, the heater is switched off and the sample is allowed to cool down naturally to room temperature in presence of vacuum.

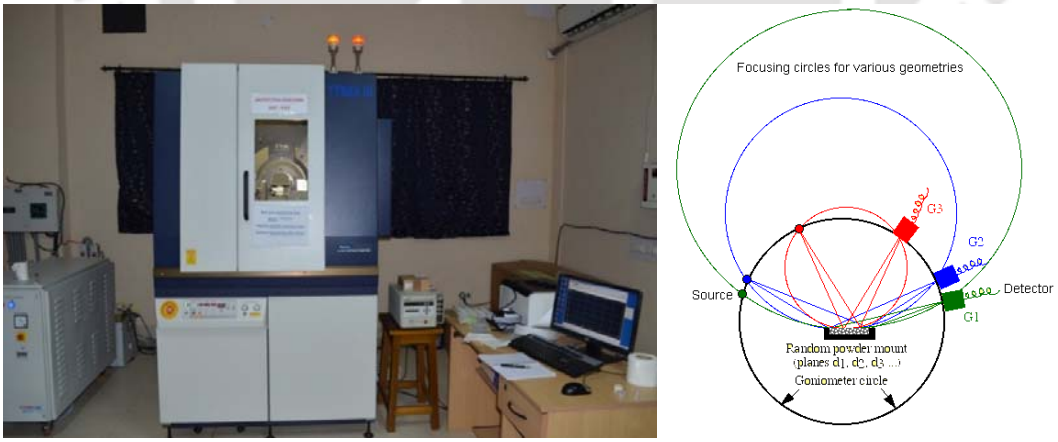

Figure 3.08: (left) Photographic view of Rigaku TTRAX III 18 kW X-ray diffractometer and (right) Bragg-Brentano diffraction geometry of a powder X-ray diffractometer.

3.3. Structural characterization

3.3.1. X-ray diffraction

Powder X-ray diffraction (XRD) is the most widely used non-destructive technique for general crystalline material characterizations. High-power (18 kW) Rigaku TTRAX III X-ray diffractometer in Bragg-Brentano diffraction geometry and parallel beam geometry is used in the thesis work. Cu-K_α X-ray radiation with a wavelength of 1.54056 Å is used in all the cases. Figure 3.08 displays the typical photographic view of the Rigaku high-power (18 kW) TTRAX III X-ray diffractometer and Bragg-Brentano geometry of powder X-ray diffractometer.

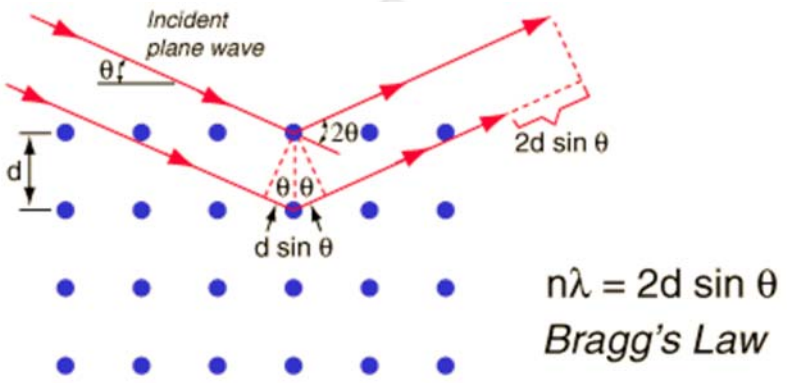

Figure 3.09: Diffraction of X-ray by a crystal.

XRD technique allows identification of various crystalline phases present in the material and provides other structural information such as size of the crystallites, strain present inside the crystallites, lattice constant, etc. It is well-known that an ideal crystal has a periodic arrangement of atoms as shown in Figure 3.09. Diffraction of X-ray occurs through constructive interference of X-ray scattered from atoms of a set of parallel planes in crystal lattice at a particular angular positions of the incident wave known as Bragg angles. This condition for obtaining constructive interference is known as Bragg's law given by the relation [CULL2001],

$$2d_{hkl}\sin\theta = n\lambda \qquad (3.01)$$

where, d_{hkl} is inter-planer spacing, θ is the angle of incidence of the X-ray beam with the atomic plane, λ is wavelength of the X-ray and n is order of diffraction (we consider only the first order diffraction, $n = 1$, because the second order peaks are mostly difficult to detect experimentally). A series of these angles can be used to determine the Miller indices (*hkl*) and the crystal structure can be identified from the systematic behavior of these indices. Figure 3.09 shows the diffraction of X-ray from crystal lattice planes illustrating Bragg's law. The structural parameters such as the average size of the crystallites (D), d-spacing,

lattice constant (a) and strain (η) present inside the crystallites, etc. can be determined by a careful analysis of the XRD patterns using various models [CULL2001]. All measurements are carried out at an accelerated voltage of 50 kV and current of 200 mA. XRD data are collected at a slow scan rate of 0.005 °/s. The exact peak position and full width half maxima (FWHM) of the XRD peak is obtained using Gaussian fitting to the experimental data. The values of D and η can be estimated from the width of the diffraction peaks. This is analogous to the diffraction of light from a grating where the line width is proportional to the number of diffracting grooves in the grating. The broadening $\Delta\theta_{size}$ due to crystallite size can be quantified by Scherrer's formula [CULL2001],

$$\Delta\theta_{size} = \frac{k\lambda}{D\cos\theta} \tag{3.02}$$

where $\Delta\theta_{size}$ is broadening due to crystallite size. Presence of strain also broadens the peak which can be quantified as [CULL2001],

$$\Delta\theta_{strain} = 4\eta\tan\theta \tag{3.03}$$

where $\Delta\theta_{strain}$ is broadening due to strain. Williamson and Hall plot (WHP) method is used to estimate the effects of crystallite size and strain due to the broadening [WILL1953], which is the combination of both equations (3.02) and (3.03) for a set of Bragg peaks. This method is a linear representative of the total broadening effect expressed as

$$\Delta\theta = \frac{k\lambda}{D_{WHP}\cos\theta} + 4\eta\tan\theta \tag{3.04}$$

or

$$\Delta\theta\cos\theta = \frac{k\lambda}{D_{WHP}} + 4\eta\sin\theta \tag{3.05}$$

In case of elastically anisotropic materials, certain Bragg peaks are affected more by strain than other peaks. In such cases, the use of WHP method for the analysis of size and strain is questionable, as the data extracted from XRD do not fall into straight line. In order to consider the different strain contribution to different peaks, Modified Williamson-Hall Plot (MWHP) method [UNGA1991, UNGA1992] can be used to analyze the diffraction peaks. According to this model, the individual contribution to the broadening of XRD peaks can be expressed as

$$(\Delta K)^2 = \left(\frac{0.9}{D}\right)^2 + \left(\frac{\pi b^2\rho}{2B}\right)K^2C_{hkl} \tag{3.06}$$

where ΔK [= $(2\cos\theta\,\Delta\theta)/\lambda$], $\Delta\theta$ is full width at half maximum (FWHM) of the Bragg reflections (in radian) after correcting instrumental broadening, $K = 2\sin\theta/\lambda$, b is modulus of Burgers vector of dislocations, B is a constant (taken as 10 for a wide range of dislocation distributions [SHEN2005]), $C_{hkl} = C_{h00}\left(1 - qH^2\right)$ is dislocation contrast factor introduced to take care elastically anisotropic materials, where the residual strains affect some Bragg reflections more than the others, $H^2 = \left(h^2k^2 + k^2l^2 + l^2h^2\right)/\left(h^2 + k^2 + l^2\right)$ for a cubical system and q is a constant. In the MWHP formulation, Ungar et al [UNGA1991, UNGA1992] considered that dislocations/defect are the main contributors to the strain. The plots between $(\Delta K)^2$ and K^2C_{hkl} can be fitted using a straight line and the values of D and ρ could be calculated from intercept and slope of the fitted straight line, respectively. Note that the dislocation density is one of the major structural parameters [HULL2001] influencing the final nanocrystalline microstructure and correlated to the induced strain and reduced crystal size as

$$\eta = \frac{\rho D b}{2\sqrt{3}} \tag{3.07}$$

Figure 3.10: Photographic view of Scanning electron microscope.

3.3.2. Morphological and microstructural characterization

3.3.2.1. Scanning electron microscopy

Scanning electron microscope (SEM, Leo 1430VP) with energy dispersive spectroscopy (EDS) attachment (Oxford) and field emission scanning electron microscope (FE-SEM, Sigma Zeiss, Germany) are used to study the surface morphology and elemental

compositions of the alloy powders. A photographic view of the FE-SEM used in the present study is shown in Figure 3.10. SEM is a microscopic technique that uses electrons to form an image of objects and to study surface morphology, fractured components, foreign particles and residues, polymers, electronic components, biological samples and countless others. The thermionically emitted electrons from a tungsten filament or field emission controlled electrons are drawn to an anode, focused by two successive condenser lenses into a beam with a narrow fine spot size (~ 50 Å). The shorter wavelength of electrons permits image magnifications of up to 100,000 times in SEM. Pair of scanning coils located at the objective lens deflects the beam either linearly or in raster fashion over a rectangular area of specimen surface.

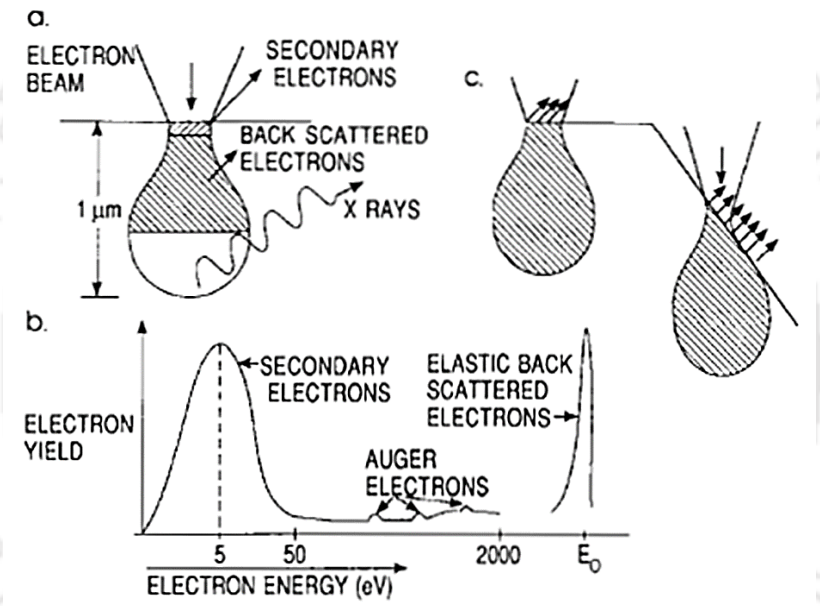

Figure 3.11: (a) Electron and photons signals emanating from tear-shaped interaction volume during electron beam impingement on specimen surface, (b) Energy spectrum of electrons emitted from the specimen surface and (c) Effect of surface topography on electron emission.

Figure 3.11 displays the interaction of electrons on the surface of the sample. Upon electron impingement on the surface, the interaction volume assumes a tear drop shape. These primary bombarding electrons on the surface of the specimen dislodge electrons called as secondary electrons from the specimen. These dislodged secondary electrons are attracted and collected by a positively biased grid or detector, and then translated into a signal. These signals are then amplified, analyzed and translated into images of the

topography being inspected. Finally, the image is shown on a cathode ray tube. The most common imaging mode relies on the detection of the very lowest portion of the emitted energy distribution. Their very lower energy means they are originated from a subsurface depth of no longer than several angstroms.

Apart from secondary electrons, the primary electron beam results in the emission of backscattered (or reflected) electrons (BSE) from the specimen. BSE possesses more energy than secondary electrons and have a definite direction. All emissions above 50 eV are considered to be backscattered electrons. It may be noted that the BSE imaging is useful in distinguishing one material from another, since the yield of the collected backscattered electrons increases monotonically with the specimen's atomic number Z (~ 0.05 $Z^{1/2}$). BSE imaging can distinguish elements with atomic number differences of at least 3, i.e., elements with atomic number differences of at least 3 would appear with good contrast on the image.

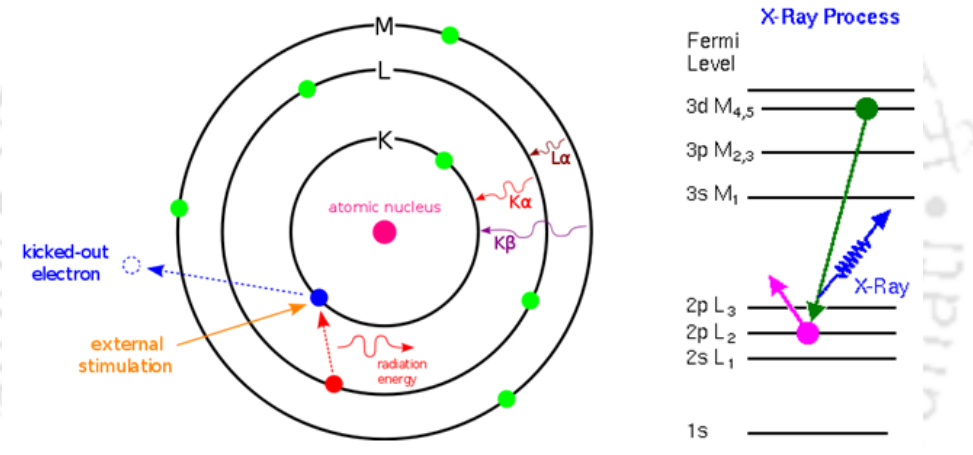

Figure 3.12: Schematic of X-ray emission during electron-atom interaction.

EDS analysis is quite useful in identifying materials and contaminants as well as estimating their relative concentrations on the surface of the specimen. During EDS analysis, the specimen is bombarded with an electron beam inside the SEM. The bombarding electrons colliding with the specimen knock off some of the electrons from the atoms, as shown in Figure 3.12. A position vacated by an ejected inner shell electron is eventually occupied by a higher-energy electron from an outer shell. To be able to do so, however, the transferring outer electron must give up some of its energy by emitting X-ray. The amount of energy released by the transferring electron depends on which shell it is transferring from, as well as which shell it is transferring to. Furthermore, the atom of every element releases X-ray with unique amounts of energy during the transferring process. Thus,

by measuring the amounts of energy present in the X-ray being released by a specimen during electron beam bombardment, the identity of the atom from which the X-ray was emitted can be established. The output of an EDS analysis is an EDS spectrum, which is just a plot of how frequently an X-ray is received for each energy level. An EDS spectrum normally displays peaks corresponding to the energy levels for which the most X-ray had been received. Each of these peaks is unique to an atom, and therefore corresponds to a single element. The higher the peak in a spectrum, the more concentrated the element is in the specimen.

In the present work, a thin layer of the as-milled and annealed powders are spread on carbon coated tape and mounted on the FE-SEM stub. Gold coating, wherever necessary, was then applied over the surface to yield an electrically conducting surface for SEM observation. For the case of thin films, the as-deposited and annealed NiO and Ni films are directly mounted on the FE-SEM stub and characterized after the necessary gold coating.

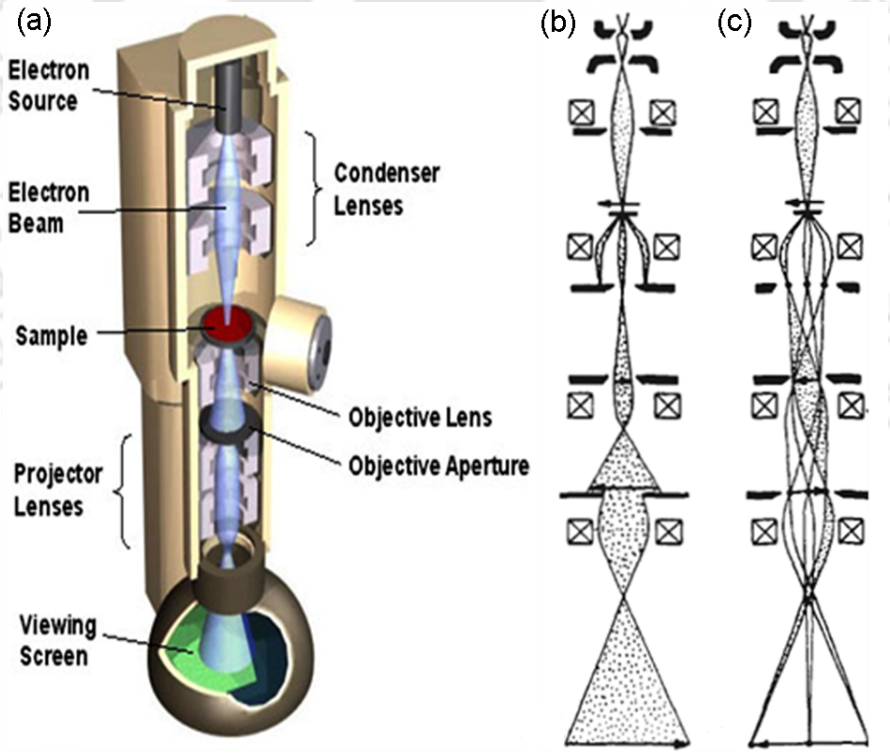

Figure 3.13: (a) Cut view of transmission electron microscope and (b) schematic ray diagrams of image mode and (c) diffraction mode.

3.3.2.2. Transmission electron microscopy

Transmission electron microscope (TEM, Jeol 2100, TECNAI G2 F30) has been used to study the microstructure of the powders. TEM is an optical analogue to the conventional

light microscope. It is based on the fact that electrons can be ascribed a wavelength (of the order of 0.25 nm), but at the same time interact with magnetic fields as a point charge. A beam of electrons is applied instead of light and the glass lenses are replaced by magnetic lenses. The lateral resolution of the best microscopes is down to atomic resolution. A schematic diagram of a TEM is shown in Figure 3.13. Electrons emitted from electron gun are accelerated to 100 - 300 keV and first projected on to the specimen by means of the electromagnetic lens systems. The scattering processes experienced by electrons during their passage through the specimen determine the kind of information obtained as shown in Figure 3.14.

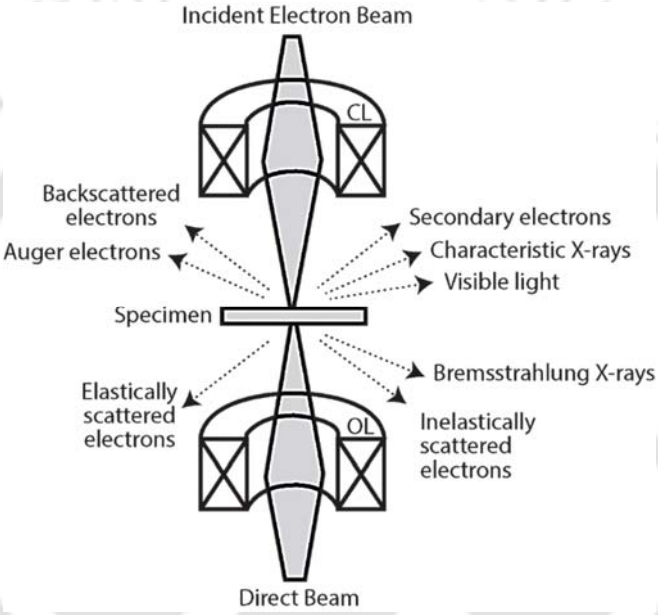

Figure 3.14: Various signals generated as a result of electron beam interaction with a thin solid specimen in TEM.

Elastic scattering involving no energy loss when electrons interact with the potential field of the ion cores gives rise to diffraction pattern. In-elastic scattering between beam and matrix electron at heterogeneities such as grain boundaries, dislocations, second-phase particles, defects, density variations cause complex absorption and scattering effects. The generation of characteristic X-ray and Auger electrons also occurs, but these by-products are not usually collected in a typical TEM measurement. The emergent primary and diffracted electron beams are now made to pass through a series of post-specimen lenses. The objective lens produces the first image of the object. Depending on how the beams reaching the back focal plan of the objective lens, the beams are subsequently processed using different operation modes. Basically, either magnified images or diffraction patterns

are obtained. The image can be studied directly by the operator or photographed with a camera.

Images can be formed in different ways. The bright-field image is obtained by intentionally excluding all diffracted beams and only allowing the selected portion of the central beam passed through the specimen. This is done by placing suitably sized apertures in the back focal plane of the objective lens. Intermediate and projection lenses then magnify this central beam. Dark-field images are also formed by magnifying a single beam by choosing one of the diffracted beams by means of an aperture that blocks the central beam and the other diffracted beams. By selected area electron diffraction pattern, ring like structure is imaged, which corresponds to the particular plane of that element or compound. If only diffused rings appear then the system must have single amorphous phase. The high-resolution TEM image obtained by allowing both the central beam passing through the specimen and one or more of the diffracted beams helps to evaluate the average grain size and dislocations more precisely.

For TEM observation, the sample in the form of powder is dispersed either in dimethyl formamide solvent or in isopropanol using an ultrasonicator. A drop of the colloidal solution is placed on a carbon coated TEM grid and allowed to dry in a clean environment. The grid with the dried powder particles is then used for the TEM observation. On the other hand, the as-deposited films and post deposition annealed films are polished mechanically from substrate side using Gatan Disc grinder to reduce the thickness down to 70 μm and subsequently thinned down using precision ion polishing system (PIPS) or Fishione ion milling systems to suitable thickness for the TEM observation [REIM1993, BRAN2008].

3.4. Spectroscopy characterization

3.4.1. Micro-Raman spectroscopy

Raman spectroscopy is a vibrational spectroscopic technique generally used to study properties such as crystalline phases, defects, strain, etc. in a material. It is basically a light scattering phenomenon based on the famous Raman effect corresponding to the photon-phonon interaction. Figure 3.15 depicts the schematic diagram and photographic view of Raman spectroscopy (LabRAM HR-800, Jobin Yvon, USA). In Raman spectroscopy, the sample is illuminated with a monochromatic laser beam which interacts with the molecular vibration and are scattered. A fraction of the scattered beam has wavelength different from

the incident wavelength and constitute the main features of Raman spectrum. If the scattered wavelength is shorter than the incident wavelength, the scattered lines are known as Stokes line, while if the scattered wavelength is longer, then they are known as anti-Stokes lines.

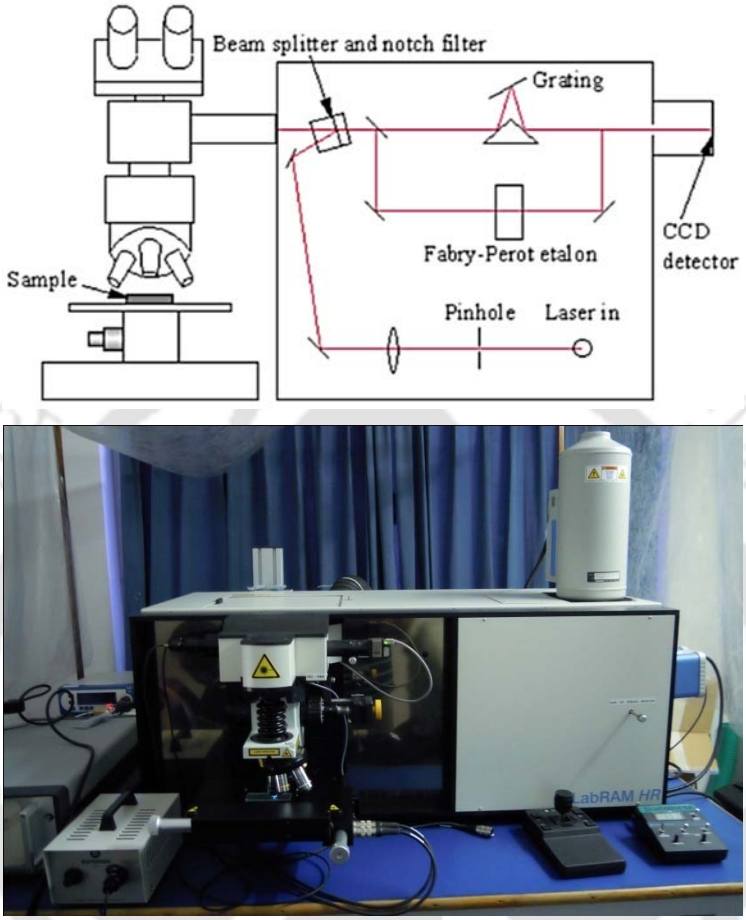

Figure 3.15: Schematic diagram (top) and photographic view (bottom) of Raman spectroscopy.

Raman spectrometer can be dispersive and non-dispersive. Dispersive spectrometer use grating or prism while non-dispersive spectrometer uses interferometer such as Michelson interferometer. Here, the intense laser beam is incident on the samples through a microscope with spot size of a few microns. The microscope is coupled confocally to an 800 mm focal length spectrograph equipped with two switchable gratings. The excitation photon can be supplied by using two sources namely He-Ne laser (wavelength 632.8 nm) or Ar laser (488 and 514 nm). The laser beam is totally reflected by the beam splitter, which splits the beam into two parts having equal wavelengths. The beam was allowed to fall on the sample where both Rayleigh and Raman scatterings occur. The notch filter allowing only the Raman scattered wavelength blocks the incident wavelength. The inelastic

scattered light was allowed to pass through the grating and etalon, which in-turn resolves the weak inelastic scattered wavelength coming from the sample more efficiently. Further, the beam was allowed to enter into a charge couple device where it detects the change in polarizability of the sample from the change in wavelength and converts into the intensity. We could see intensity versus wave number graph in the computer screen.

A high resolution micro-Raman (LabRAM HR-800, Jobin Yvon, USA) spectroscopy instrument with liquid nitrogen cooled CCD detector is used for the characterization of the pure un-milled NiO, milled NiO powders, as-deposited NiO thin films and annealed Ni thin films.

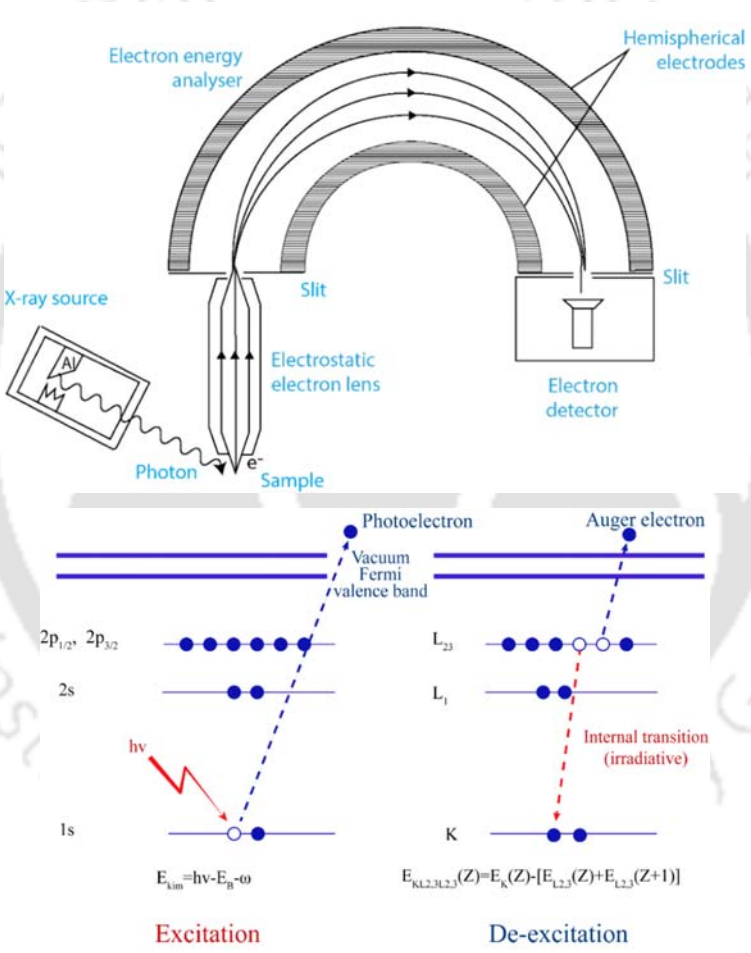

Figure 3.16: Schematic of XPS spectrometer (top) and excitation and de-excitation processes (bottom).

3.4.2. X-ray photoelectron spectroscopy

X-ray photoelectron spectroscopy (XPS) is a surface-sensitive quantitative spectroscopic technique. This measures the elemental composition at the parts per thousand range,

empirical formula, chemical state and electronic state of the elements that exist within a material. The principle of XPS is based on the photoelectric effect outlined by Einstein in 1905 and developed by Siegbahn and his research group [SIEG1967], where the concept of the photon was used to describe the ejection of electrons from a sample surface when photons impinge upon it. XPS requires high vacuum (~ 10^{-5} Pa) or ultra-high vacuum (UHV, 10^{-7} Pa) conditions. XPS spectra are obtained by irradiating surface of the given material with a beam of X-ray as shown in Figure 3.16 and simultaneously measuring the kinetic energy and number of electrons that escape from the top sub-surface (~0 to 10 nm) of the material. This process can be expressed by the following equation:

$$BE = h\upsilon - KE - \Phi \qquad (3.08)$$

where, *BE* is the binding energy of the electron in the atom, hν is the photon energy of X-ray source, *KE* is the kinetic energy of the emitted electron that is measured in the XPS spectrometer and Φ is the spectrometer work function. The XPS principle for ejecting an electron from the atom as photoelectron during excitation and release of Auger electrons during the de-excitation process is shown in Figure 3.16. After the release of photoelectron, the atom turns into an excited state. To revert back to ground state, the electron from an outer shell occupies inner shell by releasing either X-ray or Auger electron. For XPS, Al-K_α (1486.6 eV) or Mg-K_α (1253.6 eV) is generally used as the source of X-ray. The photon is absorbed by an atom of the sample, leading to emission of a core (inner shell) electron. The energy of the photoelectrons leaving the sample is determined using an appropriate electron energy analyzer and this gives a spectrum with a series of photoelectron peaks. For each and every element, there will be a characteristic binding energy associated with each core atomic orbital, i.e., each element will give rise to a characteristic set of peaks in the photoelectron spectrum at kinetic energies determined by the photon energy and respective binding energies. The peak intensities measure how much of a material is at the surface, while the peak positions indicate the elemental and chemical composition. Other values, such as the full width at half maximum (FWHM) are useful indicators of chemical state changes and physical influences.

In this study, XPS measurements were carried out in standard ultrahigh vacuum surface science chamber consisting of PSP Vacuum Technology electron energy analyzer (angle integrating ±10°) and a dual anode X-ray source with (ULVAC-PHI, Inc.) using Mg-K_α X-ray beam (1253.6 eV) at a base pressure of 2×10^{-7} Pa and energy resolution at full

width at half maximum is about 0.8 eV. The spectrometer was calibrated using Au $4f_{7/2}$ at 83.9 eV and used for the calibration of the XPS spectra recorded for various milled samples.

3.4.3. Electron spin resonance spectroscopy

Electron spin resonance (ESR) or Electron paramagnetic resonance (EPR) spectroscopy is a very powerful, sensitive, informative and nondestructive technique for the characterization of the electronic structures of materials with unpaired electrons. ESR is based on Zeeman effect that explains the splitting of energy level of a particle having spin ½ in a magnetic field. The energy difference between the two levels is given by

$$\Delta E = g\mu_B B \qquad (3.09)$$

where, g is the Landé g-factor, μ_B is Bohr magneton and B is applied magnetic field.

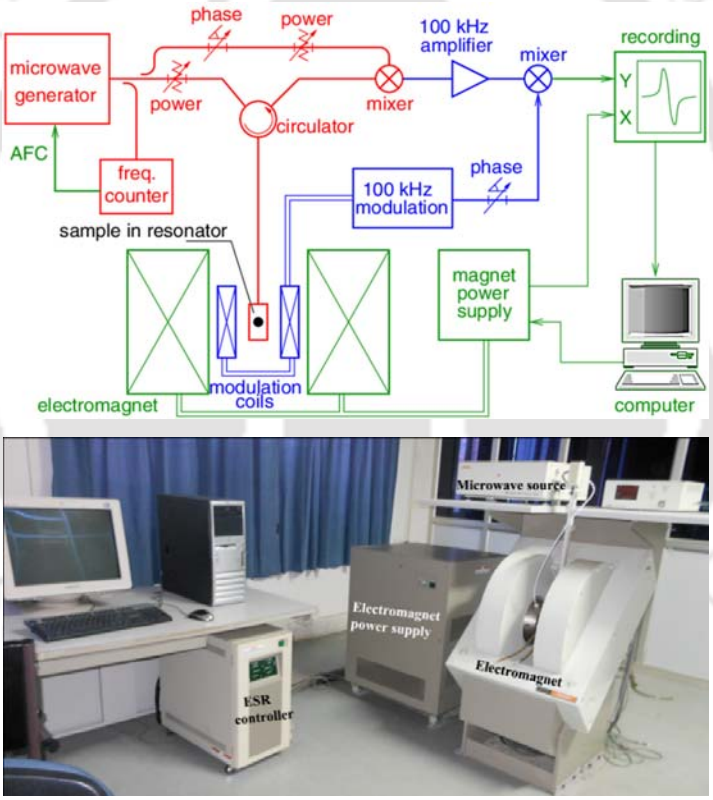

Figure 3.17: Block diagram (top) and photographic view (bottom) of ESR spectrometer.

Since the energy difference between the two states depends on the magnetic field, electrons at the lower energy state can jump to the excited state at a particular value of the magnetic field. Alternatively, one can fix the magnitude of the applied field and vary its frequency. At certain value of frequency, the electrons can jump to the higher state giving rise absorption peak in the spectra. At resonance,

$$h\upsilon = g\mu_B B \qquad (3.10)$$

where, υ is the frequency of the magnetic field, h is Planck's constant. Neither the field nor the frequency for resonance is a unique fingerprint for a system because spectra can be obtained at different value of B or frequency satisfying the eqn. (3.10). It is therefore the g-factor is the most useful parameter for the characterization of ESR spectra.

The basic building blocks of ESR are shown in Figure 3.17. The microwave generator generates and supplies microwave at controlled frequency and power, which are transmitted to the sample cavity through a waveguide. The sample cavity is mounted in the midst of the electromagnet pole pieces perpendicular to the magnetic field, B which can be varied in a controlled way. In addition to the main magnetic field, another magnetic field which is weaker comparative to the main field is generated and superimposed on the cavity by Zeeman modulation coils. Thus, the signal response from the cavity is modulated at the Zeeman modulation frequency. The ideal way for EPR spectra is to fix the magnitude of the magnetic field and continuously vary its frequency. However, microwave generators are tunable only to a limited range of frequency. Hence, the microwave frequency is fixed and magnitude of the magnetic field is varied. The magnetic field is swept until the sample absorbs the microwave frequency and jumps to the higher energy level, i.e., ESR absorption occurs.

Commercial ESR spectrometer works in the frequency range from several MHz to several GHz: 1-2 GHz (L-band) and 2-4 GHz (S-band), 8-10 GHZ (X-Band), 35 GHz (Q-band) and 95 GHz (W-band). In the present investigation, we have carried out the ESR measurement in powder and thin film forms using JEOL Spectrometer (JES-FA200) operating at X-band frequency (ν = 9.4 GHz) with 100 kHz magnetic field modulation.

3.5. Magnetic property characterization

Magnetic properties of the materials can be characterized by using various techniques. In this section, a brief outline of the principle involved in vibrating sample magnetometer (VSM), which is used in the present work, is discussed.

3.5.1. Vibrating sample magnetometer

VSM (Lakeshore Model 7410, USA) has been used to characterize room temperature and temperature dependent magnetic properties in the temperature range 20 K – 300 K and 300

K – 1000 K. VSM measures net dipole moment when material is exposed to magnetic field [JANS2004, HORS2006].

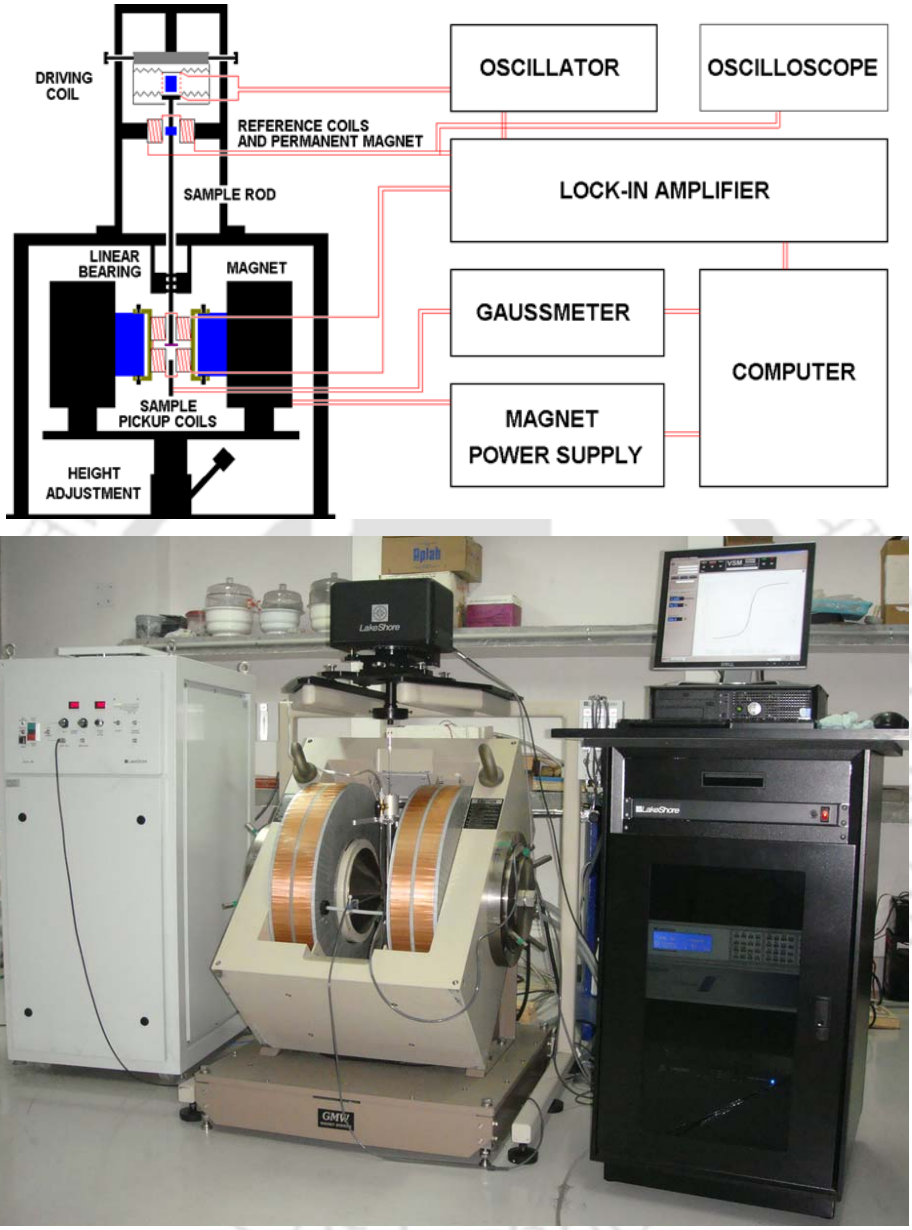

Figure 3.18: Schematic diagram (top) and photographic view (bottom) of a vibrating sample magnetometer.

The magnetic moment of the material can be obtained either as a function of field called magnetic hysteresis (*M-H*) loop to investigate the evolution of magnetic properties with field or as a function of temperature (*M-T*) to understand the magnetic phase transition of the material. Figures 3.18 displays schematic diagram and photographic view of VSM used in the present study.

When a sample is placed in a uniform magnetic field, a dipole moment proportional to the product of the sample susceptibility and the applied field induced in the sample. If the sample is made to undergo sinusoidal motion, an electrical signal can be induced in suitably located stationary pickup coils (see Figure 3.18). This signal has amplitude proportional to the magnetic moment of the sample, the vibrating amplitude and the vibration frequency. Through the use of lock-in-amplifier and feedback techniques, only that portion of the signal arising from the magnetic moment is picked up and is converted into direct read-out in the unit of magnetization (e.g. emu) on a digital panel meter. VSM consists of the following major parts: a) Vibration exciter and sample holder, b) water cooled electromagnet and power supply, c) Hall probe, d) pick-up coils, e) amplifier, f) control panel system, g) lock-in amplifier and h) computer interface. The sample was fixed at the lower end of the sample holder after completing the calibration procedure using standard Ni sample. The measurement sequence is programmed as per the users choice using the software (IDEASVSM) provided with the instrument such that the program starts either from the maximum field or from the zero applied field. The sequence is made to collect more number of data, which helps to extract the magnetic parameters (saturation magnetization, remenance magnetization, coercivity, etc.) more accurately. The exciter is vibrated at a frequency of 72 Hz (Lakeshore model 7410) and the signal received from the hall probe and the pick-up coils is converted into the magnetic moment of the sample. The magnetic field is increased automatically in user-defined steps for measuring *M-H* loops. Similarly, for high temperature *M-T* measurements, a high temperature oven attachment capable of providing a controlled heating/cooling of the sample from room temperature to 1000 K is used. For *M-T* measurements, the powders/films are loaded on a high temperature sustainable holder (ceramic holder or quartz rod) after the calibration using standard Ni sample. The oven is purged with nitrogen gas to avoid oxidization of the sample at high temperature. Magnetization is recorded at different temperatures at a constant in-plane applied magnetic field for films. The heating rate and *M-T* sequences are programmed using the IDEASVSM software.

3.6. Electrical resistivity characterization

Electrical resistivity properties of thin films can be characterized by using various techniques. In this section, a brief description of the principle involved in physical property measurement system (PPMS), used in the present work, is outlined.

3.6.1. Physical Property Measurement System

Physical Property Measurement System (PPMS, Quantum Design USA) represents a unique concept in laboratory equipment with an open architecture, variable temperature and field systems and designed to perform a variety of automated experiments. The photographic view of typical PPMS system with cryogen free option from Quantum Design, USA is shown in Figure 3.19.

Figure 3.19: Photographic view of a PPMS system with cryogen free option.

Figure 3.20: Photographic view of resistivity puck.

The resistivity option is used for making basic DC resistance measurements by applying a current and measuring the resulting voltage. Resistance measurements can also be made using the AC Transport option. The resistivity option performs a 4-point or 2-point resistance measurement on up to 3 channels at a time. The standard resistivity puck (see Figure 3.20) includes pre-mapped pads for + and – current and voltage for Channels 1 – 3. The recessed area allows the samples to fit and the base is conducting, so an insulating layer

such as Kapton tape will be necessary for samples with conductive back sides. Electrical contact between the sample and the desired channel input pads can be made via wire bonding, soldered or silver-painted wires, spring-loaded press contacts or other methods. The resistivity puck can be used to test sample-to-puck connections in advance of insertion into the PPMS using a hand-held ohm meter or other device.

In the present investigation, we have carried out room temperature electrical resistivity measurement of the as-deposited and annealed Ni films using four-probe and two-probe techniques by mounting the films with substrate directly on the user defined puck.

Chapter 4

Effect of milling speeds on the properties of NiO powders prepared by ball milling process

4.1. Introduction

The study of fine nanoparticles has received enormous interest due to their novel properties, which are considerably different from those observed in bulk materials. These nanoparticles lie between clusters whose properties are strongly dependent on its size and submicron sized particles which have almost the properties same as bulk materials. The observed novel properties provide nanomaterials with a potential for technological applications such as magneto-recording, resistive switching, supercapacitors, biomedicine, magnetic resonance imaging contrast agents, targeted drug delivery, sensors, energy conversion, electrochromics, etc [MEIK1956, HWAN1998, PANK2003, WANG2013, BARA2014, SHIH2014]. In particular, the study of magnetism and magnetic interactions in magnetic nanoparticles have been under scrutiny since the days of Néel [NEEL1949] and Brown [BROW1963], who developed the theory of magnetization relaxation for non-interacting single domain particles. However, they show complex properties due to the occurrence of structural disorder, size distribution and random orientation of the magnetization vector, but majorly correlated to the interplay between finite size and surface effects [KODA1997, TIWA2005, WINK2005, ARAG2012, DUAN2012, KISA2015]. On the other hand, Sundaresan et al proposed that ferromagnetic (FM) behaviour in nanosized particles of non-magnetic oxides is a universal feature [SUND2006, SUND2009].

Among various magnetic nanoparticles, nickel(II) oxide (NiO) has attracted much attention due to size dependent crystal structure, vibration modes and magnetic properties, and its applications in catalysis, energy conversion, storage devices, battery cathodes, antiferromagnetic (AFM) layer, gas sensors, electrochromic films, and transparent conducting films [XIAN2002, STEI2010]. In addition, the development of NiO based nanoparticles and thin films are focused to obtain FM above room temperature such that these oxides with cubic structure could easily facilitate integration of spintronic devices. Bulk NiO exhibits a cubic structure and AFM nature at room temperature along with a Néel temperature (T_N) of 523 K. However, Néel [NEEL1962] suggested that fine particles of AFM natured NiO should exhibit either a weak FM or superparamagnetism (SPM) upon size reduction. Richardson et al reported the first investigation on the size dependent magnetic properties of NiO [RICH1956]. Extensive studies have been reported over a last decade on particle size dependent magnetic properties [KODA1997, TIWA2005, WINK2005], finite size versus surface effects on magnetic properties [MAND2011], effect of substitution [CAZZ2003, PECK2011] and room temperature magnetic crossover [WANG2005, LILL2006, HONG2006, THOT2007] of NiO prepared by various

techniques. A combined experimental and computational study carried out by Yi et al [YIJB2007] showed a remarkable size-dependent magnetism with large magnetization of 105 emu/g and FM ordering temperature of 35 K, when the size of the NiO cluster is about 1 nm. With increasing the size of the NiO nanocrystals to 2 nm, they found AFM with uncompensated surface magnetization and shifted hysteresis due to the core-shell interactions. A careful review of the literature from different groups reveals that most of the reported investigations are bottom-to-top approach summarizing that the resulting magnetic properties are significantly complex in nature due to the interplay between finite size, surface effects and interface effects, etc. However, the approach of top-to-bottom method for studying the magnetic properties of un-milled NiO particles without any impurity phases are limited [DELB2008]. Recently, Kisan et al [KISA2014] reported finite size effects in magnetic and optical properties of AFM NiO nanoparticles and observation of room temperature FM in NiO prepared by ball milling process without any detectable impurities. But, the systematic investigation of effect of milling conditions on the improvement of magnetic properties have not been reported. This motivated us to perform a careful investigations on the evolution of nanostructure through top-to-bottom approach under different milling conditions and to understand the resulting magnetic properties in nanosized NiO powders.

Therefore, we present here (i) the preparation of nanosized NiO powder using a ball milling process under different milling conditions in an argon gas atmosphere, (ii) the effect of milling conditions on the microstructural, vibrational, electronic, magnetic and resonance properties, (iii) the effect of annealing of milled NiO powders at different temperatures to understand the origin of room temperature FM and (iv) the correlation between the crystal structure, microstructure, vibrational, electronic, magnetic and resonance properties of these ball milled and annealed powders and to explore the possibility to enhance their physical properties.

4.2. Experimental details

Weighed quantities of high purity NiO (> 99.9%, Sigma Aldrich, USA) powders are taken in high energy planetary ball mill filled with high purity argon gas. The milling process of NiO powders is carried out for 30 hrs under three different milling speeds [t_s = 350, 500 and 600 rotations per minute (rpm)] with a ball-to-powder weight ratio of 10:1. The optimization of the milling time and ball-to-powder weight ratio is done mainly by analyzing the variation in the structural and magnetic properties of the NiO powders. In order to avoid any local

heating during milling and its influence on the resulting properties, the milling process is programmed to halt for 15 minutes after every 15 minutes of operation. To understand the evolution of nanostructure in NiO powders, the milled powders are collected and characterized. In addition, the milled powders are also subsequently annealed at air atmosphere for 3 hrs and 5 hrs at 500 °C.

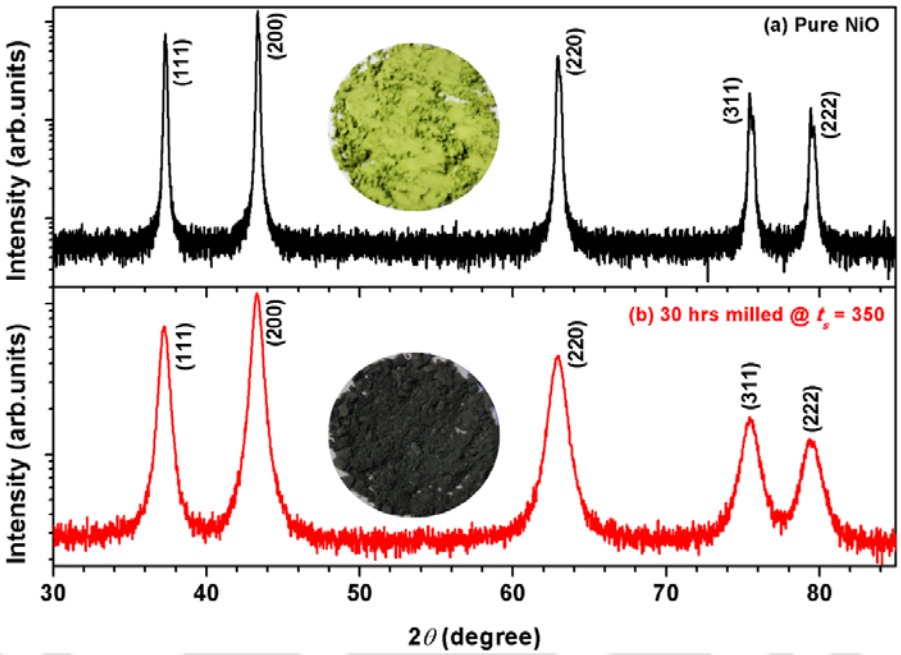

Figure 4.01: Typical room temperature XRD pattern of (a) pure un-milled NiO and (b) milled NiO powder at 350 rpm speed for 30 hrs of milling. Inset: Change in the colour of the powder before and after milling.

The phase evolution and crystal structure of NiO powders are analyzed through X-ray diffraction (XRD) patterns obtained using high-power (18 kW) X-Ray diffractometer (Rigaku TTRAX III, Japan). XRD data are collected at a slow scan rate of 0.005 °/s for analyzing the structural parameters as a function of milling speed. The changes in the surface morphology of the powders are observed using field emission scanning electron microscope (FE-SEM) and overall composition of the pure un-milled and milled powders is determined using energy dispersive spectroscopy (EDS, Oxford) attached to SEM unit. The microstructural properties of the pure un-milled and milled NiO powders are analyzed using transmission electron microscopy (TEM, JEOL 2100 and TECNAI G2 F30) technique. Raman spectra are obtained using micro-Raman spectroscopy (LabRam HR800, Jobin Yvon) using excitation wavelength of 614 nm at room temperature. X-ray

photoelectron spectroscopy (XPS) analysis is carried out in a standard ultrahigh vacuum surface science chamber consisting of a PSP vacuum technology electron energy analyzer (angle integrating ±10°) and a dual anode X-ray source with an Mg-Kα source (1253.6 eV) at a base pressure of 2×10^{-7} Pa and energy resolution at full width at half maximum (FWHM) is about 0.8 eV. The spectrometer has been calibrated using Au $4f_{7/2}$ at 83.9 eV [ZHAN20121]. Magnetic properties of the pure un-milled and milled powders are characterized using vibrating sample magnetometer (VSM, LakeShore Model 7410) by performing (i) magnetic hysteresis (*M-H*) loops at different temperatures under zero-field-cooled (ZFC) and field-cooled (FC) conditions and (ii) high-temperature thermomagnetization (*M-T*) measurements over a wide range of temperatures from 300 K to 1100 K performed at 4 °C/min heating rate with the applied field of 2 kOe. Room temperature electron paramagnetic resonance (EPR) measurements are carried out on a JEOL Spectrometer (JES-FA200) operating at X-band frequency (ν =9.4 GHz) with 100 kHz magnetic field modulation in powder form.

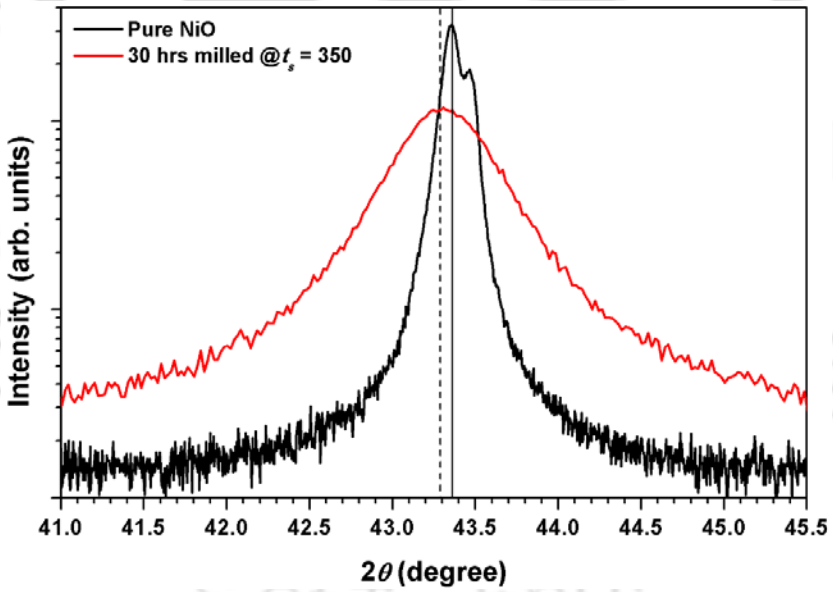

Figure 4.02: Expended view of NiO(200) XRD peak for pure un-milled NiO and milled NiO powder at 350 rpm speed for 30 hrs of milling.

4.3. Results and discussion

4.3.1. Properties of milled NiO powders

4.3.1.1. Structural properties

Figure 4.01 shows typical room temperature XRD patterns of pure un-milled NiO and milled NiO powders for 30 hrs at 350 rpm. The un-milled NiO powder shows Bragg reflections

corresponding to face centered cubic (*fcc*) structure. Similarly, the milled NiO powder also exhibits *fcc* structure without any impurity phase within the detection limit of X-ray diffractometer. Yet, as shown in inset of Figure 4.01, the ball milling process changes the color of the powder from pale green color into dark green after milling. In addition, a careful observation of the XRD peaks reveals that the sharp Bragg reflections observed in pure un-milled NiO powders broaden along with shift in peak positions towards lower diffraction angles. Figure 4.02 demonstrates the broadening of the XRD peak and shift in the peak position in pure un-milled and milled NiO powders. The peak broadening indicates the formation of highly refined and strained NiO powders upon milling, while the peak shift suggests a considerable change in the lattice parameter during the milling process.

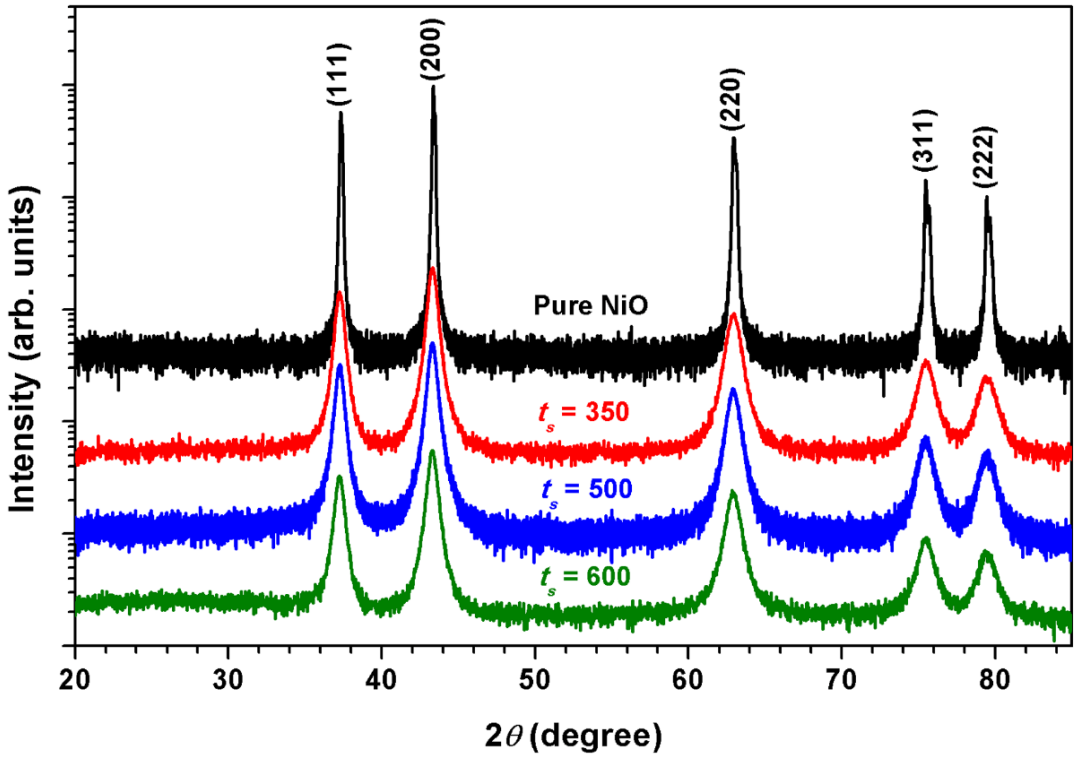

Figure 4.03: Room temperature XRD patterns for pure un-milled NiO and milled NiO powders at different milling speeds (t_s) for 30 hrs of milling.

In order to understand the evolution of nanocrystalline microstructure systematically, we have obtained XRD patterns of milled NiO powders for 30 hrs at different t_s between 350 and 600 rpm. Figure 4.03 displays the XRD patterns of NiO powders milled at different t_s. It is clearly seen that all the milled powders exhibit *fcc* structure without the presence of any other impurity phases. With increasing t_s, the peak broadening increases along with the shift in peak position to lower angles. Since the ball

milling process involves a strong deformation, fragmentation and cold welding in highly energetic grinding media, the evolution of NiO nanostructure with large strain and atomic level modification is inevitable. Therefore, the peak broadening in ball milled powders has generally been attributed to the refinement of average crystallite size (D), instrumental broadening and strain (η) caused by the density of dislocations (ρ) [DING2001, SURY2001]. To separate the individual contribution from D and η, XRD patterns are analyzed using Modified Williamson-Hall Plot (MWHP) method [UNGA1991, UNGA1992] described by the formula given in eqn.(4.01)

$$(\Delta K)^2 = \left(\frac{0.9}{D}\right)^2 + \left(\frac{\pi b^2 \rho}{2B}\right) K^2 C \qquad (4.01)$$

where ΔK [$= (2\cos\theta\,\Delta\theta)/\lambda$], $K = 2\sin\theta/\lambda$, D is average crystal size, b is modulus of the Burgers vector of dislocations taken as $b = \left(\sqrt{3}/2\right)a$ [SHEN2005], ρ is average dislocation density and B is a constant (taken as 10 for a wide range of dislocation distributions [REVE1996] and C $\left(= C_{hkl} = C_{h00}\left(1 - qH^2\right)\right)$ is dislocation contrast factor introduced to take care the elastically anisotropic materials [UNGA1992, SHEN2005, KALI2008, MHAD2010], where the residual strains affect some Bragg reflections more than the others, q is a constant and $H^2 = \left(h^2k^2 + k^2l^2 + l^2h^2\right)/\left(h^2 + k^2 + l^2\right)$ for cubic system.

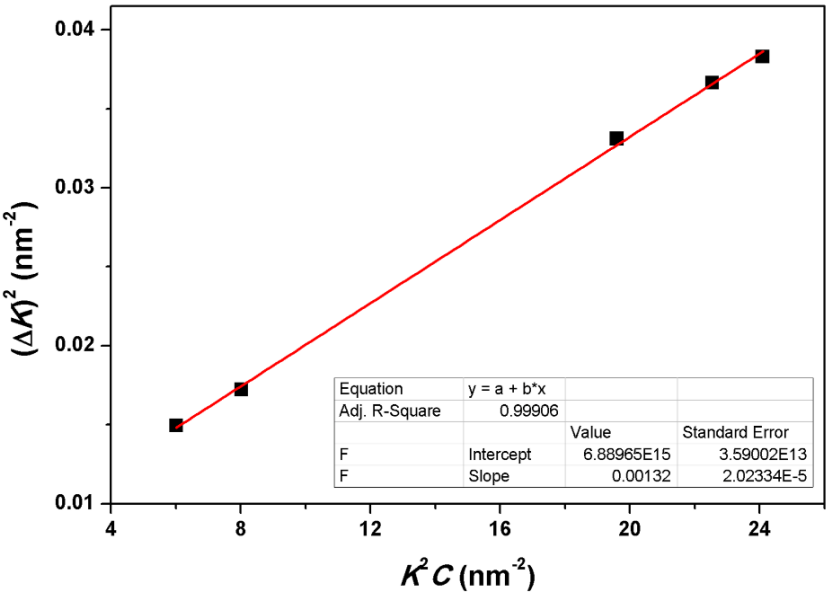

Figure 4.04: The plot of $(\Delta K)^2$ versus K^2C for 30 hrs milled NiO powder. The straight line is the linear fit to eqn.(4.01).

Figure 4.04 depicts the typical plot of $(\Delta K)^2$ versus K^2C for 30 hrs milled NiO at 500 rpm and the linear fit using eqn.(4.01) [KISA2017]. Since all the XRD data almost fall into straight line, the values of D and ρ are calculated from intercept and slope, respectively by fitting the XRD data using straight line method. It may be noted that the dislocation density is one of the major structural parameters [HULL2001] influencing the final nanocrystalline microstructure and therefore correlated to the induced strain and reduced crystal size as $\eta = \frac{\rho D b}{2\sqrt{3}}$.

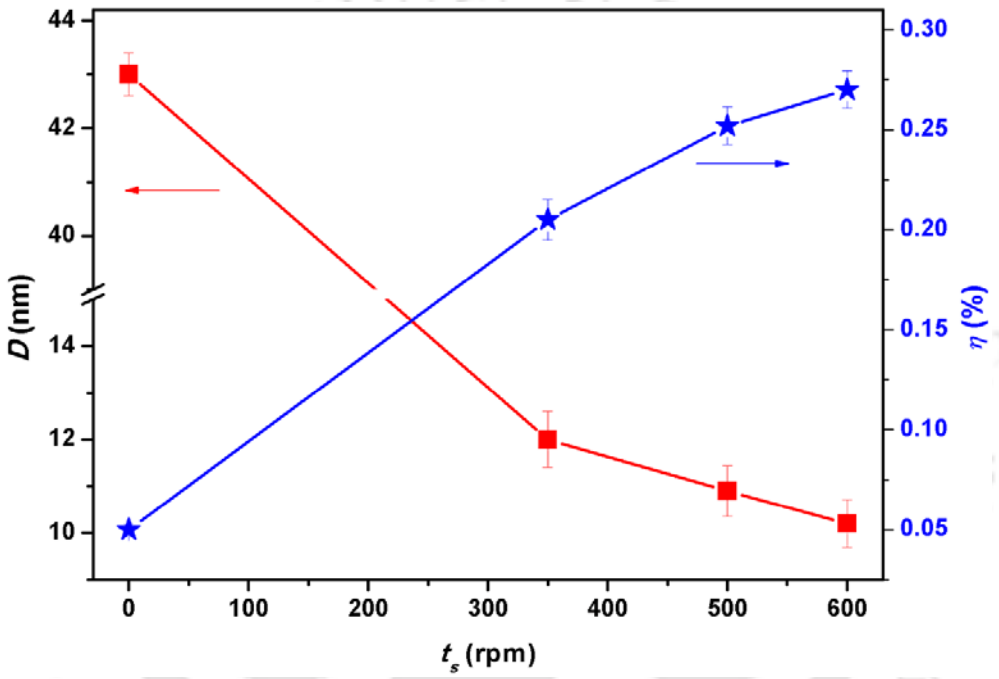

Figure 4.05: The variations of average crystal size (D) and effective strain (η) as a function of milling speed (t_s) for milled NiO powders.

The determined values of D and η are plotted as a function of t_s in Figure 4.05. It is clearly seen that the milled NiO powders show a large decrease of D and increase of η as compared to the pure un-milled NiO powder. For the un-milled NiO powder, D is found to be around 43 nm, which is reduced largely to around 12.5 nm after milling for 30 hrs at 350 rpm. On further increasing t_s, D reduces further down to 10.5 nm. The variation of D with the milling speed exhibits saturation like behaviour at higher t_s. On the other hand, the strain in the un-milled NiO powder is quite low and almost comparable to the NiO powder prepared by chemical preparation techniques [PROE2011, KISA2015]. However, the milled NiO powders exhibit quite large strain, which increases with increasing t_s. At larger t_s, the

strain also tends to saturate. As it is well understood that the ball milling process introduces a considerable disorder to reduce the average crystallite size, the ball milling of NiO results in a significant defects such as vacancies which distort the local structure by inducing localized atomic relaxation while retaining the overall crystal structure. This is evident from the fact that the pale green colour of the pure un-milled NiO powder changes into dark green with milling. This can be attributed to size reduction and existence of non-stoichiometric in NiO due to defects and oxidization of Ni^{2+} to Ni^{3+} [AHMA2006].

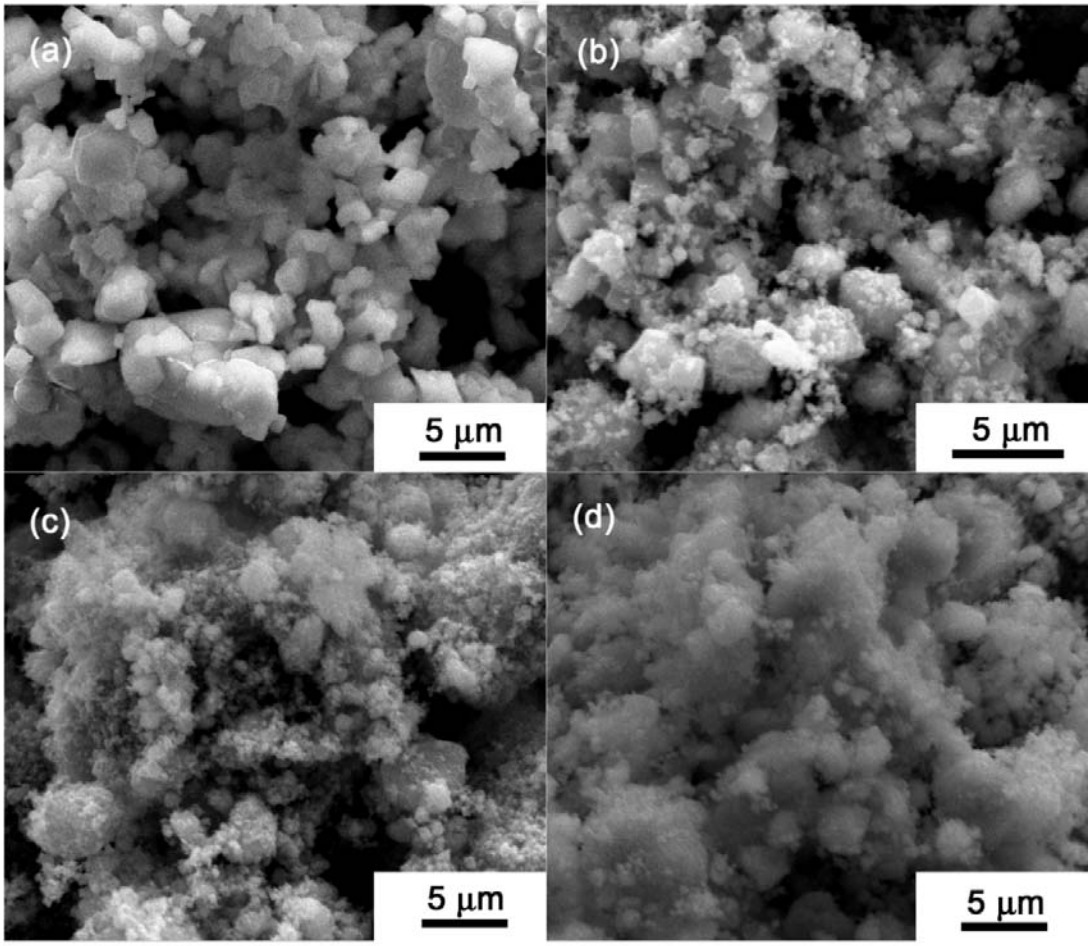

Figure 4.06: FE-SEM images of (a) pure un-milled NiO and milled NiO powders at t_s = (b) 350, (c) 500 and (d) 600 rpm for 30 hrs of milling.

In order to confirm the evolution of nanostructure in NiO powder after milling and to understand the change in the surface morphology, the pure un-milled NiO and milled NiO powders are characterized using TEM and FE-SEM techniques. Figure 4.06 displays the typical FE-SEM images of pure un-milled and milled NiO powders at different t_s. A clear

particle morphology with the average particle size of 1 to 4 μm is observed in pure un-milled NiO powders.

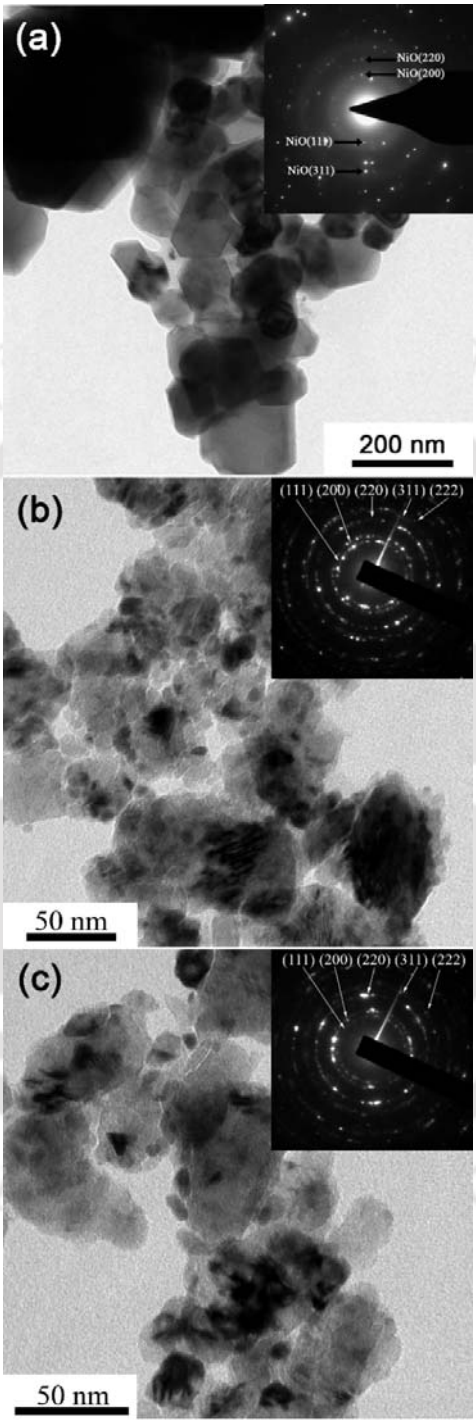

Figure 4.07: Bright-field TEM images and selected area electron diffraction patterns of (a) pure un-milled NiO and milled NiO powders at t_s = (b) 350 and (c) 500 rpm for 30 hrs of milling.

On the other hand, the milled NiO powders show reduced particle size and agglomerated particles. With increasing t_s, the average particle size of the milled powders decreases considerably below 300 nm. At the same time, the agglomeration of the fine particles increases to form aggregated particles and the number of such particles increases with increasing t_s. The aggregates are typical of ball-milled powders, which result in from the repeated cold welding and fracture of powders during milling. Figure 4.07 depicts typical plane-view bright-field TEM (BF-TEM) images and selected area electron diffraction (SAED) patterns of pure un-milled NiO and milled NiO powders at 350 and 500 rpm. BF-TEM image of the pure un-milled NiO powder reveals a clear particle morphology with size varying between 40 and 70 nm. The polycrystalline nature is evident from NiO diffraction rings in the SAED pattern. On the other hand, for milled NiO powders, the existence of nanocrystalline microstructure is seen from the BF-TEM images. The average size of the crystallites for 30 hrs milled NiO samples calculated manually using imaging software is estimated to be around 13.5 nm, 12 nm and 10.8 nm for 350, 500 and 600 rpm milled powders, respectively. These results are in close agreement with the data obtained from the analysis of the XRD data. In addition, SAED patterns show diffraction rings, which could be indexed to only *fcc* NiO structure and confirming the presence of polycrystalline nature of the NiO particles. On the other hand, the average lattice constant determined from the Bragg reflections increases largely for the milled powders as compared to the un-milled NiO powder. This supports that the lattice expansion in the NiO powder is occurred with the decrease of average crystallite size. Such observations were reported on similar metal oxide systems and attributed to strong repulsive interactions of parallel surface defect dipole [LILL2006], the valence reduction [TSUN2000], unpaired electron orbitals at outer surface [AYYU1995].

4.3.1.2. Vibrational properties

As Raman scattering is considered to be one of the most effective tools for studying crystallinity and defects structure associated with the materials, Raman spectra are obtained at room temperature for pure un-milled and milled NiO powders at different t_s and depicted in Figure 4.08. Raman spectra are analysed carefully by curve fitting method with different band combinations to obtain peak intensities, peak widths and peak positions. A typical curve fitting is also shown in the figure to identify different band combinations. While the bands observed at 380-410 cm^{-1}, 540-560 cm^{-1}, 700-730 cm^{-1}, 900 cm^{-1} and 1050-1110 cm^{-1} could be correlated to one-phonon (1P) transverse optical (TO), 1P longitudinal optical

(LO), two-phonon (2P) TO, 2P LO+TO and 2P LO of vibrational origin, respectively, the band around 1450 cm^{-1} is due to two-magnon (2M) scattering associated with Ni^{2+}-O^{2-}-Ni^{2+} super-exchange interaction. The presence of 2M band supports the existence of AFM state through Ni^{2+}-O^{2-}-Ni^{2+} super-exchange interaction in un-milled NiO at room temperature. The existence of 1P LO mode can be attributed to the disorder induced by defects, surface effects and imperfectness of the particles. On the other hand, the milled powders exhibit limited vibrational modes at 530-560 cm^{-1}, 730 cm^{-1} and 1060-1090 cm^{-1} corresponding to 1P LO, 2P TO and 2P LO excitation of NiO, respectively. The other vibrational peaks of 2P TO+LO at 900 cm^{-1} and the super-exchange interaction peak of 2M band at 1450 cm^{-1} are disappeared in all the as-milled powders.

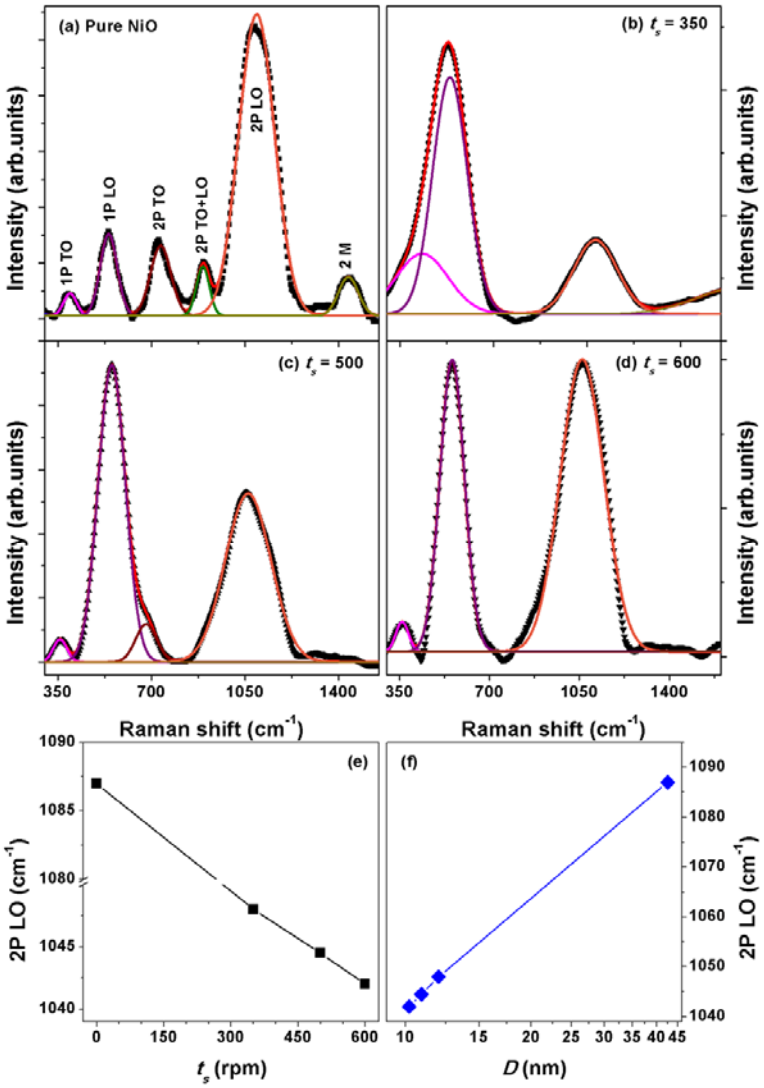

Figure 4.08: Raman spectra of pure un-milled NiO and milled NiO powders at different t_s. The variations of 2P LO band (e) as a function of t_s and (f) average crystal size (D).

The disappearance of 2M band indicates that the existence of strong AFM coupling in the pure NiO powder fades out with size reduction. Cazzanelli et al [CAZZ2003] studied vibrational and magnetic excitations in $Ni_cMg_{1-c}O$ solid solutions and observed that a large decrease in 2M band intensity upon dilution with Mn ions. This lowers local symmetry at the Ni^{2+} sites and the dependence of the 2M band in solid solutions on the composition and temperature is consistent with their magnetic phase diagram. Ulmane et al [ULMA2007] reported a dramatic reduction in 2M mode with decreasing NiO particle size and vanishing completely for crystallites below 100 nm. This was attributed to the reduction in AFM spin correlation length resulted by smaller crystallites and disorder induced by defects. Gandhi et al [GAND2011] have also observed a decrease of 2M intensity in NiO nanowalls as compared with bulk NiO. On the other hand, the intensity of 1P LO mode increases with increasing milling speed. This might be due to parity-breaking defects, since the concentration of vacancies is high as seen from the disappearance of 2M band in Raman scattering [ULMA2007, GAND2013]. It may be noted that the perfect cubic and rhombohedral structured NiO does not show 1P LO scattering [KEEM2010]. Furthermore, the peak position of 2P LO mode as shown in Figure 4.08(e) and (f) is shifted to lower wavenumber with increasing t_s and decreasing size of the crystallites, respectively. This confirms red-shift in Raman frequency, which can be ascribed to the size-induced phonon confinement effect in corroboration with the strength of the two-phonon coupling and surface relaxation. Defects and surface effects can also induce red-shift of phonon vibrations [YANG2008]. Duan et al [DUAN2012] reported a blue-shift and intensity enhancement of 2P LO mode after the nanoparticles are exposed to high power laser and interpreted that the defects observed in as-grown particles are annihilated by the laser beam heating. The vibration studies reveal that with milling at different t_s, the size reduction and defects are enhanced leading to a loss of AFM super-exchange interaction.

4.3.1.3. Electronic properties

In order to understand the chemical composition of pure un-milled and milled NiO powders, XPS survey spectra and Ni 2p, O 1s and C 1s spectra are obtained for both un-milled and milled NiO powders and depicted in Figures 4.09 and 4.10. In the survey spectra, the presence of Ni, O and its satellite peaks and C is observed. Ni 2p spectrum of pure un-milled NiO powder [see Figure 4.09(c)] depicts five fitted peaks in two regions: Ni-$2p_{3/2}$ (848-867 eV) and Ni-$2p_{1/2}$ (867-885 eV) spin-orbit levels. The Ni-$2p_{3/2}$ and Ni-$2p_{1/2}$ peaks are

observed at 854.4 eV and 873 eV, respectively along with their satellite peaks at 861.6 eV and 879.8 eV, respectively.

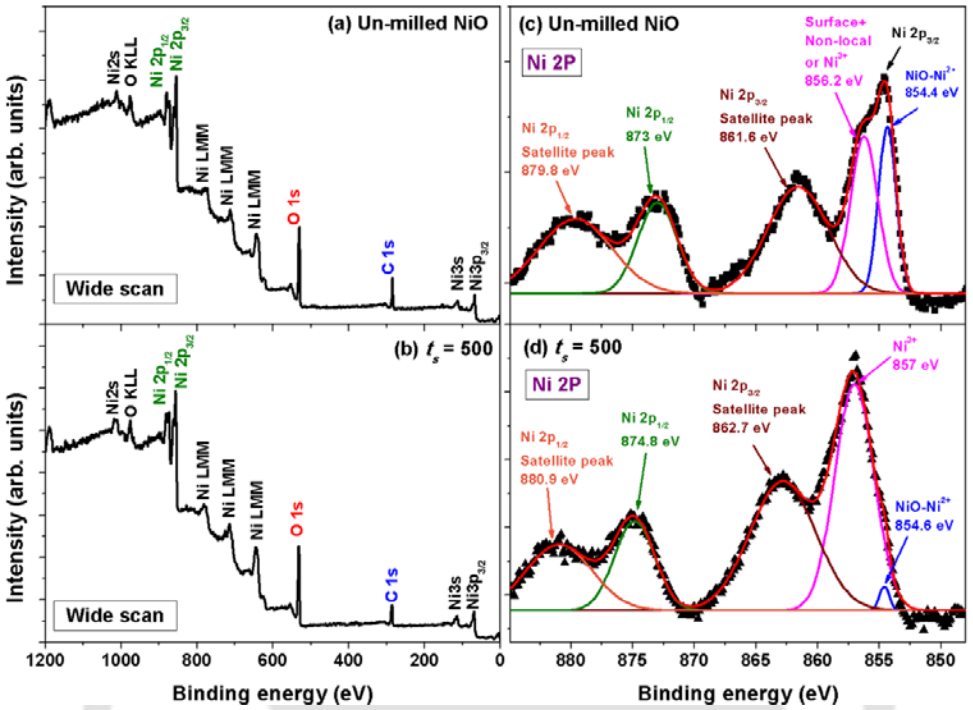

Figure 4.09: (a,b) Wide scan survey XPS spectra and (c,d) Ni 2p XPS spectra for pure un-milled NiO and 30 hrs milled NiO powders at 500 rpm.

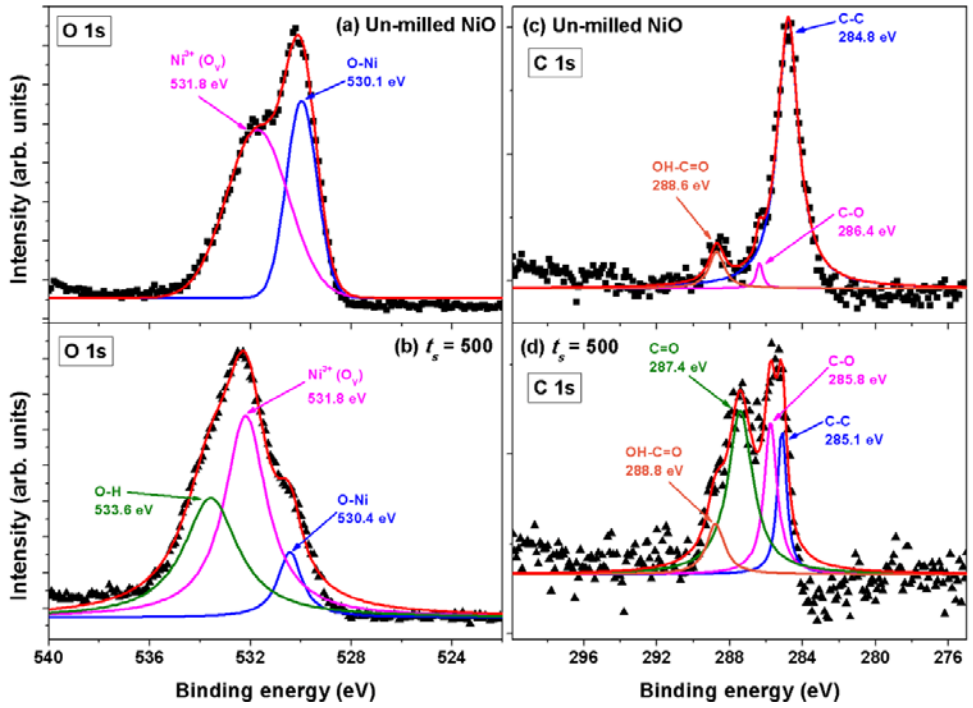

Figure 4.10: (a,b) O 1s XPS spectra and (c,d) C 1s XPS spectra for pure un-milled NiO and 30 hrs milled NiO powders at 500 rpm.

The binding energy difference between Ni-$2p_{3/2}$ and Ni-$2p_{1/2}$ peaks is about 18.6 eV. This confirms the dominance of NiO [UHLE1992]. The NiO satellite peaks may arise due to various causes such as multi-electron excitations, multiple scattering or surface plasmon loss [SANZ1996]. In addition, Ni 2p spectrum exhibits a shoulder shifted by 1.8 eV towards higher binding energies from the main line, whose interpretation is still controversial [PRED2008]. Soriano et al [SORI2007] reported that the main line intensity comes from the Ni atoms octahedrally coordinated in the bulk, while the part of the intensity of the shoulder labelled as surface and non-local effects coming from the pyramidally coordinated Ni atoms at the NiO surfaces. Peck et al [PECK2012] compared the XPS spectra of nanoscaled NiO and bulk NiO and showed that the shoulder peak exists for both bulk and nanoscale NiO down to 5 nm. The shoulder peak has been reported to contain a partial contribution from surface states [GROS2006, MOSS2011]. On the other hand, Jing et al [JING2015] proposed the observation of such peak as one of the satellite peaks of Ni-$2p_{3/2}$. Recently, Reddy et al [RAJA2016] reported that the observation of peak at 856.2 eV is due to Ni^{3+}, as Ni^{2+} ions oxidize to Ni^{3+} ions to maintain neutral charge [JIAN2002]. To understand the origin of the shoulder in details, the detailed O 1s and C 1s spectra of the bulk NiO are recorded between 522 eV and 540 eV, and between 275 eV and 300 eV, respectively and shown in Figure 4.10. We observed two distinct peaks at 530.1 and 531.8 eV specifically related to the typical Ni-O bonds from Ni^{2+} and Ni^{3+}, respectively [ZHAO2009, RAJA2016, YOON2016, ADHI2017]. The signal from the former Ni-O is stronger than the latter, which suggests that Ni^{2+} is the dominant species [LIUC2016]. The C 1s spectrum reveals three peaks at 284.8, 286.4 and 288.6 eV, which are due to adventitious carbon species corresponding to the C-C, C-O and OH-C=O bonds, respectively. On the other hand, the milled NiO powders exhibit significantly different features in Ni 2p, O 1s and C 1s spectra, despite having similar survey spectrum. For instance, the binding energy difference between Ni-$2p_{3/2}$ and Ni-$2p_{1/2}$ peaks increases slightly to 20.2 eV and the peaks of Ni 2p are broadened. Importantly, the signal from Ni^{3+} peak at 857 eV enhances largely at the expense of Ni^{2+} peak intensity at 854.6 eV. This clearly supports the presence of non-stoichiometry in the milled samples due to decrease in Ni^{2+}-O^{2-}-Ni^{2+} spin correlation length caused by defects and size reduction. This is further supported from the O 1s spectrum, where the signal from O-Ni bond of Ni^{2+} decreases and Ni^{3+} increases largely after the milling process. In addition, we observed an additional peak at 533.6 eV, which can be ascribed to adsorbed water on the surface. The C 1s spectrum of milled NiO powders shows four peaks at 285.1, 285.8, 287.4 and 288.8 eV that are due to

C-C, formation of C-O, C=O and OH-C=O bonds, respectively. The relative intensities of the peaks strongly depends on the milling conditions. These results are in close agreement with the vibrational properties of the presently investigated samples.

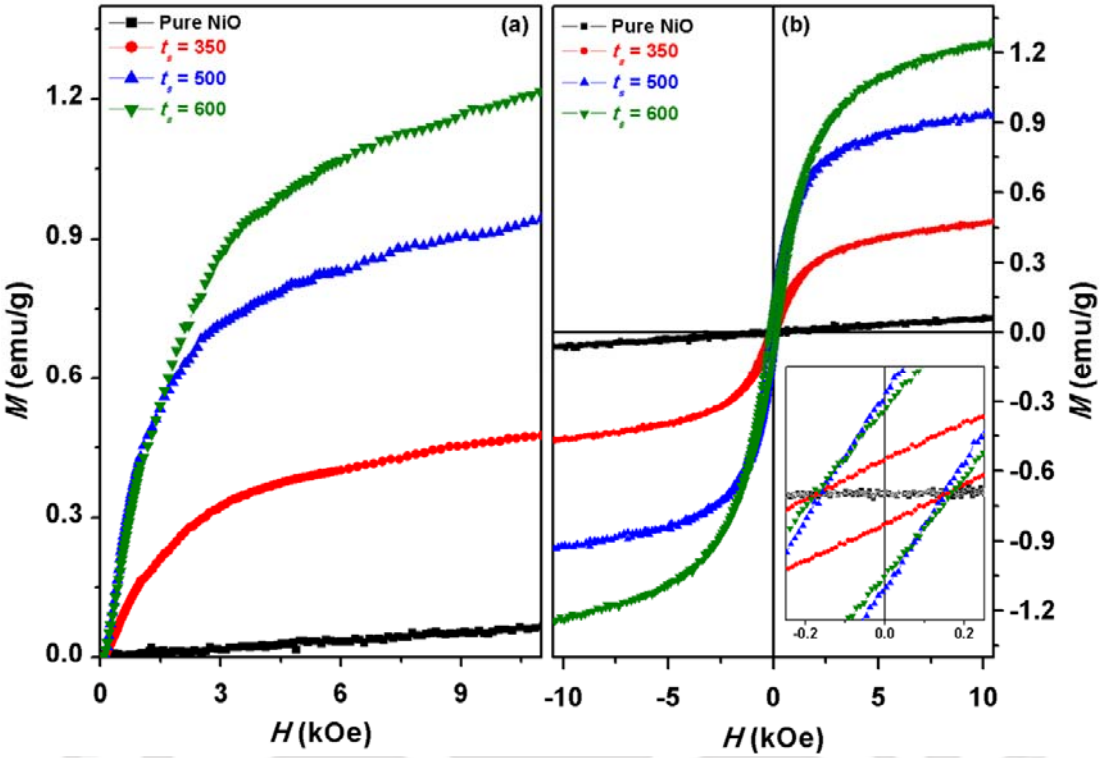

Figure 4.11: Room temperature (a) initial magnetization curves and (b) *M-H* loops of pure un-milled NiO and milled NiO powders at different t_s. Inset shows the expanded view of *M-H* loops close to origin.

4.3.1.4. Magnetic properties

In order to understand the effect of milling speed dependent nanocrystalline microstructure on the magnetic properties at room temperature, *M-H* loops are measured for all the un-milled and milled powders. Figure 4.11 depicts the initial magnetization (*IM*) curves and *M-H* loops for un-milled NiO and milled NiO powders under different t_s, and expanded view of the *M-H* loops close to origin in the inset. It is clearly seen that the magnetic properties strongly dependent on the milling condition. The un-milled NiO powder exhibits almost weak and linear response to the applied magnetic field in the field range of up to 12 kOe. In addition, the loop passes through the origin with no remanence magnetization (M_R) and coercivity (H_C). This evidently confirms the existence of AFM nature in the un-milled NiO powder as supported by the Raman spectrum showing 2M band associated with Ni^{2+}-O^{2-}-

Ni^{2+} super-exchange interaction and XPS spectra displaying Ni^{2+} as the dominant species. On the other hand, the milled NiO powder exhibits different nature, i.e., all samples exhibit clear hysteresis behaviours at room temperature confirming the induced FM at room temperature. During the initial magnetization process, the magnetization increases significantly with increasing applied field in lower-field region. However the increase of magnetization slows down as we further increase the applied magnetic field. Finally, the magnetization increases almost linearly with increasing the magnetic field up to 12 kOe, but does not saturate.

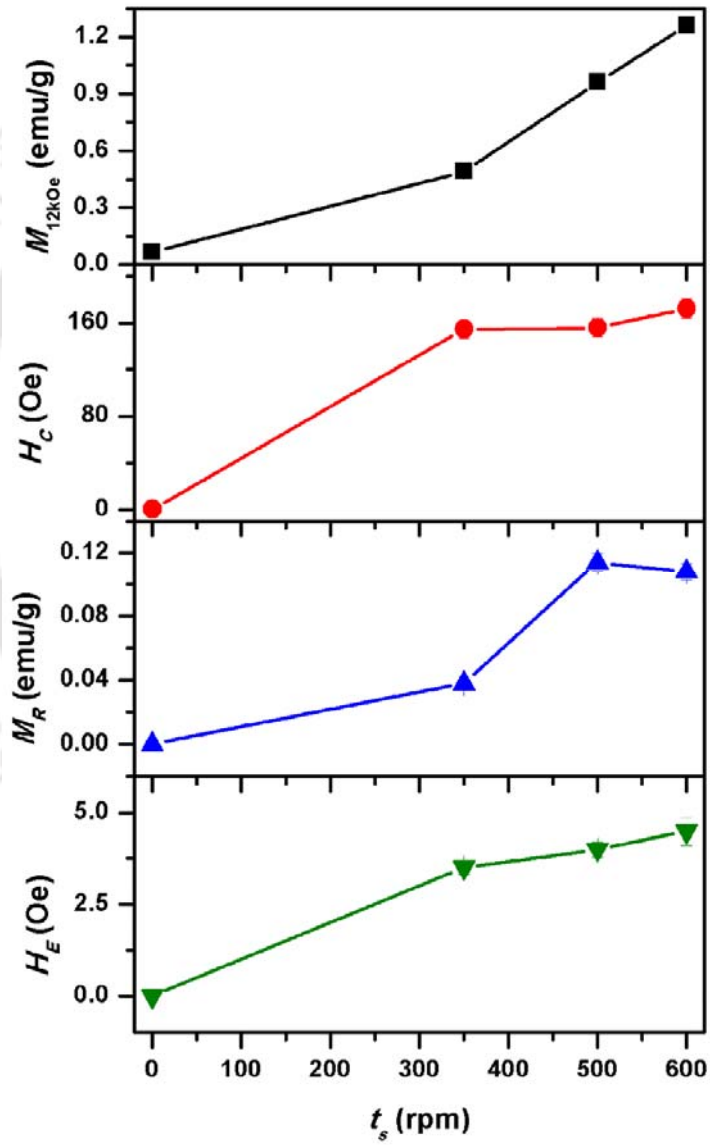

Figure 4.12: The variations of (a) magnetization obtained at 12 kOe (M_{12kOe}), (b) coercivity (H_C), (c) remanence (M_R) and (d) exchange bias (H_E) as a function of t_s.

These results suggest that there are two possible components associated with the magnetization reversal process: (i) an easily magnetizing component at low-field region and (ii) a non-saturating component responsible for almost linear variation in the high-field region [THOT2007, DUAN2012]. In order to separate these two components, the field dependent magnetization curves are analysed using eqn. (4.02).

$$M(H) = M_{FM}(H) + \chi_{AFM}(H) \tag{4.02}$$

where χ_{AFM} is AFM susceptibility of the core and M_{FM} is ascribed to the magnetization due to uncompensated surface spins. χ_{AFM} is determined by fitting the linear portion of *M-H* curves at high-fields. The extracted parameters from the fitting procures are summarized in Table 4.01.

Table 4.01: Room temperature M_{FM} and χ_{AFM} for the pure un-milled NiO and milled NiO powders at different t_s.

Sample	M_{FM} (emu/g.)	χ_{AFM} (emu/g.-Oe)
un-milled NiO	0	0.61×10^{-5}
NiO milled at 350 rpm	0.41	1.51×10^{-5}
NiO milled at 500 rpm	0.89	1.82×10^{-5}
NiO milled at 600 rpm	1.02	2.84×10^{-5}

It is clearly evident that both the values of M_{FM} and χ_{AFM} increase with increasing t_s, but the relative increase of M_{FM} is quite higher as compared to χ_{AFM}. This confirms that the number of uncompensated spins on the surface of the NiO particles is increased and hence resulting enhanced FM properties. In addition, the applied field required for saturating M_{FM} components increases with increasing t_s. Saturation fields of about 10–20 kOe have been reported by various groups on similar systems [MAKH2002, PUNN2002]. The various magnetic parameters such as magnetization at 12 kOe (M_{12kOe}), H_C, M_R and exchange bias $[H_E = (|H_{C+}| - |H_{C-}|)/2]$ for the milled samples are extracted from *M-H* loops and shown in Figure 4.12. M_{12kOe} increases significantly with increasing t_s and reach the maximum value of 1.26 emu/g for NiO powders milled at 600 rpm. H_C of pure NiO, observed as zero due to its AFM nature, has increased significantly after milling. With increasing t_s, H_C increases and attains a maximum of 173 Oe after milling for 30 hrs at 600 rpm. The values of M_R are also increasing initially for the powders milled up to 500 rpm speed and almost remain constant for 600 rpm speed milled powders. Similarly H_E, observed as zero for pure

NiO due to its AFM nature, increases for the milled NiO powders, but tends to saturate at higher t_s.

In order to understand the milling speed dependent magnetic properties, the structural, vibrational, electronic and magnetic properties are correlated carefully. In un-milled NiO powder, the spins within AFM coupled (111) planes are compensated and hence show a weak response to applied field [BHUA2012]. In this case, the exchange interaction between two neighbouring Ni^{2+} ions is mediated by an oxygen ion through super-exchange interaction. This is supported by the observation of 2M band in the Raman spectrum and dominant Ni^{2+} in the XPS spectrum. In addition, the colour of the un-milled powder is observed to be pale green colour. It is well-known that the ball milling process promotes a large size reduction and massive defects including the formation of oxygen and/or nickel vacancies in NiO. The structural properties reveal that the values of D decrease and η increase with increasing t_s. As a result, the pale green colour of the un-milled NiO changes into dark green with milling. This can be attributed to size reduction and existence of non-stoichiometric in NiO due to defects and oxidization of Ni^{2+} into Ni^{3+} [AHMA2006]. Furthermore, when the size of NiO is reduced into nanoscale, the super-exchange interaction between two neighbouring Ni atoms would be broken if an oxygen ion is missing from the surface and the exchange interaction energy would be reduced. As a result, the average coordination number for Ni^{2+} ions at the surface would be less than that in the bulk, which can result in a distribution of exchange energy barriers for the surface spins [ROYA2004]. As the super-exchange interaction is sensitive to bond angles and bond lengths, they are likely to be modified at the surface as compared to that in the bulk. This is supported by the absence of 2M mode in Raman spectra and development of Ni^{3+} peak at the expense of Ni^{2+} peak in Ni 2P spectrum and increase of Ni^{3+} at the expense of O-Ni bond of Ni^{2+} in O 1s spectrum. Therefore, the magnetic properties of the NiO powders change as described below: With the size reduction of NiO, the double sublattice in bulk NiO may be transferred into multi-sublattice states [KODA1997] and the number of uncompensated spins on the surfaces with respect to particle core increases [WINK2008, PECK2011], which results in to an alignment of particles' net moment under low applied magnetic fields. Also, the formation of structural disorder due to the creation of defects enhances the net magnetic moment. Furthermore, the lattice constant in the milled powder is increased with decreasing the average crystallite size. Such expansion in the presence of defects and surface anisotropy plays a significant role in controlling the interaction between the uncompensated surface spins and particle core spins. Li et al [LILL2006] reported room temperature magnetic

crossover of NiO is due to the lattice expansion. Del Bianco et al [DELB2008] reported that saturation magnetization of NiO increases at a rate of 0.62 emu/g per Ni weight percent (wt.%) in hydrogenated NiO. A quantitative comparison with the current samples implies the existence of around 1.2 – 1.55 wt.% Ni enriched spatial regions due to finite size effects and defects density of oxygen-related defects. This results in a change in oxidation of Ni and colour of milled NiO powder. The ball milling process involving a repeated cold welding and fracturing to form nanostructure materials introduces massively lattice defects. If the ball milling process increases the defect density with t_s or milling period, then the FM ordering is also expected to increase with defect density as observed in the present case.

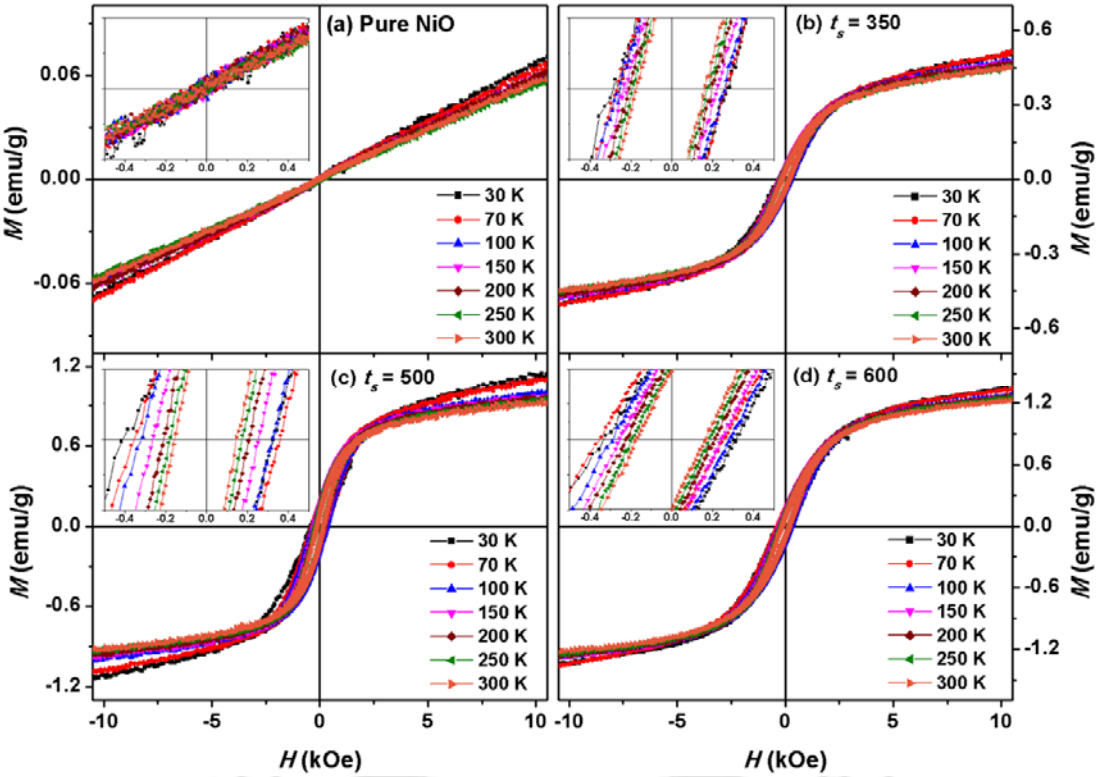

Figure 4.13: Temperature dependent *M-H* loops of pure un-milled NiO and milled NiO powders at different t_s measured under zero-field-cooled condition.

To study the development of FM properties in the milled powders in more details, temperature dependent magnetic measurements are carried out both at low temperature and high temperature regions. Figure 4.13 depicts typical *M-H* loops measured at different temperatures under zero-field-cooled (ZFC) condition for un-milled NiO and milled NiO powders. The expanded views of the loops close to origin are also shown as inset for realizing the variations clearly. It is observed that un-milled NiO powder shows almost

linear curves down to 30 K without any change in the loop shape. However, as expected, M_{12kOe} increases slightly with decreasing temperature. The milled NiO powders also show similar loop shapes at all temperatures with a marginal increase in the magnetization values and area under the curves. In order to understand the change in the magnetic parameters, M_{12kOe} and H_C are extracted from the loops and plotted as a function of temperature in Figure 4.14. M_{12kOe} and H_C increases significantly with decreasing temperature. This is a typical behaviour expected for a simple FM material.

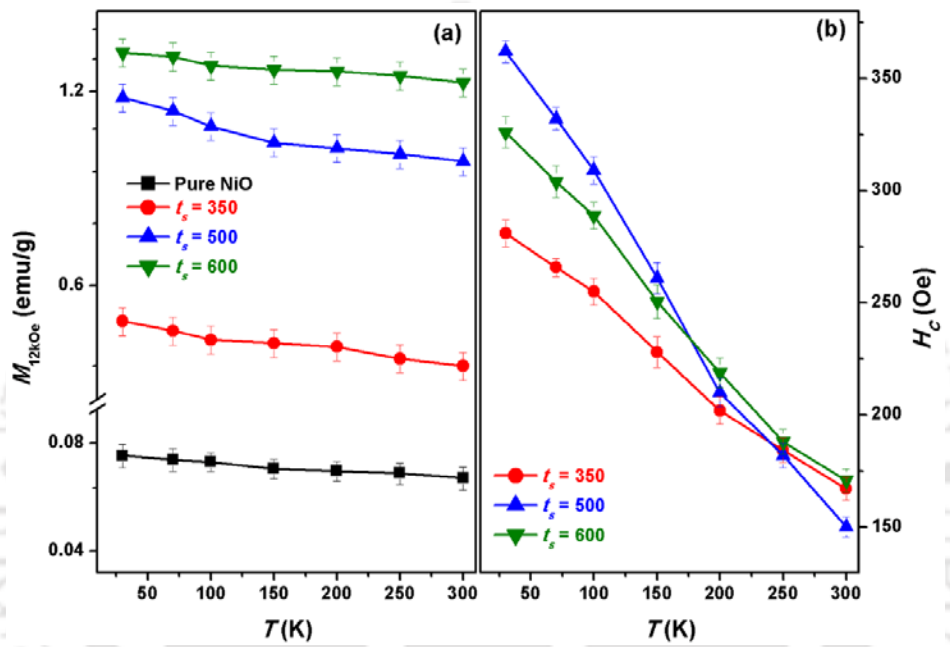

Figure 4.14: The variations of M_{12kOe} and H_C as a function of temperature for pure un-milled NiO and milled NiO powders under ZFC condition.

Nevertheless, the rate of increase of magnetization with decreasing temperature is significantly weak suggesting that the magnetization is mainly contributed from the uncompensated surface spins which are limited in the presently investigated samples. On the other hand, H_C of the milled powders varies almost linearly with a slope of 0.439 Oe/K, 0.822 Oe/K and 0.604 Oe/K for 350, 500 and 600 rpm milled NiO powders, respectively. The extrapolation of the fitting procedure gives the maximum H_C values of 295 Oe, 386 Oe and 344 Oe for 350, 500 and 600 rpm milled NiO powders, respectively. This is in good agreement with the values reported for NiO and Ni nanoparticles prepared by high-temperature oxidation and reduction methods [FEYG2010, KISA2015]. The linear increase in the values of H_C can be attributed to the anisotropy between the uncompensated surface spins and compensated spins at the core.

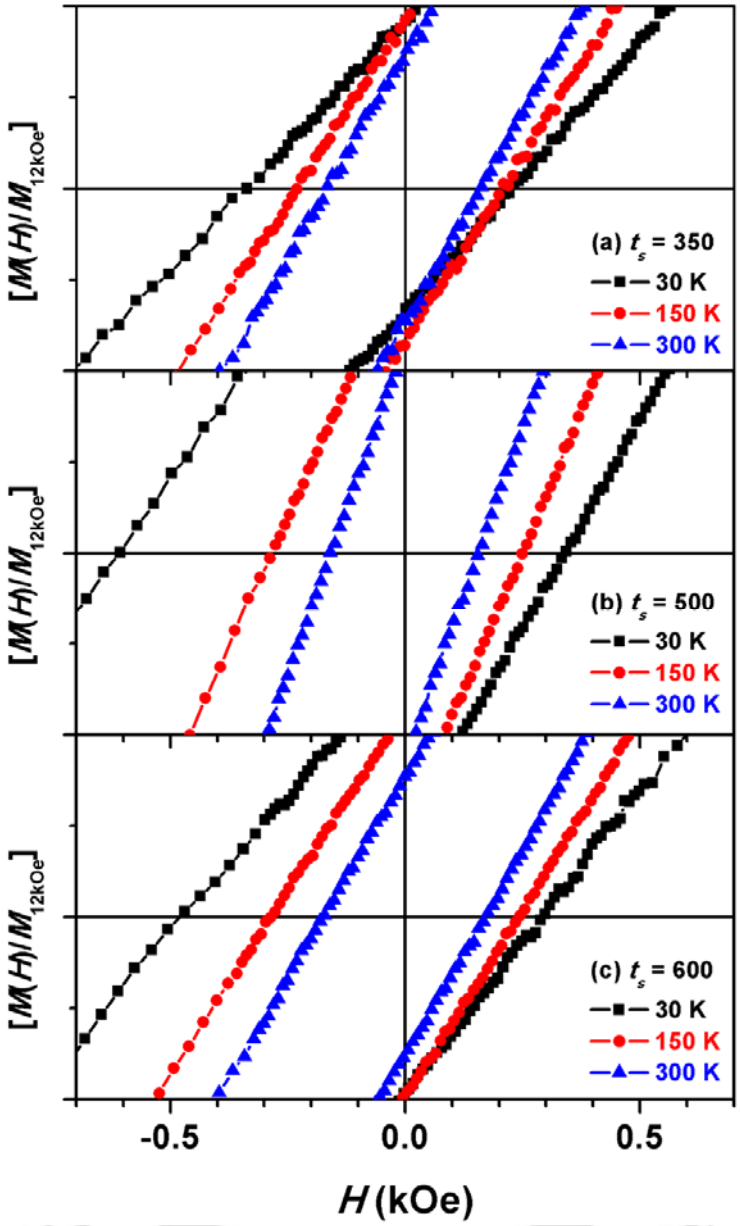

Figure 4.15: Expanded view of temperature dependent *M-H* loops of milled NiO powders at different t_s measured under field-cooled condition.

To understand the temperature dependent magnetic properties in more details, we measured *M-H* loops of NiO powders milled at different t_s under FC conditions (at 1 kOe) in the temperature range between 30 and 300 K. Figure 4.15 displays expanded views of temperature dependent *M-H* loops at a few selected temperatures for clarity. While the nature of the loops does not change with the temperature, H_C and area under the loop increases considerably with decreasing temperature. As compared to the *M-H* loops

measured under ZFC condition, the FC loops are shifted more towards negative field axis, revealing enhanced H_E. The values of H_E determined from the FC loops are plotted as a function of temperature in Figure 4.16. $H_E(T)$ show larger variations with decreasing temperature, particularly at low temperatures below 150 K. The maximum H_E of 55 Oe, 133 Oe and 80 Oe is observed at 30 K for the NiO powders milled at 350, 500 and 600 rpm, respectively. This could be related to the fact that FC condition promotes additional anisotropy between freezing surface spins and compensated spins at the core due to the existence of spin-glass like phase [KISA2017].

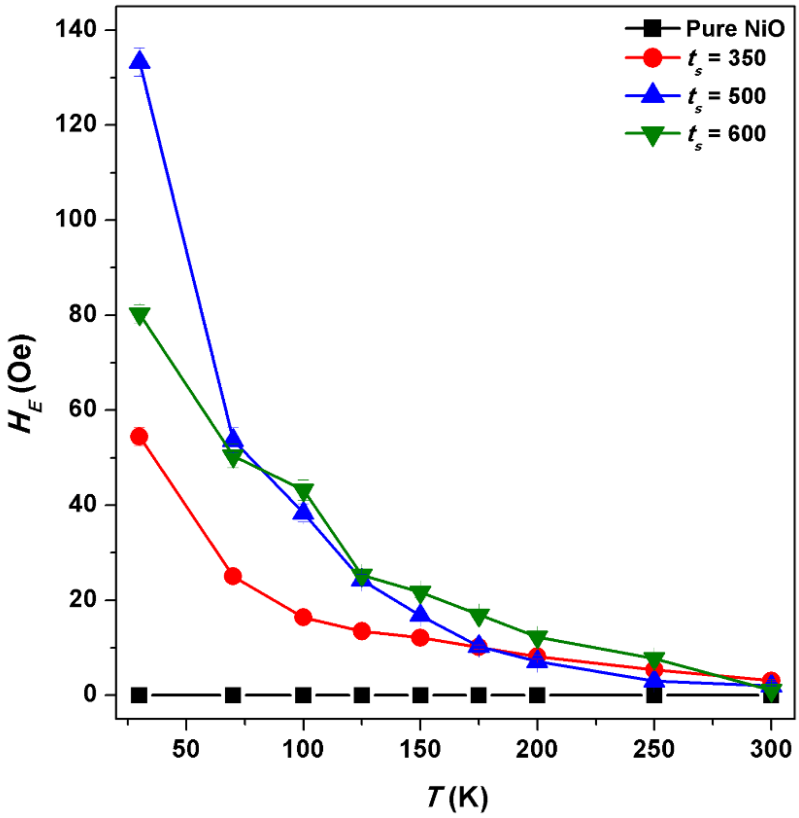

Figure 4.16: The variations of H_E as a function of temperature for pure un-milled NiO and milled NiO powders under field-cooled condition.

To understand the stability of induced FM in the NiO powders above room temperature, high temperature *M-T* data are measured using VSM at 2 kOe applied field. Figure 4.17 shows typical *M-T* curves obtained for pure un-milled NiO and as-milled NiO powders at 500 rpm speed. For comparison, we have also shown the *M-T* curve of the NiO powder prepared by sol-gel process [KISA2015]. For pure NiO powder, the magnetization increases gradually up to 525 K and then decreases above 525 K. The value of T_N determined from peak in the *M–T* curve is found to be nearly 525 K. On the contrary, milled NiO powder

at 500 rpm exhibits nearly a constant magnetization close to room temperature regime and shows a continuous decrease in magnetization with increasing temperature. The magnetization becomes zero at around 900 K. Thermal derivative of the *M-T* data exhibit two minima: one close to T_N and another broad minimum around 780 K corresponding to possible Ni phase transition (T_C). This confirms the existence of two magnetic phases in milled NiO powders, but the T_C of the Ni phase seems to be quite high as compared to its bulk counterpart (~ 630 K).

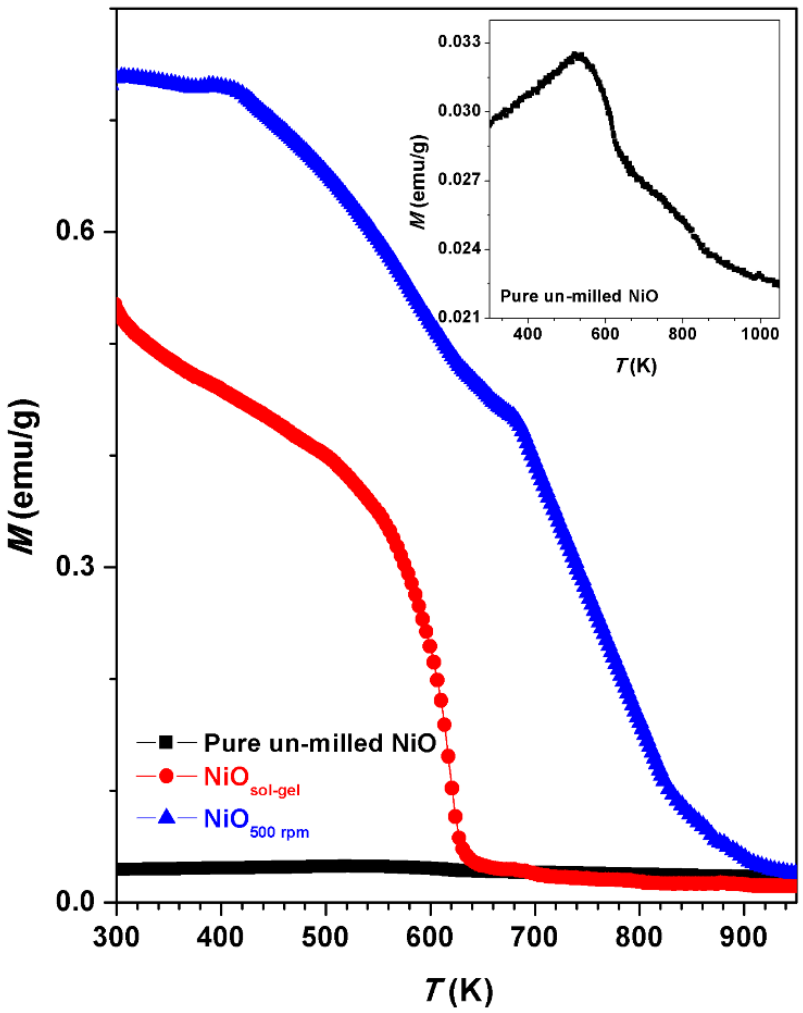

Figure 4.17: High temperature *M-T* data of pure un-milled NiO, milled NiO powders at 500 rpm and NiO powders prepared by sol-gel method. All the curves are measured under the applied magnetic field of 2 kOe. Inset: *M-T* curve of pure un-milled NiO powder.

In order to compare the magnetic phase transition in NiO nanoparticles, we have also shown the magnetic phase transition of NiO nanoparticles prepared by sol-gel process. These particles exhibit a clear magnetic phase transition from FM to paramagnetic state at

high temperature. T_C is determined to be around 620 K, which is slightly lower than the bulk Ni (~ 630 K) [MAND2009]. These results clearly indicate that milled powders exhibit high T_C as compared to the NiO nanoparticles prepared by sol-gel method. This could be due to the high stress induced during the ball milling process [LEGE1972, GORR2009] or strain due to lattice mismatch between Ni and NiO arising at the interface [FEYG2010] and possible competing exchange interaction between the induced FM and AFM core. The presence of such strains acts more like hydrostatic one, which is expected to increase T_C as reported in bulk Ni [LEGE1972]. The presence of strain is evident from the non-smooth reduction in magnetization with increasing temperature. A careful review on the literature also reveals the observation of high T_C (~ 750 K) in Ni doped TiO_2 powders (~820 K) [BHUA2012] and Ni/NiO [FEYG2010].

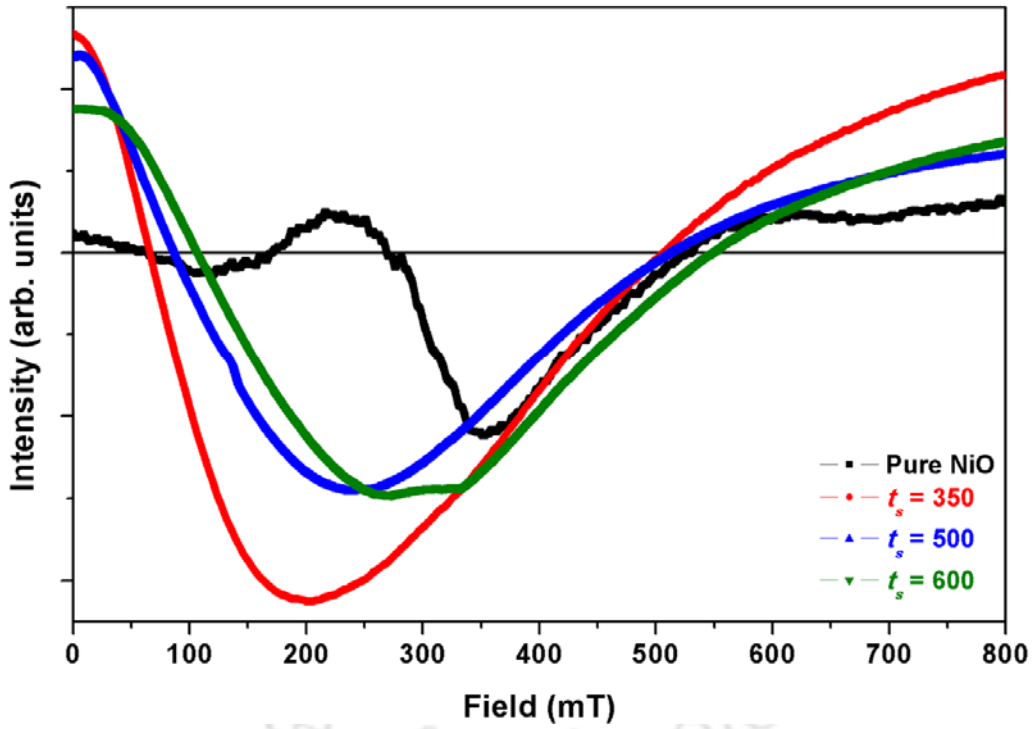

Figure 4.18: EPR spectra of pure un-milled NiO and milled NiO powders at different t_s.

4.3.1.5. Resonance properties

EPR spectroscopy is a suitable technique for studying the materials with defects and states with unpaired electrons. As the presently investigated samples exhibit high defects due to ball milling process, EPR measurement is carried out on all the as-milled powders and the results are depicted in Figure 4.18. It is observed that the milled NiO powders exhibit broad resonant peaks at low field in contrast to the un-milled NiO powder. The relative position

of the absorption lines depends on the milling speed, i.e., with increasing t_s, the peak position shifts slightly to higher fields indicating a clear FM signature in the material. In contrast, the un-milled NiO powder shows completely a different spectrum, i.e., the spectrum with reduced intensity. It is well known that the EPR signal of the bulk stoichiometric NiO disappears in its AFM state due to the effect of very strong exchange fields. On the other hand, the NiO powders with the particle size less than 100 nm may have non-stoichiometric resulting a significant Ni^{3+} in the NiO powder and exhibit paramagnetism at room temperature [KAKA2014]. A careful investigation by Ulmane et al [ULMA2007] and Gandhi et al [GAND2011] on the size dependent properties of NiO revealed that with decreasing the particle size of NiO below 100 nm, a large reduction in 2M mode along with the increase in 1P LO mode was observed and correlated to the development of surface disorder. Therefore, the existence of weak signal in un-milled NiO powder might be due to the presence of small disorder as evident in vibrational spectrum (see Figure 4.08) and causes the reduction in size dependent exchange interaction between two neighbouring Ni^{2+} ions mediated through oxygen ion and induces anisotropy of Ni^{3+} [YIJB2007]. Similarly, the observation of EPR signal in the spectra for the milled powders can be correlated to one of the following possible mechanisms: (i) formation of uncompensated spins on the surface of the particle due to size reduction [NEEL1962] (ii) creation of a spin-glass-like shell on the particle surface [TIWA2005], (iii) formation of a weak magnetic moment caused by the canting of the magnetic sublattices [KODA1997] and (iv) extraneous FM impurities in the milled samples. In the presently investigated samples, the formation of EPR signal in comparison with magnetic properties could be attributed to the existence of uncompensated spin on the surface of NiO particles, which provides supportable explanation for temperature and field dependent magnetic properties. The above results suggest that nanoscale NiO powders prepared by ball milling process have high T_C and enhanced FM at room temperature with cubic structure, which could easily facilitate integration of spintronic devices.

In order to understand the origin of the induced FM and to rule out any impurities contribution to the magnetic properties, the magnetic structure, chemical bonding state and chemical compositions are analyzed using ^{57}Fe Mössbauer spectroscopy, XPS and EDS, respectively for the un-milled and milled NiO powders. The presence of impurities could not be detected in the magnetic structure using ^{57}Fe Mössbauer spectroscopy, chemical bonding using XPS (see Figures 4.09 and 4.10) and composition analysis using EDS (see Figure 4.19) at least to the detection limit of these techniques. As depicted in Figures 4.09

and 4.10, XPS spectra of milled NiO powders reveal the existence of a mixed valency state of Ni supporting the presence of non-stoichiometry in the milled NiO powders [JIAN2002, GROS2006, MOSS2011, RAJA2016] to exhibit room temperature FM.

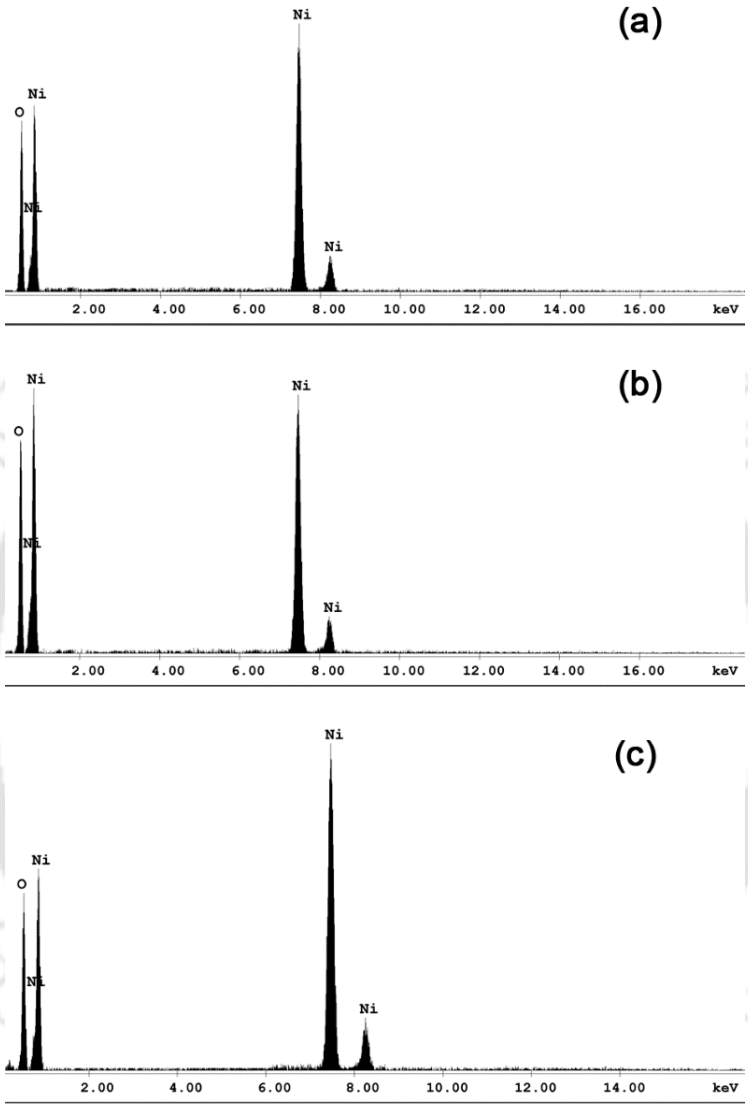

Figure 4.19: Energy dispersive X-ray spectrum for (a) pure un-milled NiO and milled NiO powders at (b) t_s = 350 rpm and (c) t_s = 500 rpm.

4.3.2. Properties of annealed NiO powders

In order to further confirm the development of FM in milled NiO powders, the milled NiO powders at different t_s are annealed systematically at 500 °C for different annealing times of 3 and 5 hrs. The effect of annealing on the milled NiO powders and the resulting properties of annealed powders are discussed here.

4.3.2.1. Structural properties

Figure 4.20 displays typical room temperature XRD patterns of milled NiO powders at different t_s and annealed NiO powders at 500 °C for 3 and 5 hrs. Figure 4.21 shows the enlarged view of NiO(200) peak of both milled and annealed NiO powders. It is observed that the peak broadening of the Bragg reflections decreases and the peak position shifts to higher angle for the annealed NiO powders.

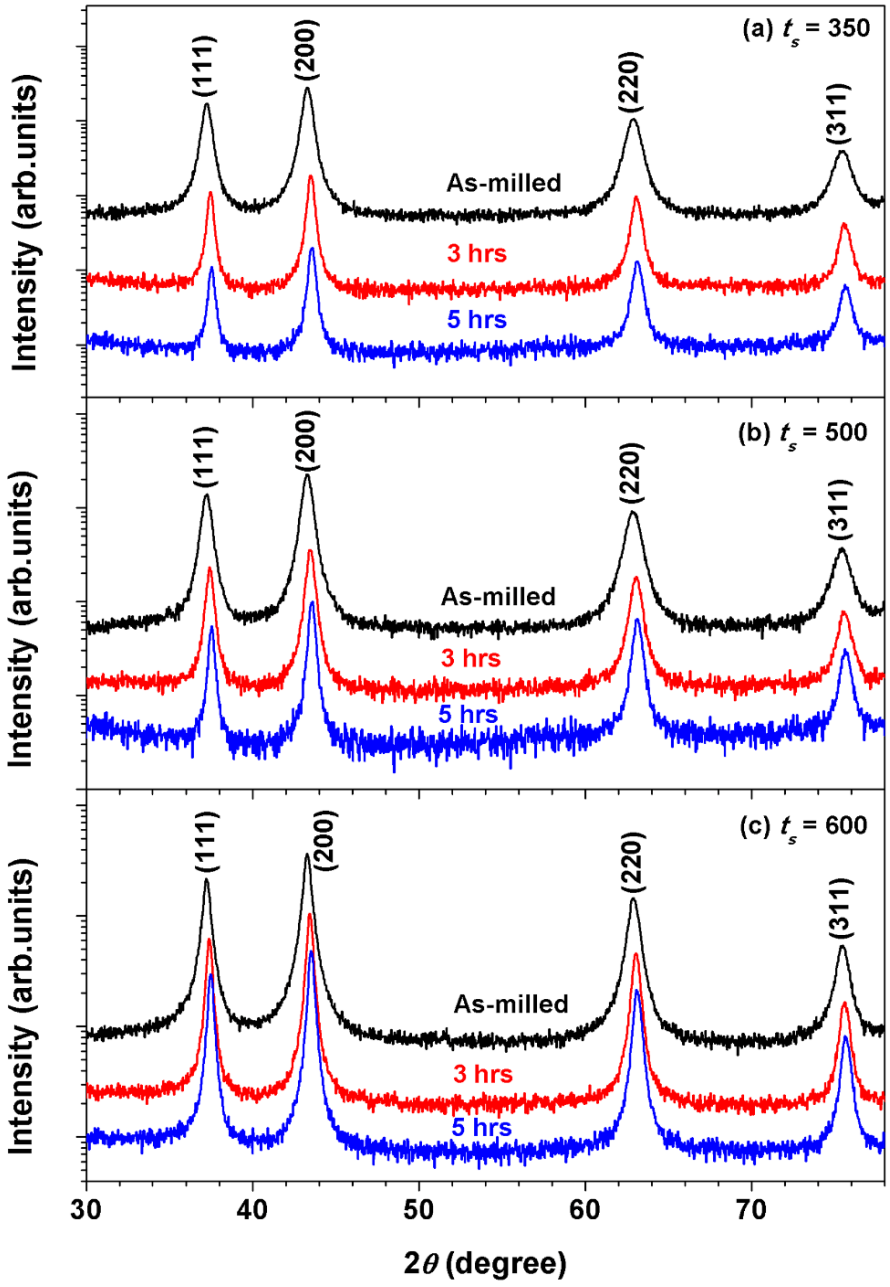

Figure 4.20: Room temperature XRD patterns of milled NiO powders at different t_s and annealed NiO powders at 500 °C for 3 and 5 hrs.

All the annealed powders exhibit *fcc* structure without the formation of any other additional phases. With increasing annealing time, the peak width of the Bragg reflections decreases and the peak position tends to shift higher angle. However, the amount of shift in the peak position decreases with increasing annealing time. The decrease in the peak width with increasing annealing time in the annealed powders can be correlated to the growth of the NiO crystals and the relaxation of strain accumulated in the milled powders. On the other hand, the shift in the peak position indicates a considerable change in the lattice parameter upon annealing.

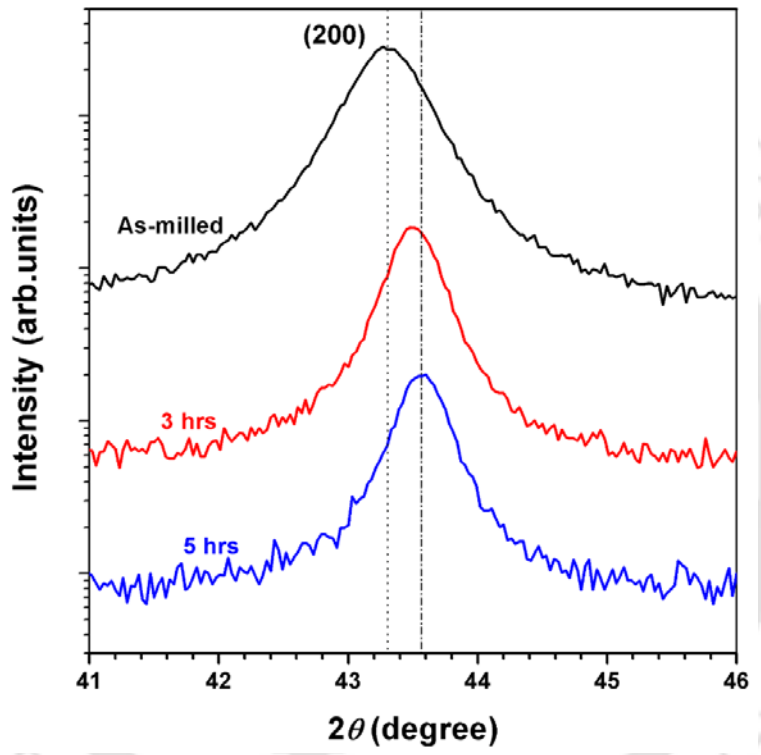

Figure 4.21: Expanded view of the NiO (200) XRD peak for both milled NiO powders at 350 rpm and annealed NiO powders at 500 °C for 3 and 5 hrs.

In order to evaluate the structural modifications, XRD patterns are analyzed and the determined values of D, η and a are plotted as a function of annealing time in Figure 4.22. D (η) increases (decreases) with increasing annealing time, but tends to saturate for 5 hrs annealed NiO powders. However, the amount of increase in D and decrease in η depends on the milling conditions. These results confirm that the annealing process not only reduces the strain, but increases D significantly. NiO powders milled at 350 rpm and annealed at 500 °C for 5 hrs show the average crystallite size of about 21 nm. On the other hand, the

lattice constant decreases considerably for annealed powders due to the release of strain accumulated in the milled powders and increase in NiO crystal size upon annealing. These results are in close agreement with the earlier reports on similar systems [DUAN2012, GHOS2006].

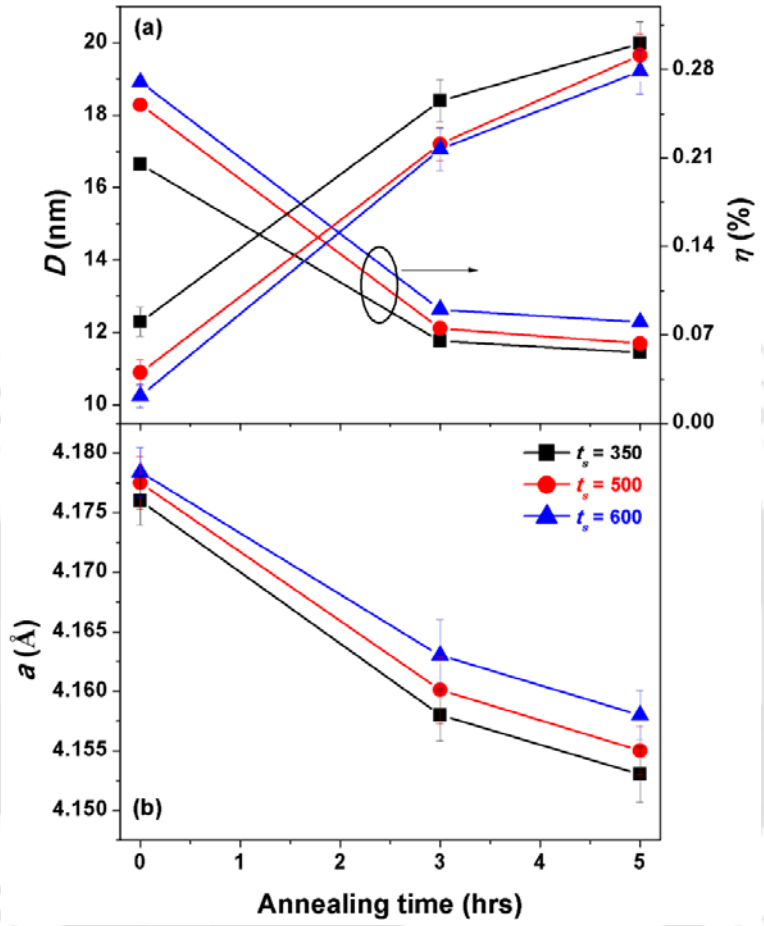

Figure 4.22: The variations of average crystal size (D), strain (η) and lattice constant (a) for the milled NiO powders at different t_s and annealed NiO powders at 500 °C for 3 and 5 hrs.

4.3.2.2. Magnetic properties

To study the effect of annealing on the induced FM magnetic properties of the as-milled powders and to understand the origin of FM, room temperature *IM* curves and *M-H* loops are measured using VSM for all the annealed powders and displayed in Figure 4.23. The extracted values of M_{12kOe} for milled and annealed NiO powders are shown as a function of annealing time in Figure 4.24. It is clear from the Figure 4.23 that the magnetization of the as-milled NiO powders is decreased substantially after annealing. In order to separate the

FM and AFM components, the field dependent magnetization curves are analysed using eqn. (4.02) and the determined parameters are summarized in Table 4.02.

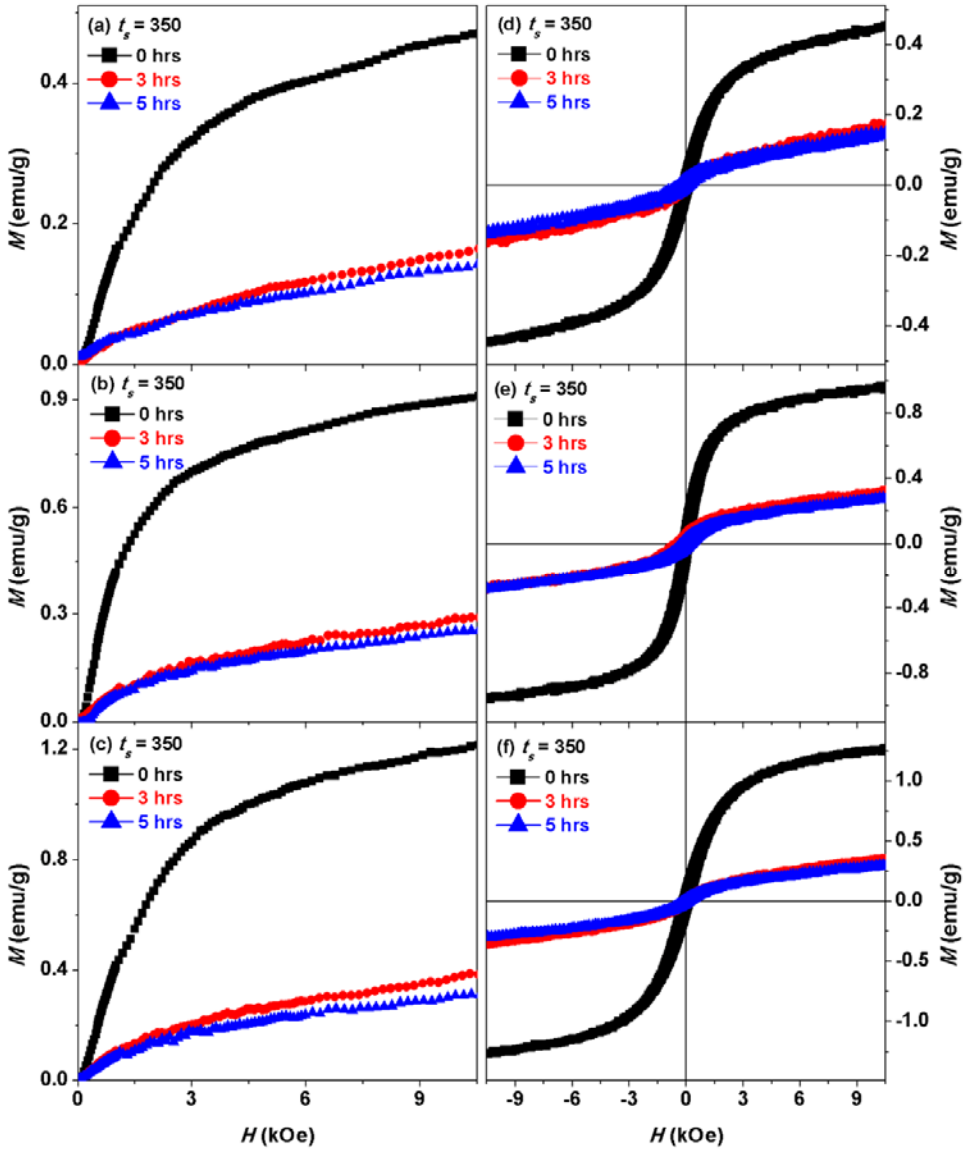

Figure 4.23: Room temperature (a,b,c) initial magnetization curves and (d,e,f) *M-H* loops of milled NiO powders at different t_s and annealed NiO powders at 500 °C for 3 and 5 hrs.

It is observed from the Table 4.02 that both the values of M_{FM} and χ_{AFM} decrease with increasing annealing time. Similarly, M_{12kOe} decreases from 0.48 to 0.15 for 350 rpm, from 0.97 to 0.26 for 500 rpm, and from 1.26 to 0.33 emu/g for 600 rpm milled NiO powders after 5 hrs of annealing. The rate of decrease in magnetization strongly depends on the milling conditions. The structural studies revealed that the average crystallite size increases with increasing the annealing time. This leads to a considerable decrease in surface-to-

volume ratio and hence the ratio of uncompensated surface spins over particle core decreases. Therefore, the lower magnetization obtained in annealed NiO powders is mainly from the reduced uncompensated surface spins and reduction of Ni^{3+} into Ni^{2+} [TADI2011] and increase in the average crystal size upon annealing.

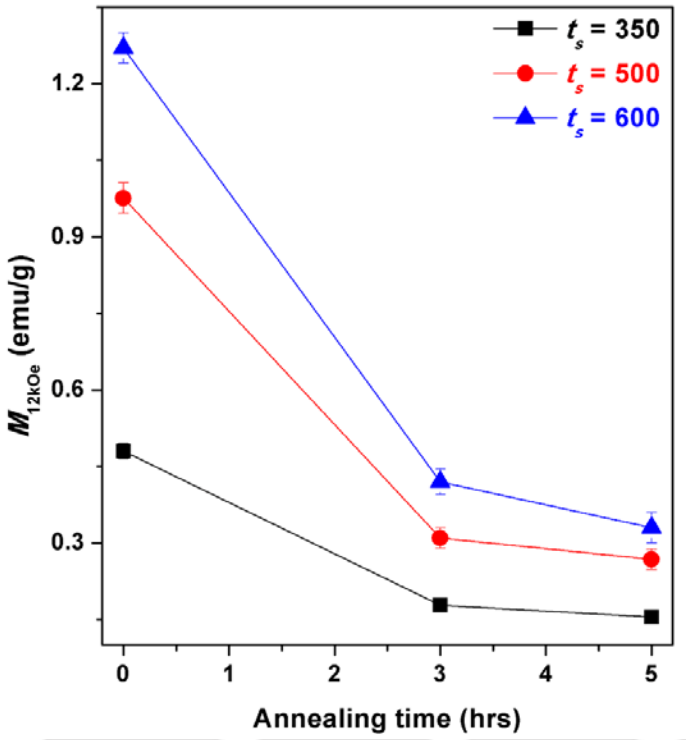

Figure 4.24: The variations of M_{12kOe} for the milled NiO powders at different t_s and annealed NiO powders at 500 °C for 3 and 5 hrs.

Table 4.02: Room temperature M_{FM} and χ_{AFM} for the milled and annealed NiO powders.

Sample		M_{FM} (emu/g)	χ_{AFM} (emu/g.-Oe)
350 rpm	milled	0.41	1.51×10^{-5}
350 rpm	3 hrs	0.07	1.33×10^{-5}
350 rpm	5 hrs	0.06	0.91×10^{-5}
500 rpm	milled	0.89	1.82×10^{-5}
500 rpm	3 hrs	0.15	1.46×10^{-5}
500 rpm	5 hrs	0.14	1.23×10^{-5}
600 rpm	milled	1.02	2.84×10^{-5}
600 rpm	3 hrs	0.17	2.17×10^{-5}
600 rpm	5 hrs	0.15	1.70×10^{-5}

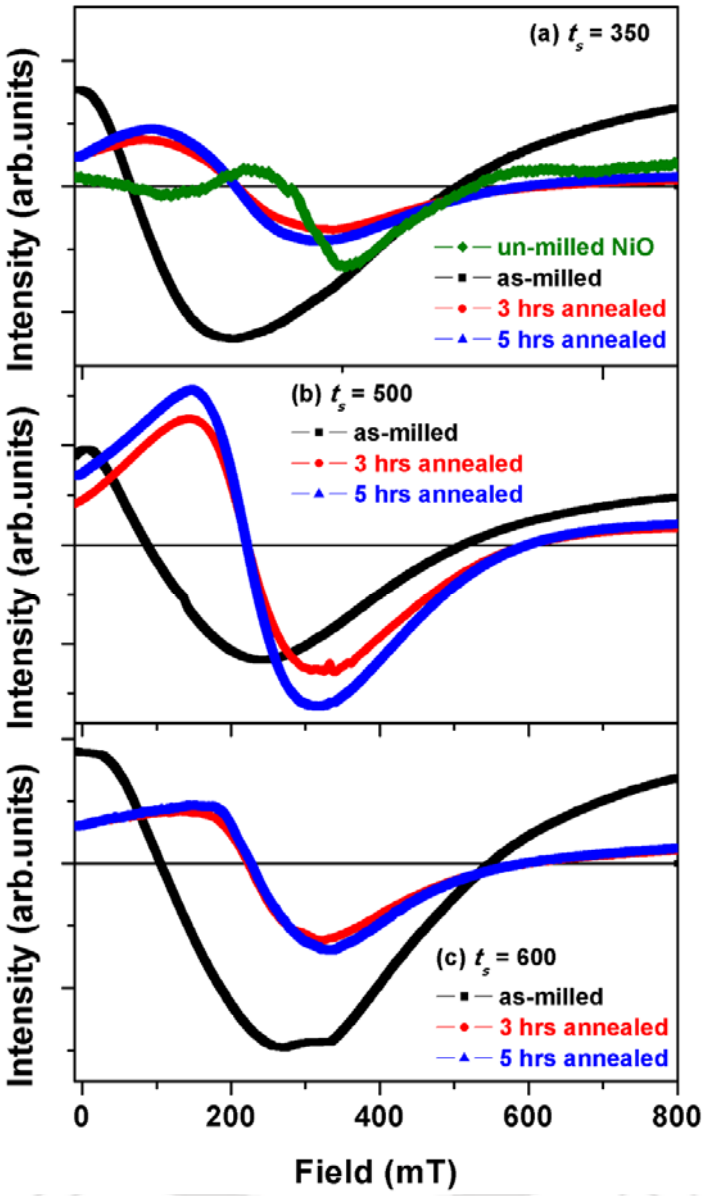

Figure 4.25: EPR spectra for the milled NiO powders at different t_s and annealed NiO powders at 500 °C for 3 and 5 hrs. For comparison, the EPR spectrum of pure un-milled NiO powders is also shown.

4.3.2.3. Resonance properties

To study the effect of annealing on the resonance properties, EPR spectra are obtained for all the annealed NiO powders and presented in Figure 4.25. In order to compare with the bulk un-milled NiO powders, the EPR spectra of the pure un-milled NiO powder is also included in the figure. The pure un-milled NiO displays spectrum with large broadening and

reduced intensity due to AFM nature [YIJB2007, SHIM2008, LYUK2010, ZHAN2016] associated with Ni^{2+}-O^{2-}-Ni^{2+} super-exchange interaction at larger crystal size. As described earlier, the milled NiO powders exhibit a broad resonant peak at low field in contrast to the un-milled NiO powder [KAKA2014]. On the other hand, the annealed NiO powders display different EPR spectra with different strength of the signals, i.e., the resonant peak exhibits reduced intensity and shifts to higher magnetic field and approaches to the one obtained for pure un-milled NiO powders. This could be attributed to the decrease in FM ordering upon annealing due to reduction in strain, increase in average crystal size and reduction of Ni^{3+} into Ni^{2+}. Such observations are in close agreement with *M-H* measurements as shown in Figure 4.23. The annealing study suggests that the annealing of as-milled NiO powders at much higher temperatures (> 700 °C) may increase the average size of NiO crystals largely and transform into complete AFM. However, the transformation of NiO into AFM may strongly depend on the milling condition.

Nevertheless, the observed results suggest that the nanoscale NiO with high T_C and a moderately induced magnetization at room temperature with a cubic structure would be useful to facilitate these materials for spintronic devices.

4.4. Summary

A systematic study on the evolution of structural, vibrational, electronic, magnetic and resonance properties of NiO powders prepared by ball milling process in a planetary ball mill under dry mill conditions and at argon atmosphere has been carried out as a function of milling speed and annealing time. The salient features of the NiO powders from the current investigations are as follows:

- The ball mill process produces single phase face centered cubic nanocrystalline NiO powders with the average crystallite size of nanometer range without any impurities within the detection limit of the techniques utilized. The average crystallite size decreases and lattice constant increases with increasing milling speed. Microstructural studies reveal that the agglomeration of fine particles increases with increasing t_s and the nanocrystalline powders exhibit irregular shapes with broad size distribution. The analyses of both TEM and XRD observations are in good agreement with each other.
- Vibrational properties reveal that two-magnon band associated with Ni^{2+}-O^{2-}-Ni^{2+} super-exchange interaction and observed in pure un-milled NiO powder disappears

dramatically in milled NiO due to defects and/or size reduction. In addition, with increasing t_s, 1P LO band becomes dominant along with considerable broadening due to defects, 2P TO and 2P TO+LO bands disappear, 2P LO band broadens and shifts to lower value of Raman shift due to size-induced phonon confinement. This changes the color of the powder from the pale green for pure un-milled NiO into dark green for milled NiO powders.

- XPS spectra confirm the existence of non-stoichiometry in the milled NiO powders, caused by the defects, size reduction, oxidization of Ni^{2+} into Ni^{3+} due to breaking of Ni^{2+}-O^{2-}-Ni^{2+} super-exchange interaction.
- AFM nature of the un-milled NiO powders transforms into induced FM after milling due to defects and size reduction. The average room temperature magnetization increases with increasing t_s and obtained a maximum magnetization of 1.26 emu/g at 12 kOe applied field for the NiO powders milled at 600 rpm.
- High temperature magnetization in the temperature range between 300 K and 1000 K shows a well-defined magnetic phase transition at high temperature around 780 K due to induced FM phase.
- EPR study reveals a close correlation between the EPR results and magnetic properties.
- Annealing of as-milled NiO powders results in a large reduction in magnetization, but the rate of reduction in magnetization strongly depends on the milling conditions. Furthermore, the annealing studies confirm the origin of FM as intrinsic one.

Chapter 5

Thickness dependent ferromagnetism in thermally decomposed NiO thin films

5.1. Introduction

Recently, nanostructured nickel oxide (NiO) materials have received enormous interest due to their novel properties, which are considerably different from those observed in bulk material and potential applications in a wide variety of technological areas such as spin-valves, magnetic recording, resistive random access memory, electrochromic, supercapacitors, alkaline batteries, etc [LIXI2010, OHJH2013, WANG2013, ZHUY2013, BARA2014, RAVI2015]. However, the proper control of size, shape, morphology and surface of nanostructures remains a challenge as the properties are strongly depending on the structures at the nanoscale. In particular, the development of magnetism in NiO based thin films has been focused to obtain ferromagnetism (FM) above room temperature such that these oxides with cubic structure could easily facilitate integration of spintronic devices. As a result, different fabrication methods such as sol-gel [NALA2012], vacuum evaporation [SASI2002], pulsed laser deposition [SUGI2013], magnetron sputtering [YOUS2007, VALL2014, LUOX2015, VERM2015] and reactive ion beam sputtering [LIER2002] were employed for the preparation of NiO films.

It is well known that the bulk NiO is an antiferromagnetic (AFM) material with a Néel temperature (T_N) of 523 K and transforms from cubic to rhombohedral structure below T_N [SARM2010, DUAN2012]. However, NiO thin films interestingly show unusual properties due to the occurrence of structural disorder, vacancies of nickel and/or oxygen, aligned dislocations into NiO crystal, finite size effect, etc. For instance, Sugiyama et al [SUGI2013] demonstrated that dislocations in NiO crystals show unique magnetic properties with high coercivity (H_C) due to the strong interaction between the FM dislocations and surrounding AFM bulk phase. Jang et al [JANG2009] reported that the enhanced electrical properties of sputtered NiO thin films are mainly due to the nickel vacancy based defects. Yang et al [YANG2005] shown that the non-stoichiometric NiO thin films should contain excess oxygen at interstitial positions, which diffuse out during the annealing process and hence tune the electrical, chemical and optical properties. Bruckner et al [BRUC2003] reported that the sputtered NiO films having non-stoichiometric NiO decompose during heating at high temperatures into thermally stable oxygen poorer NiO and/or metallic Ni. Similarly, Kawai et al [KAWA2010] reported that annealing of NiO films above 400 °C under high vacuum environment produces conducting filaments in single crystalline NiO, which results in memory cell. Recently, Jang et al [JANG2011] reported that the decomposition reaction of NiO films strongly depends on annealing

temperature (T_A) and thickness of the films (t). These results suggest that the thermal decomposition of sputtered NiO is very much important for selected practical applications such as resistive random access memory and spintronic devices. However, the related mechanism of thermal decomposition as a function of t and T_A, and the resulting magnetic properties are not reported in detail.

Therefore, to understand the thermal decomposition of NiO thin films and the resulting magnetic properties as a function of decomposition in more details, in this chapter, NiO thin films with different thicknesses are fabricated using magnetron sputtering technique at ambient temperature directly on thermally oxidized Si substrate and post annealed at different T_A under high vacuum environment. A careful review of the literature on similar oxide materials suggests that the properties of sputtered oxide thin films strongly depend on the initial size of the powders used for fabricating target materials [BHUY2015]. As described in Chapter 04, the detailed investigation of ball milled NiO powders under different milling speed shows the size dependent properties. Thus, the NiO targets are prepared from the ball milled NiO powders with different crystallite size to study the effects of initial crystal size of the powders used for fabricating target on the dynamics of thickness dependent thermal decomposition and the resulting magnetic properties of NiO thin films. To compare the results of samples annealed under vacuum conditions, the as-deposited NiO films are also post annealed under oxygen environment.

5.2. Experimental details

NiO (t nm) single layer thin films with various thicknesses (t = 50, 100, 200 and 300 nm) are deposited directly on thermally oxidized Si substrate at ambient temperature by sputtering NiO target (50.8 mm diameter and 3 mm thickness) using magnetron sputtering technique with various process parameters. NiO sputtering targets are prepared by ball milling the high purity NiO (99.9% Sigma Aldrich, USA) powders using high energy planetary ball mill under different milling speeds. Subsequently, the milled powders at different rpm (350 and 600) are sieved, uniaxially pressed and sintered. The substrates (0.5mm thick) are cut into 2×2 cm^2 pieces, cleaned with acetone, isopropyl alcohol and ultrasound bathed for 15 min. Before starting the deposition, the base pressure of the chamber is evacuated below 1×10^{-4} Pa. Sputtering of NiO is carried out at ambient temperature in an argon (Ar) atmosphere of 21 mTorr. The optimization of Ar gas pressure is done mainly by analysing the formation of NiO thin films with AFM nature. The

deposition rate of NiO films is pre-calibrated using *ex situ* surface profilometer (Vecco, Dektak 150 model). Accordingly, the deposition rate for NiO thin film under the above sputtering conditions is optimized to be 1.67 nm/min. During the deposition, the substrates are maintained at room temperature in order to characterize only the post thermal annealing induced decomposition. All the as-deposited films are post annealed ex-situ in a separate custom built high vacuum ($<10^{-3}$ Pa) annealing setup at different heat treatment temperatures (T_A): 300 °C, 400 °C and 500 °C for 70 minutes duration. In order to compare the resulting properties of NiO thin films annealed under vacuum condition, the NiO films are also annealed at 500 °C in oxygen atmosphere. The annealing temperature and annealing time are optimized based on the thermal decomposition behaviour of NiO thin films.

The phase evolution and crystal structure of NiO thin films are analyzed through X-ray diffraction (XRD) patterns obtained using high-power (18 kW) X-Ray diffractometer (Rigaku TTRAX III, Japan). XRD data are collected at a slow scan rate of 0.005 °/s for analyzing the structural parameters as a function of t and T_A. The microstructural properties of the as-deposited and annealed NiO thin films are analyzed using transmission electron microscopy (TEM, JEOL 2100 and TECNAI G2 F30) technique. Raman spectra are obtained using micro-Raman spectroscopy (LabRam HR800, Jobin Yvon) using excitation wavelength of 614 nm at room temperature. Magnetic properties of the as-deposited and annealed NiO thin films are characterized by using vibrating sample magnetometer (VSM, Lake Shore Model 7410) by performing magnetic hysteresis loops (M-H) along the film plane at different constant temperatures in the temperature range between 30 K and 300 K.

5.3. Results and discussion

5.3.1. Properties of NiO films prepared from target of 350 rpm NiO powder

5.3.1.1. Structural properties

Figure 5.01 displays the room temperature XRD patterns of the milled NiO powder at 350 rpm, as-deposited NiO thin film of 300 nm thickness and the substrate. It is clear from the figure that both the NiO target and 300 nm thick NiO film exhibit Bragg reflections corresponding to face centred cubic (*fcc*) structure. The absence of any other impurity peaks within the detection limit of X-ray diffractometer confirms the formation of high purity NiO thin film. However, a close comparison between the as-deposited films and target material confirms that (i) the Bragg reflections in NiO thin films are considerably broad in nature

and the peak positions are shifted noticeably to lower angles (see Figure 5.02). (ii) NiO thin films show maximum intensity for NiO(200) peak.

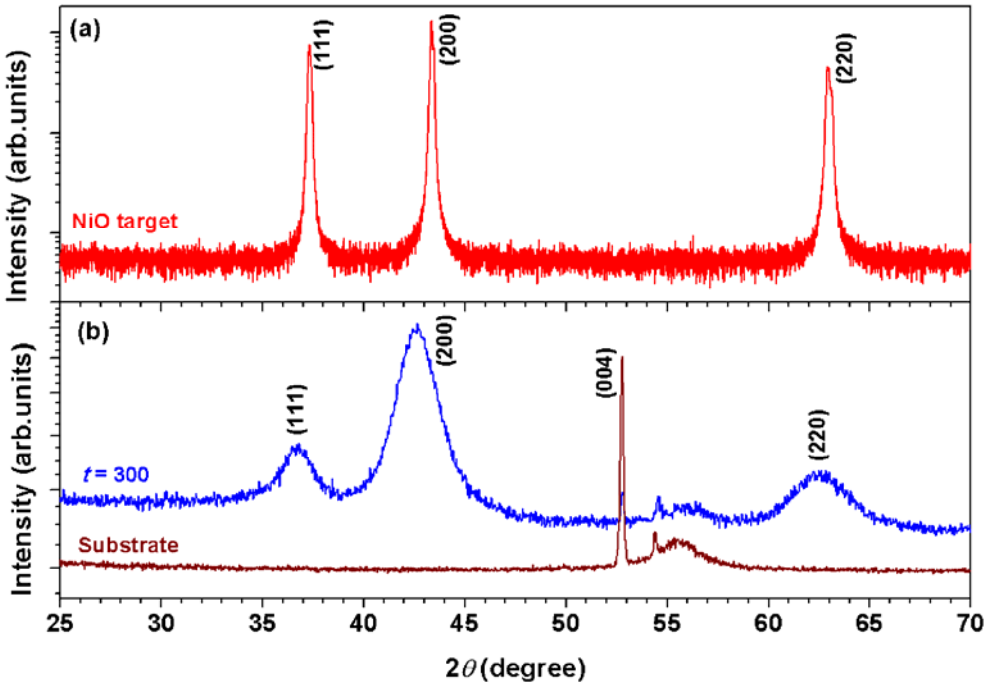

Figure 5.01: Room temperature XRD patterns of (a) NiO target prepared using 350 rpm milled powders for 30 hrs and (b) as-deposited NiO thin film with 300 nm thickness and substrate.

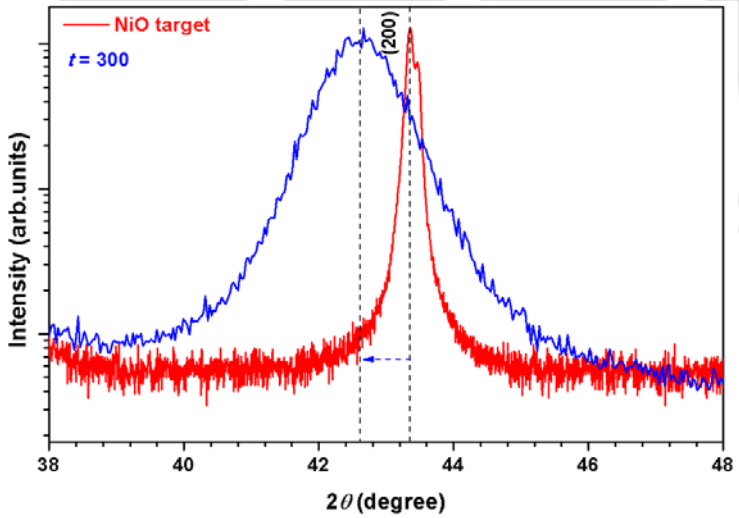

Figure 5.02: Expended view of NiO(200) peak for the NiO target and as-deposited NiO thin film with 300 nm thickness.

In order to understand the effect of film thickness carefully, XRD patterns are obtained for NiO films with different thicknesses and presented in Figure 5.03. In order to

compare the XRD patterns of the thin films with the bulk counterpart, XRD pattern of the bulk NiO powder with scaled intensity is also included.

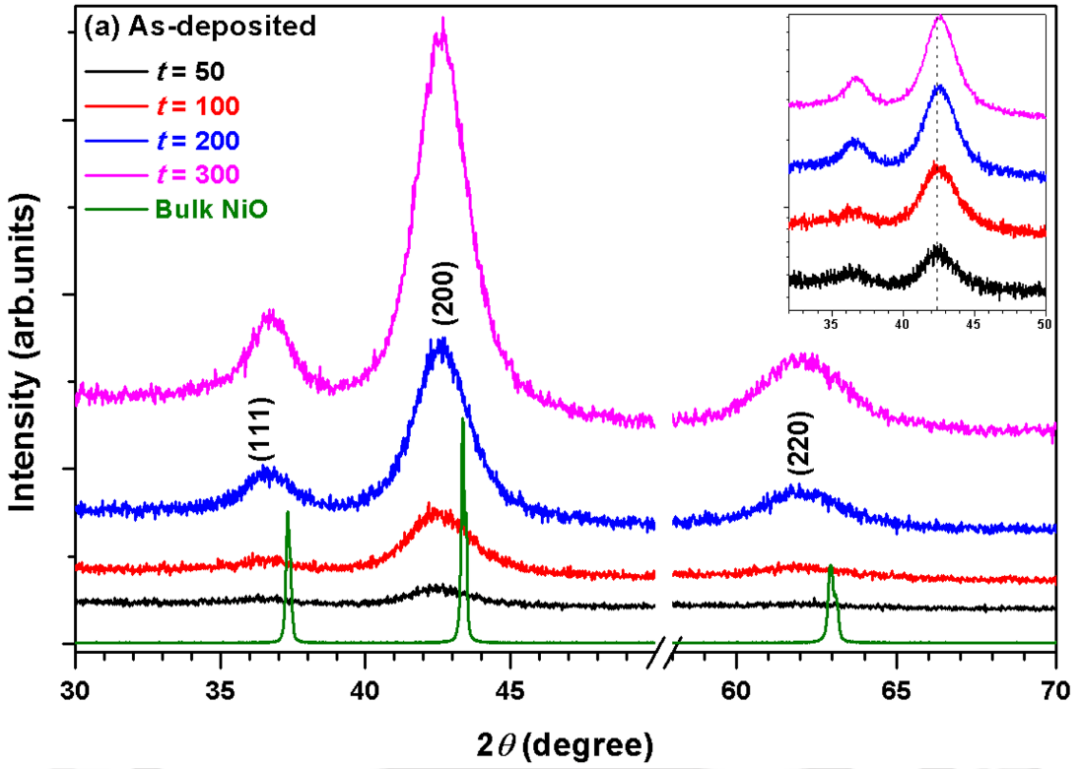

Figure 5.03: Room temperature XRD patterns of as-deposited NiO thin films with different thicknesses. XRD pattern of bulk NiO with scaled intensity is also shown for comparison. Inset: Expanded view of the XRD patterns for NiO thin films.

The XRD patterns of the as-deposited films show the following features: (i) All the NiO films grown with different thicknesses exhibit *fcc* structure without any impurity peaks. This confirms the formation of high purity NiO thin films. (ii) The films are highly oriented along (200) plane and the intensity of the (200) peak increases with increasing NiO film thickness. (iii) The comparison between as-deposited films and bulk NiO powder confirms that the peaks of the films are considerably broadened and the peak positions are shifted noticeably to lower angles. This suggests that the as-deposited films have fine crystallites and large lattice constant as compared to the bulk NiO. (iv) With increasing *t* from 50 to 300 nm, the XRD peaks shift sluggishly to higher diffraction angle. This indicates that the lattice parameter of the NiO films decreases slightly with increasing film thickness due to distribution of stress accumulated during the growth of the films.

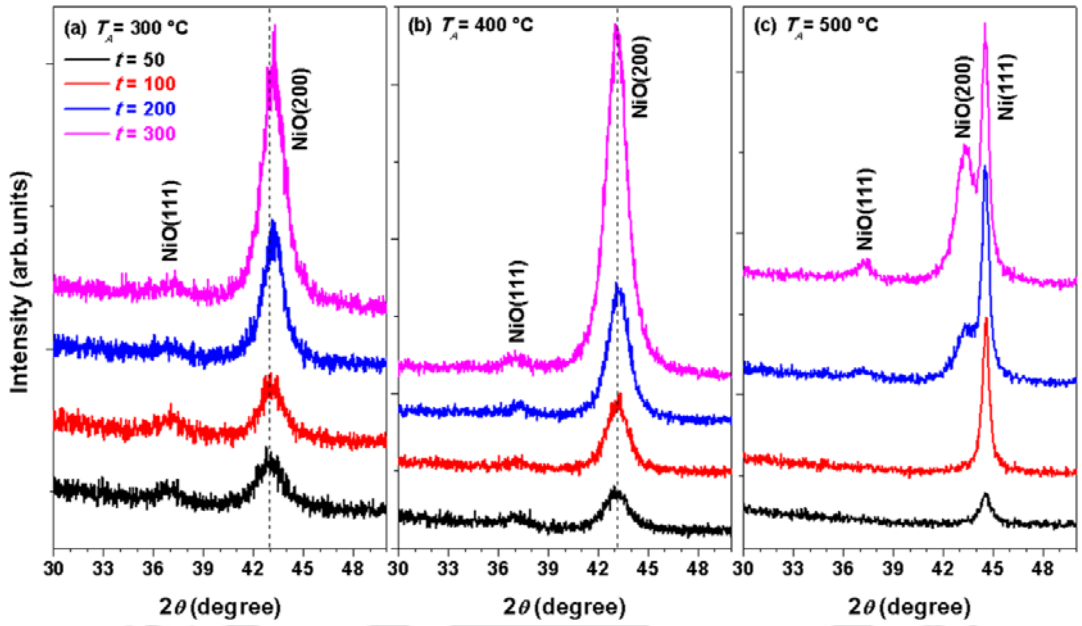

Figure 5.04: Room temperature XRD patterns of NiO thin films with different thicknesses annealed at different temperatures [(a) 300 °C, (b) 400 °C and (c) 500 °C] under vacuum condition.

To understand the effect of thermal induced decomposition behaviour in as-deposited NiO thin films, all the as-deposited films are post annealed at different temperatures under vacuum environment and the room temperature XRD patterns of the annealed NiO films with different thicknesses are depicted in Figure 5.04. It is observed from the figure that (i) with increasing T_A up to 400 °C, the peak broadening decreases progressively along with a considerable shift in the peak position to higher diffraction angles as shown in Figures 5.04(a) and (b). While the first one confirms the increase in the average crystallite size and reduction of strain in as-deposited films, the latter one suggests the decrease in lattice constant with increasing T_A. (ii) The amount of shift in the peak position with increasing t from 50 to 300 nm decreases with increasing T_A and the films annealed at T_A = 400 °C exhibit nearly the same positions for all the thicknesses. This indicates that the thickness dependent strain relaxation in the as-deposited films decreases with increasing T_A. (iii) On further increasing T_A to 500 °C, the NiO films with $t \leq 100$ nm exhibit no detectable peaks related to *fcc* phase of NiO, but display only the peak corresponding to Ni phase only [see Figure 5.04(c)]. This confirms that the NiO films decompose into Ni for $t \leq 100$ nm. With increasing $t > 100$ nm, we observed the existence of two peaks corresponding to (200) peak of NiO and (111) peak of Ni. Interestingly, the relatively intensity of the NiO(200)

peak increases with increasing NiO film thickness from 200 nm to 300 nm. This indicates that the amount of decomposition reaction from NiO into Ni decreases with increasing NiO film thickness. These results clearly suggest that the thermal decomposition reaction of NiO into Ni under vacuum condition strongly depends on the NiO film thickness.

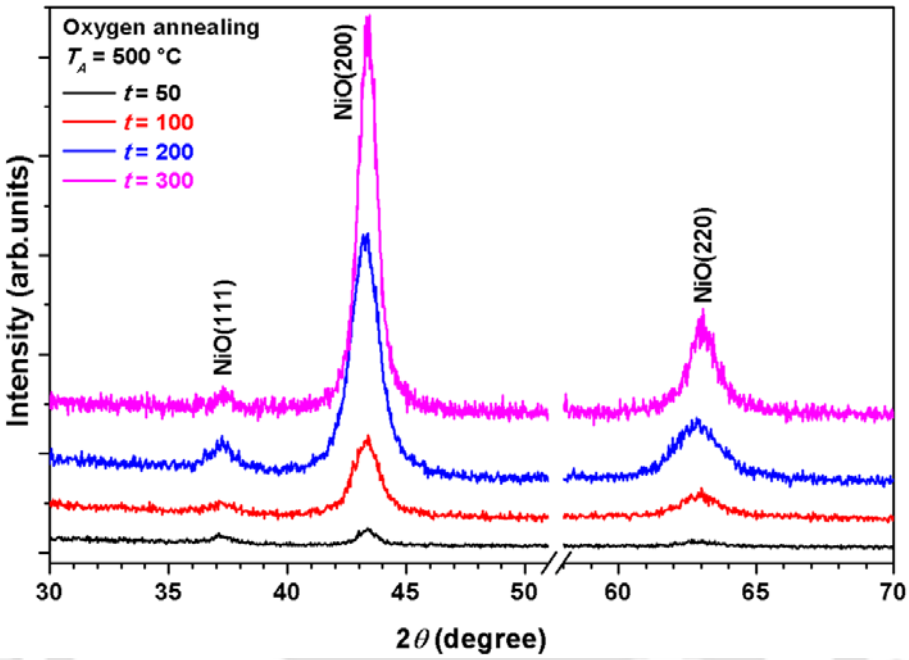

Figure 5.05: Room temperature XRD patterns of NiO thin films with different thicknesses annealed at 500 °C under oxygen annealing condition.

To study the decomposition reaction under different environments, the annealing process is also carried out at 500 °C under oxygen atmosphere. Figure 5.05 depicts the room temperature XRD patterns of the annealed NiO films at 500 °C under oxygen environment. It is clearly evident that the annealing of NiO thin films under oxygen atmosphere does not promote any decomposition behaviour and exhibits highly oriented NiO(200). However, a considerable reduction in peak broadening is observed and the peak position of NiO(200) almost matches with the peak position of the bulk NiO powder. This indicates that the average crystallite size increases and the lattice constant approaches to that of bulk NiO.

To quantify the changes in the structural parameters such as lattice constant (a), crystallite size (D) and strain (η) in the as-deposited films and annealed films, the XRD data are analysed using the following equations:

$$a = \left(\frac{\lambda \sqrt{h^2 + k^2 + l^2}}{2 \sin \theta} \right) \qquad (5.01)$$

$$D = \left(\frac{0.94\lambda}{\beta \cos\theta} \right) \tag{5.02}$$

$$\eta(\%) = \left(\frac{a_{film} - a_{bulk}}{a_{bulk}} \right) \times 100 \tag{5.03}$$

where, λ is the wavelength of the X-ray (λ = 1.54056 Å), *h*,*k*,*l* are the Miller indices, *D* is the crystallite size calculated from the full width at half maximum (β) of (200) peak for NiO and (111) peak for Ni from the Scherrer's formula, a_{bulk} is unstrained lattice constant measured for bulk NiO and its value is 4.1687 Å and a_{film} is the lattice constant of the NiO thin film. The strain in NiO thin films is mainly caused by the combined effect of thickness and dynamics of the deposition.

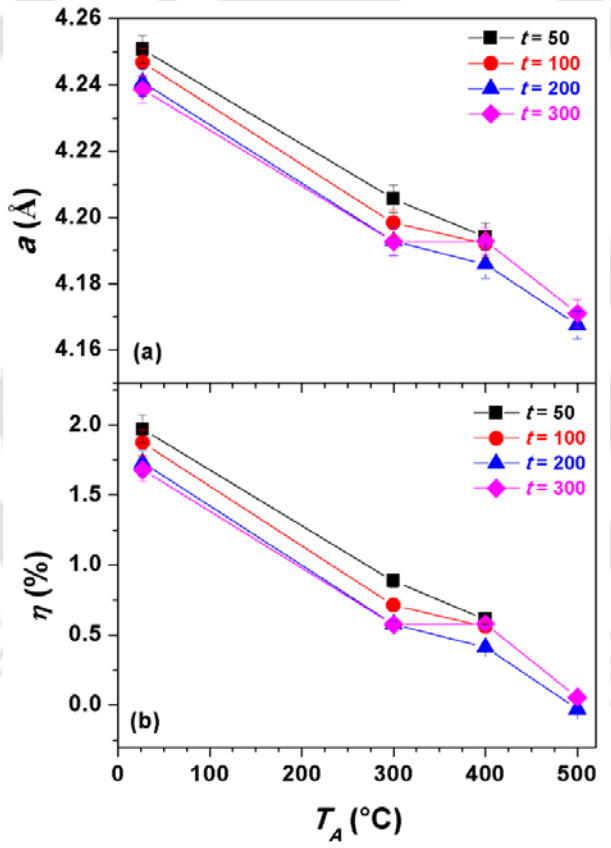

Figure 5.06: The variations of (a) lattice constant (*a*) and (b) strain (η) as a function of annealing temperature (T_A) for the NiO thin films with different thicknesses.

Figure 5.06 displays the variations of *a* and η with increasing T_A for NiO thin films with different thicknesses. As-deposited films exhibit significantly a large lattice constant

in the range between 4.239 Å to 4.251 Å, but decreases slightly with increasing film thickness. On other hand, the lattice constant decreases with increasing T_A and approaches to bulk value for the films annealed at 500 °C. Kuo et al [KUOT2011] reported suppression of intensity of (111) and (220) peaks and enhancement of (200) peak intensity along with the shift of all the peaks to lower angle with increasing Ar gas pressure during the sputtering. This behaver was correlated to the increase of Ar content in sputtered NiO film deposited at higher Ar pressure, which expanded the lattice parameter when Ar atoms occupied the interstitial positions. On the other hand, Bruckner et al [BRUC2003] and Kim et al [KIMD2012] confirmed that the sputtered NiO films have non-stoichiometric and poor crystallinity due to excess oxygen state, which makes them thermally unstable. Youssef et al [YOUS2007] reported that the NiO microstructure can be modified by changing the stoichiometry through the control of argon gas pressure during the sputtering growth. These results in correlation with the presently observed results indicate that the observation of large lattice constant in the as-deposited NiO thin films could be attributed to the strain induced in the film possibly due to the existence of interstitial argon atoms in the NiO lattice, which expands the lattice constant when argon pressure is high and/or increase of nickel vacancies created from the non-stoichiometry.

With increasing T_A up to 400 °C, the lattice constant decreases gradually and reaches almost to the bulk value for the NiO films annealed at T_A = 500 °C. This could be related to the release of interstitial Ar atoms from NiO lattice during the post annealing process. In addition, NiO films annealed at 500 °C exhibit thermal decomposition reaction, which is strongly depend on the film thickness. The decomposition reaction could be attributed to the existence of considerable nickel vacancies. According to the ideal model, the vacancy of each Ni in NiO lattice causes six oxygen neighbours to become incompletely bonded, which might induce decomposition under less stringent conditions [YANG2005, JANG2009]. Furthermore, this decomposition behaviour typically occurs from the upper surface of the films, which is evident from the thickness dependent decomposition process [JANG2011]. Das et al [DASJ2015] have also demonstrated that the creation of oxygen vacancies at the freshly deposited NiO film surface by ultrahigh vacuum annealing is more effective in case of thinner NiO films. These results further confirm that there is a critical thickness, which is currently 100 nm, for the decomposition reaction under vacuum annealing conditions. On the other hand, the strain, calculated using eqn.(5.03) for NiO thin films annealed at different T_A, displays the variations almost similar to those observed for

lattice constant with increasing T_A. This could be correlated to the release of interstitial Ar atoms with increasing T_A. The average crystallite size of the NiO phase calculated from the (200) peak exhibits weak dependence on the film thickness, but increases from about 5 nm (without taking strain into consideration) to 10 nm with increasing T_A. Similarly, for the NiO films annealed at 500 °C, the average crystallite size of the Ni, calculated from (111) peak, increases from about 10 nm for the 50 nm thick film to 18 nm for the 200 nm thick film and then decreases slightly to 15 nm for the 300 nm thick decomposed film. This could be attributed to the thickness dependent decomposition behaviour of NiO into Ni with increasing film thickness.

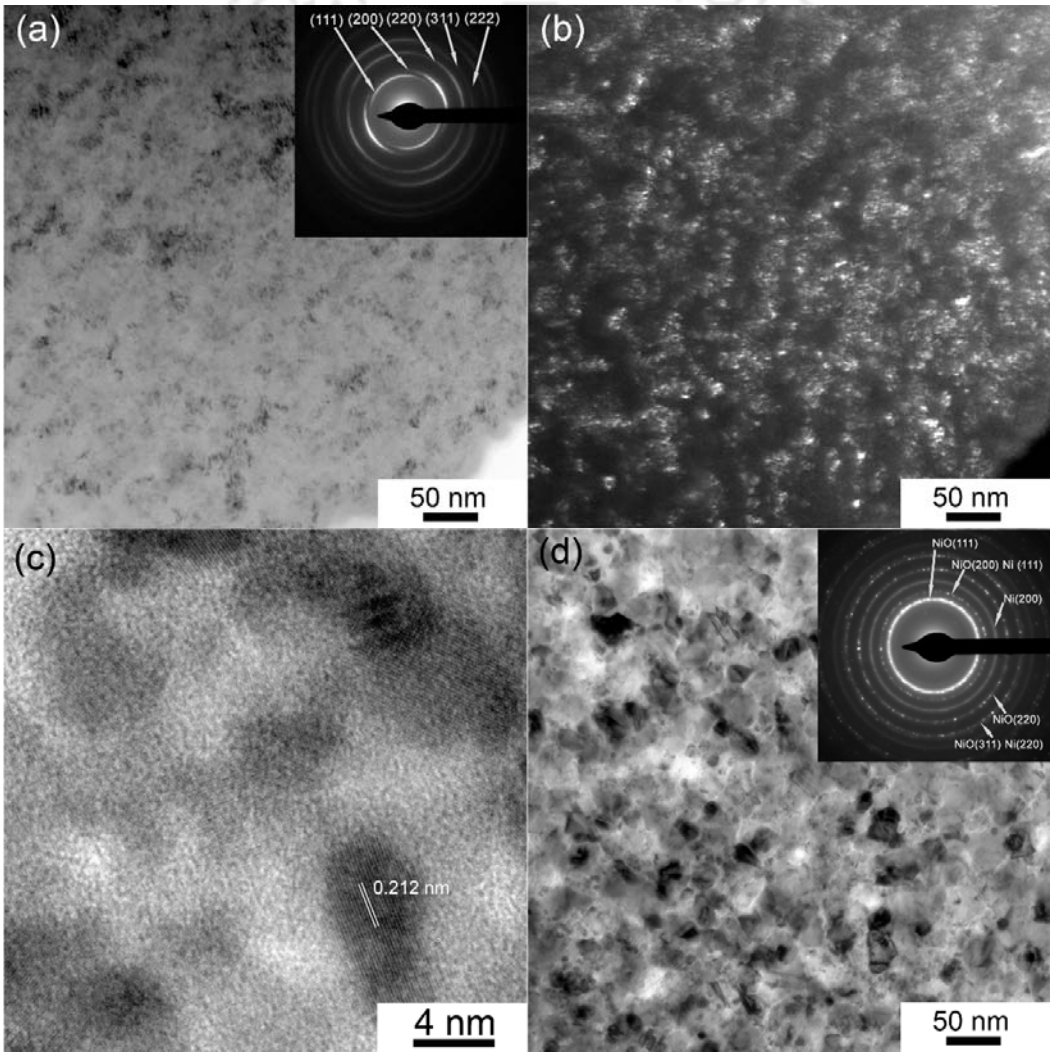

Figure 5.07: (a) Bright-field TEM micrograph and SAED pattern, (b) dark-field TEM micrograph, (c) high-resolution TEM micrograph for as-deposited NiO(200 nm) film, and (d) bright-field TEM and SAED pattern for annealed NiO (200 nm) film at 500 °C.

In order to understand the changes in the microstructure of NiO films with annealing, we have analysed the microstructure of the as-deposited and annealed films using TEM. Figure 5.07 displays typical TEM micrographs and selected area electron diffraction (SAED) patterns of the as-deposited and annealed NiO (t = 200 nm) thin films at 500 °C. The bright-field TEM micrograph and the SAED pattern of as-deposited film displays very fine particles and the diffraction rings corresponding to *fcc* structure, respectively. In order to understand the microstructure more in detail, dark-field TEM micrograph corresponding to NiO(200) plane and high-resolution TEM micrograph is shown in Figures 5.07(b) and 5.07(c), respectively. While the dark-field TEM micrograph clearly reveals the existence of fine nanocrystals with the average size of around 5 nm, the high-resolution TEM micrograph confirms the NiO phase with enhanced lattice constant. On the other hand, the annealed film exhibits well-defined polycrystalline nature mainly due to the formation of Ni nanocrystals out of NiO matrix with the size ranging between 12 to 20 nm. The presence of both the NiO and Ni phases is also supported by the SAED pattern. The lattice constant calculated using SAED pattern is found to be 4.167 Å and 3.517 Å for NiO and Ni, respectively. These results are in good agreement with the results obtained from XRD analysis. These structural changes with annealing temperature in NiO films with different thicknesses are also expected to play a significant role on the vibrational and magnetic properties.

5.3.1.2. Vibrational properties

As Raman scattering is considered to be one of the most effective tools for studying crystallinity and defects structure associated with the materials, Raman spectra are obtained at room temperature for as-deposited NiO film with different thicknesses and depicted in Figure 5.08. As shown in the figure, Raman spectra are analysed carefully by curve fitting method with different band combinations to obtain peak position, peak intensities and peak widths. In order to compare the bands, Raman spectrum of the commercially available NiO powder is also shown in the figure. The commercially available NiO powder exhibits several bands above 300 cm^{-1}. While the bands observed at 380-410 cm^{-1}, 540-560 cm^{-1}, 700-730 cm^{-1}, 900 cm^{-1} and 1050-1110 cm^{-1} could be correlated to one-phonon (1P) transverse optical (TO), 1P longitudinal optical (LO), two-phonon (2P) TO, 2P TO+LO and 2P LO of vibrational origin, respectively, the band around 1450 cm^{-1} is due to two-magnon (2M) scattering associated with Ni^{2+}-O^{2-}-Ni^{2+} super-exchange interaction. The presence of 2M

band supports the existence of AFM state through Ni^{2+}-O^{2-}-Ni^{2+} super-exchange interaction in commercially available NiO at room temperature.

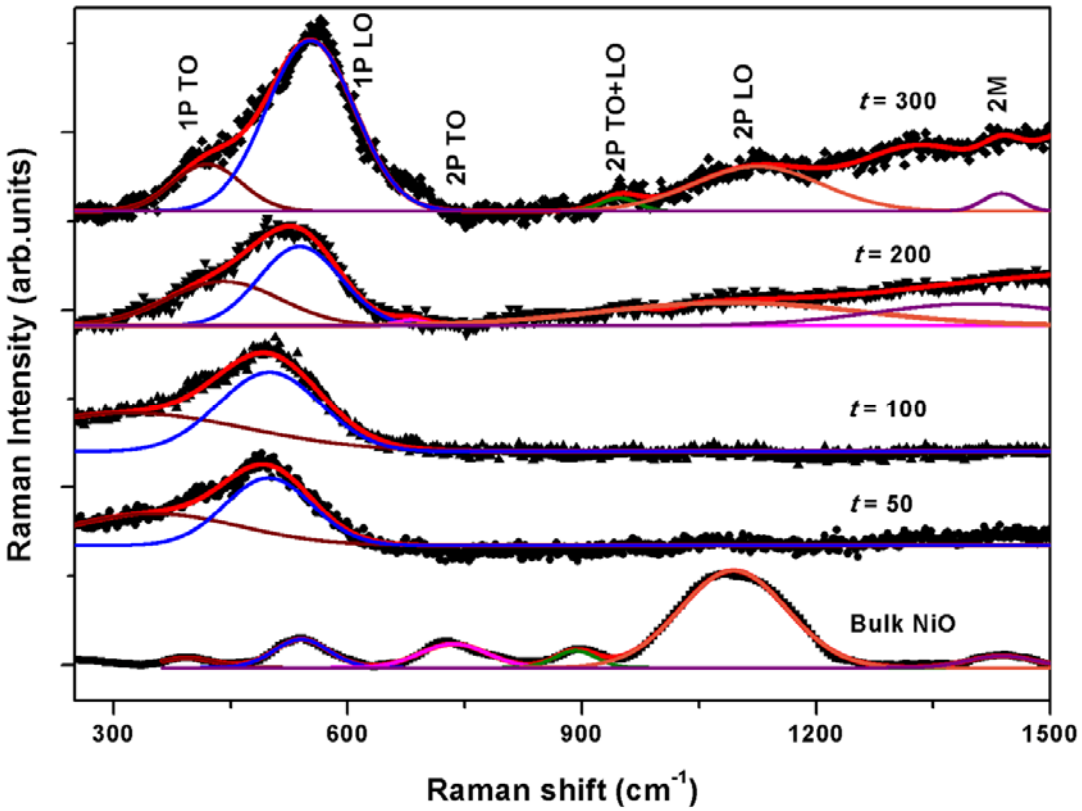

Figure 5.08: Room temperature Raman spectra of as-deposited NiO thin films with different thicknesses. Raman spectrum for bulk NiO is also shown for comparison. The solid lines passing through the data are the results of curve fitting method.

Although the perfect cubic and rhombohedral structured NiO should not show 1P LO band, which is generally attributed to the disordered induced defects, surface effects, imperfectness of the particles size and shapes [ULMA2007], the existence of a weak 1P LO band has been observed in NiO by many groups [WANG2002, LUML2011] including for single crystal like particles [ULMA2007]. Therefore, the observation a weak 1P LO band in pure NiO is assumed to be typically good quality NiO crystals. On the other hand, as-deposited NiO films show different modes depending on the film thickness. For instance, 50 nm thick NiO film exhibit only two bands at 380-410 cm^{-1} and 540-560 cm^{-1} corresponding to 1P TO and 1P LO, respectively. The band positions are observed at lower Raman shift as compared to commercial NiO powder. Interestingly, with increasing *t*, the band positions are shifted to higher value of Raman shift and approach to value of commercial NiO for 300 nm thick NiO films. In addition, with increasing *t*, the other Raman

bands are also resolvable around 900-950 cm^{-1}, 1050-1110 cm^{-1} and 1450 cm^{-1} corresponding to 2P TO+LO, 2P LO and 2M, respectively. The presence of 2M band supports the existence of AFM state through Ni^{2+}-O^{2-}-Ni^{2+} super-exchange interaction in NiO thin films at room temperature. The non-observation of certain Raman bands at lower thickness NiO films is possibly due to the detection limit of the system for lower thickness films.

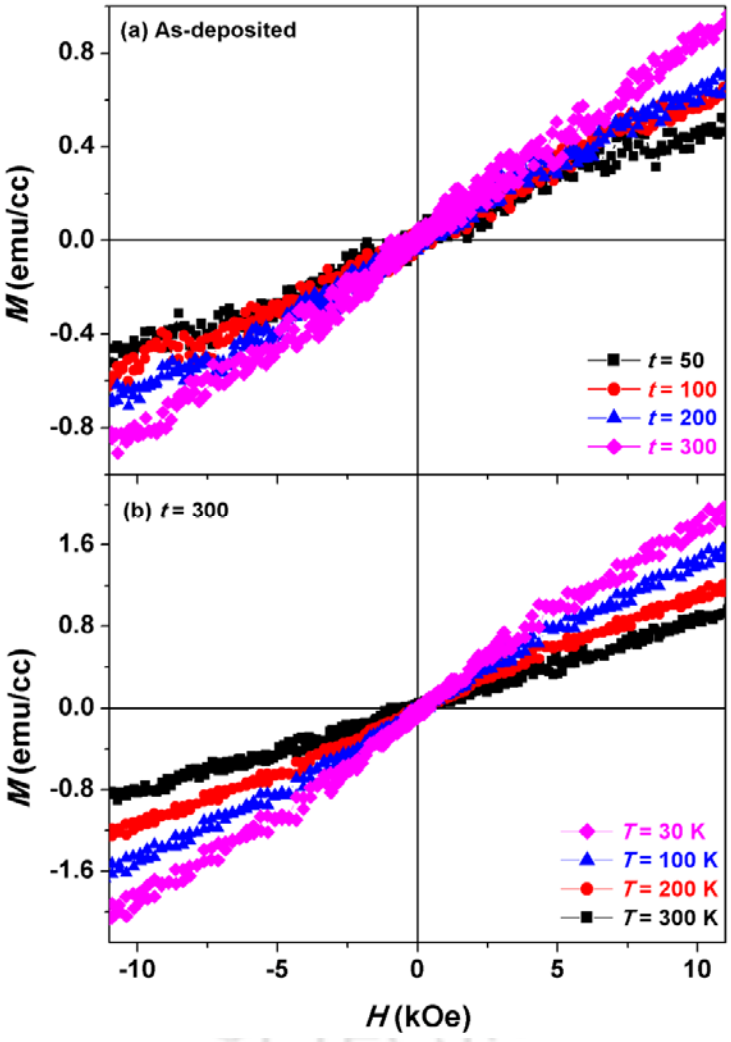

Figure. 5.09: Room temperature in-plane *M-H* loops of (a) as-deposited NiO films with different thicknesses and (b) temperature dependent *M-H* loops for 300 nm thick as-deposited NiO films measured at different temperatures.

5.3.1.3. Magnetic properties

To study the changes in the magnetic properties, we have measured room temperature and temperature dependent in-plane *M-H* loops in the temperature range of 30 K to 300 K for

the as-deposited and annealed films. Figure 5.09 displays room temperature in-plane *M-H* loops for as-deposited NiO thin films with different thicknesses and temperature dependent *M-H* loops for 300 nm thick as-deposited NiO films. All the as-deposited films exhibit weak magnetic signals without any clear trace of hysteresis loop. In addition, the noise in the substrate corrected data is mainly due to the small moment from the AFM nature of the as-deposited films [SARM2010] to be detected by the instrument in the presence of large diamagnetic contribution from the substrate. It has been reported that the nanoscale NiO powders show induced FM behaviour due to uncompensated surface spins and the average magnetization increases with decreasing the average crystal size [LILL2006, KISA2014, RINA2014, KISA2015].

In order to understand the role of presence of fine NiO crystals on the magnetic properties of the as-deposited films, *M-H* loops are obtained at low temperatures down to 30 K and shown in Figure 5.09(b). It is observed that the magnetization increases slightly with decreasing temperature, but the nature of *M-H* loops does not change substantially down to 30 K. This could be explained as follows: Although the size reduction in NiO is expected to produce induced FM properties due to uncompensated spins, the observation of pronounced lattice expansion in the presence of many broken bonds and defects is most likely to give an increased bond length of Ni-O by significantly weakening the strength of the super-exchange interactions of magnetic ions [LILL2006]. As a result, no induced FM properties within the detection limit of the instrument could clearly be seen in the presently investigated samples down to 30 K. Similarly, the films annealed up to 400 °C don't exhibit any hysteresis loop [see inset (i) of Figure 5.10]. This is mainly due to the existence of NiO phase in the annealed films up to 400 °C and in good agreement with the XRD results.

On the other hand, the NiO thin films annealed at 500 °C show FM nature with clear hysteresis loops, as demonstrated in Figure 5.10, which saturates at moderate applied magnetic fields. However, with increasing *t*, the shape of the *M-H* loop changes and the field required for saturating the films' magnetization increases with increasing film thickness. This could be attributed to the observed thickness dependent thermal decomposition behaviour for the NiO films annealed at 500 °C under vacuum environment. Nevertheless, the NiO thin films annealed at 500 °C under oxygen atmosphere [see inset (ii) of Figure 5.10] interestingly exhibit only a weak magnetic signal without any hysteresis behaviour. This could be correlated to the non-observation of decomposition reaction in NiO films under oxygen conditions.

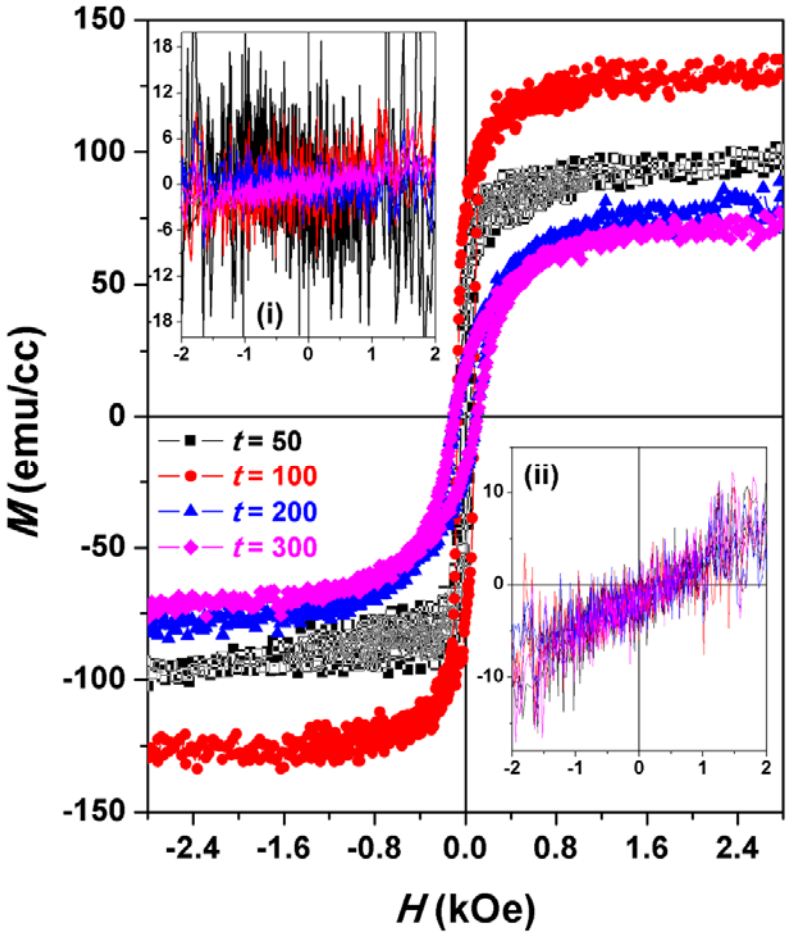

Figure 5.10: Room temperature in-plane *M-H* loops of NiO thin films annealed under vacuum annealing condition at 500 °C. Inset: *M-H* loops of NiO thin films annealed at (i) 400 °C under vacuum annealing and (ii) 500 °C under oxygen annealing conditions.

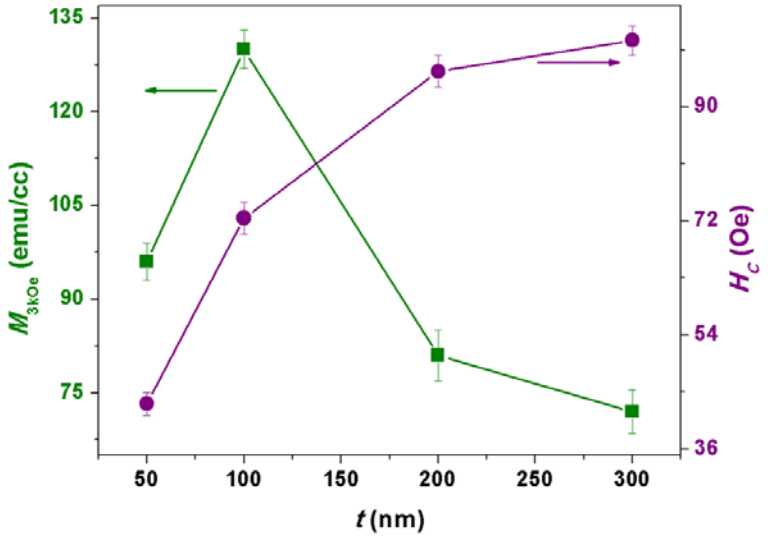

Figure 5.11: The variations of M_{3kOe} and H_C with NiO film thickness annealed at 500 °C.

The extracted values of magnetization at 3 kOe (M_{3kOe}) and coercivity (H_C) from the *M-H* loops for the NiO films annealed at 500 °C under vacuum environment are depicted in Figure 5.11. M_S increases from 95 emu/cc to 130 emu/cc with increasing *t* from 50 to 100 nm and then decrease to 80 emu/cc and 71 emu/cc with the further increase in film thickness to 200 and 300 nm, respectively. This reveals that M_S is strongly depending on the film thickness. The increase in M_S in lower thickness films up to 100 nm thickness can be explained to the complete decomposition of NiO into Ni. However, the decrease in M_S for higher thickness NiO films is mainly due to reduction in the decomposition reaction with increasing NiO film thickness above 100 nm, which results in a reduced amount of Ni in the NiO matrix, as demonstrated in the structural properties using XRD and TEM. Zhang et al [ZHAN2014] reported that M_S values in Fe doped NiO thin films increase initially with increasing film thickness up to 250 nm and then decreases due to the enhanced stress in the film which induces AFM exchange interaction and resulting in a weaker magnetization. On the other hand, H_C increases from 43 Oe to 100 Oe with increasing *t*, but the amount of increase in H_C decreases with increasing *t* above 100 nm. While the low value of H_C in smaller thickness is related to soft magnetic nature of Ni, the increase in H_C may be attributed to the strong interaction between Ni and NiO phases, which results in a higher anisotropy and hence enhances H_C. Miller et al [MILL1994] reported that H_C in pure Ni film increases initially with increasing Ni thickness nearly up to 80 nm. Nacereddine et al [NACE2007] reported H_C variation between 30 and 146 Oe for the film thicknesses ranging between 31 and 165 nm deposited on glass substrate. Rumpf et al [RUMP2007] also reported H_C values of 90 to 150 Oe for Ni films deposited on Si substrate by chemical vapour deposition. The observed results show goo agreement with the earlier reported results on thickness dependent magnetic properties of Ni. Yi et al [YIJB2005] reported that high values of H_C in NiO films prepared under different O_2 partial pressures are mainly due to the interface structure of Ni/NiO during the formation of NiO under magnetic field annealing.

To study the magnetic properties of the NiO films annealed at 500 °C under vacuum annealing condition in more detail, we have carried out *M-H* loops at different temperatures under zero-field-cooling (ZFC) and field-cooling (FC) conditions. Figure 5.12 displays the typical *M-H* loops measured under zero-field cooled conditions for NiO thin films annealed at 500 °C with different thicknesses. It is clear from the figure that the shape of the *M-H* loops does not change with decreasing temperature for each film thickness. However, the

area under the loop increases gradually with decreasing temperature as expected for a typical ferromagnetic material and resulting in an increase in H_C.

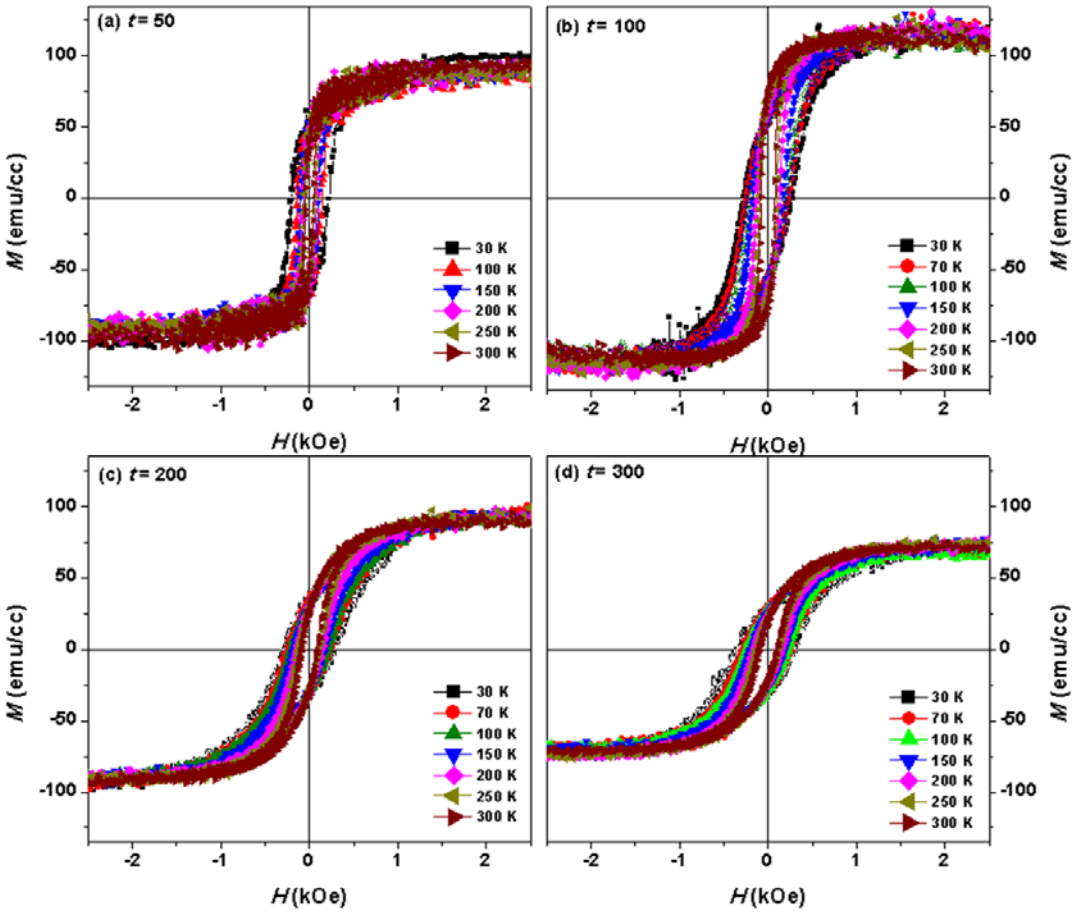

Figure 5.12: *M-H* loops measured at different temperatures under ZFC for NiO films with different thicknesses annealed at 500 °C under vacuum annealing condition.

The extracted values of H_C from the *M-H* loops at different temperatures for different film thicknesses are summarized in Figure 5.13. H_C increases incessantly for all the films with decreasing temperature and the rate of increase in H_C considerably depends on the NiO film thickness. To study the exchange bias properties in these NiO and Ni systems, we have also carried out *M-H* loop measurements at different temperatures from 30 to 300 K after cooling down the films under the field of 2 kOe. Figure 5.14 shows the *M-H* loops measured under FC condition at different temperatures for 300 nm thick NiO films and expanded view of the *M-H* loops close to origin for the ZFC and FC conditions at 30 K. It is clear from the figure that the *M-H* loops measured under FC condition show a large shift towards negative

axis. This results in a considerable exchange bias as compared to the films measured under ZFC condition.

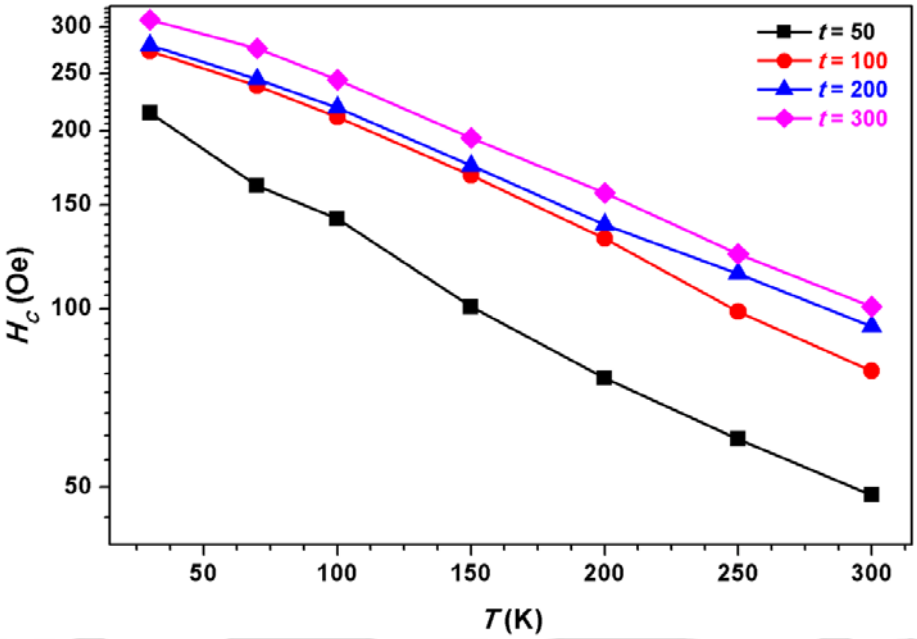

Figure 5.13: The variations of H_C with temperature for NiO films with different thicknesses annealed at 500 °C under vacuum condition.

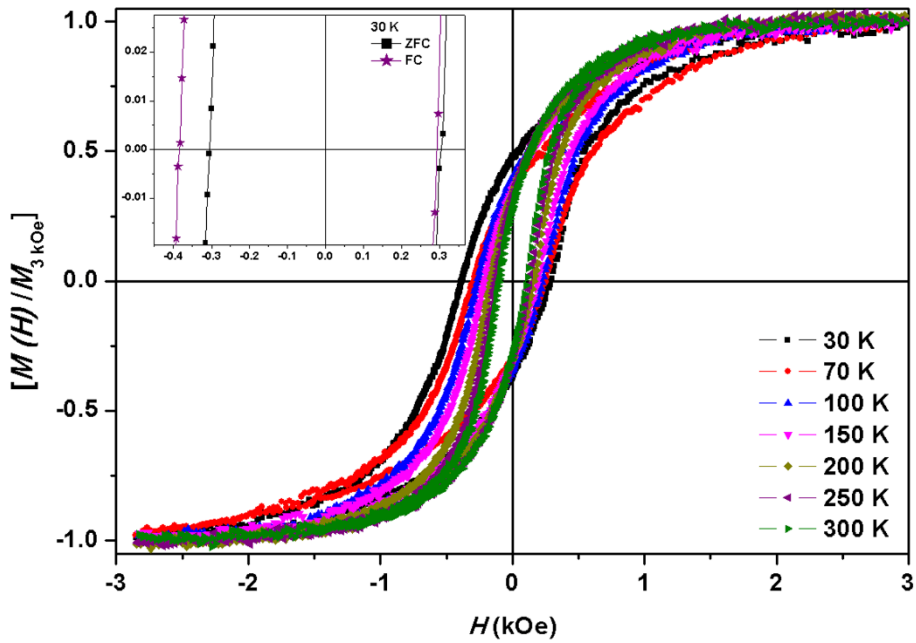

Figure 5.14: *M-H* loops measured at different temperatures under FC condition for 300 nm thick NiO film annealed at 500 °C under vacuum condition. Inset: Expanded view of *M-H* loops close to origin measured at 30 K under ZFC and FC conditions.

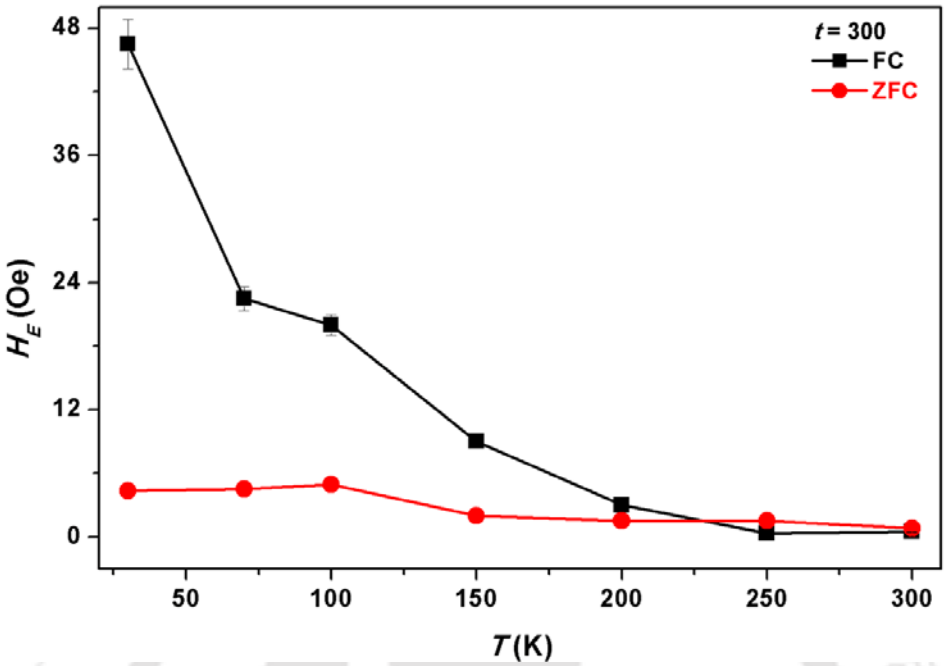

Figure 5.15: The variations of H_E with temperature for 300 nm thick NiO film annealed at 500 °C under vacuum condition.

Figure 5.15 depicts the calculated values of exchange bias, H_E (=($|H_{C-}|-|H_{C+}|$)/2) under ZFC and FC conditions as a function of temperature for 300 nm thick NiO film annealed at 500 °C under vacuum condition. It is clearly evident from the figure that H_E in ZFC films is almost zero down to 150 K and then increases weakly at low temperatures. On the other hand, the FC films exhibit significantly large H_E at low temperature. Rinaldi-Montes et al [RINA2014] reported that the size effects in NiO induce surface spin frustration which competes with the expected AFM order and giving rise to a threshold size for the AFM phase to nucleate. While the larger NiO particles form uncompensated AFM core with a net magnetic moment surrounded by a spin-glass shell resulting in exchange bias effect, the NiO nanoparticle of size less than 3 nm seems to be in a spin-glass state. Kisan et al [KISA2015] reported that the NiO nanoparticles with different particle sizes prepared by sol-gel process showed large variation in exchange bias under FC condition due to the existence of spin-glass phase, which induce additional anisotropy between surface spins and compensated core spins. On the other hand, Valladares et al [VALL2014] reported that the magnitude of exchange bias field in annealed NiO thin films strongly depends on the relative fraction of Ni and NiO phases providing more prominent interfaces between Ni and NiO crystals. Therefore, the exchange bias in the presently investigated system is mainly due to

the enhanced anisotropy caused by the improved interaction between Ni and NiO crystallites having sharp and small mixed interface areas [VALL2014, KISA2015]. The disappearance of H_E above 200 K reflects the existence of thermal dependence of anisotropy in these films.

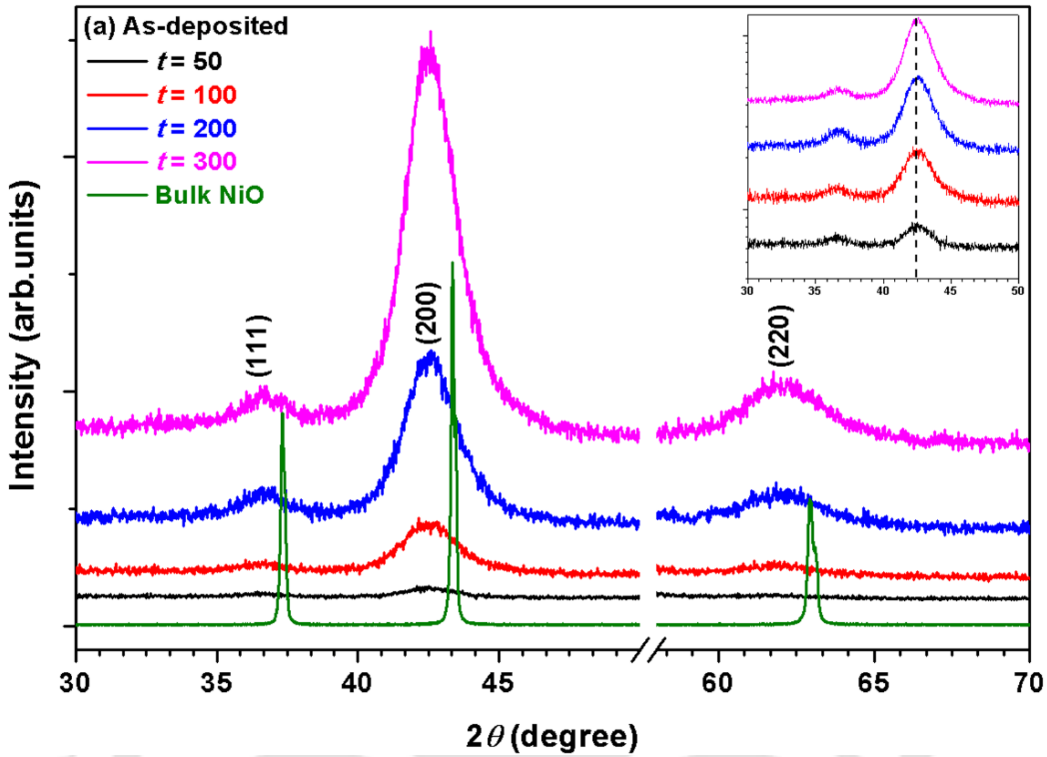

Figure 5.16: Room temperature XRD patterns of as-deposited NiO thin films with different thicknesses. XRD pattern of bulk NiO with scaled intensity is also shown for comparison. Inset: Expanded view of the XRD patterns for NiO thin films.

5.3.2. Properties of NiO films prepared from target of 600 rpm NiO powder

5.3.2.1. Structural properties

To study the effect of milling speed and initial crystal size of the NiO target prepared from the ball milled NiO powders on the properties of sputtered NiO thin films, we have executed similar procedures on making the NiO target using the NiO powders prepared at 600 rpm and fabricated NiO thin films with different thicknesses in the range between 50 and 300 nm using magnetron sputtering technique under the similar conditions. Subsequently, the as-deposited films are annealed at different heat treatment temperatures (T_A): 300 °C, 400 °C and 500 °C for 70 minutes duration and characterized to understand the thermal decomposition properties of the NiO films.

Figure 5.16 displays the room temperature XRD patterns of the NiO thin films with different thicknesses. In order to compare the XRD patterns of the thin films with the bulk

counterpart, XRD pattern of the bulk NiO powder with scaled intensity is also included. It is clear from the figure that both bulk NiO and NiO thin films exhibit Bragg reflections corresponding to *fcc* structure without any other impurity peaks within the detection limit of X-ray diffractometer. This confirms the formation of high purity NiO thin film. The comparison between the as-deposited films and bulk NiO confirms that (i) the Bragg reflections in NiO thin films are considerably broad in nature and the peak positions are shifted noticeably to lower angles. (ii) The films are highly oriented along (200) plane and the intensity of the (200) peak increases with increasing NiO film thickness. The above results suggest that the as-deposited films have fine crystallites and large lattice constant as compared to the bulk NiO.

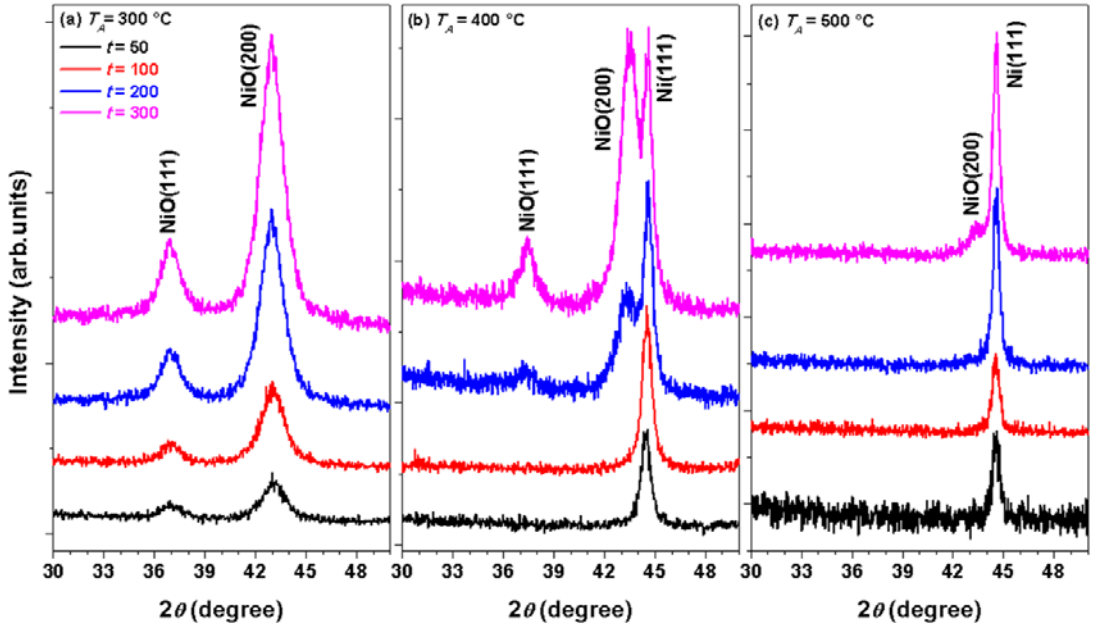

Figure 5.17: Room temperature XRD patterns of NiO thin films with different thicknesses annealed at different temperatures [(a) 300 °C, (b) 400 °C and (c) 500 °C] under vacuum condition.

Figure 5.17 displays the XRD patterns of the NiO films with different thicknesses and annealed at different temperatures under vacuum environment. It is observed from the figure that (i) for the NiO films annealed at 300 °C, the peak broadening decreases gradually along with a considerable shift in the peak position to higher diffraction angles. While the first one confirms the increase in the average crystallite size and reduction of strain in as-deposited films, the latter one suggests the decrease in lattice constant with increasing T_A. (ii) With increasing T_A to 400 °C, the NiO films with $t \leq 100$ nm exhibit no detectable Bragg

reflections related to *fcc* phase of NiO, but display only the reflections corresponding to Ni phase [see Figure 5.04(b)]. This indicates that the NiO films decompose into Ni for $t \leq 100$ nm even at 400 °C. With increasing $t > 100$ nm, the existence of NiO phase along with Ni phase is observed. Interestingly, the relatively intensity of the NiO(200) peak increases with increasing NiO film thickness from 200 nm to 300 nm. This indicates that the amount of decomposition reaction from NiO into Ni decreases with increasing NiO film thickness [JANG2011]. (iii) On further increasing T_A to 500 °C, the NiO films with $t \leq 200$ nm transform completely into Ni. With increasing $t > 200$ nm, the presence of weak NiO(200) peak without the NiO(111) peaks is observed. This indicates the existence of small NiO phase still in 300 nm thick NiO film.

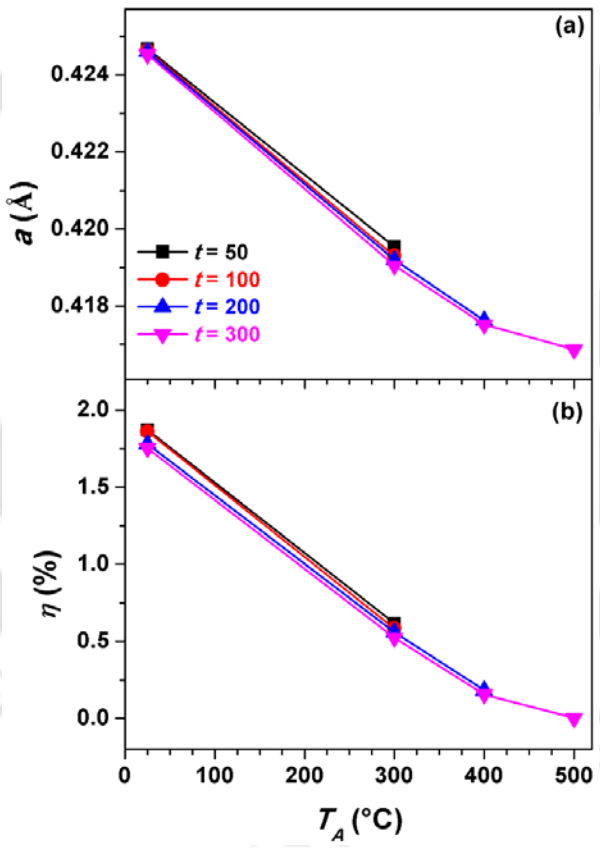

Figure 5.18: The variations of (a) lattice constant (a) and (b) strain (η) as a function of annealing temperature (T_A) for the NiO thin films with different thicknesses.

These results clearly indicate that the thermal decomposition reaction of NiO into Ni under vacuum condition decreases by 100 °C for the NiO films prepared from the NiO target made using 600 rpm milled powders as compared to the films prepared from the NiO target made using 350 rpm milled powders. This evidently supports that the properties of

sputtered NiO thin films strongly depend on the initial crystal size of the powders used for fabricating target materials. Therefore, the systematic tuning of the initial crystal size would be helpful to control the thermal decomposition properties in NiO powders.

To quantify the changes in the structural parameters such as lattice constant (a), crystallite size (D) and strain (η) in the as-deposited films and annealed films, the XRD data are analysed using eqns.(5.01) & (5.03) and the variations of a and η are depicted as a function of T_A in Figure 5.18. As-deposited films exhibit significantly a large lattice constant of about 4.246 Å, but decreases with increasing T_A and approaches to bulk value for the films annealed above 400 °C. As discussed earlier, the observation of large lattice constant in the as-deposited NiO thin films could be attributed to the strain induced in the film possibly due to the existence of interstitial argon atoms in the NiO lattice, which expands the lattice constant when argon pressure is high and/or increase of nickel vacancies created from the non-stoichiometry. Upon heat treatment, the lattice constant decreases gradually and reaches to the bulk value due to the release of interstitial argon atoms from NiO lattice during the post annealing process. Similarly, the strain displays the variations almost similar to those observed for lattice constant with increasing T_A. The average crystallite size of the NiO phase calculated from the (200) peak exhibits weak dependence on the film thickness, but increases from about 6 nm (without taking strain into consideration) to 15 nm with increasing T_A. Similarly, the average crystallite size of the Ni, calculated from (111) peak, increases from about 15 nm to 24 nm with increasing T_A from 400 °C to 500 °C, respectively. These structural changes are expected to play a significant role on the magnetic properties.

5.3.2.2. Magnetic properties

To study the changes in the magnetic properties, we have measured room temperature in-plane *M-H* loops for the as-deposited and annealed films. Figure 5.19 shows room temperature in-plane *M-H* loops for as-deposited NiO thin films with different thicknesses. All the as-deposited films exhibit weak magnetic signals without any clear trace of hysteresis loop. In addition, the noise in the substrate corrected data is mainly due to the small moment from the AFM nature of the as-deposited films [SARM2010] to be detected by the instrument in the presence of large diamagnetic contribution from the substrate. Similarly, the films annealed up to 300 °C don't exhibit any hysteresis loop [see inset (a) of Figure 5.20]. This is mainly due to the existence of only NiO phase in the annealed films up to 300 °C, which is in good agreement with the XRD results.

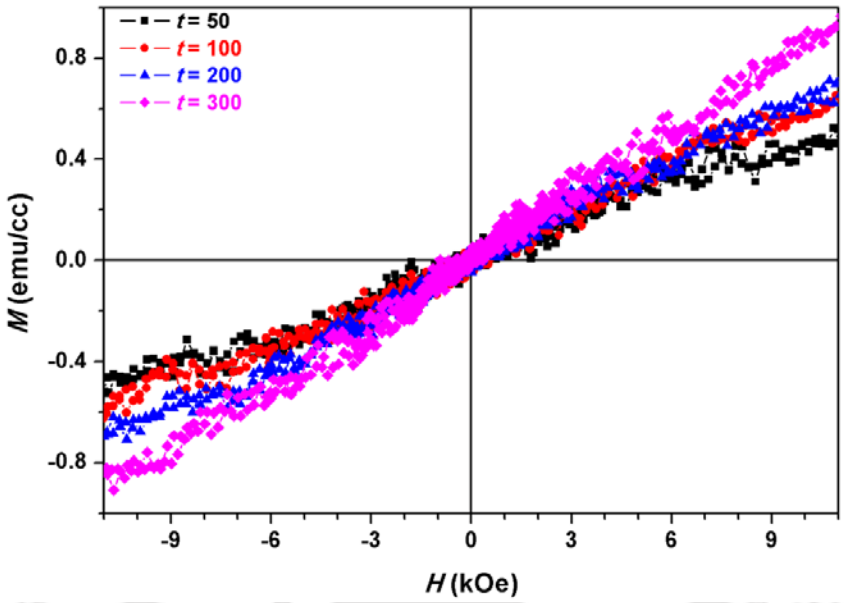

Figure 5.19: Room temperature in-plane *M-H* loops of as-deposited NiO films with different thicknesses.

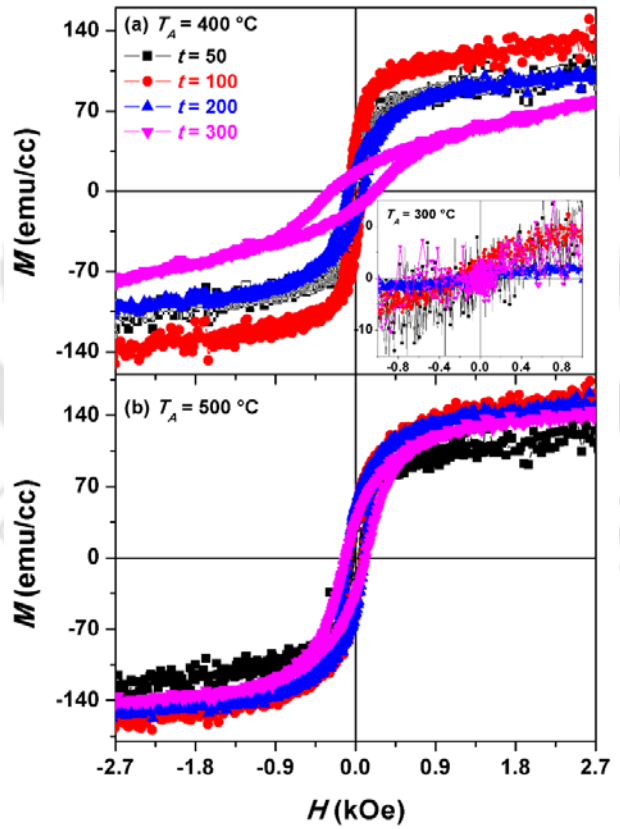

Figure 5.20: Room temperature in-plane *M-H* loops of NiO thin films annealed under vacuum annealing condition at (a) 400 °C and (b) 500 °C. Inset: *M-H* loops of NiO thin films annealed at 300 °C under vacuum annealing condition.

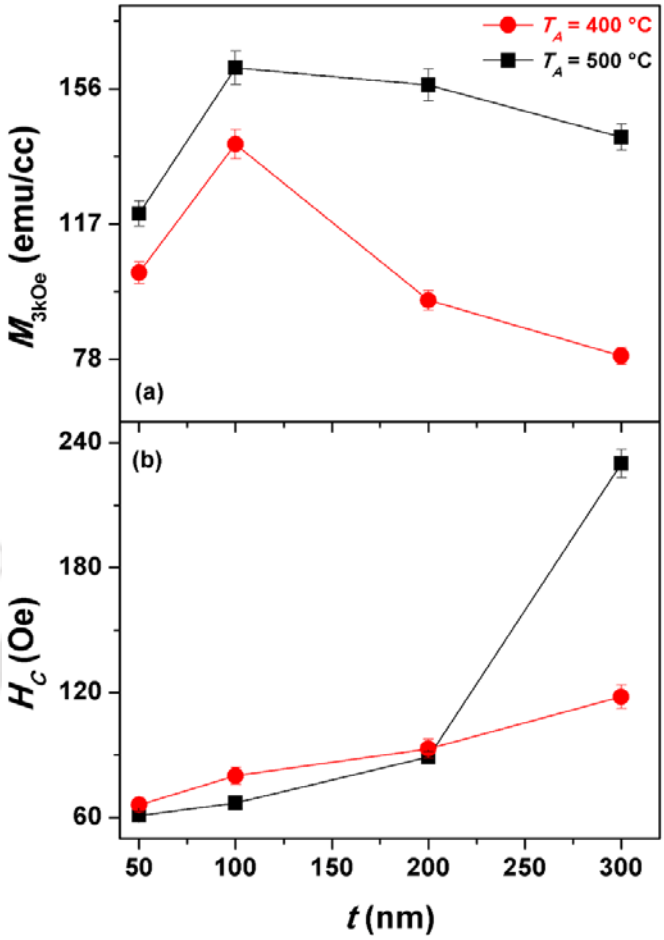

Figure 5.21: The variations of M_{3kOe} and H_C with NiO film thickness annealed at 400 °C and 500 °C under vacuum annealing condition.

On the other hand, all the NiO thin films annealed at 400 °C show FM nature with clear hysteresis loops, as demonstrated in Figure 5.20(a). The loops tend to saturate at moderate applied magnetic fields. However, with increasing *t*, the shape of the *M-H* loop changes and the field required for saturating the films' magnetization increases with increasing film thickness. This is mainly due to the thickness dependent decomposition behaviour of the NiO films annealed at 400 °C under vacuum environment. On further increasing the annealing temperature to 500 °C, all the NiO films exhibit room temperature *M-H* loops with slightly enhanced magnetization. The extracted values of magnetization (M_{3kOe}) and coercivity (H_C) from the *M-H* loops for the NiO films annealed at 400 °C and 500 °C are depicted in Figure 5.21. M_S increases from about 103 emu/cc to 140 emu/cc with increasing *t* from 50 to 100 nm for the NiO film annealed at 400 °C and then decrease to 95 emu/cc and 80 emu/cc on further increasing thickness to 200 and 300 nm, respectively. This

reveals that M_S is strongly depending on the film thickness. The increase in M_S in lower thickness films up to 100 nm thickness can be explained to the complete decomposition of NiO into Ni. However, the decrease in M_S for higher thickness NiO films is mainly due to reduction in the decomposition reaction with increasing NiO film thickness above 100 nm, which results in a reduced amount of Ni in the NiO matrix. Similarly, the NiO films annealed at 500 °C exhibit a significant increase in magnetization with increasing *t* from 50 to 100 nm and then remain almost constant for 200 nm thick NiO film. On further increasing *t* to 300 nm, the magnetization decreases to about 142 emu/cc. This is mainly to due to incomplete decomposition of NiO into Ni at higher thickness films. On the other hand, H_C increases progressively from 61 Oe to 89 Oe with increasing *t* from 50 to 200 nm for the NiO films annealed at 400 °C and then exhibits a large increase up to 230 Oe for 300 nm thick NiO films. While the low value of H_C in smaller thickness is related to soft magnetic nature of Ni, the increase in H_C may be attributed to the strong interaction between Ni and NiO phases, which results in a higher anisotropy and hence enhances H_C. With increasing the annealing temperature to 500 °C, the variation of H_C versus *t* becomes almost linear due to the nearly complete decomposition of the NiO into Ni for the NiO films annealed at 500 °C.

The above results clearly reveal the effect of initial crystallite size of the target powders on the thermal decomposition of the NiO thin films annealed at different temperature under vacuum annealing. With decreasing the average crystallite size of the target powders, (i) the as-deposited NiO films show only *fcc* structure of NiO with AFM nature, but (ii) the annealing temperature required for thermal decomposition of NiO into Ni decreases by about 100 °C. As a result, the magnetic properties of annealed NiO films tunable systematically by optimizing the thickness of NiO films, annealing temperature and initial average crystallite size of the target powders. The observed results also reveal that the NiO films with cubic structure are potential candidates for resistive random access memory and possible spintronic applications.

5.4. Summary

We have studied the effects of initial crystallite size of the target powders, NiO film thickness and annealing temperature under different environments on the decomposition reaction of NiO into Ni and the resulting magnetic properties of the NiO films deposited directly on thermally oxidized Si substrate using magnetron sputtering technique at ambient

temperature. The salient feature of the NiO thin films from the current investigations are as follows:

- All the as-deposited NiO films exhibit *fcc* structure and highly orient along (200) plane. The as-deposited NiO films show large lattice constant due to the existence of interstitial argon atoms in the sputtered films and/or increase of nickel vacancies created from the non-stoichiometry.
- With increasing annealing temperature, the lattice constant and strain decreases due to the release of interstitial argon atoms. The observation of thickness dependent decomposition reaction of NiO into Ni under vacuum annealing could be explained based on the ideal model. However, the decomposition reaction is completely suppressed for the NiO films annealed under oxygen condition.
- The effect of initial crystallite size of the target powders on the thermal decomposition of the sputtered NiO films reveals a considerable decrease in the decomposition temperature (by about 100 °C) for the NiO films.
- All the as-deposited and annealed NiO films up to 400 °C (300 °C) under vacuum condition prepared from the NiO target made using 350 (600) rpm milled NiO powders and 500 °C under oxygen conditions show only AFM nature. On further increasing annealing temperature, NiO decomposes into Ni and exhibits room temperature ferromagnetism.
- The amount of induced ferromagnetism strongly depends on the NiO film thickness.
- A close correlation between the structural and magnetic properties is observed for all the NiO films. The observed results are explained on the basis of thickness dependent thermal decomposition with increasing annealing temperatures under different environments.

Chapter 6

Thickness dependent thermal oxidation in Ni thin films

6.1. Introduction

The artificial engineering of structural and magnetic properties of low dimensional metallic or semiconductor thin films by modulating the surface/interface morphology has attracted significant attention for its great importance in both fundamental research and potential applications [GAOJ2008, LIUH2015, RAVI2016]. Among various fundamental ferromagnetic (FM) materials, nickel (Ni) thin films have received notable interest in recent years, because of its rich physical properties and potential application in various fields such as recording media, spin-valve, semiconductor technology, sensors, resistive switching, etc [HELI2011, SAMA2012, LIUH2015, OLIV2016, XIAN2016]. Ni is a FM transition metal (TM) with a Curie temperature (T_C) of 625 K and magnetic moment of 0.6 μ_B per atom [FERT1991]. Its magnetization derives from the spin polarization of the 3*d* electrons, which are very sensitive to the local environment. For instance, Tamura et al [TAMU1969] reported that T_C and spontaneous magnetization of the crystalline Ni thin films can be reduced by preparing amorphous form of Ni. Snigirev et al [SNIG1997] reported a one-domain structure with in-plane magnetization of the magnetic moment in Ni thin films with thickness exceeding 2.6 nm. However, a drastic decrease of the magnetization of Ni film was reported when the film thickness is less than 2.6 nm. Liu et al [LIUH2015] studied surface morphology induced changes of magnetic anisotropy, magnetization reversal and symmetry of the anisotropic magnetoresistance (AMR) in ion sputtered Ni thin films grown on MgO single crystal substrates. They demonstrated that in contrast to bulk Ni, the symmetry of AMR and magnetic properties of Ni thin films are very sensitive to the surface morphology of the thin films. Recently, Yoo et al [YOOT2017] reported the magnetic properties of Ni films deposited on molecular beam epitaxy (MBE) grown Bi_2Se_3 topological insulator and on GaAs. They reported that coercivity (H_C) of the Ni film strongly depends on the surface it was grown and revealed the investigation of spin dependent phenomena in magnetic systems involving a FM and topological insulator interface.

On the other hand, the realization of materials that combine semiconducting behaviour with robust magnetism for the application of spintronics has long been a dream of material physics. Particularly, in the area of semiconductor spintronics, one of the precondition is the use of FM semiconductors with large Curie temperature (T_C) above room temperature [JUND2006]. With this connection, thin films of NiO with FM are attractive for applications as antiferromagnetic (AFM) layers in spin-valve heterostructures [SHAN2016], gas sensors [WANG2015], *p*-type transparent conducting electrodes

[CHAN2002], thermoelectric devices [LIUY2017] and in electrochromic display devices [CAIG2016]. Furthermore, the development of NiO based nanoparticles and thin films has been focused to obtain FM above room temperature such that these oxides with cubic structure could facilitate integration of spintronic devices where both charge and spin are used to transport, store, and process information in novel ways [DORM1997, FIOR2005, RAVI2015].

In order to obtain NiO thin films, the direct deposition of NiO thin films onto substrate have been extensively carried out by magnetron sputtering [WRUC1991], thermal evaporation [VALL2014], electro-deposition [TORR1991], chemical vapour deposition [FUJI1993], reactive chemical ion beam deposition [LIER2002] and sol-gel deposition [WANG1993]. A careful review reveals that the control of amount of oxidation in these techniques is significantly difficult. On the other hand, thermal oxidation of as-deposited Ni films *ex situ* seems to provide easy way of obtaining metal-oxide film [VALL2014]. During the thermal oxidation process [ROYA2004, WANG2015], Ni oxidizes to chemically stable NiO which has a cubic NaCl-type structure and behaves antiferromagnetically below the Néel temperature (T_N) of 523 K [ADLE1970]. As a result of oxidation, every oxygen atom destroys FM of one Ni atom due to the formation of strong super-exchange interaction of Ni^{2+}-O^{2-}-Ni^{2+} [KAIH1993]. Such oxidation process is very much suitable in resistive switching characteristics of NiO based Resistive Random Access Memory (ReRAM) devices [GOUX2010]. It may be noted that there are only a few reports on oxidation evolution of Ni thin films at higher temperatures (> 900 °C). Recently Valladares et al [VALL2014] studied thermal oxidation of 50 nm thick Ni thin films fabricated by conventional thermal evaporation process and post annealed in air at different temperature between 300 °C and 700 °C. However, the systematic investigations of thermal decomposition of NiO thin films in Chapter 05 reveal that the decomposition behaviour of NiO strongly depends on the NiO film thickness and annealing temperatures. Hence, it is also expected that the oxidation behaviour of Ni thin films may depend on the thickness of the Ni film and annealing temperature. But, there is no report on the oxidation process of Ni thin films as a function of thickness, the nature of oxidation mechanism and its effects on the vibrational, magnetic and electrical transport properties.

Thus, to understand the thermal oxidation of Ni thin films in more details, in this chapter, (i) Ni thin films with different thicknesses in the range of 10 to 300 nm are fabricated using magnetron sputtering technique at ambient temperature directly on

thermally oxidized Si substrate and post annealed at different temperatures (T_A) under air atmosphere, (ii) characterized using X-ray diffraction, X-ray reflectivity, Raman spectroscopy, vibration sample magnetometer, physical property measurement system and (iii) investigated the effect of thickness dependent phase formation, nature of oxidation mechanism and the effect of thermal oxidation on vibrational, magnetic and electrical transport properties. The observed results demonstrate that the magnetic and electrical properties of Ni thin films depends strongly on the thickness dependent crystallization of the oxide phase formed.

6.2. Experimental details

Ni (t nm) single layer thin films with various thicknesses (t = 10, 30, 50, 100, 200 and 300 nm) are deposited directly on thermally oxidized Si substrate by sputtering commercial Ni target (50.8 mm diameter and 1.2 mm thickness) using magnetron sputtering technique with various process parameters. The substrates (0.5mm thick) are cut into 2×2 cm^2 pieces, cleaned with acetone, isopropyl alcohol and ultrasound bathed for 15 min. Before starting the deposition, the base pressure of the chamber is evacuated below 1×10^{-4} Pa and the sputtering of Ni is carried out at ambient temperature in an argon (Ar) atmosphere of 10 mTorr. The optimization of Ar gas pressure is done mainly by analysing the formation of FM Ni thin films. The deposition rate of Ni films is pre-calibrated using *ex situ* surface profilometer (Vecco, Dektak 150 model). During the deposition, the substrates are maintained at room temperature in order to characterize only the post thermal annealing induced oxide formation. All the as-deposited films are post annealed *ex situ* in air atmosphere at different T_A: 250 °C, 400 °C and 500 °C for 30 minutes duration. The annealing temperature and annealing time are optimized based on the thermal oxidation behavior of Ni thin films.

The phase formation and crystal structure of as-deposited and annealed Ni thin films are analyzed through X-ray diffraction (XRD) patterns obtained using high-power (18 kW) X-Ray diffractometer (Rigaku TTRAX III, Japan) with Cu-K_α radiation (λ = 1.54056 Å). XRD data are collected at a slow scan rate of 0.005 °/s for analyzing the structural parameters as a function of t and T_A. The changes in the surface morphology of the as-deposited and oxidized films are observed using field emission scanning electron microscope (FE-SEM) and overall composition of the pure un-milled and milled powders is determined using energy dispersive spectroscopy (EDS, Oxford) attached to SEM unit.

Raman spectra are obtained using micro-Raman spectroscopy (LabRam HR800, Jobin Yvon) using excitation wavelength of 614 nm at room temperature. Magnetic properties of the as-deposited and annealed Ni thin films are characterized using vibrating sample magnetometer (VSM, Lake Shore Model 7410) by performing (i) magnetic hysteresis loops (*M-H*) along the film plane at different constant temperatures in the temperature range between 30 K and 300 K and (ii) thermomagnetization (*M-T*) measurements at high temperatures in the temperature range of 300 K to 1000 K. Room temperature electrical resistivity behavior of the as-deposited and annealed Ni films is characterized using physical property measurement system (PPMS, Quantum Design, USA).

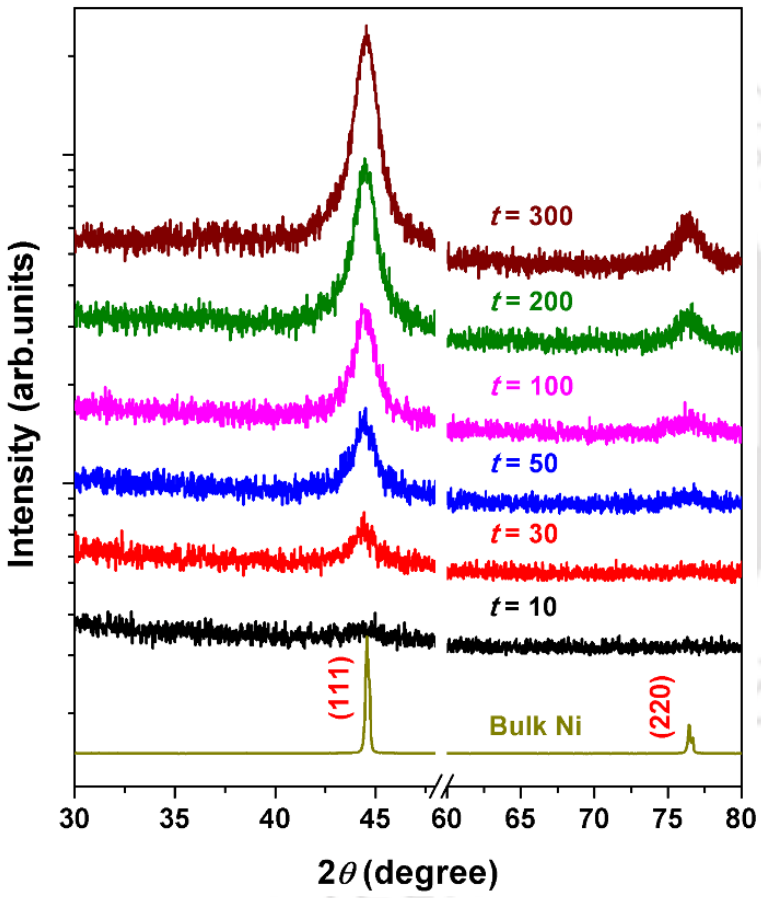

Figure 6.01: Room temperature XRD patterns of as-deposited Ni thin films with different thicknesses. XRD pattern for bulk Ni with scaled intensity is also shown for comparison.

6.3. Results and discussion

6.3.1. Structural properties

Figure 6.01 depicts the room temperature XRD patterns of the as-deposited Ni (t = 10 - 300 nm) thin films with different thicknesses. To compare with bulk Ni, XRD pattern of bulk

Ni with scaled intensity is also shown for comparison. The XRD patterns reveal the following features: (i) all the as-deposited Ni films with different thicknesses show face centered cubic (*fcc*) structure with three main diffractions peaks at (2θ) ~ 44.6°, 52.1° (not shown due to overlapping peak from substrate) and 76.4° corresponding to the (111), (200) and (220) Miller indices of Ni (PDF #870712, cubic structure $Fm\bar{3}m$). This is in good agreement with the bulk Ni. (ii) The absence of any other impurity phases within the detection limit of X-ray diffractometer confirms the formation of high purity Ni thin films. (iii) Despite Ni being oxidized in contact with air, no peaks corresponding to oxide phase are detected. (iv) A close observation of XRD peaks confirms that the peak position of Ni(111) shifts to higher diffraction angle with increasing *t*.

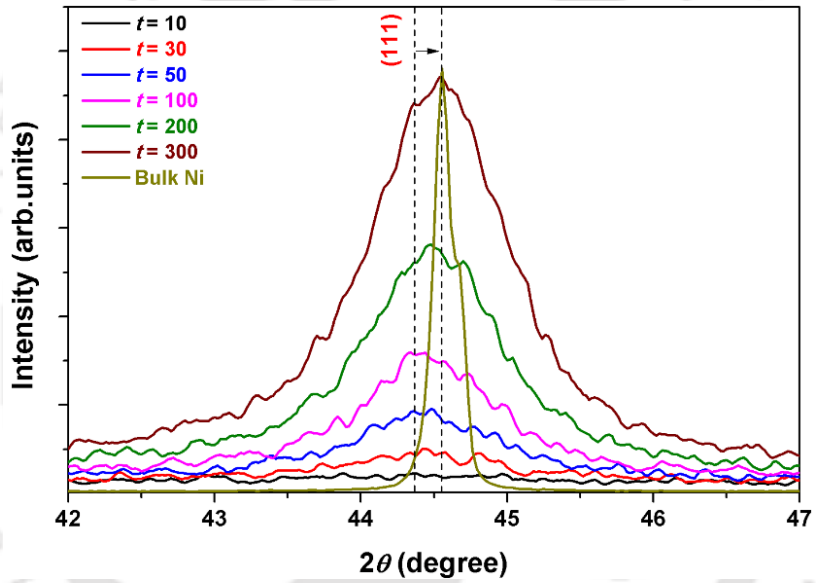

Figure 6.02: Expanded view of Ni(111) peak for different thicknesses.

Figure 6.02 displays the expanded view of Ni(111) peak for the as-deposited Ni thin films with different thicknesses and bulk Ni. It is clearly evident that as the film thickness increases the peak position is shifted towards higher angle and approaches to the peak position of bulk Ni. This confirms that lattice parameter of the Ni thin films changes with *t*, which could be attributed to the strain induced in the film due to the faster deposition. In addition, the films show larger broadening of the XRD peaks as compared to bulk Ni. This suggests that the films have fine Ni crystallites and large lattice constant as compared to the bulk Ni.

To study the effect of thermal oxidation process in as-deposited Ni thin films systematically, all the as-deposited films are post annealed at different T_A under air

atmosphere. Figure 6.03 shows the room temperature XRD patterns of the annealed Ni films with different thicknesses. The XRD patterns reveal the following features: (i) With increasing T_A to 250 °C, (a) Ni films with $t < 50$ show the peaks corresponding to Ni without any trace of NiO peaks within the detection limit of X-ray diffractometer. (b) On further increasing t (≥ 50 nm), the Ni(111) peak exhibits a clear asymmetric feature along with the formation of additional peak at $2\theta \sim 37.3°$. Both the asymmetric nature and intensity of the peak at 37.3° increase with increasing t.

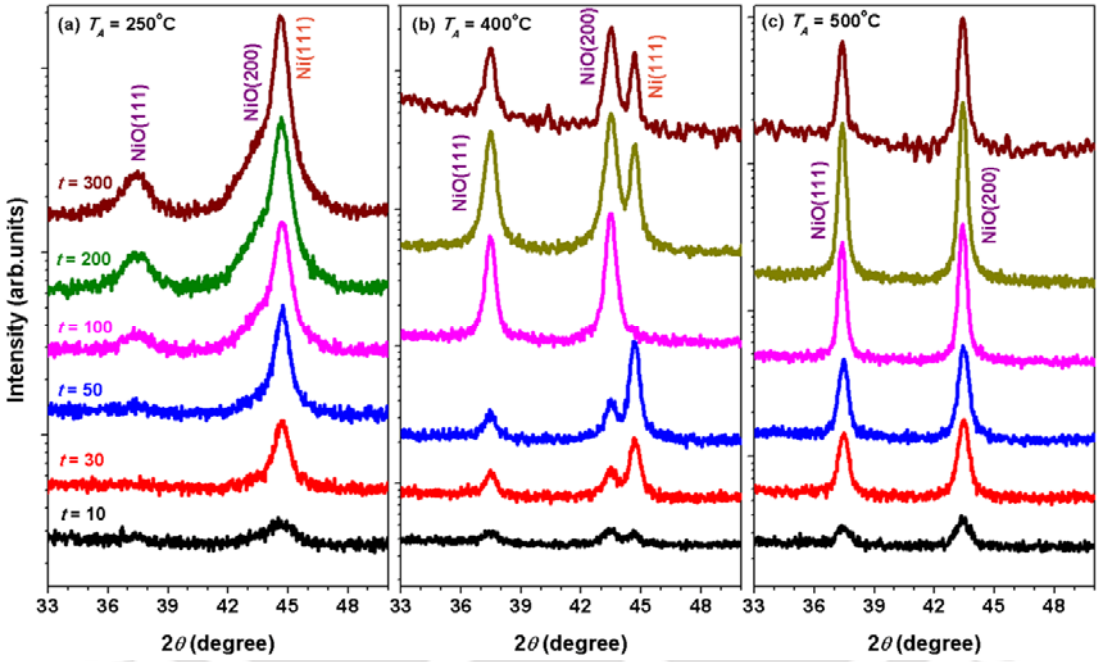

Figure 6.03: XRD patterns of Ni thin films with different thicknesses and annealed at different T_A: (a) 250 °C, (b) 400 °C and (c) 500 °C.

While the development of asymmetric nature of Ni(111) peak is mainly attributable to the formation of NiO(200) peak at $2\theta \sim 43.3°$, the peak at $2\theta \sim 37.3°$ corresponds to NiO(111) peak (PDF #780643, cubic structure $Fm\bar{3}m$). (c) Furthermore, the broadening of Ni(111) peak in the annealed films decreases progressively with increasing t. This suggests that that the annealing process not only improves crystallization in as-deposited films, but also promotes some bonding of Ni-O due to thermal oxidation in higher thickness films. (ii) On further increasing T_A to 400 °C [see Figure 6.03(b)], (a) the existence of both Ni and NiO phases is observed in all the films except for 100 nm thick Ni films, which is completely oxidized. (b) The relative intensity of Ni(111) and NiO(200) peaks completely depends on the film thickness, i.e., the intensity of Ni(111) peak is dominant over NiO(200) peak for t

< 100 nm, while the intensity of NiO(200) dominates over Ni(111) with increasing t > 100 nm. This clearly suggests that the oxidation of Ni into NiO strongly depends on t. (c) Nevertheless, 100 nm thick Ni film annealed at 400 °C shows merely NiO phase without any Ni phase. This is observed to be quite unusual as compared to other film thickness. (iii) Upon increasing T_A to 500 °C [see Figure 6.03(c)], a complete oxidation process is obtained for all the films without the trace of any Ni phase within the detection limit of X-ray diffractometer. Furthermore, the broadening of the NiO peaks decreases significantly with increasing t, indicating the promotion of NiO crystals with increasing t.

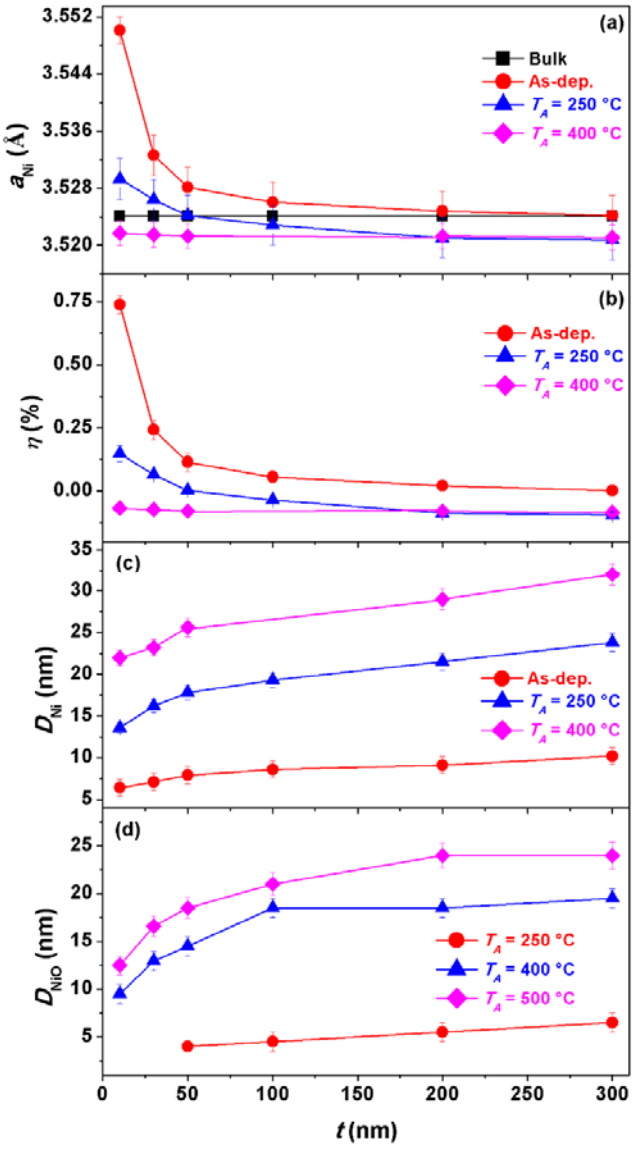

Figure 6.04: The variation of (a) lattice constant, a_{Ni}, (b) strain, η, (c) average crystal size of Ni (D_{Ni}) and (d) average crystal size of NiO (D_{NiO}) with film thickness, t for the as-deposited Ni films and annealed Ni films at different T_A.

In order to study the variation in the structural parameters such as lattice constant of Ni (a_{Ni}), strain (η), average crystal size of Ni (D_{Ni}) and NiO (D_{NiO}) with increasing T_A and oxidation process, we determined the values of a_{Ni}, η, D_{Ni} and D_{NiO} from XRD patterns using the following formulae:

$$a_{Ni} = \left(\frac{\lambda\sqrt{h^2 + k^2 + l^2}}{2\sin\theta} \right) \tag{6.01}$$

$$\eta(\%) = \left(\frac{a_{film} - a_{bulk}}{a_{bulk}} \right) \times 100 \tag{6.02}$$

$$D = \left(\frac{0.94\lambda}{\beta\cos\theta} \right) \tag{6.03}$$

where λ is the wavelength of the X-ray (λ = 1.54056 Å), *h,k,l* are the Miller indices, a_{bulk} is unstrained lattice constant measured for bulk Ni (taken as 3.524 Å), a_{film} is the lattice constant of the Ni thin film determined from XRD pattern and *D* is the average crystal size. Figure 6.04 depicts the variations of a_{Ni}, η, D_{Ni} and D_{NiO} as a function of Ni film thickness for as-deposited and annealed films at different T_A. It is clear from the figure that as-deposited Ni films at lower thickness exhibit larger values of a_{Ni}. This might be correlated to the strain induced in the film by the substrate during the deposition process. A similar kind of variation is observed for NiO thin films as reported in Chapter 05. With increasing *t*, a_{Ni} decreases and approaches to the bulk Ni value for t > 200 nm. Upon increasing T_A to 250 °C, a_{Ni} decreases largely as compared to the as-deposited films and decreases progressively for films with t < 50 nm and approaches to the bulk Ni value, i.e., a trend similar to the one observed for as-deposited Ni films. On further increasing t > 50 nm, the lattice constant decreases further and crosses over to the bulk Ni. This could be attributed to the strain due to the Ni and NiO lattice-constant mismatch arising at the interface and possibly competing exchange interaction between the FM Ni and AFM NiO caused by the development of NiO phase during thermal oxidation. Similarly, the films annealed at 400 °C also exhibit smaller lattice constant as compared to bulk Ni due to the oxidation of Ni into NiO. The strain calculated using the eqn.(6.02) and depicted in Figure 6.04(b) also exhibits the same trend, as strain is calculated from the lattice constant of the films. D_{Ni} and D_{NiO} are calculated from XRD patterns carefully by curve fitting method with different peaks combination. D_{Ni} calculated using eqn.(6.03) is found to be about 6.5 nm for 10 nm thick as-deposited Ni films, but increases not only with increasing *t*, but also with increasing

T_A. This clearly supports that the thermal oxidation process not only promotes the formation of Ni-O phase, but also improves the crystallization due to the growth of the Ni crystallites. The thickness dependent growth of the Ni crystals might possibly be due to less strain from the substrate on the thicker films. The maximum size of the Ni crystal is found to be about 32 nm for the 300 nm thick film annealed at 400 °C. Similarly, D_{NiO} is also calculated using eqn.(6.03) and depicted in Figure 6.04(d). For the films annealed at 250 °C, D_{NiO} is found to be about 4.5 nm for 50 nm thick Ni film and increases up to 7 nm with increase t to 300 nm. Upon increasing T_A to 400 °C and 500 °C, the average size of NiO crystals increases to 19 nm and 24 nm, respectively for the 300 nm thick annealed Ni film. The growth of the NiO is also found to be depending on t, which could be attributed to the enhanced oxidation process at higher film thickness.

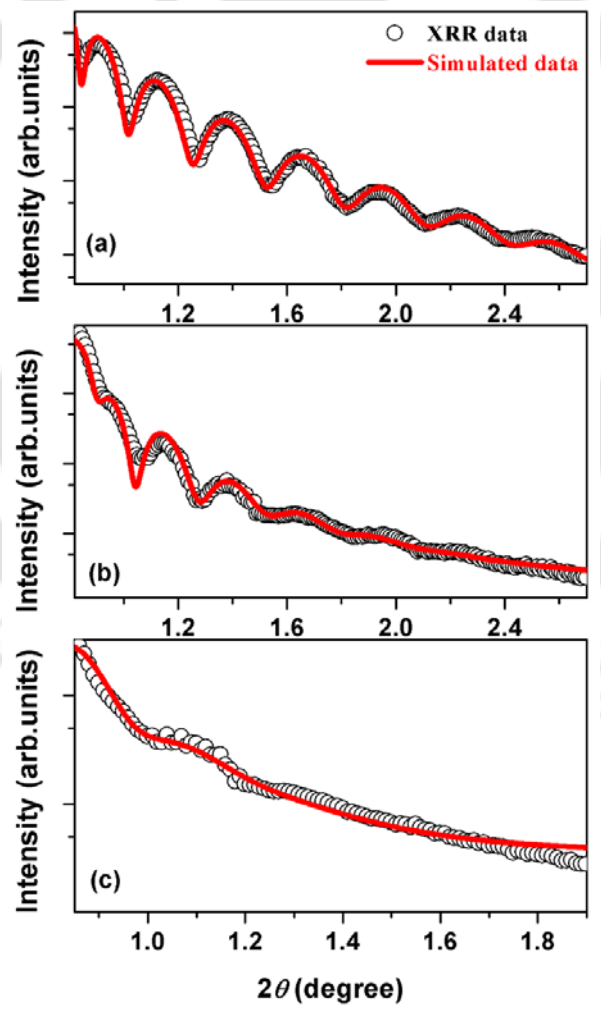

Figure 6.05: X-ray reflectivity curves for 30 nm thick (a) as-deposited, (b) annealed at 400 °C and (c) 500 °C Ni thin films. The solid lines passing through the data is best fit using Globalfit software for the layered sample model.

6.3.2. Thermal oxidation process

It is well known that the oxidation kinetics in metal thin films depends on various factors such as oxygen pressure, T_A, annealing time, annealing environment, etc. Furthermore, Pinnel et al [PINN1979] reported that the oxidation of Ni starts as slow and natural process immediately after the fabrication due to the exposure of Ni to air. The growth rate of oxidation evaluated using Auger electron spectroscopy and contact resistance measurements confirmed that the oxide thickness is limited to a maximum of 10 Å and essentially temperature independent for temperatures below 100 °C. Hence, the understanding of thermal oxidation process in thin films is quite essential to extend these materials in suitable applications such as ReRAM. To understand the oxidation mechanism, we have chosen lower thickness as-deposited and annealed Ni films for the investigation of X-ray reflectivity (XRR). This is mainly due to the fact that with increasing t and T_A, the adhesion of the films to the substrate becomes poorer and the film starts to exfoliate. XRR is one of the techniques widely used to evaluate various layer parameters such as film thickness, film density, surface/interface roughness, etc.

For the presently investigated films, the XRR curves are recorded at first for the as-deposited Ni films and the films annealed at different T_A. Figure 6.05 shows typical XRR curves of 30 nm thick as-deposited Ni films (a) and the films annealed at 400 °C (b) and 500 °C (c). The interference pattern (open circles) with clear oscillation peaks is observed for the 30 nm thick as-deposited film. The oscillation intensity becomes smaller and attains the same level as the noise in the higher angle region. This is possibly due to the roughness of the films along with the limitations of the instrument. With increasing T_A to 400 °C, the film shows altered XRR curve with reduced oscillation intensity and oscillation frequency. On further increasing T_A to 500 °C, the XRR curve displays weak oscillation intensity with a few oscillation peaks. To understand the changes in the XRR curves with increasing T_A, fitting of the XRR curves is preceded by a pattern fitting process between the measured and the calculated XRR pattern using the GlobalFit software. During the analysis, a layered sample model is constructed to generate a simulated reflectivity curves. The model consists of four simulated layers: (i) bulk Si(100), (ii) a thin film of SiO_2, (iii) Ni and (iv) NiO layers. The solid lines in Figure 6.05 represents the best fits to the X-ray reflectivity data using this model. The analysis of XRR curves reveals the following information: (i) The thickness of the as-deposited Ni film is determined to be 28.2 nm along with the interface roughness and surface roughness of 0.4 and 0.8 nm, respectively. This is in close agreement with the results

of surface profilometer data of 28.6±0.8 nm. Following the description of Pinnel et al [PINN1979], we tried to include a thin layer of NiO in as-deposited films. However, the inclusion of NiO layer in the fitting of as-deposited XRR curve does not provide proper fit. This confirms that the as-deposited film has only Ni phase without the formation of any NiO. This is in good agreement with the XRD results. (ii) On the other hand, the XRR curve of 400 °C annealed film could be fitted only using layered structure with the lower layer as Ni having thickness of 17 nm along with the interface roughness of 1 nm and upper layer as NiO with thickness of 9.0 nm along with the surface roughness of nearly 2.1 nm. It may be noted that we could not fit the XRR curve with Ni as top layer and NiO as bottom layer. (iii) As like as-deposited film, the film annealed at 500 °C also reveals a single layer structure with thickness of about 24.3 nm with a large surface roughness of about 4 nm. Furthermore, the disappearance of oscillation peaks in the XRR curve, as compared to as-deposited film, indicates that the NiO layer may not be continuous in growth nature. From the fitting results of the XRR curves and from the structural analysis of the XRD patterns, the possible mechanism of oxidation is schematically represented in Figure 6.06.

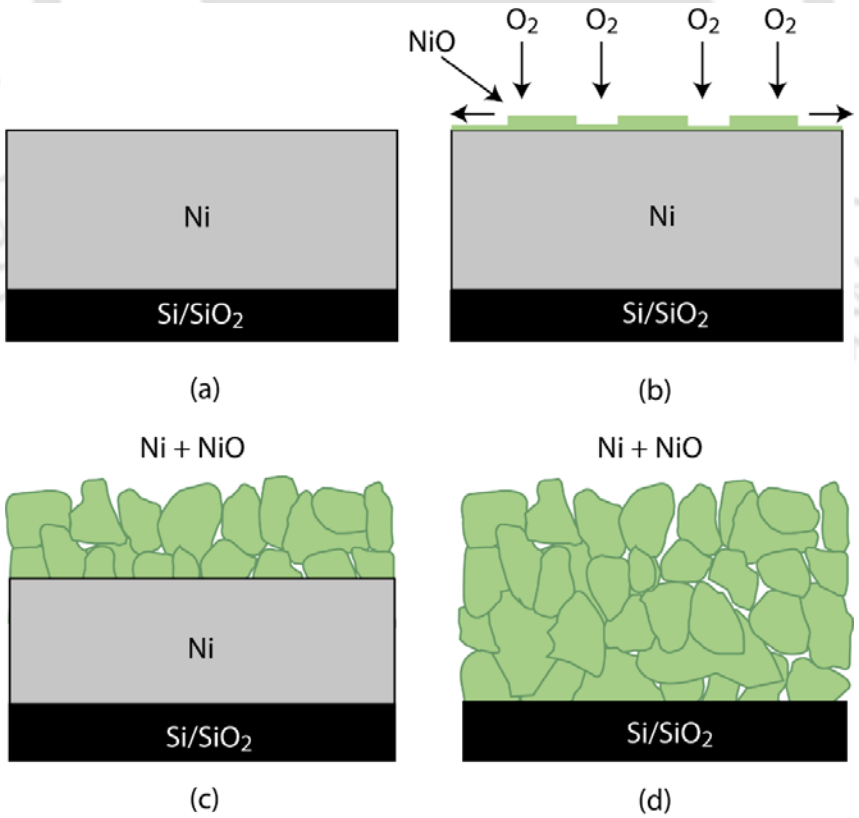

Figure 6.06: Schematic representation of the thermal oxidation process of Ni films at different T_A.

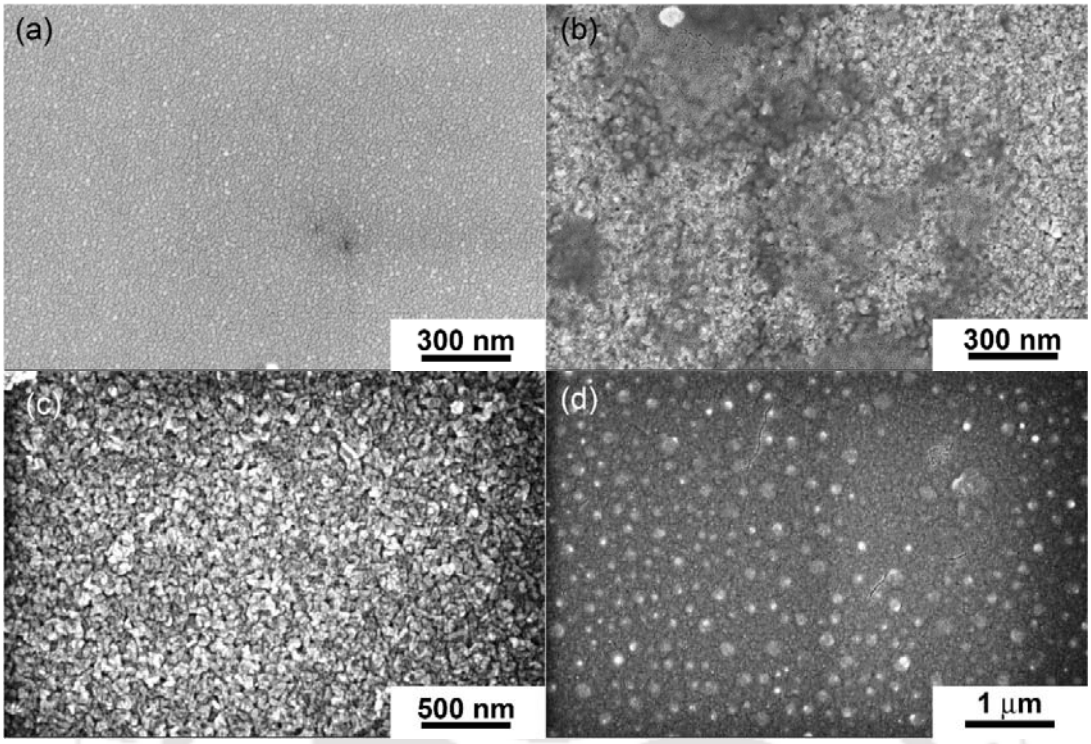

Figure 6.07: FE-SEM images of (a) as-deposited and oxidized Ni films at different T_A: (b) 250 °C, (c) 400 °C and (d) 500 °C.

The as-deposited Ni films exhibit a continuous morphology without any porosity, cracks and thin oxide layer formation [see Figure 6.06(a)]. With increasing T_A to 250 °C, Ni atoms redistribute to preferred site and increases the average crystallite size. In addition, the film interact with air atmosphere, where the oxygen partial pressure is presumed to be constant, to form nucleation sites for NiO on the surface and they extend laterally to form a layer of NiO film, which protect the rest of the Ni film from air [See Figure 6.06(b)]. The increase of T_A to 400 °C accelerates the growth of the NiO film vertically either due to the diffusion of Ni cations into the NiO layer or diffusion of oxygen anions into Ni layer. This would indeed form a layered structure with the lower surface as Ni and upper surface as NiO as evident from the XRR. However, the thicknesses of Ni and NiO layers depend on the thickness of the film and T_A. This is in good agreement with the results of XRD as well. The careful observation of XRD results of NiO phase [see Figures 6.03(b) and (c)] indicates that the intensity of NiO(200) peak is higher than the rest of the NiO peaks, which confirms the randomly oriented NiO grains [HOTO2004, TAOD2004, KISA2014, PADH2017]. This would affect the surface morphology of NiO making it granular with large surface roughness. As a result, the oscillation intensity of the XRR curve decreases largely as

compared to the as-deposited film. On further increasing T_A to 500 °C, the complete oxidation of Ni film consists of randomly oriented NiO grains with a rough top surface (average roughness of 4 nm from XRR analysis) accompanied by porosity and cracks formation [see Figure 6.06(d)]. As a result, the XRR curve show a limited oscillation peaks with reduced intensity.

To further confirm the morphological nature of the as-deposited and oxidized Ni films, FE-SEM images are obtained for all the films and depicted in Figure 6.07. As-deposited Ni(200 nm) thick film shows quite uniform grains on the surface, which is in good agreement with the earlier reports on similar systems [ABDE2016, DRAG2016]. After annealing at 250 °C, we observed two different surface nature corresponding to pure Ni and formation of NiO with rough surface. This could be attributed to the formation of nucleation sites for NiO on the surface, which extend laterally to form a layer of NiO film. With increasing T_A to 400 °C, we observed only a clear rough surface with a considerable increase in size of the particles and pores. This implies that the surface of the Ni film is oxidized into NiO due to annealing under air and protecting the rest of the Ni films from air. This is clearly supported by the coexistence of Ni and NiO phases as evidenced from the XRD analysis and schematic shown in Figures 6.03 and 6.06(c), respectively. On further increasing T_A to 500 °C, the average size of the NiO particles is increased along with the development of cracks and porosity, leaving a rough top surface [MINK2007]. This is mainly due to the reduced adhesion of the film to the substrate upon the formation of NiO with increasing T_A and hence starts exfoliating. This might be related to the large difference between the heat capacities of the Ni film and the thermally oxidized Si substrate [ANDE1992, HAYN2012]. The above results clearly show a close correlation between the XRD, XRR results and morphological observations.

6.3.3. Vibrational properties

Figure 6.08 depicts room temperature Raman spectra of Ni films with different thicknesses annealed at 500 °C. Raman spectra are analysed carefully by curve fitting method with different band combinations to obtain peak intensities, peak width and peak positions. A typical curve fitting is shown in the figure to identify different band combinations. XRD results suggest that Ni films annealed at 500 °C exhibit complete oxidation of Ni and form NiO. Hence, the analysis of Raman spectra is expected to provide details of growth of the NiO particles and associated defects. For all films annealed at 500 °C, Raman bands are

observed from NiO in the spectral range above 350 cm^{-1}. The Raman bands below 1200 cm^{-1} are due to first order and second order Raman scattering by phonons in NiO, while the bands above 1200 cm^{-1} originates from the scattering by two magnon in NiO [ULMA2007, GAND2011, ULMA2011, DUAN2012, GAND2013]. While the bands observed at 380-410 cm^{-1}, 520-550 cm^{-1}, 730-780 cm^{-1}, 900-950 cm^{-1} and 1050-1110 cm^{-1} could be correlated to one-phonon (1P) transverse optical (TO), 1P longitudinal optical (LO), two-phonon (2P) TO, 2P LO+TO and 2P LO of vibrational origin, respectively, the band around 1450-1500 cm^{-1} is due to two-magnon (2M) scattering associated with Ni^{2+}-O^{2-}-Ni^{2+} super-exchange interaction.

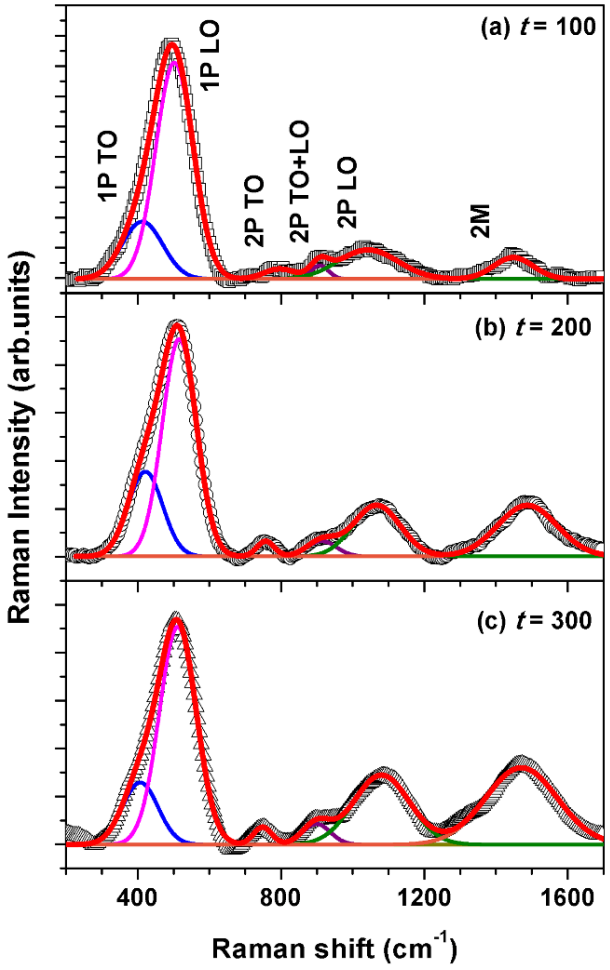

Figure 6.08: Raman spectra of Ni films with different thicknesses annealed at 500 °C.

The presence of 2M band in annealed films supports the existence of AFM state through Ni^{2+}-O^{2-}-Ni^{2+} super-exchange interaction at room temperature. The 2M band in combination with the first-order Raman band can be used to monitor the amount of defects-

induced disorder, since its full-width at half maximum experiences a broadening in presence of disorder or substitutional defects [CAZZ2003, YANG2008, KEEM2010]. The results of curve fitting reveal that the intensity ratio between the 1P LO band and 2P LO band decreases and intensity of 2M band increases with increasing t for the films annealed at particular T_A. This suggests the growth of the NiO grains [DUAN2012] not only increases with increasing T_A, but also with t as evidenced from XRD results.

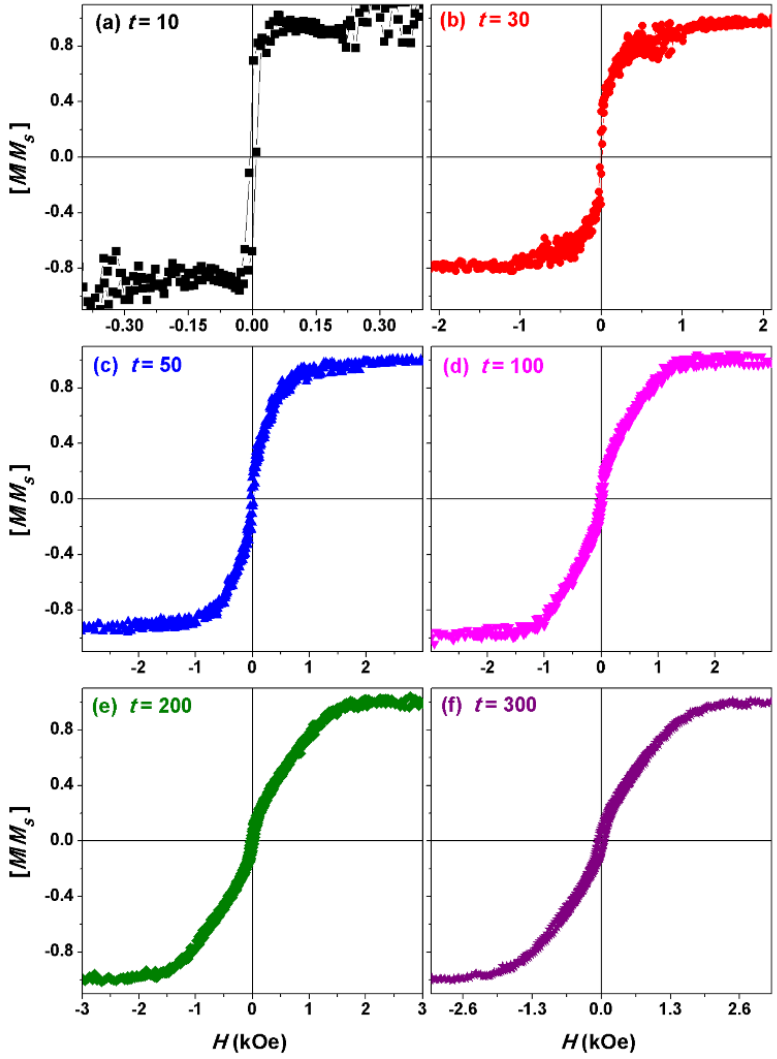

Figure 6.09: Room temperature *M-H* loops measured along the film plane for Ni thin films with different thicknesses (t = 10 – 300 nm).

6.3.4. Magnetic properties

To study the effect of Ni film thickness and oxidation on the magnetic properties of the as-deposited and annealed films, we have carried out *M-H* loops at room temperature and at low temperatures in the temperature range of 30-300 K and *M-T* measurements under

constant applied magnetic field in the temperature range from 300 K to 700 K. Figure 6.09 displays room temperature in-plane *M-H* loops of as-deposited Ni film with different thicknesses measured along the film plane. *M-H* loops reveal the following features: (i) Ni film of 10 nm thick exhibits almost a clear rectangular shaped loop, which saturates at low applied magnetic fields. This can be correlated to the existence of in-plane/uniaxial anisotropy parallel to film plane resulting in domains with magnetization parallel to applied field direction. With increasing *t* to 30, the loop shape changes into round shaped loop. This may be attributed to the change in the magnetic anisotropy from uniaxial to random anisotropy with increasing film thickness. On further increasing $t \geq 50$, the shape of the loops changes from round shape into transcritical type, where the *M-H* loops are constituted by two distinct magnetization reversal process: (a) in-plane magnetic components, which reverse quickly at fields close to coercive field (H_C) and (b) perpendicular components, which rotate progressively under the application of magnetic field and results in almost a linear variation of magnetization before saturation. The linear variation of magnetization increases with increasing *t*.

As a result, the field required for saturation (H_{Sat}) increases largely (> 1 kOe). Such type of loop has been often referred to as a transcritical loop [CAOD2015], which is correlated to decrease in the in-plane magnetic anisotropy [HEMM2015] and increase in effective random magnetic anisotropy of the system, which randomizes the orientation of magnetization. These results clearly show that low thickness Ni film (~ 10 nm) exhibit in-plane uniaxial magnetic anisotropy. Such anisotropy causes the magnetization to be parallel to the film plane. Therefore, this arrangement of in-plane orientation of magnetization provides the shape of the *M-H* loops as rectangular shaped loops when the loops are recorded along the easy-axis. Upon increasing film thickness continuously, the in-plane anisotropy changes into random magnetic anisotropy, which changes the loop shape into round and transcritical types, which require sufficiently large applied magnetic field to saturate the magnetization of the as-deposited films.

Figure 6.10 depicts room temperature *M-H* loops of annealed Ni films at different T_A. In order to see any changes in the loop shape clearly, the normalized magnetization is plotted as a function of field for all the films in Figures 6.10(a) and (b). It is observed that the shape of the loops does not change considerably for the films annealed at 250 °C, as compared to the as-deposited films. However, the magnetization, H_C, and H_{Sat} varies significantly with increasing *t* due to the growth of the Ni crystal and formation of a thin

NiO layer upon annealing at 250 °C. With increasing T_A to 400 °C, the loop shape changes notably for all the films: (i) the loops exhibit large hysteresis for the films with t < 100 nm and (ii) the loop shape changes from transcritical into round shaped loops with enhanced hysteresis behaviour for t > 50 nm. In addition, the loops are slightly shifted to negative axis. On the other hand, 100 nm thick film exhibits almost a linear variation of magnetization with the applied field up to 3 kOe. On further increasing T_A to 500 °C, we observed almost a linear like variation of magnetization with the applied field for all the films with different thicknesses.

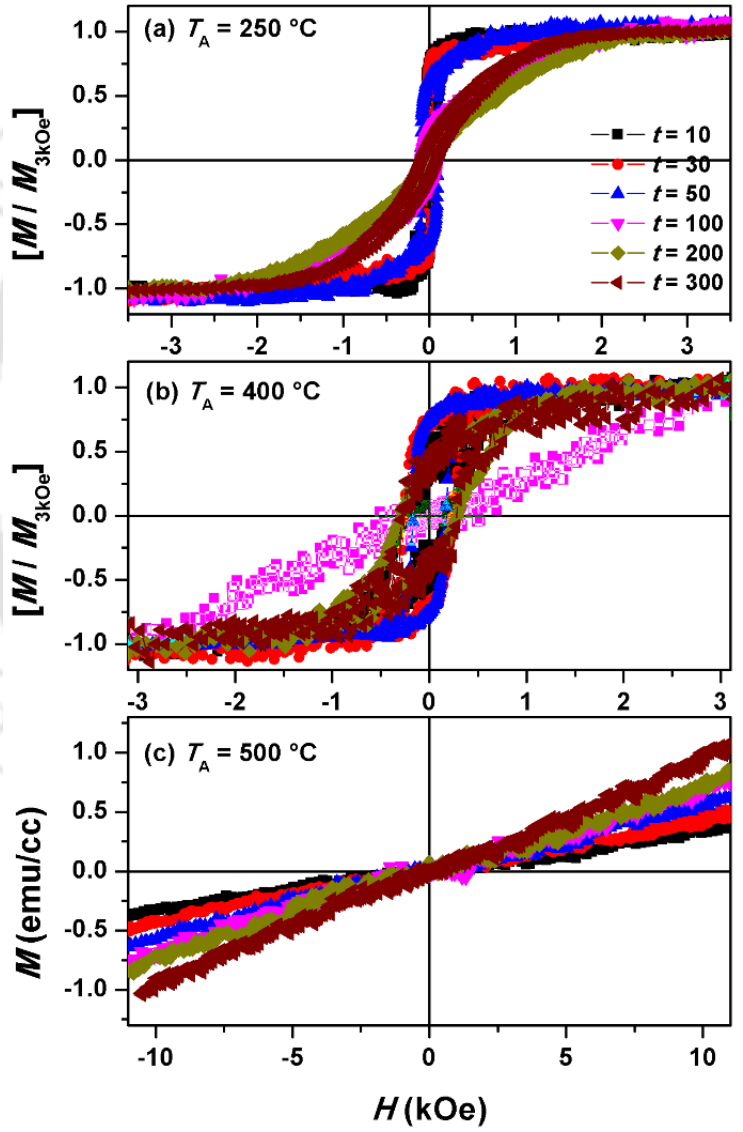

Figure 6.10: Room temperature *M-H* loops measured along the film plane for Ni thin films with different thicknesses (t = 10 – 300 nm) annealed at T_A of (a) 250 °C, (b) 400 °C and (c) 500 °C.

In order to understand the effect of film thickness in as-deposited films and the effect of oxidation on various magnetic parameters, the extracted values of H_C and magnetization at 3 kOe (M_S) from the *M-H* loops are plotted as a function of thickness for as-deposited and annealed films in Figure 6.11. For as-deposited Ni films, H_C increases non-linearly from about 9 Oe to 63 Oe with increasing t from 10 to 300, respectively. H_C observed in the presently investigated films is smaller than the one reported in literature, i.e., Nacereddine et al [NACE2007] reported H_C variation between 30 and 146 Oe for the film thicknesses ranging between 31 and 165 nm deposited on glass substrate. The increase in H_C is mainly associated with nucleation of reverse domains rather than with the pinning of domain walls. Rumpf et al [RUMP2007] also reported H_C values of 90 to 150 Oe for Ni films deposited on Si substrate by chemical vapour deposition.

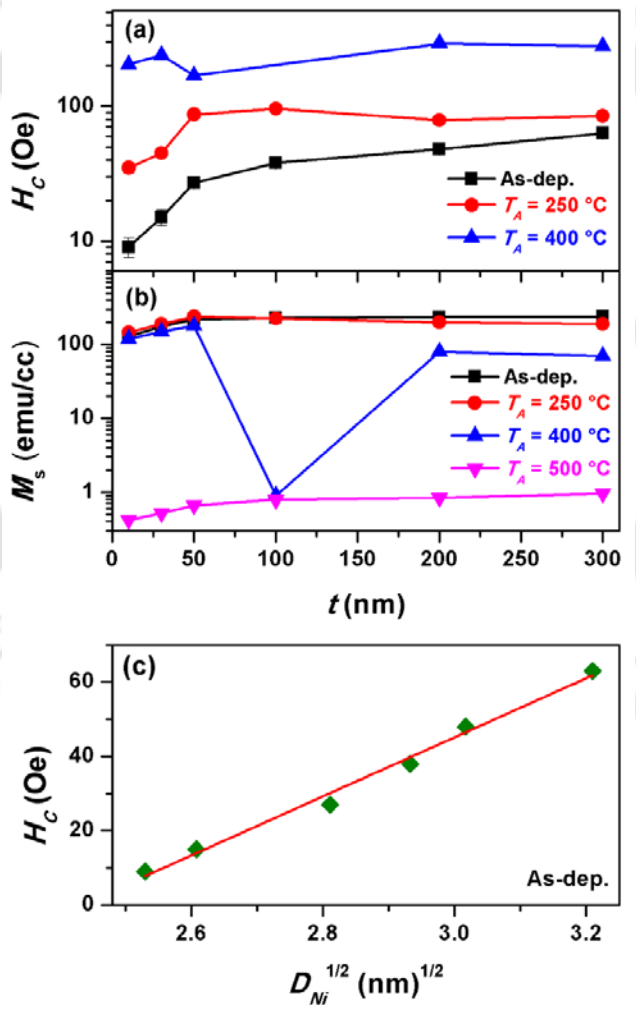

Figure 6.11: The variations of (a) H_C and (b) M_S with thickness for as-deposited and annealed Ni films at different temperatures. (c) The plot of H_C versus $D_{Ni}^{1/2}$ for the as-deposited Ni thin films.

To study any correlation between structural and magnetic parameters in as-deposited Ni films, we plotted the variation of H_C as a function of D_{Ni} in Figure 6.11(c). It is clear from the figure that H_C increases with increasing D_{Ni} and almost follow linear variation for the plot of H_C *vs* $D_{Ni}^{1/2}$, which is predicted by the Hoffmann's theory. According to this theory, H_C is related to D_{Ni} by the relation

$$H_C = \frac{BS\sqrt{2D_{Ni}}}{\pi L M_S}\left(\frac{K_U}{A}\right)^{1/4} \qquad (6.04)$$

where B is filling factor, S is structural factor, L is coupling length, A is exchange constant, K_U is magnetocrystalline anisotropy constant, and M_S is saturation magnetization. This suggests that the properties of the Ni thin films is determined by the structural parameters for the presently investigated films. With increasing T_A up to 400 °C, H_C varies differently and found to be larger than those observed for as-deposited films. This is mainly due to the crystallization of Ni film and partial oxidation of Ni by the thermal annealing process. The partial oxidation provides the coexistence of Ni and NiO and promotes Ni and NiO competing interaction to increase H_C. The films annealed at 500 °C show no H_C due to complete oxidation of Ni into NiO and develops AFM nature of NiO. On the other hand, the magnetization measured at 3 kOe (M_S) for the as-deposited Ni films increases gradually with increasing film thickness and tends to saturate at higher film thickness. The maximum magnetization of about 250 emu/cc is observed. This is considerably low as compared to bulk Ni. This could be correlated to the surface disorder and reduced grain size in thin films [TAMU1969, CHIN1984]. M_S is observed to be increased for the low thickness films annealed at 250 °C, but decreases significantly at higher thicknesses as compared to as-deposited films due to the formation of NiO on the surface of the film. This is in close agreement with the earlier reports that M_S increases during the vacuum annealing process [YIAJ2004]. With increasing T_A to 400 °C, M_S decreases largely at higher t due to increased oxidation of Ni into NiO with increasing t, as supported from XRD results. Interestingly, 100 nm thick Ni film annealed at 400 °C exhibits large reduction in the M_S due to complete oxidation. However, we need more careful studies to understand this unusual behaviour. Furthermore, the films annealed at 500 °C show low M_S due to complete oxidation of Ni into NiO. These results show a good correlation between structural and magnetic properties in as-deposited Ni films and thickness dependent oxidation in annealed Ni films.

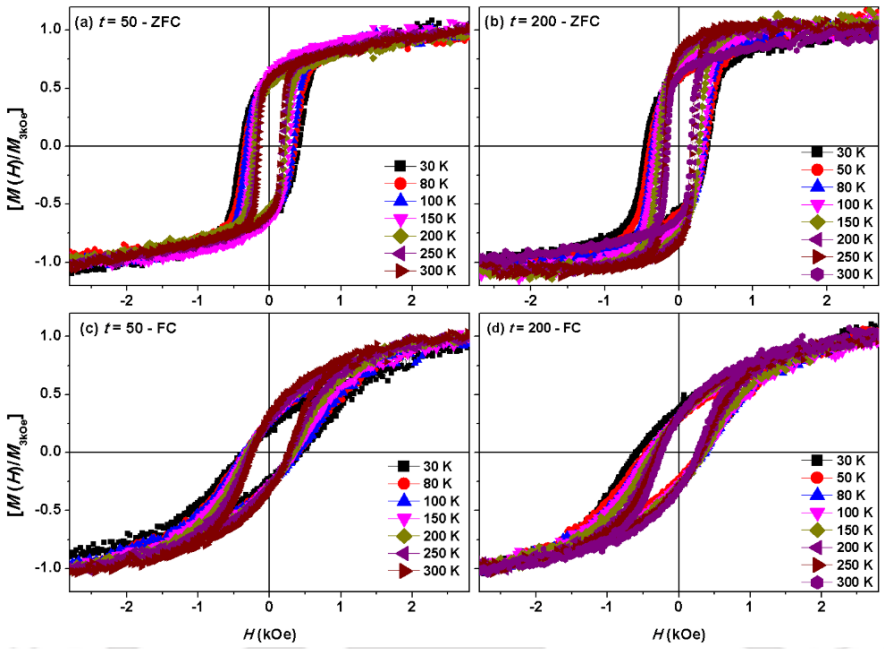

Figure 6.12: *M-H* loops measured along the film plane at different temperatures under ZFC and FC conditions for Ni thin films with different thicknesses (t = 50 nm, 200 nm) annealed at 400 °C.

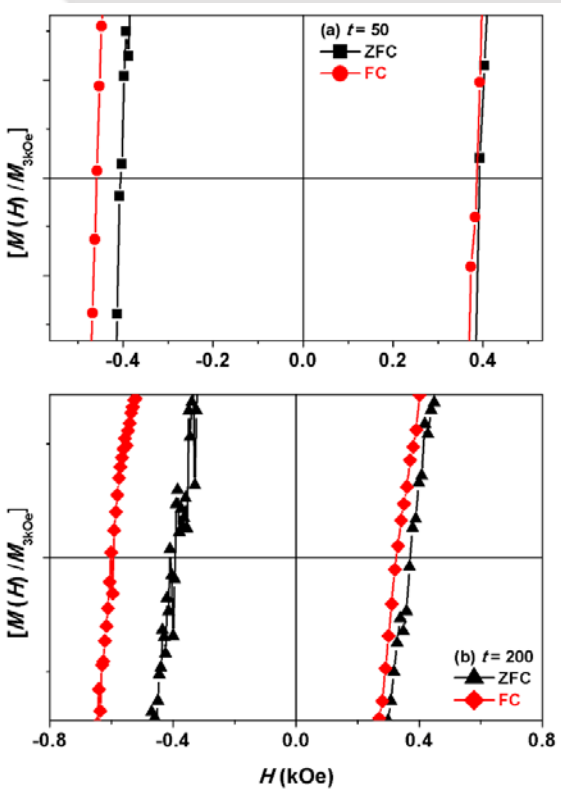

Figure 6.13: Expanded view of *M-H* loops measured under ZFC and FC conditions at 30 K for (a) 50 nm and (b) 200 nm thick Ni films annealed at 400 °C.

To understand the exchange interaction between the Ni and NiO phases and the resulting magnetic properties of the annealed Ni films in more details, we have carried out *M-H* loops at different temperatures under zero-field-cooled (ZFC) and field-cooled (FC) conditions for selected samples with different ratio of Ni and NiO phases. Figure 6.12 displays the typical *M-H* loops of 50 nm and 200 nm thick Ni films annealed at 400 °C. The structural properties revealed that these films have thickness dependent oxidation process [see Figure 6.03(b)], i.e., the relative intensity of the Ni peak over NiO peak decreases with increasing *t* from 50 to 200 nm. For the ZFC cases, (i) the loops exhibit large reversal of magnetization close to H_C and the area under the loop increases without any noticeable changes in the loop shape with decreasing temperature. On the other hand, the shape of the loops is changed considerably for the FC cases, i.e., the magnetization reversing close to H_C decreases and loops are titled with decreasing temperature. In addition, the coercive field increases with decreasing temperatures and the loops are shifted to negative axis significantly, as shown in Figure 6.13.

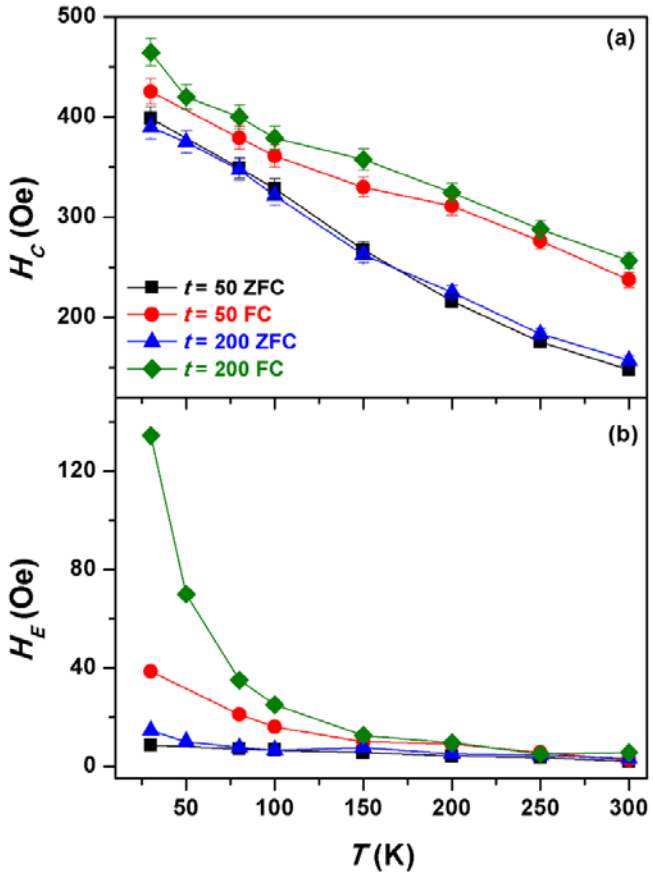

Figure 6.14: The variations of H_C and H_E with temperature for Ni thin films with different thicknesses annealed at 400 °C.

To study temperature dependent magnetic parameters, the extracted values of H_C and determined values of exchange bias, $[H_E = (|H_{C+}| - |H_{C-}|)/2]$ from the *M-H* loops are plotted as a function of temperature in Figure 6.14. It is clear from the figure that H_C increases almost linearly at a rate of 0.9641 Oe/K and 0.652 Oe/K for 50 nm and 200 nm thick films, respectively under ZFC with decreasing temperature. Upon FC, H_C increases linearly at a rate of 0.904 Oe/K and 0.702 Oe/K for 50 nm and 200 nm thick films, respectively with decreasing temperature. H_C is found to be larger for FC samples than the ZFC samples. This can be attributed to the enhanced anisotropy in the film due to the FC induced exchange interaction between Ni and NiO phases. H_E is observed to be small for the ZFC samples, but increases slightly with decreasing temperature. On the other hand, H_E of the FC samples is observed to be larger, but depends on the relative magnitude of Ni and NiO phases. A comparison between XRD results and magnetic properties reveals that H_E is notably larger for the FC films having larger NiO phase over Ni phase, which is also more sensitive to the measurement temperature.

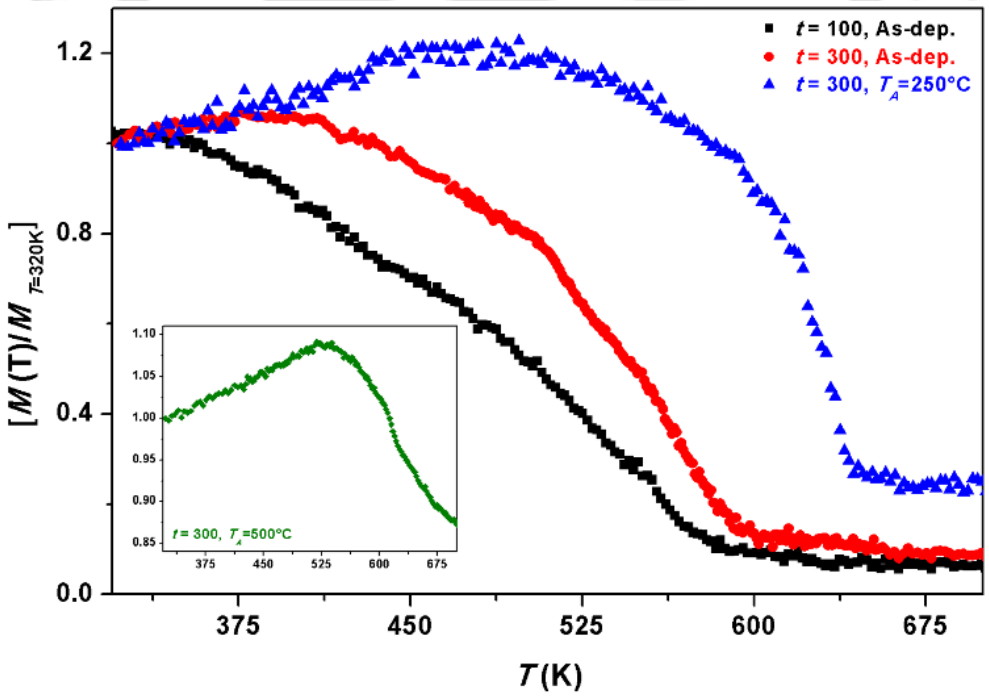

Figure 6.15: High temperature *M-T* data of as-deposited Ni thin films with different thicknesses and annealed Ni films at 250 °C and 500 °C (inset).

To understand the magnetic phase transition behaviour of the as-deposited and annealed Ni films, high temperature *M-T* data are measured using VSM at 2 kOe applied field for T_A < 500 °C and at 5 kOe for sample annealed at 500 °C. Figure 6.15 shows the

typical *M-T* curves obtained for as-deposited Ni films with different thicknesses (t = 100 and 300) and annealed Ni films (t = 300, T_A = 250 °C and 500 °C). In order to compare all the *M-T* curves, the magnetization data is normalized with respect to 320 K data for the respective samples and plotted the normalized magnetization as a function of temperature. It is clear from the figure that (i) For as-deposited Ni films, the magnetization decreases progressively with increasing temperature and approaches zero around 600 K. (ii) With increasing t from 100 to 300, the tendency of decrease of magnetization with increasing temperature changes and exhibits a sharp transition. In addition, the temperature at which magnetization approaches zero shifts to slightly higher temperature. This could be attributed to the thickness dependent magnetic phase transition in the as-deposited films due to size effect, which changes the spin-spin correlations lengths [ZHAN2001]. This thickness dependent effect has been reported to be strongly dependent on the substrates in which the films are grown [BABE1996]. On the other hand, the Ni (300 nm) film annealed at 250 °C shows a clear sharp magnetic phase transition with T_C, determined from thermal derivative of the magnetization data, of about 625 K. This is close to the value obtained for bulk Ni [FERT1991]. D_{Ni} calculated from XRD data for this film is about 24 nm, which is much larger than D_{Ni} (< 10 nm) obtained for as-deposited Ni films. On further increasing T_A = 500 °C, the magnetization increases gradually up to 525 K and then decreases above 525 K. This could be attributed to the formation of complete NiO with AFM nature. Hence, the value of T_N is determined from peak in the *M–T* curve and found to be nearly 525 K. This is in good agreement with the T_N of bulk NiO [ADLE1970].

6.3.5. Electrical properties

To study the effect of film thickness in the as-deposited films and effect of oxidation in the annealed films on the electrical resistivity behaviour, the sheet resistance of the as-deposited and annealed films is measured at room temperature using PPMS system with four- and two-probe techniques. Figure 6.16 displays the typical sheet resistance of as-deposited Ni and annealed Ni films as a function of t and T_A. For as-deposited films, the resistance decreases largely with increasing thickness for lower thickness films and then tend to saturate for higher thickness films. This is in good agreement with the earlier reported results on similar systems [GALK1962, LIGO2001, LIUH2001]. The variation of resistance with film thickness indicates a considerable thickness dependent roughness scattering [NAMB1970] in addition to surface and interface scatterings [FUCH1938, SOND1952].

According to the model proposed by Namba [NAMB1970], the ratio of the roughness to mean free path of the conduction electrons enhances the resistivity of the as-deposited films largely at lower thickness. This model also agrees with thickness dependence of the resistivity predicted by Fuchs-Sondheimer theory [FUCH1938, SOND1952], when the ratio of the roughness to mean free path of the conduction electrons turns out to be zero. Many of the earlier published results on the resistivity properties of the simple metallic thin films agreed with this model and showed linear variations of resistance when resistance plotted as a function of inverse of film thickness [LIGO2001, LIUH2001].

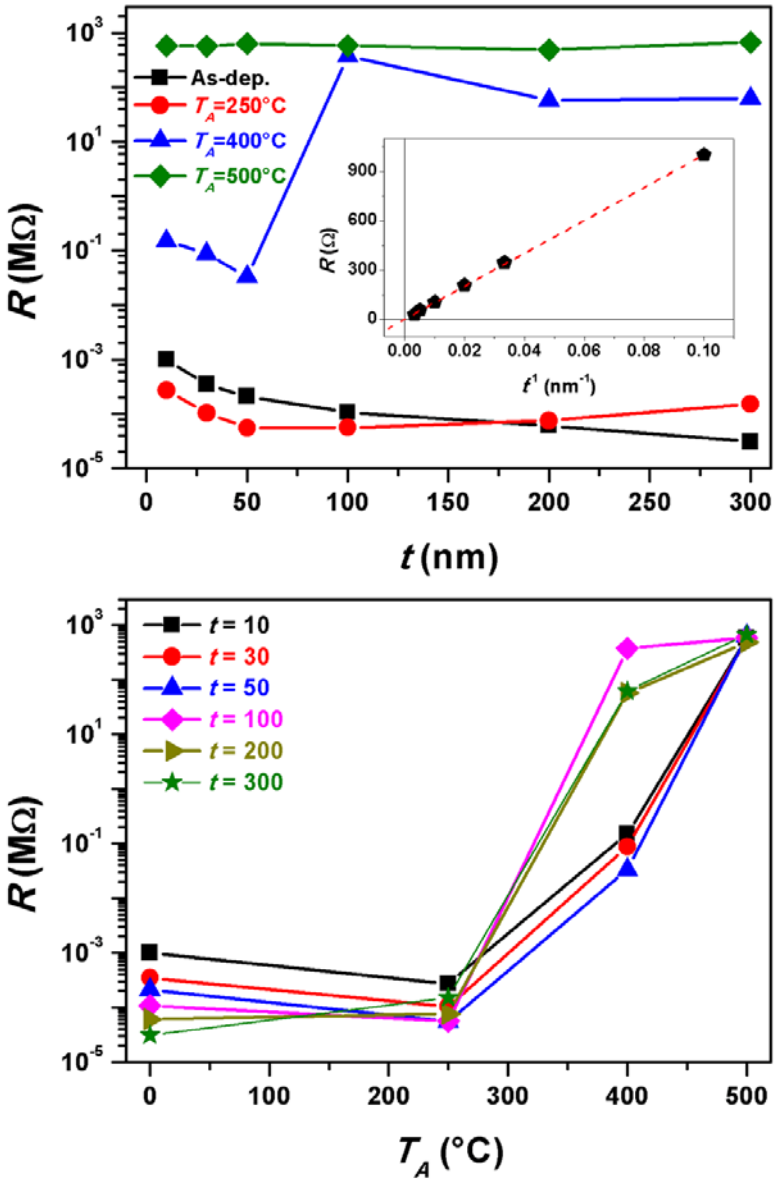

Figure 6.16: Thickness dependent electrical resistance of as-deposited and annealed Ni thin films at different T_A: 250, 400 and 500 °C.

Hence, to understand the thickness dependence of the resistance in the presently investigated films, we plot the variation of resistance as a function of inverse of thickness in the inset of Figure 6.16(a). The plot leads to a clear straight line behaviour for the whole thickness range of 10 nm to 300 nm in the present investigation and the linear fitting to the data crosses almost the origin of the plot with the slope, representing the limit resistivity value, as 9.95μΩ-m. On the other hand, the resistance of the annealed films strongly depends on T_A. For the films annealed at 250 °C, the resistance decreases marginally at lower thickness up to 50 nm due to strain relaxation in the as-deposited films, but increases with the further increase in thickness. This could be correlated to the formation of oxide (NiO) phase on the surface of the films, as evidenced from XRD and FE-SEM images. With increasing T_A to 400 °C, the resistance of the films increases largely as compared to as-deposited films and films annealed at 250 °C. This is due to the formation of clear NiO phases on the top surface of the films. It may be noted from the structural properties that the relative phases of NiO over Ni increases with increasing *t*. Therefore, the resistance increases for the films with thickness larger than 50 nm. On further increasing T_A to 500 °C, all the films exhibit very large resistance on the order of 10^8 Ω mainly due to the complete oxidation of Ni into NiO. This is in close agreement with the earlier results on NiO thin films [MORI1954, VARK1993, PEJO2000, VENT2011]. On the other hand, the plot of resistance versus T_A for different film thickness shows that the resistance increases largely for the higher thickness films as compared low thickness films when Ni and NiO phases co-exists. Nevertheless, the complete oxidation of Ni films displays nearly similar range of resistance for all the films of present investigation.

The above results clearly demonstrate the thickness dependent oxidation behaviour in Ni thin films and systematic control of Ni and NiO phases in annealed Ni films. This results in tunable magnetic properties by optimizing *t* and T_A, which are possibly potential candidates for memory and spintronic applications.

6.4. Summary

We have studied the effect of film thickness in the as-deposited Ni films and thickness dependent oxidation process in annealed Ni films exposed to air annealing and the resulting vibrational, magnetic and electrical properties of the Ni films deposited directly on thermally oxidized Si substrate using magnetron sputtering technique at ambient

temperature. The salient feature of the Ni thin films from the current investigations are as follows:

- All the as-deposited Ni films exhibit *fcc* structure and highly orient along (111) plane. The as-deposited Ni films show smaller crystals with large lattice constant at lower films thickness (< 50 nm) and the lattice constant decreases with increasing film thickness approaching to its bulk value.
- With increasing annealing temperature, the lattice constant decreases towards bulk Ni value due to the improvement in crystallization and further reduces below bulk Ni value for thickness more than 50 nm due to the formation of NiO phase caused by the oxidation process. The relative fraction of Ni and NiO phase in annealed films up to 400 °C strongly depends on the thickness due to thickness dependent oxidation process. Annealing Ni films at 500 °C results into complete oxidation of Ni into granular type NiO films.
- XRR studies reveal that the thermal oxidation process occurs from the surface of the films converting Ni into NiO through layer by layer process, which is again subtle to the thickness of the films.
- Raman spectra show that the intensity ratio between the 1P LO band and 2P LO band decreases and intensity of 2M band increases with increasing t for the films annealed at particular T_A. This suggests the growth of the NiO grains not only increases with increasing T_A, but also with t.
- As-deposited films exhibit ferromagnetism at room temperature. The presence of Ni and NiO crystallites in the annealed films implies the coexistence of ferromagnetic and antiferromagnetic interactions, leading to tunable exchange bias under zero-field-cooled and field-cooled conditions. The amount of exchange bias strongly depends on the ratio of Ni to NiO phases in the annealed Ni films.
- The electrical resistance of the as-deposited Ni films decreases largely with increasing t and follows the model proposed by Namba. Upon annealing, the resistance increases largely due to the formation of NiO phase. Furthermore, the increase in resistance strongly on t due to thickness dependent oxidation process.
- A close correlation between the structural, magnetic and electrical resistance properties is observed for all the as-deposited and annealed films. The observed results are explained on the basis of thickness dependent thermal oxidation process with increasing annealing temperatures.

Chapter 7

Summary and scope for future work

The overall summary of the salient results obtained on (a) the structural, vibrational, electronic, magnetic and resonance properties of pure un-milled NiO, milled NiO and annealed NiO powders and (b) the structural, vibrational, magnetic and electrical properties of as-deposited and annealed NiO and Ni thin films prepared by sputtering technique is listed in this chapter. Highlights of the current investigations and the possibilities for future work are also summarized below:

7.1. Summary of the results

Nanocrystalline NiO powders were prepared by ball mill process under dry mill conditions in high energy planetary ball mill filled with high purity argon gas. Systematic studies of the evolution of nanocrystalline structure, vibrational, electronic, magnetic and resonance properties of NiO powders were carried out as a function of milling speed to tune the properties of NiO powders. The milled NiO powders were subsequently heat treated at elevated temperatures under air atmosphere and the changes occurring in the structure and physical properties of the annealed powders were evaluated to study the origin of ferromagnetism in nanocrystalline NiO powders. Subsequently, NiO targets were prepared from the milled NiO powders with different crystallites and fabricated NiO thin films with different thicknesses directly on thermally oxidized Si substrate at ambient temperature. The effects of initial crystal size of the NiO powders used for fabricating NiO target on the dynamics of thickness dependent thermal decomposition and the resulting magnetic properties of NiO thin films were investigated. To compare the results of samples annealed under vacuum conditions, the as-deposited NiO films were also post annealed under oxygen environment. Finally, the fabrication of NiO thin films was also attempted through thermal oxidation of Ni thin films and investigated the effect of thickness dependent phase formation, nature of oxidation mechanism and the effect of thermal oxidation on vibrational, magnetic and electrical transport properties.

Structural evolution in NiO powders during the course of milling at different milling speeds and annealing at different temperatures, and in NiO and Ni thin films during the course of fabrication and annealing was analyzed from the X-ray diffraction (XRD) using Williamson-Hall plot and Modified Williamson-Hall plot methods and microscopy techniques. The physical properties of the NiO powders and NiO thin films were characterized using Raman spectroscopy, X-ray photoelectron spectroscopy, Electron spin resonance spectroscopy, Vibrating sample magnetometer and Physical property measurement system.

For NiO powders, the ball mill process produced single phase face centered cubic (*fcc*) nanocrystalline NiO powders with the average crystallite size of nanometer range without any

impurities within the detection limit of the techniques utilized. The average crystallite size decreased and lattice constant increased with increasing milling speed. Microstructural studies revealed that the agglomeration of fine particles increased with increasing milling speed and the nanocrystalline powders exhibited irregular shapes with broad size distribution. Raman spectra showed that two-magnon band associated with Ni^{2+}-O^{2-}-Ni^{2+} super-exchange interaction and observed in pure un-milled NiO powder disappeared dramatically, 1P LO band dominated along with considerable broadening, 2P TO and 2P TO+LO bands disappeared, 2P LO band broadened and shifted to lower value of Raman shift in milled NiO powders due to defects, size reduction and size-induced phonon confinement. This changed the color of the powder from the pale green for pure un-milled NiO into dark green for milled NiO powders due to non-stoichiometry, which was evidenced clearly from X-ray photoelectron spectroscopy (XPS) spectra. AFM nature of the un-milled NiO powders transformed into induced FM after milling due to defects and size reduction. The average room temperature magnetization increased with increasing milling speed and obtained a maximum magnetization of 1.26 emu/g at 12 kOe applied field for the NiO powders milled at 600 rpm. High temperature magnetization obtained in the temperature range between 300 K and 1000 K showed a well-defined magnetic phase transition at high temperature around 780 K due to induced FM phase. Electron paramagnetic resonance (EPR) results disclosed a close correlation with magnetic properties. Annealing of as-milled NiO powders resulted in a large reduction in magnetization, but the rate of reduction in magnetization strongly dependent on the milling speed. Furthermore, the annealing studies confirmed the origin of FM as intrinsic one due to defects, size reduction and non-stoichiometry.

For NiO thin films, all the as-deposited NiO films exhibited *fcc* structure and highly oriented along (200) plane. The as-deposited NiO films showed large lattice constant due to the existence of interstitial argon atoms in the sputtered films and/or increase of nickel vacancies created from the non-stoichiometry. With increasing annealing temperature, the lattice constant and strain decreased due to the release of interstitial argon atoms. The observation of thickness dependent decomposition reaction of NiO into Ni under vacuum annealing was explained based on the ideal model. However, the decomposition reaction was completely suppressed for the NiO films annealed under oxygen condition. The effect of initial crystallite size of the target powders on the thermal decomposition of the sputtered NiO films revealed a considerable decrease in the decomposition temperature (by about 100 °C) for the NiO films. All the as-deposited and annealed NiO films up to 400 °C (300 °C) under vacuum condition prepared from the NiO target made using 350 (600) rpm milled NiO powders showed

only AFM nature. On further increasing annealing temperature, NiO decomposed into Ni and exhibited room temperature ferromagnetism. The amount of induced ferromagnetism strongly dependent on the NiO film thickness. On the other hand, NiO thin films annealed at 500 ℃ under oxygen atmosphere exhibited AFM nature. A close correlation between the structural and magnetic properties was observed for all the NiO films. The observed results were explained on the basis of thickness dependent thermal decomposition with increasing annealing temperatures under different environments.

The development of NiO thin films had also been attempted through alternative method of thermal oxidation of Ni thin films under air atmosphere. For pure Ni thin films, all the as-deposited films exhibited *fcc* structure and highly oriented along (111) plane. The as-deposited Ni films showed smaller Ni crystals with large lattice constant at lower films thickness (< 50 nm) and the lattice constant decreased with increasing film thickness, approaching to its bulk value. With increasing annealing temperature, the lattice constant decreased towards bulk Ni value due to the improvement in crystallization and further reduced below bulk Ni value for thickness more than 50 nm due to the formation of NiO phase caused by the oxidation process. The relative fraction of Ni and NiO phases in annealed films up to 400 ℃ strongly dependent on the thickness due to thickness dependent oxidation process. Annealing Ni films at 500 ℃ resulted into complete oxidation of Ni into granular type NiO films. XRR studies revealed that the thermal oxidation process occurs from the surface of the films converting Ni into NiO through layer by layer process, which was again subtle to the thickness of the films. Raman spectra showed that the intensity ratio between the 1P LO band and 2P LO band decreased and intensity of 2M band increased with increasing film thickness for the films annealed at particular temperature. This suggested the growth of the NiO grains not only increased with increasing annealing temperature, but also with increasing film thickness. As-deposited films exhibited ferromagnetism at room temperature. The presence of Ni and NiO crystallites in the annealed films implied coexistence of ferromagnetic and antiferromagnetic interactions, leading to tunable exchange bias under zero-field-cooled and field-cooled conditions. The amount of exchange bias strongly dependent on the ratio of Ni to NiO phases in the annealed Ni films. The electrical resistance of the as-deposited Ni films decreased largely with increasing film thickness and followed the model proposed by Namba. Upon annealing, the resistance increased largely due to the formation of NiO phase. Furthermore, the increase in resistance strongly on the film thickness due to thickness dependent oxidation process. A close correlation between the structural, magnetic and electrical resistance properties was observed

for all the as-deposited and annealed films. The observed results were explained on the basis of thickness dependent thermal oxidation process with increasing annealing temperatures.

The present studies have brought out several interesting results which contribute to (i) the understanding of physical properties in nanocrystalline NiO powders under different milling speed conditions and (ii) the study of thickness dependent thermal decomposition of NiO into Ni and thickness dependent thermal oxidation of Ni into NiO and the resulting ferromagnetic properties with tunable competing exchange interaction between Ni and NiO phases. These studies have also revealed the strong correlation between structure, vibrational, electronic, magnetic, resonance and electrical properties of NiO prepared under optimum conditions.

7.2. Scope for future work

The present investigations on milled and annealed NiO powders revealed that there are several aspects of interest in these materials. A study of the local environment of Ni and O in these powders milled for various milling speeds (at lower speeds) would help in understanding (i) the development of defects such as vacancies of Ni and O, (ii) the oxidation and reduction of Ni during milling and annealing, respectively, and (ii) the manner in which the super-exchange interaction fades away with decreasing the average crystal size and increasing defects. In the case of thin films, the as-deposited NiO thin films showed AFM nature despite having fine crystallites below 10 nm. However, the careful literature reveals that the nanoscale sized NiO produce either ferromagnetism or superparamagnetism. Hence, the systematic investigation of NiO thin films with different thicknesses using X-ray photoelectron spectroscopy would reveal the stoichiometric nature of Ni and O in the as-deposited NiO thin films. X-ray magnetic circular dichroism studies on the pure and milled NiO thin films would reveal the magnetic interactions in these films and might provide insights on enhancing the magnetic properties. For the case of Ni thin film, the XRR results suggested the formation of layer-by-layer oxidation of Ni into NiO. Although the FE-SEM studies supported the formation of NiO from top surface, a detailed analysis of thermal oxidation of Ni using cross sectional transmission electron microscopy would reveal the nature of oxidation mechanism markedly and the artificial engineering of structural and magnetic properties of low dimensional metallic thin films by modulating surface and interface morphology. The detailed study as a function of thickness would reveal the growth rate, surface reaction and oxygen diffusion systematically and to enable these types of controlled decomposition in NiO and thermal oxidation in Ni for suitable application such as Resistive random access memory and semiconductor spintronics.

References

[ABDE2016] Abdel-Karim R, Electrodeposition of Composite Materials, Edt. Mohamed A. M. A, Golden T.D, INTECH open science, ISBN: 978-953-51-2270-8, http://dx.doi.org/10.5772/62189.

[ACHA2013] Acharyya D, Hazra A, Dutta K, Gupta R. K, Bhattacharyya P, Sem. Sci. Tech. 28 (2013) 125001.

[ADHI2017] Adhikari S, Madras G, Phys. Chem. Chem. Phys. 19 (2017) 13895.

[ADLE1970] Adler D, Feinleib J, Phys. Rev. B 2 (1970) 3112.

[AHMA2006] Ahmad T, Ramanujachary K. V, Lofland S. E, Ganguli A. K, Solid State Sci. 8 (2006) 425.

[ALSE2014] Al-Sehemi A. G, Al-Shihri A. S, Kalam A, Du G, Ahmad T, J. Molecular Struc. 1058 (2014) 56.

[ANDE1955] Anderson P. W, Hasegawa H, Phys. Rev. 100 (1955) 675.

[ANDE1958] Anderson P. W, Phys. Rev. 109 (1958) 1492.

[ANDE1992] Andersson S, Dzhavadov L, J. Phys.: Condens. Matter 4 (1992) 6209.

[ANDO2015] Ando Y, Jpn. J. Appl. Phys. 54 (2015) 070101.

[ARAG2012] Aragon F. H, de Souza P. E. N, Caoquira J. A. H, Hidalgo P, and Gouvea D, Phys. B 407, 2601 (2012).

[AYYU1995] Ayyub P, Palkar V. R, Chattopadhyay S, Multani M, Phys. Rev. B 51 (1995) 6135.

[BABE1996] Baberschke K, Appl. Phys. A 62 (1996) 417.

[BAND2016] Bandyopadhyay S, Cahay M, Introduction to Spintronics, 2nd Edition, CRC Press, Taylor & Francis Group, London (2016).

[BANE2007] Banerjee S, Mandal M, Gayathri N, Sardar M, Appl. Phys. Lett. 91 (2007) 182501.

[BARA2014] Barani A, Aghazadeh M, Ganjali M. R, Sabour B, Barmi A. A. M, and Davand S, Mater. Sci. Sem. Process. 23 (2014) 85.

[BASO1964] Basolo F, Johnson R. C, Coordination Chemistry; the Chemistry of Metals Complexes, Benjamin W. A, New York (1964).

[BATL2002] Batlle X, Labarta A, J. Phys. D 35 (2002) R15.

[BENA2014] Ben Amor M, Boukhachem A, Boubaker K, Amlouk M, Mater. Sci. Semi. Proc. 27 (2014) 994.

[BERK1999] Berkowitz A. E, Takano K, J. Magn. Magn. Mater. 200 (1999) 552.

[BERT1971] Bertel L. C, Morosin B, Phys. Rev. B 3 (1971) 1039.

[BHUA2012] Bhuadur N, R. Govind R. P, Chand S, and Kotnala R. K, Mat. Chem. Phys. 133 (2012) 471.

[BHUY2015] Bhuyan R, PhD Thesis, Indian Institute of Technology Guwahati (2015).

[BINN2002] Binns C, Baker S. H, Maher M. J, Louch S, Thornton S. C, Edmonds K. W, Dhesi S. S, Brookes N. B, Phys. Status Solidi A 189 (2002) 339.

[BIRK2006] Birks N, Meier G. H, Pettit F. S, Introduction to the high temperature oxidation of metals, 2nd Ed. Cambridge University Press (2006).

[BLIN1996] Blinowski J, Kacman P, Majewski J. A, Phys. Rev. B 53 (1996) 9524.

[BLUN2003] Blundell S, Magnetism in Condensed Matter, Oxford University Press, Chapter 3 (2003).

[BOUZ2003] Bouzerar G, Kudrnovsky J, Bergqvist L, Bruno P, Phys. Rev. B 68 (2003) 081203(R).

[BRAN1992] Brandes E. A, Brook G. B, Smithells Metals Reference Book 7th edn, Butterworth-Heinemann, UK (1992).

[BRAN2008] Brandon D, Kaplan W.D, Microstructural Characterization of Materials, Wiley, UK (2008).

[BROW1963] Brown W. F, Jr., Phys. Rev. 130 (1963) 1677.

[BRUC2003] Bruckner W, Kaltofen R, Thomas J, Hecker M, Uhlemann M, Oswald S, Elefant D, Schneider C M, J. Appl. Phys. 94 (2003) 4853.

[BRUM2001] Brumage W. H, Dorman C. F, Quade C. R, Phys. Rev. B 63 (2001) 104411.

[CAIG2016] Cai G, Wang J, Lee P. S, Acc. Chem. Res. 49 (2016) 1469.

[CAOD2015] Cao D, Jin C, Pan L, Wang J, Liu Q, IEEE International Magnetics Conference (INTERMAG-2015), CQ-07.

[CAZZ2003] Cazzanelli E, Kuzmin A, Mariotto G, Ulmane N. M, J. Phys. Condens. Matter. 15 (2003) 2045.

[CHAN2002] Chan I. M, Hsu T. Y, Hong F. C, Appl. Phys. Lett. 81 (2002) 1899.

[CHAN2007] Chang Y. H, Park C. H, Sato K, Katayama-Yoshida H, Phys. Rev. B 76 (2007) 125211.

[CHEN2013] Chen X, Liu L, Liu Z, Marcus M. A, Wang W. C, Oyler N. A, Grass M. E, Mao B, Glans P. A, Yu P. Y, Guo J, Mao S. S, Scientific Reports 3 (2013) 1510.

[CHEN2015] Chen Y, Sun Y, Dai X, Zhang B, Ye Z, Wang M, Wu J, Thin Solid Films 592 (2015) 195.

[CHIN1984] Ching W. Y, Song L. W and Jaswal S. S Phys. Rev. B 30 (1984) 544

[COEY2004] Coey J. M. D, Douvails A. P, Fitzgerald C. B, Venkatesan M, Appl. Phys. Lett. 84 (2004) 1332.

[COEY2010] Coey J. M. D, Magnetism and Magnetic Materials, Cambridge university press, Cambridge (2010).

[COPP2013] Copper J. F. K, Lonescu A, Langford R. M, Ziebeck K. R. A, Barnes C. H. W, Gruar R, Tighe C, Darr J. A, Thanh N. T. K, Ouladdiaf B, J. Appl. Phys. 114 (2013) 083906.

[COUR2008] Courtade L, Turquat Ch, Muller Ch, Lisoni J G, Goux L, Wouters D J, Goguenheim D, Roussel P, Ortega L, Thin Solid Films 516 (2008) 4083.

[CULL2001] Cullity B. D, Stock S. R, Elements of X-ray diffraction, 3rd Ed., Pearson Education, Boston (2001).

[DASJ2015] Das J, Krishnakumar S. R. Menon. Applied Surface Science 359 (2015) 61.

[DELB2008] Del Bianco L, Boscherini F, Fiorini A. L, Tamisari M, Spizzo F, Antisari M. V, Piscopiello E, Phys. Rev. B 77 (2008) 094408.

[DIET1997] Dietl T, Haury A, d'Aubigne Y. M, Phys. Rev. B 55 (1997) R33447(R).

[DIET2000] Dietl T, Ohno H, Matsukura F, Cibert J, Ferrand D, Science 287 (2000) 1019.

[DING2001] Ding J, Li Y, Chen L. F, Deng C. R, Shi Y, Chow Y. S, Gang T. B, J. Alloys Compd. 314 (2001) 262.

[DOBR2005] Dobrynin A. N, Levlev D. N, Temst K, Lievens P, Margueritat J, Gonzalo J, Afonso C. N, Zhou S. Q, Vantomme A, Piscopiello E, Van Tendeloo G, Appl. Phys. Lett. 87 (2005) 012501.

[DOOL1994] Dooley K. M, Chen S. Y, Ross J. R. H, J. Catalysis, 145 (1994) 402.

[DORM1997] Dormann J. L, Fiorani D, Tronc E, Adv. Chem. Phys. 98 (1997) 283.

[DRAG2016] Dragos O, Chiriac H, Lupu N, Grigoras M, Tabakovic I, J. Electrochem. Soc. 163 (2016) D83.

[DUAN2012] Duan W. J, Lu S. H, Wu Z. L, Wang Y. S, J. Phys. Chem. C 116 (2012) 26043.

[DUOL2010] Duo L, Finazzi M, Ciccacci F, Magnetic Properties of Antiferromagnetic Oxide Materials: surfaces, interfaces and thin films, Wiley-VCH Verlag GmbH & Co, Weinheim (2010).

[DUTT2010] Dutta T, Gupta P, Gupta A, Narayan J, J. Appl. Phys. 108 (2010) 083715.

[DZYA1958] Dzyaloshinsky I, J. Phys. Chem. Solids 4 (1958) 241.

[EKUM2011] Ekuma C. E, Bagayoko D, Japn. J. Appl. Phys. 50 (2011) 101103.

[FANY2013] Fan Y, Smith K. J, Lüpke G, Hanbicki A. T, Goswami R, Li C. H, Zhao H. B, Jonker B. T, Nature Nanotechnology 8 (2013) 438.

[FERT1991] Fert A, Guntherodt G, Heinrich B, Marinero E. E, Maurer M, Elsevier Science Publishers, North-Holland (1991).

[FEYG2010] Feygenson M, Kou A, Kreno L. E, Tiano A. L, Patete J. M, Zhang F, Kim M. S, Solovyov V, Wong S. S, Aronson M. C, Phys. Rev. B 81 (2010) 014420.

[FIOR2005] Fiorani D, Surface effects in magnetic nanoparticles, New York, XIV USA: Springer (2005) 300.

[FUCH1938] Fuchs K, Proc. Cambridge Philos. Soc. 34 (1938) 100.

[FUJI1993] Fujii E, Tomozawa, Fujii S, Torii H, Hattori M, Takayama R, Jpn. J. Appl. Phys. Part 2 32 (1993) L1448.

[GALK1962] Galkina O. S, Chernikova L. A, Chang K. T, Kondorskii E. I, Sov. Phys. JETP 14 (1962) 1254.

[GAND2011] Gandhi A. C, Huang C. Y, Yang C. C, Chan T. S, Cheng C. L, Ma Y. R, Wu S. Y, Nanoscale Res. Lett. 6 (2011) 485.

[GAND2013] Gandhi A. C, Pant J, Swarada, Pandit D, Sunanda K. Dalimbkar, Chan T. S, Cheng C. L, Ma Y. R, and Wu S. Y, J. Phys. Chem. C 117 (2013) 18666.

[GAOJ2008] Gao J. H, Girard Y, Repain V, Tejeda A, Belkhou R, Rougemaille N, Chacon C, Rodary G, and Rousset S, Phys. Rev. B 77 (2008) 134429.

[GHOS2006] Ghosh M, Biswas K, Sundaresana A, Rao C. N. R, J. Mater. Chem. 16 (2006) 106.

[GOOD1995] Goodenough J. B, Phys. Rev. 100 (1995) 564.

[GOPI2008] Gopinadhan K, Kashyap S. C, Pandya D. K, Chaudhary S, J. Phys.: Condens. Matter 20 (2008) 125208.

[GORR2009] Gorria P, Martínez-Blanco D, Pérez M. J, Blanco J. A, Hernando A, Laguna-Marco M. A, Haskel D, Souza-Neto N, Ronald I. Smith, William G. Marshall, Garbarino G, Mezouar M, Fernández-Martínez A, Chaboy J, Fernandez Barquín L, Rodriguez Castrillón J. A, Moldovan M, García Alonso J I, Zhang J, Llobet A, Jiang J. S, Phys. Rev. B 80 (2009) 064421.

[GOUX2010] Goux L, Lisoni J. G, Jurczak M, Wouters D. J, Courtade L, Muller C, J. Appl. Phys. 107 (2010) 024512.

[GROS2006] Grosvenor A. P, Biesinger M. C, Smart R. C. St, McIntyre N. S, Surf. Sci. 600 (2006) 1771.

[HAUG2003] Haugsrud H, Corros. Sci. 45 (2003) 211.

[HAYN2012] Haynes W. M, CRC Handbook of Chemistry and Physics, 93rd ed., CRC, Taylor and Francis Group, Florida (2012).

[HEDI2014] Hedin E. R, Joe Y. S, Spintronics in Nanoscale Devices, CRC Press, USA (2014).

[HEJH2008] He J. H, Yuan S. L, Tian Z. M, Yin Y. S, Li P, Wang Y. Q, Liu K. L,Yuan S. J, Wang X. L, Liu L, J. Magn. Magn. Mater. 320 (2008) 3293.

[HELI2011] He L, Zhi-M L, Han-C. W, Xiao-Xue T, Xu D. S, Graham L. W. Cross,Georg S. Duesberg,I. V. Shvets,and Da-Peng Yu Nano Lett. 11 (2011) 4601.

[HEMM2015] Hemmous M, Layadi A, Kerkache L, Tiercelin N, Preobrazhensky V, Pernod P, Metall. Mater. Trans. A 46(9) (2015) 4143.

[HEIS1928] Heisenberg V. W, für. Z. Phys. 49 (1928) 619.

[HOCH2006] Ho C. H, Lai C. H, IEEE Trans. Magn. 42 (2006) 3069.

[HONG2006] Hong N. H, Sakai J, Poirot N, Brize V, Phys. Rev. B 73 (2006) 132404.

[HONG2007] Hong N. H, Sakai J, Brize V, J. Phys.: Condens. Matter 19 (2007) 036219.

[HORS2006] Horst C, Saito T, Smith L, Handbook of materials measurements methods, Springer, Berlin (2006).

[HOTO2000] Hotový I, Huran J, Spiess L, Čapkovic R, Š. Haščík, Vacuum 58 (2000) 300.

[HOTO2004] Hotovy I, Huran J, Spiess L, J. Mater. Sci. 39 (2004) 2609.

[HTTP0001] https://www.jsap.or.jp/english/images/academic_roadmap/arm_e_11.pdf.

[HULL2001] Hull D, Bacon D. J, Introduction to Dislocations, 4th Ed., Pergamon Press, Oxford (2001).

[HUNG2017] Hung M-Y, Hahn C, Chang H, Wu M, Ohldag H, Kent A. D, AIP Adv. 7 (2017) 055903.

[HWAN1998] Hwang D. G, Lee S. S, and Park C. M, Appl. Phys. Lett. 72 (1998) 2162.

[ICHI2003] Ichiyanagi Y, Wakabayashi N, Yamazaki J, Yamada S, Kimishima Y, Komatsu E, Tajima H, Physica B 329 (2003) 862.

[JAGO2009] Jagodic M, Jaglicic Z, Jelen A, Lee J. B, Kim Y. M, Kim H. J, Dolinsek J, J. Phys.: Condens. Matter. 21 (2009) 215302.

[JAME2001] Jamet M, Wernsdorfer W, Thirion C, Mailly D, Dupuis V, Melinon P, Perez A, Phys. Rev. Lett. 86 (2001) 4676.

[JAME2004] Jamet M, Wernsdorfer W, Thirion C, Dupuis V, Mélinon P, Pérez L, Mailly D, Phys. Rev. B 69 (2004) 024401.

[JANG2009] Jang W. L, Lu Y. M, Hwang W. S, Hsiung T. L, Wang H. P, Appl. Phys. Lett. 94 (2009) 062103.

[JANG2011] Jang W. L, Lu Y. M, Hwang W. S, Dong C. L, Hsieh P. H, Chen C. L, Chan T. S, Lee J. F, Europhys. Lett. 96 (2011) 37009.

[JANS2004] Jan Svoboda, Magnetic Techniques for the Treatment of Materials, Kluwer Academic Publishers, Dordrecht (2004).

[JIAN2002] Jiang S. R, Yan P. X, Feng B. X, Cai X. M, Wang J, Mater. Chem. Phys. 77 (2002) 384.

[JILE1997] Jiles. D, Introduction to Magnetism and Magnetic Materials, Chapman and Hall, Boca Raton (1997).

[JING2006] Jing L, Xin B, Yuan F, Xue L, Wang B, Fu H, The J. Phys. Chem. B 110 (2006) 17860.

[JING2015] Jing M. J, Wang C. W, Hou H. S, Wu Z. B, Zhu Y. R, Yang Y. C, Jia X. N, Zhang Y, Ji X. B, J. Power Sources 298 (2015) 241.

[JUAN2014] Juang J, Chen C-Y, Yang C-F, Proceedings of the 2nd International Conference on Intelligent Technologies and Engineering System, Springer Science & Business, New York (2014).

[JUND2006] Jundwirth T, Sinova J, Masek J, Kucera J, MacDeonald A. H, Rev. Mod. Phys. 78 (2006) 809.

[KAIH1993] Kai H. Y, "Nanocrystalline Materials, A Study on their Preparation and Characterization," Ph.D. Thesis, University of Amsterdam, (1993).

[KAKA2014] Kakazey M, Vlasova M, Vorobiev Y, Leon I, Gonezalez M. C, and Urbiola E. A. C, Physica B 453 (2014) 116.

[KALI2008] Kalita M. P. C, Perumal A, Srinivasan A, J. Magn. Magn. Mater. 320 (2008) 2780.

[KANA1959] Kanamori J, J. Phys. Chem Solids 10 (1959) 87.

[KART2011] Karthik K, Selvan G. K, Kanagaraj M, Arumugam S, Jaya N. V, J. Alloys. Compd. 509 (2011) 181.

[KASU1956] Kasuya T, Prog. Thror. Phys. 16 (1956) 58.

[KAWA2010] Kawai M, Ito K, Ichikawa N, Shimakawa Y, Appl. Phys. Lett. 96 (2010) 072106.

[KEEM2010] Keemenovic A, Antic B, Vucinic-vasic M, Colomban P, Jovalekic C, Bibic N, Kahlenberg V, and Leoni M, J. Appl. Crystallography 43 (2010) 699.

[KEFF1957] Keffer F, O'Sullivan W, Phys. Rev 108 (1957) 637.

[KHAI2012] Khairya M, El-Safty S. A, Ismaela M, Kawarada H, Applied Catalysis B: Environmental 127 (2012) 1.

[KHEM2011] Khemprasit J, Kaen-Ngam S, Khumpaitool B, Kamkhou P, J. Magn. Magn. Mater. 323 (2011) 2408.

[KIMD2012] Kim D. S, Lee H. C, J. Appl. Phys. 112 (2012) 034504.

[KISA2014] Kisan B, Shyni P. C, Layek S, Verma H. C, Hesp D, Dhanak V, Krishnamurthy S, Perumal A, IEEE Trans. Magn. 50 (2014) 2300704.

[KISA2015] Kisan B, Ravikumar P, Das A, Srinivasan A, Perumal A, Sci. Lett. 4 (2015) 160.

[KISA2017] Kisan B, Ph.D. Thesis, Indian Institute of Technology Guwahati, Guwahati (2017).

[KITT2004] Kittel C, Introduction to Solid state Physics, 7th edn Wiley, Singapore (2004).

[KOCH2006] Koch C. C, Nanostructured materials: Processing, properties and potential applications, Noyes Publications, New York (2006).

[KODA1997] Kodama R. H, Makhlouf S. A, Berkowitz A. E, Phys. Rev. Lett. 79 (1997) 1393.

[KODA19991] Kodama R. H, Berkowitz A. E, Phys. Rev. B 59 (1999) 6321.

[KODA19992] Kodama R. H, J. Magn. Magn. Mater. 200 (1999) 359.

[KRAM1934] Kramers H. A, Physica 1 (1934) 182.

[KRON2003] Kronmuller H, Fahnle M, Micromagnetism and the Microstructure of Ferromagnetic Solids, Cambridge University Press, New York (2003).

[KUDR2004] Kudrnovsky J, Turek L, Drchal V, Maca F, Weiberger P, Bruno P, Phys. Rev. B 69 (2004) 115208.

[KUOT2011] Kuo T. Y, Chen S. C, Peng W. C, Lin Y. C, Lin H. C, Thin Solid Films 519 (2011) 4940.

[LABA2005] Labarta A, Batle X, Iglesias O, Surface Effects in Magnetic Nanoparticles; Fiorani, D, (Edts.) Springer: Berlin/Heidelberg, Germany (2005) 105.

[LEGE1972] Leger J. M, Susse C. L, Vodar B, Phys. Rev. B 6 (1972) 4250.

[LIER2002] Lierop J. V, Lewis L. H, Williams K. E, Gambino R J, J. Appl. Phys. 91 (2002) 7233.

[LIGO2001] Ligot J, Benayoun S, Hantzpergue J, J. Vac. Sci. Tech. 19 (2001) 798.

[LIM2000] Li M, Hebenstreit W, Diebold U, Tyryshkin A. M, Bowman M. K, Dunham G. G, Hendersan M. A, J. Chem. Phys. B 104 (2000) 4944.

[LILL2006] Li L, Chen L, Qihe R, Li G, Appl. Phys. Lett. 89 (2006) 134102.

[LINY20061] Lin Y. H, Wang J, Cai J, Ying M, Zhao R, Li M, Nan C. W, Phys. Rev. B 73 (2006) 193308.

[LINY20062] Lin Y. H, Zhao R, Nan C. W, Ying M, Kobayashi M, Ooki Y, Fujimori A, Appl. Phys. Lett. 89 (2006) 202501.

[LINY2011] Lin Y-H, Zhan B, Nan C-W, Zhao R, Xu X, Kobayashi M, J. Appl. Phys. 110 (2011) 043921.

[LIUC2005] Liu C, Yun F, Mokoc H, J. Mater. Sci.: Mater. Electron.16 (2005) 555.

[LIUC2016] Liu C, Li C, Ahmed K, Mutlu Z, Ozkan C. S, Ozkan M, Sci. Rep. 6 (2016) 29183.

[LIUH2001] Liu H. D, Zhao Y. P, Ramanath G, Murarka S. P, Wang G. C, Thin Solid Films 384 (2001) 151.

[LIUH2015] Liu H. L, Skeren T, Volodin A, Temst K, Vantomee A, Haesendonck C. V, Phys. Rev. B 91 (2015) 104403.

[LIUX2013] Liu X, Gao S, Xu H, Lou Z, Wang W, Huang B, Dai Y, Nanoscale 5 (2013) 1870.

[LIUY2017] Liu Y, Xu L, Zhao C, Shao M, Hu B, Phys. Chem. Chem. Phys. 19 (2017) 14793.

[LIX2007] Li X, Xia C, Pei G, He X, J. Phys. Chem. Solids 68 (2007) 1836.

[LIXI2010] Li X, Dhanabalan A, Bechtold K, Wang C, Electro. Chem. Commun. 12 (2010) 1222.

[LUIS2002] Luis F, Torres J. M, Garcaí L. M, Bartolomé J, Stankiewicz J, Petroff F, Fettar F, Maurice J. L, Vaurès A, Phys. Rev. B 65 (2002) 094409.

[LUML2011] Lu M. L, Lin T. Y, Weng T. M, Chen Y. F, Opt. Express 19 (2011) 16266.

[LUOX2015] Luo X, Tseng L. T, Li S, Yi J. B, Mater. Sci. Semicond Proc. 30 (2015) 228.

[LUOY2012] Luo Y. D, Lin Y. H, Feng Y. N, Zhang Y. J, Yu Song, Shen Y, Wen C, J. Appl. Phys. 112 (2012) 116101.

[LYUK2010] Lyu K. K, Phan T. L, Yu S. C, Oh S. K, Dan N. H, IEEE Trans. Magn. 46 (2010) 2028.

[MAKH2002] Makhlouf S. A, J. Magn. Magn. Mater. 246 (2002) 184.

[MAKH2008] Makhlouf S. A, Al-Attar H, Kodama R. H, Sol. State Commun. 145 (2008) 1.

[MAKO2009] Makovec D, Kodre A, Arčon I, Drofenik M, J. Nanoparticle Res., 11 (2009) 1145.

[MAND2009] Mandal S, Banerjee S, Menon K. S. R, Phys. Rev. B 80 (2009) 214420.

[MAND2011] Mandal S, Menon K. S. R, Mahatha S. K, Banerjee S, Appl. Phys. Lett. 99 (2011) 232507.

[MANN2008] Manna S, Deb A. K, Jagannath J, De S. K, J. Phys. Chem. C 112 (2008) 10659.

[MAST2014] Master R, Karandikar M, Jambhale R, Tarachand, Shukla D. K., Choudhary R. J., Phase D. M, J. Physics: Conf. Series 534 (2014) 012025.

[MATS2001] Matsumoto Y, Murakami M, Shono T, Hasegawa T, Fukumura T, Kawasaki M, Ahmet P, Chikyow T, Koshihara S, Koinuma H, Science 291 (2001) 854.

[MEIK1956] Meiklejohn W. H, Bean C. P, Phys. Rev. 105 (1956) 904.

[MENE2010] Meneses C. T, Duque J. G. S, de Biasi E, Nunes W. C, Sharma S. K, Knobel M, J. Appl. Phys. 108 (2010) 013909.

[MHAD2010] Mhadhbi M, Khitouni M, Escoda L, Sunol J. J, Mater. Lett. 64 (2010) 1802.

[MILL1994] Miller M. S, Stageberg F. E, Chow Y. M, Rook K, Heuer L A, J. Appl. Phys. 75 (1994) 5779.

[MILL1997] Miller E. L, Rocheleau R. E, J. Electron Soc. 144 (1997) 3072.

[MINK2007] Min K. C, Kim M, You, Y. H, Lee S. S, Lee Y. K, Chung T. M, Kim C. G, Hwang J. H, An K. S, Lee N. S, Kim Y. Surf. Coatings Tech. 201 (2007) 9252.

[MISH2004] Mishra S. R, Losby J, Dubenko I, Roy S, Ali N, Marasinghe K, J. Magn. Magn. Mater. 279 (2004) 111.

[MORI1954] Morin, F. J, Phys. Rev. 93 (1954) 1199.

[MORI1960] Moriya T, Phys. Rev. 120 (1960) 91.

[MORU2013] Mørup S, Brok E, Frandsen C, J. Nanomaterials 720629 (2013) 1.

[MOSS2011] Mossanek R. J. O, Preda I, Abbate M, Rubio-Zuazo J, Castro G. R, Vollmer A, Gutierrez A, Soriano L, Chem. Phys. Lett. 501 (2011) 437.

[NACE2007] Nacereddine C, Layadi A, Guittoum A, Cherif S. M, Chauveau T, Billet D, Youssef J. B, Bourzami A, Bourahli M.-H, Mater. Sci. Eng. B 136 (2007) 97.

[NADO2002] Nadolny A. J, Sadowski J, Taliashvili B, Areiszewska M, Dobrowolski W, Domukhovski V, Lusakowska E, Myeielski A, Osinniy V, Story T, Swiatek K, Galazka, Diduszko R, J. Mag. Magn. Mater. 248 (2002) 134.

[NALA2012] Nalage S. R, Chougule M. A, Sen S, Joshi P. B, Patil V. B, Thin Solid Films 520 (2012) 4835.

[NAMB1970] Namba Y, Jpn. J. Appl. Phys. 9 (1970) 1326.

[NEAL1994] Neal H. B, Theory of Magnetic Recording, Cambridge University Press, New York (1994).

[NEEL1949] Néel L, Ann. Geophys. (C.N.R.S.) 5 (1949) 99.

[NEEL1962] Néel L in: C. Dewitt, B. Dreyfus, P. D. de Gennes (Eds.), Low Temperature Physics, Gordon and Breach, New York (1962) 413.

[NUNE1998] Nunes A. C, Yang L, Surf. Sci. 399 (1998) 225.

[OHAN2000] O'Handley R. C, Modern Magnetic Materials Principles and Applications, Wiley, New York (2000).

[OHJH2013] Oh J. H, Hwang S. Y, Kim Y. D, Song J. H, Seong T Y, Mater. Sci. Semicond. Process 16 (2013) 1346.

[OHNO1998] Ohno H, Science 281 (1998) 951.

[OHRI1992] Ohring M, Materials Science of Thin Films, Academic Press, London (1992).

[OLIV2016] Sean M. Oliver, Jessamyn A. Fairfield, Allen T. Bellew, Sunghun Lee, James G. Champlain, Laura B. Ruppalt, John J. Boland, and Patrick M. Vora Appl. Phys. Lett. 109 (2016) 203101.

[PADH2017] Padhan A. M, Sathish M, Saravanan P, Perumal A, J. Phys. D: Appl. Phys. 50 (2017) 21LT01.

[PANK2003] Pankhurst Q. A, Connolly J, Jones S. K, and Dobson J, J. Phys. D: Appl. Phys. 36 R167 (2003).

[PANX2013] Pan X, Yang M. Q, Fu X, Zhang N, Xu Y. J, Nanoscale 5 (2013) 3601.

[PEAR2003] Pearton S. J, Abernathy C. R, Norton D. P, Hebard A. F, Park Y. D, Boatner L. A, Budai J. D, Mat. Sci. Engg. R 40 (2003) 137.

[PECK2011] Peck M. A, Huh Y, Skomski R, Zhang R, Kharel P, Allison M. D, Sellmyer D. J, Langell M. A, J. Appl. Phys. 109 (2011) 07B518.

[PECK2012] Peck M. A, Langell M. A, Chem. Mater. 24 (2012) 4483.

[PEJO2000] Pejova B, Kocareva T, Najdoski M, Grozdanov I, Appl. Surf. Sci. 165 (2000) 271.

[PINN1979] Pinnel M. R, Tompkins H.G, Heath D.E, J. Electrochem. Soc. 126(7) (1979) 1274.

[PODI2010] Podila R, Queen W, Nath A, Arantes J. T, Schoenhalz A. L, Fazzio A, Dalpian G. M, He J, Hwu S. J, Skove M. J, Rao A. M, Nano Lett. 10 (2010) 1383.

[PRED2008] Preda I, Gutiérrez A, Abbate M, Yubero F, Méndez J, Alvarez L, Soriano L, Phys. Rev. B 77 (2008) 075411.

[PROE2011] Proenca M. P, Sousa C. T, Pereira A. M, Tavares P. B, Ventura J, Vazquez M, Araujo J. P, Phys. Chem. Chem. Phys. 13 (2011) 9561.

[PUNN2002] Punnoose A, Seehra M. S, J. Appl. Phys. 91 (2002) 7766.

[QIXW2016] Qi X, Zheng W, Li X, He G, Sci. Rep. 6 (2016) 33241.

[RAJA2016] Rajagopal R V, Sekhar Reddy P. R, Neelakanta Reddy I, Choi C. J, RSC Adv. 6 (2016) 105761.

[RAMC2004] Ramchandran S, Tiwari A, Narayan J, Appl. Phys. Lett. 84 (2004) 5255.

[RAVI2015] Ravikumar P, Kisan B, Perumal A, AIP Advances 5 (2015) 087116.

[RAVI2016] Ravikumar P, Kisan B, Perumal A, J. Magn. Magn. Mater. 418 (2016) 86.

[REIM1993] Reimer L, Transmission Electron Microscopy, Springer-verlag, Germany (1993).

[RESP1998] Respaud M, Broto J. M, Rakoto H, Fert A. R, Thomas L, Barbara B, Verelst M, Snoeck E, Lecante P, Mosset A, Osuna J, Ely T. O, Amiens C, Chaudret B, Phys. Rev. B 57 (1998) 2925.

[REVE1996] Reves A, Ungar T, Borbely A, Lendvai J, Nano. Mat. 7 (1996) 779.

[RICH1956] Richardson J. T, Milligan W. O, Phys. Rev. 102 (1956) 1289.

[RINA2014] Rinaldi-Montes N, Gorria P, Martınez-Blanco D, Fuertes A. B, Fern´andez Barquın L, Rodrıguez Fernandez J, de Pedro I, Fdez-Gubieda M. L, Alonso J, Olivi L, Aquilanti G, Blanco J. A, Nanoscale 6 (2014) 457.

[RISB2003] Risbud A. S, Spaldin N. A, Chen Z. Q, Stemmer S, Seshadri R, Phys. Rev. B 68 (2003) 205202.

[ROBE1984] Roberts M. W, Smart R. S. C, J. Chem. Soc., Faraday Trans. 1, 80 (1984) 2957.

[RODE2003] Rode K, Anane A, Mattana R, Contour J. P, Durand O, LeBourgeois R, Appl. Phys. 93 (2003) 7676.

[ROTH1958] Roth W. L, Phys. Rev. 110 (1958) 1333.

[ROYA2004] Aparna Roy, V. Srinivas V, Ram S, J. A. De Toro J. A. D, Riveiro J. M, J. Appl. Phys. 96 (2004) 6782.

[RUDE1954] Ruderman M. A, Kittel C, Phys. Rev. 96 (1954) 99.

[RUMP2007] Rumpf K, Granitzer P, Polt P, Reichmann A, Krenn H, J. Magn. Magn. Mater. 316 (2007) 114.

[SAMA2012] Samardak A. S, Sukovatitsina E. V, Ognev A. V, Chebotkevich L. Mahmoodi R, Peighambari S. M, Hosseini M. G, Nasirpouri F, Journal of Physics: Conference Series 345 (2012) 012011.

[SANY2008] Sanyal D, Roy T. K, Chakrabarti M, Dechoudhury S, Bhowmick D, Chakrabarti A. J. Phys.: Condens. Matter. 20 (2008) 045217.

[SANZ1996] Sanz J. M, Tyuliev G. T, Surf. Sci. 367 (1996) 196.

[SASI2002] Sasi B, Gopchandran K. G, Manoj P. K, Koshy P, Prabhakara Rao P, Vaidyan V K, Vacuum 68 (2002) 149.

[SATO2015] Sato K, Saitoh E, Spintronics for next generation innovative devices, Wiley Series in materials for electronic & optoelectronic applications, Willoughby A, Capper P, Kasap S (Edts). Wiley, UK (2015).

[SARM2010] Sarma S. K, Vargas J. M, Biasi E De, Beron F, Knobel M, Pirota K. R, Meneses C. T, Kumar S, Lee C. G, Pagliuso P. G, Rettori C, Nanotechnology 21 (2010) 035602.

[SCHA2016] Schapers T, Semiconductor spintronics, Walter de Gruyter GmbH & Co KG, Germany (2016).

[SEEH2005] Seehra M. S, Shim H, Dutta P, Manivannan A, Bonevich J, J. Appl. Phys. 97 (2005) 10J509.

[SESH2002] Seshan K, Handbook of Thin-film Deposition Processes and Techniques: Principles, Methods, Equipment, and Applications, Noyes publication, New York (2002).

[SHAN2016] Shang T, Zhan Q. F, Yang H. L, Zuo Z. H, Xie Y. L, Liu L. P, Zhang S. L, Zhang Y, Li H. H, Wang B. M, Wu Y. H, Zhang S, Li R. W, Appl. Phys. Lett. 109 (2016) 032410.

[SHAR2003] Sharma P, Gupta A, Rao K. V, Owens F. J, Sharma R, Ahuja R, Guillen J. M. O, Johansson B, Gehring G. A, Nat. Mater. 2 (2003) 673.

[SHAR2014] Sharma R, Acharya A.D, Shrivastava S. B, Shripathi T, Ganesan V, Optik 125 (2014) 6751.

[SHEN2005] Shen T. D, Schwarz R. B, Thompson J. D, Phys. Rev. B 72 (2005) 014431.

[SHIH2014] Shih Y. T, Su C. Y, Tsai C. W, Pan W, AIP Adv. 04 (2014) 027117.

[SHIM2008] Shim H, Dutta P, Seehra M. S, Bonevich J, Solid State Commun. 145 (2008) 192.

[SHIN2003] Shinde S. R, Ogale S. B, Das Sarma S, Simpson J. R, Drew H. D, Lofland S. E, Lanci C, Buban J. P, Browning N. D, Kulkarni V. N, J. Higgins, Sharma R. P, Greene R. L, Venkatesan T, Phys. Rev. B 67 (2003) 115211.

[SHIN2004] Shinde S. R, Ogale S. B, Higgins J. S, Zheng H, Millis A. J, Kulkarni V. N, Ramesh R, Greene R. L, Venkatesan T, Phys. Rev. Lett. 92 (2004) 166601.

[SIEG1967] Siegbahn K, Nordling C, Fahlman A, Nordberg R, Hamrin K, Hedman J, Johansson G, Bergmark T, Kerlsson S. E, Lindgren I, Lindberg B, Nova Acta Regiae Soc. Sci., Ser IV 20 (1967).

[SNIG1997] Snigirev O.V, Andreev E, and Tishin A. M, Gudoshnikov S. A, J. Bohr Phys. Rev. B 21 (1997) 55.

[SOND1952] Sondheimer E. H, Adv. Phys. 1 (1952) 1.

[SONI2001] Soni P. R, Mechanical alloying: Fundamental and applications, Cambridge International Science Publishing, UK (2001).

[SORI2007] Soriano L, Preda I, Gutiérrez A, Palacín S, Abbate M, Vollmer A, Phys. Rev. B 75 (2007) 233417.

[SRIR2013] Sriram S, Thaymanavan A, Int. J. Mat. Sci. Engg. 1 (2013) 118.

[STAM2008] Stamataki M, Tsamakis D, Brilis N, Fasaki I, Giannoudakos A, Kompitsas M Phys. Status Solidi A 205 (2008) 2064.

[STEI2010] Steineback H, Kannan S, Rieth L, and Solzbacher F, Sens. Actuators B 151 (2010) 162.

[STOR1986] Story T, Galstroka-cedillazka R R, Frankel R. B, Wolff P. A, Phys. Rev. Lett. 56 (1986) 777.

[SUGI2013] Sugiyama I, Shibata N, Wang Z, Kobayashi S, Yamamoto T, Ikuhara Y, Nature Nanotechnology 8 (2013) 266.

[SUJ2013] Su J, Zou X. X, Zou Y. C, Li G. D, Wang P. P, Chen J. S, Inorganic Chemistry 52 (2013) 5924.

[SUND2006] Sundaresan A, Bhargavi R, Rangarajan N, Siddesh U, Rao C. N. R, Phys. Rev. B 74 (2006) 161306.

[SUND2009] Sundaresan A, Rao C. N. R, Nano Today, 4 (2009) 96.

[SURY2001] Suryanarayana C, Prog. Mater. Sci. 46 (2001) 1.

[SURY2004] Suryanarayana C, Mechanical alloying and Milling, Marcel Dekker, NewYork (2004).

[TADI2011] Tadic M, Panjan M, Markovi D, Milosevi I, Spasojevi V, J. Alloys Compd. 509 (2011) 7134.

[TAMU1969] Tamura K, Endo H, Phys. Lett. 29A (1969) 52.

[TAOD2004] Tao D, Wei F, Mater. Lett. 58 (2004) 3226.

[THEO2006] Theodoropouloua N, Misra V, Philip J, LeClair P, Berera G. P, Moodera J. S, Satpati B, Som T, J. Mag. Magn. Mater. 300 (2006) 407.

[THOT2007] Thota S, Kumar J, J. Phys. Chem. Solids 68 (2007) 1951.

[TIWA2005] Tiwari S. D, Rajeev K. P, Phys. Rev. B 72 (2005) 104433.

[TOKU2000] Tokura Y, Nagaosa N, Science 288 (2000) 462.

[TORR1991] Torrsi S. I. C, Gabrielli C, Goff A. H, Torresi R, J. Electrochem. Soc. 138 (1991) 1548.

[TSUN2000] Tsunekawa S, Ishikawa K, Li Z. Q, Kawazoe Y, Kasuya A, Phys. Rev. Lett. 85 (2000) 3440.

[TSYM2016] Tsymbal E. Y, Zutic I, Handbook of spin transport and magnetism, CRC press, New York (2016).

[UEDA2001] Ueda K, Tabata H, Kawai T, Appl. Phys. Lett. 79 (2001) 988.

[UHLE1992] Uhlenbrock S, Scharfschwerdt C, Neumann M, Illing G, Freund H. J, J. Phys. Condens. Matter 4 (1992) 7973.

[ULMA2007] Ulmane N. M, Kuzmin A, Steins I, Grabis J, Sildos I, Pärs M, J. Phys. Conf. series 93 (2007) 012039.

[ULMA2011] Ulmane N. M, Kuzmin A, Grabis J, Sildos I, Voronin V. I, Berger I. F, Kazantsev V. A, Sol. State Phenomena 168 (2011) 341.

[UNGA1991] Ungar T, Tichy G, Physica Status Solidi A 171 (1999) 425.

[UNGA1992] Ungar T, Dragomir I, Revesz A, Borbely A, J. Appl. Cryst. 32 (1999) 992.

[UNUT2017] Unutulmazsoy Y, Merkle R, Rastegar I, Maier J, Mannhart J, APL Mater. 5 (2017) 042302.

[VALL2012] Valladares L. D. L. S, Salinas D. H, Dominguez A. B, Najarro D. A, Khondaker S. I, Mitrelias T, Barnes C. H. W, Aguiar J. A, Majima Y, Thin Solid Films 520 (2012) 6368.

[VALL2014] Valladares L. D. L. S, Ionescu A, Holmes S, Barnes C. H. W, Domínguez A B, Quispe O. A, González J. C, Milana S, Barbone M, Ferrari A. C, Ramos H, Majima Y, J. Vac. Sci. Tech. 32 (2014) 051808.

[VARK1993] Varkey A. J, Fort A. F, Thin Solid Films 235 (1993) 47.

[VEGA2001] Vega D, Polla G, Leyva G, Konig P, Lanza H, Esteban A, Aliaga H, Causa M. T, Tovar M, Alascio B, J. Solid State Chem. 156 (2001) 458.

[VENT2011] Venter A, A, Botha J.R, S Afr J Sci 107(1/2) (2011) 268.

[VERM2015] Verma V, Katiyar M, J. Phys. D: Appl. Phys. 48 (2015) 235003.

[WAGE1994] Wagendristel A, Wang Y, An Introduction to Physics and Technology of Thin Films, World Scientific, Singapore, (1994).

[WANG1993] Wang L, Wang Z, Cao Y. J. Ceram. Soc. Jpn. 101 (1993) 227.

[WANG2002] Wang W. Z, Liu Y. K, Xu C. K, Zheng C. L, Wang G. H, Chem. Phys. Lett. 362 (2002) 119.

[WANG2005] Wang X, Song J, Gao L, Jin J, Zheng H, and Zhang Z, Nanotechnology 16, 37 (2005).

[WANG20051] Wang J, Cai J, Lin Y. H, Nan C. W, Appl. Phys. Lett. 87 (2005) 202501.

[WANG20052] Wang X, Song J, Gao L, Jin J, Zheng H, Zhang Z, Nanotechnology 16 (2005) 37.

[WANG2011] Wang X, Wan L, Yu T, Zhou Y, Guan J, Yu Z, Li Z, Zou Z, Mater. Chem. Phys. 126 (2011) 494.

[WANG20121] Wang G, Lu X, Zhai T, Ling Y, Wang H, Tong Y, Li Y, Nanoscale 4 (2012) 3123.

[WANG2013] Wang X. L, Ku P. S, Shao Q, Cheng W. F, Leung C. W, Ruotolo A, Appl. Phys. Lett. 103 (2013) 223508.

[WANG2015] Wang J, Wei X, Wangyang P, Nano scale Res. Lett. 10 (2015) 461.

[WILL1953] Williamson G. K, Hall W. H, Acta Met. 1 (1953) 22.

[WINK2005] Winkler E, Zysler R. D, Vasquez Mansilla M, Fiorani D, Phys. Rev. B 72 (2005) 132409.

[WINK2008] Winkler E, Zysler R. D, Mansilla M. V, Fiorani D, Rinaldi D, Vasilakaki M, Trohidou K. N, Nanotechnology 19 (2008) 185702.

[WRUC1991] Wruck D. A, Dixon M. A, Rubin M, Bogy S. N, J. Vac. Sci. Technol. A 9 (1991) 2170.

[WUJB2003] Wu J. B, Nan J, Nan C. W, Lin Y, Deng Y, Zhao S, Mater. Sci. Engg. B 99 (2003) 294.

[XIAN2002] Xiang L, Deng X. Y, and Jin Y, Scr. Mater. 47 (2002) 219.

[XIAN2016] Xiao W, Song W, Herng T. S, Qin Q, Yang Y, Zheng M, Hong X, Feng Y. P, and Ding J, Nanoscale, 8 (2016) 15737.

[XIEY2004] Xie Y, Blackman J. A, Phys. Rev. B 69 (2004) 172407.

[XUY2015] Xu Y, Awschalom D. D, J. Nitta, Handbook of Spintronics, Springer Netherlands (2015).

[YANG2005] Yang J. L, Lai Y. S, Chen J. S, Thin Solid Films 488 (2005) 242.

[YANG2008] Yang C. C, Li S, J. Phys. Chem. B 112 (2008) 14193.

[YANW2008] Yan W, Weng W, Zhang G, Sun Z, Liu Q, Pan Z, Guo Y, Xu P, Wei S, Zhang Y, Yan S, Appl. Phys. Lett. 92 (2008) 052508.

[YIAJ2004] Yia J. B, Zhoua Y. Z, J. Dinga J, Chowa G. M, Dongb Z L, Whiteb T, XingYu Gaoc, Weec A. T. S, Yud X. J Journal of Magnetism and Magnetic Materials 284 (2004) 303.

[YIJB2005] Yi J. B, J.Ding, Z. L. Zhao, B. H. Liu, J. Appl. Phys. 97 (2005) 10K306.

[YIJB2007] Yi J. B, Ding J, Feng Y. P, Peng G. W, Chow G. M, Kawazoe Y, Liu B.H, Yin J. H, Thongmee S, Phys. Rev. B 76 (2007) 224402.

[YOON2016] Yoon K. R, Ko J. W, Youn D.Y, Park C. B, Kim I.-D, Green Chem. 18 (2016) 944.

[YOOT2017] Yoo T, Nasir A. R, Bac S. K, Lee S, Choi S, Lee S, Liu X, and Furdyna J. K, AIP advances 7 (2017) 055819.

[YOSI1957] Yosida K, Phys. Rev 106 (1957) 893.

[YOUS2007] Youssef J. B, Castel V, Garello K, Gargam N, Pogossian S, Spenato D, Dekadjevi D T, Suvorova A, Charlton T. R, Dalgliesh R. M, Langridge S, Phys. Rev. B 76 (2007) 134401.

[ZHAN2001] Zhang R, Willis R. F, Phys. Rev. Lett. 86 (2001) 2665.

[ZHAN20121] Zhang K. H. L, McLeod I. M, Lahti M, Pussi K, Dhanak V. R, J. Phys.: Cond. Matter. 24 (2012) 435502.

[ZHAN2014] Zhang Y. J, Luo Y. D, Lin Y. H, Nan C. W, Appl. Phys. Lett. 104 (2014) 072402.

[ZHAN2016] Zhang J, Zeng D, Zhu Q, Wu J, Huang Q, Xie C, J. Phys. Chem. C 20 (2016) 3936.

[ZHAO2009] Zhao B, Ke X. K, Bao J. H, Wang C. L, Dong L, Chen Y. W, Chen H. L, J. Phys. Chem. C 113 (2009) 14440.

[ZHOU2007] Zhou Y. Z, Chen J. S, Tay B. K, Hu J. F, Chow G. M, Liu T, Yang P, Appl. Phys. Lett. 90 (2007) 043111.

[ZHUY2013] Zhu Y. G, Cao G. S, Sun C. Y, Xie J, Liu S. Y, Zhu T. J, Zho X. B, Yang H. Y, RSC Advances 3 (2013) 19409.

Publications

LIST OF PUBLICATIONS:

	Published:
[1].	Enhanced room temperature ferromagnetism in antiferromagnetic NiO nanoparticles, **Patta Ravikumar**, Bhagaban Kisan, and A. Perumal, AIP Advances 5 (2015) 087116.
[2].	Structural, vibrational, optical and magnetic properties of NiO nanoparticles, Bhagaban Kisan, **Patta Ravikumar**, A. Das, A. Srinivasan and A. Perumal, Science Letters Journal 4 (2015) 160.
[3].	Thickness dependent ferromagnetism in thermally decomposed NiO thin films, **Patta Ravikumar**, Bhagaban Kisan, A. Perumal, Journal of Magnetism and Magnetic Materials 418 (2016) 86.
[4].	Enhanced magnetic properties of NiO powders by the mechanical activation of aluminothermic reduction of NiO prepared by ball milling process, Aneeta Manjari Padhan, **Patta Ravikumar**, P. Saravanan, A. Perumal, Journal of Magnetism and Magnetic Materials 418 (2016) 253.
[5].	Effect of oxidation on the structural, vibrational, magnetic and electrical properties of Fe thin films, Amol Nande, **Patta Ravikumar**, and A. Perumal, AIP Conference Proceeding 1832 (2017) 130028.
	Under communication:
[6].	Thermal oxidation mechanism and magnetic properties of Ni thin films, **Patta Ravikumar**, Dolly Taparia, and A. Perumal, J. Phys. D: Applied Physics (under submission).
[7].	Effect of initial crystallite size of NiO target powder on the decomposition properties of NiO thin films, **Patta Ravikumar**, Bhagaban Kisan, and A. Perumal, Thin Solid Films (under submission).
[8].	Effect of annealing on the magnetic properties of milled NiO powders, **Patta Ravikumar**, Bhagaban Kisan, and A. Perumal, (under preparation).

PAPERS PRESENTED IN CONFERENCES:

[1].	Room temperature ferromagnetism in thermally decomposed NiO thin films Bhagaban Kisan, **Patta Ravikumar** and A. Perumal Presented in the Indo-Japan Workshop on Magnetism at Nanoscale (IJWMN), January 9-12, 2015, National Institute of Science Education and Research, Bhubaneswar, India.
[2].	Thickness dependent ferromagnetism in thermally decomposed NiO thin films, **Patta Ravikumar**, Bhagaban Kisan, A. Perumal, Presented in the International conference on magnetic materials and application (IC-MagMA)-2015, 2 – 4, Dec. 2015 at VIT University, Vellore, India.
[3].	Effect of oxidation on the structural, vibrational, magnetic and electrical properties of Fe thin films, Amol Nande, **Patta Ravikumar**, and A. Perumal, DAE Solid State Physics Symposium 2016, 26-30 December 2016, Bhubaneswar, Odisha, India.
[4].	Role of nanostructure on the magnetic properties of novel materials and its applications in future magnetoelectronics devices A. Perumal, K. Bhagaban, **Patta Ravikumar**, D. Camelia, Anabil Gayen, Anneta Padhan Manjari Invited Talk given in School of Physics, Madurai Kamaraj University, July 06, 2017.